AGARDograph 121

Techniques for Measurement of Dynamic Stability Derivatives in Ground Test Facilities

by C. J. Schueler, L. K. Ward and A. E. Hodapp, Jr

OCTOBER 1967

DISCLAIMER NOTICE

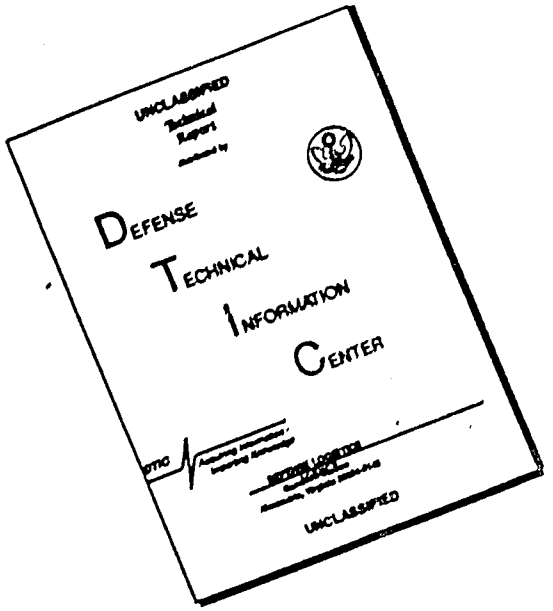

THIS DOCUMENT IS BEST QUALITY AVAILABLE. THE COPY FURNISHED TO DTIC CONTAINED A SIGNIFICANT NUMBER OF PAGES WHICH DO NOT REPRODUCE LEGIBLY.

AGARDograph 121

NORTH ATLANTIC TREATY ORGANIZATION

ADVISORY GROUP FOR AEROSPACE RESEARCH AND DEVELOPMENT

(ORGANISATION DU TRAITE DE L'ATLANTIQUE NORD)

TECHNIQUES FOR MEASUREMENT OF DYNAMIC STABILITY DERIVATIVES IN GROUND TEST FACILITIES

by

C.J.Schueler, L.K.Ward and A.E.Hodapp, Jr

October 1967

This is one of a series of publications by the AGARD-NATO Fluid Dynamics Panel.
Professor Wilbur C.Nelson of The University of Michigan is the editor.

SUMMARY

Some of the techniques in current use for measuring dynamic stability derivatives in wind tunnels are described, with emphasis given to the important features of balance system design, data reduction methods, instrumentation and typical balance systems. The use of gas bearings for dynamic stability and roll damping balances is treated and a three-degree-of-freedom balance system employing a spherical gas bearing is described.

RESUME

Quelques-unes des techniques courantes pour la mesure des dérivées de la stabilité dynamique dans les tunnels aérodynamiques sont décrivées en soulignant les particularités importantes du dessin des systèmes de compensation, des méthodes pour la réduction de données, l'instrumentation et des systèmes de compensation typiques. On trait l'emploi des paliers à gaz afin d'obtenir de stabilité dynamique et des compensateurs pour l'amortissement de roulis ainsi qu'un système de compensation en trois degrés de liberté avec l'utilisation d'un palier à gaz.

629.7.017.2:629.7.018.08

PREFACE

The authors wish to express their appreciation to the numerous organizations and individuals who supported the preparation of this AGARDograph by making information and material available.

In particular, the authors are indebted to the Arnold Engineering Development Center, Arnold Air Force Station, Tennessee, USA for approval of the use of AEDC material and assistance in preparation of the figures.

Personal thanks are extended to James C. Uselton for compiling information on Magnus force and moment testing, Dr W. S. Norman for his consultation on several of the sections, Arthur R. Wallace for checking portions of the manuscripts, Mrs L. F. Dean, Mrs J. A. Young, and Mrs W. C. Scott for typing the manuscript and reference research and to Mrs T. R. Hester for coordinating the preparation of illustration work.

CONTENTS

	Page
SUMMARY	ii
RESUME	ii
PREFACE	iii
LIST OF FIGURES	v
NOTATION AND ABBREVIATIONS	xi
1. INTRODUCTION	1
2. STATEMENT OF THE PROBLEM	3
2.1 DEVELOPMENT TRENDS	3
2.2 EQUATIONS OF MOTION	4
2.2.1 Axes Systems	4
2.2.2 Inertial Moments	5
2.2.3 Aerodynamic Moments	7
2.2.4 Single Degree of Freedom	9
2.2.5 Stability Derivative Coefficients	11
3. CAPTIVE MODEL TESTING TECHNIQUE	13
3.1 GENERAL DESCRIPTION OF TECHNIQUE	13
3.1.1 Model Pivots	13
3.1.2 Suspension System	18
3.1.3 Balance Tare Damping	21
3.2 DYNAMIC STABILITY DERIVATIVES - PITCH OR YAW	24
3.2.1 Theory	25
3.2.2 Representative Systems for Tests of Complete Models	55
3.2.3 Representative Systems for Tests of Control and Lifting Surfaces	69
3.3 DYNAMIC ROLL DERIVATIVES	71
3.3.1 Theory	71
3.3.2 Representative Systems	74
3.4 MAGNUS EFFECT	76
3.4.1 Types of Magnus Forces	76
3.4.2 Test Procedure	77
3.4.3 Representative Systems and Drive Units	77
3.5 PRESSURE MEASUREMENTS	81
3.5.1 Transducer Installation	82
3.5.2 Pressure System Response	82
3.5.3 Calibration Technique	83
REFERENCES	84
BIBLIOGRAPHY	92
FIGURES	120
DISTRIBUTION	

LIST OF FIGURES

		Page
Fig. 1	Methods of measuring dynamic stability derivatives	120
Fig. 2	Axes systems	121
Fig. 3	Orientation of coordinate systems	122
Fig. 4	Multipiece crossed flexures	123
Fig. 5	Cross-flexure, cruciform and torque tube pivots	124
Fig. 6	Small scale instrument flexure pivot	125
Fig. 7	Knife edge pivot	126
Fig. 8	Cone pivot - three degrees of freedom	126
Fig. 9	Ball bearing pivot	127
Fig. 10	High amplitude forced oscillation balance with ball bearing pivot	128
Fig. 11	Gas bearing pivot	129
Fig. 12	Gas bearing load characteristics	130
Fig. 13	Damping characteristics of AEDC-VKF gas bearing	131
Fig. 14	Gas bearing for roll-damping system	132
Fig. 15	Spherical gas bearing	132
Fig. 16	Two-dimensional oscillatory apparatus	133
Fig. 17	Half-model oscillating rig	134
Fig. 18	Half-models and reflection planes	135
Fig. 19	Support interference effects	
	(a) $M_\infty = 2.5$, $d_s/d = 0.4$, $\alpha = \pm 2$ deg	136
	(b) $M_\infty = 2.5$, $d_s/d = 0.8$, $\alpha = \pm 1.5$ deg	137
Fig. 20	Support interference effects	
	(a) $M_\infty = 3$, $d_s/d = 0.4$, $\alpha = \pm 2$ deg	138
	(b) $M_\infty = 3$, $d_s/d = 0.8$, $\alpha = \pm 1.5$ deg	139

		Page
Fig. 21	Support interference effects	
	(a) $M_\infty = 4$, $d_s/d = 0.4$, $\alpha = \pm 2$ deg	140
	(b) $M_\infty = 4$, $d_s/d = 0.8$, $\alpha = \pm 1.5$ deg	141
Fig. 22	Variation of static and dynamic stability coefficient and base pressure ratio with sting diameter for $l_s/d = 3$	142
Fig. 23	Model balance and support assembly for hotshot (AEDC-VKF Tunnel F) tunnel	143
Fig. 24	Free oscillation balance system	143
Fig. 25	Transverse rod and yoke system installed in test section tank	144
Fig. 26	Dynamic stability derivatives versus amplitude of oscillation, Mach 10	145
Fig. 27	Damping derivatives for the flared and straight afterbody configurations measured in conjunction with a series of simulated transverse rod configurations, forced-oscillation tests, amplitude 1.5 deg, Mach 5	146
Fig. 28	Magnetic suspension system, end view	147
Fig. 29	Basic "V" configuration magnetic suspension system	147
Fig. 30	Contribution of aerodynamic, still-air and structural damping to total damping	148
Fig. 31	Sketch of the vacuum system used to evaluate still-air damping	148
Fig. 32	Variation of structural damping with static pressure	149
Fig. 33	Variation of the ratio of model still-air damping to model aerodynamic damping with Mach number	149
Fig. 34	Variation of the angular viscous-damping-moment parameter with angular restoring-moment parameter	150
Fig. 35	Tricyclic pitching and yawing	150
Fig. 36	Typical free-flight epicyclic pitching and yawing motions of a nonrolling statically stable symmetrical missile	151
Fig. 37	Typical free-flight epicyclic pitching and yawing motions of a rolling statically stable symmetrical missile	151
Fig. 38	Typical free-flight pitching and yawing motion of rapidly rolling statically unstable symmetrical missile	152

		Page
Fig. 39	Motion transformation	152
Fig. 40	Complex angular motion	153
Fig. 41	Exponential decay of the modal vectors	153
Fig. 42	Phase diagram	154
Fig. 43	High frequency free-oscillation balance for Hotshot tunnel tests	155
Fig. 44	Model displacement system	156
Fig. 45	Free oscillation balance and displacement mechanism	157
Fig. 46	Large amplitude (±15 deg), free-oscillation balance	158
Fig. 47	Free-oscillation transverse rod balance	159
Fig. 48	Photographs of the free-oscillation (±35 deg) transverse rod balance	160
Fig. 49	Free-oscillation balance	161
Fig. 50	Transverse rod balance for low density hypersonic flow tunnel	162
Fig. 51	Photograph of the assembled balance	162
Fig. 52	Small scale free-oscillation balance	163
Fig. 53	Basic mass injection balance and porous model	163
Fig. 54	Dynamic stability balance suitable for gas injection	164
Fig. 55	Oltronix dampometer	165
Fig. 56	Typical calibrated slotted discs and principle of dampometer operation	165
Fig. 57	Free-oscillation data reduction	166
Fig. 58	Sting balance assembly of the forced-oscillation balance system	166
Fig. 59	Small amplitude (±3 deg), forced-oscillation balance	167
Fig. 60	Dynamic stability control and readout system	168
Fig. 61	On-line data system for forced-oscillation dynamic stability testing	169

		Page
Fig. 62	Control panel for forced-oscillation system	170
Fig. 63	Forced-oscillation balance	171
Fig. 64	System block diagram for forced-oscillation balance	172
Fig. 65	Photograph of the forward portion of the forced-oscillation balance mechanism	173
Fig. 66	Schematic view of model and driving-system components	174
Fig. 67	Details of oscillating mechanism	175
Fig. 68	Block diagram of electronic circuits used to measure model displacement of applied moment	176
Fig. 69	Forced-oscillation dynamic stability balance	177
Fig. 70	Yaw-roll balance and accelerometers	178
Fig. 71	Forced-oscillation balance with electromagnetic excitation	179
Fig. 72	Cutaway view of torsional flexure pivot with strain gages for forced-oscillation balance with electromagnetic excitation	179
Fig. 73	Magnetic model suspension system	180
Fig. 74	Cone model for magnetic suspension	181
Fig. 75	Basic L configuration magnetic suspension system	181
Fig. 76	Magnetic suspension system	182
Fig. 77	Magnetic suspension working section. 7 in. × 7 in. hypersonic wind tunnel	183
Fig. 78	Schematic diagram of the suspension magnet array of a six-component magnetic wind tunnel balance and suspension system	184
Fig. 79	Model subjected to a forced oscillation in roll while suspended in the six-component balance	185
Fig. 80	View of control surface drive	186
Fig. 81	Apparatus for elevator oscillation	187
Fig. 82	Apparatus for elevator oscillation	188
Fig. 83	Sketch of control surface plucking mechanism	189

		Page
Fig. 84	Elastic model suspension and electromagnetic oscillator for oscillation in pitch	190
Fig. 85	Free oscillation with automatically recycled feedback excitation	191
Fig. 86	Half-model oscillating rig	192
Fig. 87	Roll-damping system	193
Fig. 88	Air bearing roll-damping mechanism	193
Fig. 89	Air bearing roll-damping balance	194
Fig. 90	Dynamic steady-roll balance	195
Fig. 91	Forced-oscillation balance	196
Fig. 92	Pictorial drawing, forced-oscillation balance	197
Fig. 93	Illustrations of the various Magnus effects	
	(a) Magnus force at low angles of attack	198
	(b) Magnus force at large angles of attack	198
	(c) Magnus effects on canted fins	198
	(d) Magnus effects on driven fins	198
Fig. 94	Effect of spin parameter on the Magnus characteristics	199
Fig. 95	Effect of boundary layer on the Magnus force	200
Fig. 96	Electric motor drive Magnus force system	201
Fig. 97	Magnus force system, turbine drive within the model	201
Fig. 98	Magnus force system, turbine drive within the model	202
Fig. 99	Magnus force balance	203
Fig. 100	Magnus roll-damping balance with air bearings	203
Fig. 101	Variation of bearing temperature with spin rate for bypass air cooling	204
Fig. 102	Oil mist lubricating system and other instrumentation	205
Fig. 103	Two types of Magnus balance gage sections	
	(a) Sandia strain gage balance	206
	(b) AEDC-VKF strain gage balance	206

		Page
Fig. 104	Comparison of semiconductor and conventional gage outputs	207
Fig. 105	Experimental response magnitude and phase-angle calibration for 1.38 in. of 0.030 in. nominal-diameter tubing connected to a gage volume of 0.02 $in.^3$ for air at sea-level conditions	208
Fig. 106	Pump for sinusoidal oscillating pressure	209
Fig. 107	Cam-type pulsator calibrator	209

NOTATION AND ABBREVIATIONS

Notation

A	reference area or general constant
C	total damping coefficient or general constant
C_1	tare damping coefficient
$C_A(-C_x)$	total axial-force coefficient, $-2F_X/\rho_\infty V_c^2 A$
C_c	cross-wind coefficient, $2F_Y/\rho_\infty V_c^2 A$, $(C_Y = C_c)$
C_D	total drag coefficient, $2D/\rho_\infty V_c^2 A$
C_L	lift coefficient, $2L/\rho_\infty V_c^2 A$
C_l	rolling-moment coefficient, $2M_X/\rho_\infty V_c^2 Ad$
C_{lp}	$\partial C_l/\partial(Pd/2V_c)$
C_{lr}	$\partial C_l/\partial(rd/2V_c)$
$C_{l\beta}$	$\partial C_l/\partial\beta$
$C_{l\dot{\beta}}$	$\partial C_l/\partial(\dot{\beta}d/2V_c)$
$C_{l\delta^\star}$	$\partial C_l/\partial\delta^\star$
C_M	pitching moment coefficient of a model which has triagonal or greater symmetry, $2M_Y/\rho_\infty V_c^2 Ad$
$C_{Mp\alpha}$	$= C_{np\alpha} = C_{mp\beta}$
C_{Mq}	$= C_{nr} = C_{mq}$
$C_{M\alpha}$	$= C_{m\alpha} = -C_{n\beta}$
$C_{M\dot{\alpha}}$	$= C_{m\dot{\alpha}} = -C_{n\dot{\beta}}$
C_m	pitching moment coefficient, $2M_Y/\rho_\infty V_c^2 Ad$
C_{mpr}	$= \partial^2 C_m/\partial(Pd/2V_c)\partial(rd/2V_c)$
$C_{mp\beta}$	$= \partial^2 C_m/\partial(Pd/2V_c)\partial\beta$
$C_{mp\dot{\beta}}$	$= \partial^2 C_m/\partial(Pd/2V_c)\partial(\dot{\beta}d/2V_c)$
C_{mq}	$= \partial C_m/\partial(qd/2V_c)$

$C_{m\beta}$ = $\partial C_m/\partial\beta$

$C_{m\alpha}$ = $\partial C_m/\partial\alpha$

$C_{m\dot{\alpha}}$ = $\partial C_m/\partial(\dot{\alpha}d/2V_c)$

C_N $(-C_Z)$ normal force coefficient, $-2F_Z/\rho_\infty V_c^2 A$

C_{Nq} = $\partial C_N/\partial(qd/2V_c)$

$C_{N\alpha}$ = $\partial C_N/\partial\alpha$

$C_{N\dot{\alpha}}$ = $\partial C_N/\partial(\dot{\alpha}d/2V_c)$

C_n yawing moment coefficient, $2M_Z/\rho_\infty V_c^2 Ad$

C_{np} = $\partial C_n/\partial(Pd/2V_c)$

C_{npq} = $\partial^2 C_n/\partial(Pd/2V_c)\partial(qd/2V_c)$

$C_{np\alpha}$ = $\partial^2 C_n/\partial(Pd/2V_c)\partial\alpha$

$C_{np\dot{\alpha}}$ = $\partial^2 C_n/\partial(Pd/2V_c)\partial(\dot{\alpha}d/2V_c)$

C_{nr} = $\partial C_n/\partial(rd/2V_c)$

$C_{n\beta}$ = $\partial C_n/\partial\beta$

$C_{n\dot{\beta}}$ = $\partial C_n/\partial(\dot{\beta}d/2V_c)$

C_Y side force coefficient, $2F_Y/\rho_\infty V_c^2 A$

C_{yR} cycles to damp to a given amplitude ratio R

c velocity of sound in a cylindrical tube

D drag force or general constant

d model reference length, base diameter

d_s sting diameter

E voltage

F_X $(-F_A)$, F_Y, F_Z $(-F_N)$ forces along the XYZ axes, respectively

f frequency of oscillation

$f(\theta)$		viscous damping as a function of θ
$f(\theta_0)$		viscous damping as a function of θ_0
H_X, H_Y, H_Z		moments of momentum about the X , Y and Z axes, respectively
$\bar{H}$		angular momentum vector
I_X, I_Y, I_Z		mass moments of inertia about the X , Y and Z axes, respectively
i	$= \sqrt{(-1)}$	
$\bar{I}, \bar{J}, \bar{K}$		unit vectors in the X , Y and Z directions, respectively
$\hat{i}, \hat{j}, \hat{k}$		unit vectors in the $\tilde{X}$, $\tilde{Y}$ and $\tilde{Z}$ directions, respectively
J_{ZX}, J_{XY}, J_{YZ}		products of inertia
K		total stiffness
K_i		flexure stiffness
L		lift force
l		model length or tubing length
l_s		sting length of constant diameter
$\bar{M}$		vector resultant of the external moments acting on the model, $(M_X\bar{I} + M_y\bar{J} + M_Z\bar{K})$ or $(M_X\hat{i} + M_Y\hat{j} + M_Z\hat{k})$
M		moment about Y axis (M_Y)
M_i		out-of-phase moment
M_r		in-phase moment
M_X, M_Y, M_Z		moments about the X , Y and Z axes, respectively
M_{X_P}	$= \partial M_X/\partial P$	
$M_{X\delta^*}$	$= \partial M_X/\partial \delta^*$	
$M_{\dot{\alpha}}$	$= \partial M_Y/\partial \dot{\alpha}$	
M_θ	$= \partial M_Y/\partial \theta$	
$M_{\dot{\theta}}$	$= \partial M_Y/\partial \dot{\theta}$	
M_∞		free-stream Mach number

n		number
P, Q, R		scalar components of $\bar{\omega}$ in the X, Y and Z directions ($P = p_0 + p$, $Q = q_0 + q$, $R = r_0 + r$)
$\hat{P}$	=	$Pd/2V_c$
P_s		steady-state rolling velocity
p, q, r		perturbations of P, Q, R
p_i		input pressure
p_m		measured pressure at gage
p_b		model base pressure
p_∞		free-stream static pressure
$\bar{p}$		mean pressure
q_∞		free-stream dynamic pressure
R		ratio of final amplitude to initial amplitude
Re		free-stream unit Reynolds number
r		tubing radius or radial distance
t		time
U, V, W		scalar components of $\tilde{V}_c$ in the X, Y and Z directions ($U = u_0 + u$, $V = v_0 + v$, $W = w_0 + w$)
u, v, w		perturbations of U, V, W
V_c or V		velocity of the model center-of-gravity with respect to the media ($U\bar{i} + v\bar{j} + w\bar{k}$, $v_0 = w_0 = 0$)
V_g		volume of pressure gage
V_t		volume of tube
XYZ		body-fixed axes system (Fig. 3) or components of external forces
$X_e Y_e Z_e$		earth-fixed axes system (Fig. 2)
$\tilde{X}\ \tilde{Y}\ \tilde{Z}$		nonrolling axes system (Fig. 3)
$X_s Y_s Z_s$		stability axes system (Fig. 2)

$X_T Y_T Z_T$	tunnel-fixed axes system (inertial reference, Figure 3)
$X_w Y_w Z_w$	wind axes system (Fig. 2)
x, z	transfer distance
x_{cg}	distance from the model nose to the model pivot axis (rearward positive)
α	angle of attack
β	angle of side slip
γ	reference phase angle
Δ	log decrement
δ^*	control surface deflection angle
θ	instantaneous angular displacement from the reference flight condition
θ_i	out-of-phase position
θ_0	oscillation peak amplitude or initial amplitude
θ_r	in-phase position
λ	damping rate
μ	viscosity
ρ_∞	free-stream or ambient density
ξ	complex angle of attack $(v + iw)/V_c$ or, for small angular displacements, $\beta + i\alpha$
ϕ	arbitrary phase angle or roll perturbation
Ψ, Θ, Φ	Euler angles; angles of yaw, pitch and roll, Figure 2(b) ($\Psi = \psi_0 + \psi$, $\Theta = \theta_0 + \theta$, $\Phi = \phi_0 + \phi$)
ψ, θ, ϕ	perturbations of Ψ, Θ, Φ
$\bar{\Omega}$	vector angular velocity of the non-rolling coordinate system with respect to inertial space $(0\hat{i} + q\hat{j} + r\hat{k})$
ω	angular circular frequency
ω_d	natural damped circular frequency
$\bar{\omega}$	vector angular velocity of the body coordinate system with respect to inertial space $(P\bar{i} + q\bar{j} + \bar{r}k,\ q_0 = r_0 = 0)$

$\omega d/2V_\infty$	reduced frequency parameter
$(\dot{}), (\ddot{})$	first and second derivatives with respect to time t
$(\bar{})$	vector notation
$(\tilde{})$	nonrolling coordinate system notation

Subscripts

a	aerodynamic
t	tare
E	effective values
i	initial conditions
L	local values
0	initial pitch axis or reference flight conditions
1 or 2	new pitch axes, times, or nutation and precession modes
w	wind on
v	vacuum
∞	free-stream

Abbreviations

AEDC	Arnold Engineering Development Center (US Air Force), Arnold Center, Tennessee.
PWT	Propulsion Wind Tunnel Facility, AEDC.
VKF	von Kármán Gas Dynamics Facility, AEDC.
AGARD	Advisory Group for Aerospace Research and Development, a Division of the North Atlantic Treaty Organization, NATO.
BRL	Ballistic Research Laboratory, Aberdeen Proving Ground, Maryland.
DTMB	David Taylor Model Basin (US Navy), Carderock, Maryland.
HSD	Hawker Siddeley Dynamics Ltd, Coventry, England.
LRC	Langley Research Center (NASA), Langley Field, Virginia.
LTV	Ling-Temco-Vought Aerospace Corporation, Dallas, Texas.

MIT	Massachusetts Institute of Technology, Cambridge, Massachusetts.
NACA	National Advisory Committee on Aeronautics (now the National Aeronautics and Space Agency, NASA).
NAE	National Aeronautical Establishment, Ottawa, Canada.
NASA	National Aeronautical and Space Agency, Washington, DC.
NOL	Naval Ordnance Laboratory, White Oaks, Maryland.
OAL	Ordnance Aerophysics Laboratory, Dangerfield, Texas.
ONERA	Office National d'Etudes et de Recherches Aérospatiales (National Bureau of the Aerospace Research), Paris, France.
PU	Princeton University, Princeton, New Jersey.
RAE	Royal Aeronautical Establishment, Farnborough, Hants, England.
SU	Southampton University, Southampton, England.
UC	University of California, Berkeley, California.
UM	University of Michigan, Ann Arbor, Michigan.
WADD	Wright Air Development Division, Wright-Patterson Air Force Base, Ohio.

SECTION 1

INTRODUCTION

Analysis of aircraft and missile aerodynamic performance and stability requires knowledge of the forces and moments which act under conditions of steady and unsteady flight. One of the first studies of aircraft stability was that of Lanchester[1] around 1900, followed later by more complete and rigorous analysis by Bryan[2], which is still the basis for much of the dynamic stability work today.

Requirements for supplying aerodynamic characteristics for performance analysis have been met, to some extent, by relying on theories supported by experimental measurements to establish the validity of the theories. In some cases, the theory has only limited application especially when viscous flow has a pronounced influence on the flow field, as in the case of high speed flow (hypersonic speeds and above) and low Reynolds numbers. There are some situations for which the phenomena cannot be described adequately by theory. In other cases theory is not applicable because the configuration and flow field are so complex that the many approximations required invalidate a wholly theoretical approach. Thus, in practice, strong reliance is placed on experimental results for use in analyzing the modes of motion of the aircraft or missile.

Early experimental techniques making use of oscillating models to dynamically simulate rigid modes of motion for determining stability derivatives are well summarized by Jones[3]. It is of interest to note that no fundamental changes in the basic experimental methods have taken place since that time, 1934, although much work has been done toward refinement of the methods, equipment and instrumentation. Little emphasis was placed on dynamic stability experiments until about 1940, and from that time to 1945 experimentation was primarily concerned with subsonic flow and tests were made for small perturbations. Wind tunnel experiments and flight tests within the early forties were directed more toward static stability and control problems. With the advent of high speed aircraft, missiles, rockets, and re-entry vehicles, increased emphasis has been placed on performance and dynamic stability problems since missions demand precise control not only in small disturbances from level flight, but also in large scale maneuvers. As a result, dynamic stability measurements have become increasingly important at supersonic, hypersonic and hypervelocity speeds and at large perturbations. The experimental methods suggested by earlier experiments have been used in different forms, and many improvements have been made in the experimental techniques since about 1950 These improvements have been in the areas of balance system, model and support system design, instrumentation, data acquisition, and data reduction.

In 1954 Valensi[4] presented a review of the techniques primarily in use in Europe for measuring oscillatory aerodynamic forces and moments on models oscillating in wind tunnels. The following year AGARDograph 11 (Ref.5) by Arnold was published on the subject of dynamic measurements in wind tunnels. The most recent summary of techniques

for measuring oscillatory derivatives in wind tunnels was published by Bratt[6] in 1963 as a part of the AGARD Manual on Aeroelasticity. The paper discusses the basic principles employed in measuring derivatives and gives some account of the associated instrumentation. Much of the report deals with the methods and instrumentation employed in England.

Since these earlier works, the emphasis on dynamic stability testing has increased, and many reports have been prepared on the subject, so there exists a need for a review and summary of the current dynamic stability testing techniques in use at supersonic speeds and above.

There are many experimental techniques which are suitable for measuring dynamic stability derivatives; however, only those techniques that are in most common use in wind tunnels will be described. In addition, many different systems exist for measuring the same quantities and, since they differ primarily in the specific application, no attempt will be made to describe all systems; only systems considered to be representative and those having unique features will be discussed. The report is organized primarily around the aspects of dynamic stability testing in wind tunnels at supersonic speeds and above, although much of the report is pertinent to aspects of testing at transonic and subsonic speeds. Although free-flight testing in ground test facilities encompasses the use of the wind tunnel and aeroballistic range for measurements of dynamic stability derivatives, these techniques are not included as a part of this AGARDograph because other publications on these subjects have been published and are in preparation[7,8].

SECTION 2

STATEMENT OF THE PROBLEM

2.1 DEVELOPMENT TRENDS

Aircraft or missiles in high speed flight are free to respond to disturbances with motions involving many degrees of freedom. During various stages of aerodynamic design of a vehicle, as the configuration is developed, dynamic characteristics must be known and progressively refined to a high degree for the final configuration performance specification. The designer must necessarily be concerned with the interpretation of aerodynamic stability data and with the evaluation of the influence of their accuracy on an integrated system design.

There are three methods of obtaining stability data:

(i) Theory and empirical data.

(ii) Wind tunnel and aeroballistic range model testing.

(iii) Sub- or full-scale flight testing.

During the preliminary design stage, it is most expedient to rely primarily on theory and empirical data for performance evaluation whereas, in the later stages, design concepts inevitably require evaluation through the use of some scale model tests. As a final phase in the design development, sub- or full-scale flight tests are required to verify performance and obtain in-flight measurements for verification of theory and prediction methods.

There are certain speed regimes where theoretical results may be inaccurate due to insufficient or inaccurate basic data. For example, in the transonic speed regime ($0.9 < M_\infty < 1.5$) theoretical methods for determining dynamic stability derivatives are very limited, and, therefore, reliance is placed on methods involving the use of empirical data on similar configurations and correlation plots showing the manner in which the stability derivatives vary with Mach number for similar configurations.

Within the supersonic and hypersonic region ($1.5 < M_\infty < 10$), theoretical methods are available for estimating derivatives for bodies of revolution and relatively simple lifting configurations. At Mach numbers above 10 in the hypervelocity speed regime, theories generally fail to predict the derivatives because viscous effects have a strong influence on the vehicle aerodynamic characteristics.

In order to improve the accuracy of aerodynamic derivatives that are used in performance predictions and to validate theoretical estimates, model tests in ground test facilities are recognized as being essential to the development of aircraft, missiles and re-entry vehicles.

Study of vehicle motions in flight involves consideration of many degrees of freedom. When the vehicle is considered as a rigid body, six degrees of freedom are required. Since the vehicle is not a rigid structure, additional relative motions of components such as aeroelastic deflection of lifting surfaces and movable controls constitute additional degrees of freedom.

The vehicle motions may be separated into high frequency and low frequency motions, where high frequency motions studies such as flutter are primarily concerned with structural elasticity and unsteady aerodynamics. At low frequencies the motions involve rigid body motions and are studied as dynamic stability using quasi-static aerodynamics. The mode of model testing discussed in the present AGARDograph is concerned with this latter type motion and the determination of rotary damping derivatives.

In scaling down a vehicle for model tests the parameter that must be considered in addition to the Mach number and Reynolds number is the angular velocity or frequency of model oscillation in relation to full-scale conditions. The scaling parameter, called the reduced frequency, in the form $\omega d/2V_\infty$ contains the frequency of oscillation and represents the ratio of some characteristic dimension of the vehicle to the wave length of the oscillation. This type of scaling parameter also applies to dynamic roll tests and has the form $Pd/2V_\infty$.

Experimental techniques for measuring dynamic stability derivatives in ground test facilities may be classified in many different ways. The classification that will be followed here is presented in Figure 1. The two major classifications are derived on the basis of whether the model is free to move in all basic degrees of freedom or whether it is restricted in several degrees of freedom. The subtopics shown in Figure 1 for discussion were selected as those methods currently being employed for most high speed testing; however, it should be emphasized that the outline does not show the case of the model fixed in the test section with perturbations generated in the flow. As noted in the Introduction, only those methods which apply to captive model testing techniques will be discussed in this AGARDograph since free-flight tests in the wind tunnel and range are the subject of AGARDographs published and now in preparation[7,8]. Additional general information on methods not described herein may be found in Reference 9.

2.2 EQUATIONS OF MOTION

In order to place the role of dynamic stability testing in perspective, it is helpful to examine the equations of motion. Although the mathematical treatment of vehicle dynamics is well known and found in many tests[10-12], a brief derivation of the equations of motion is included to illustrate the basis for the experimental techniques used in the study of dynamic stability.

2.2.1 Axes Systems

The equations of motion will be developed using the axes systems shown in Figures 2 and 3. Model orientation is determined relative to the tunnel fixed axes $X_TY_TZ_T$ (inertial reference). The XYZ axes are fixed in the model with the X and Z axes in the model's plane of symmetry. When the origin of this system lies at the center of gravity, these axes are then defined as the body axes. The angular orientation of the XYZ system with respect to the $X_TY_TZ_T$ system and inertial space is given by the

Euler angles Ψ, Θ, and Φ. Sometimes it is convenient to use the nonrolling axes system $(\tilde{X}\tilde{Y}\tilde{Z})$. These are special body axes whose angular orientation in space relative to the $X_T Y_T Z_T$ system is determined by the angles Ψ and Θ. This axis system can be used even though the model is rotating about the $\tilde{X}$ axis. The origins of all systems are assumed to occupy the same point in space (Fig. 3).

2.2.2 Inertial Moments

The angular momentum of the model may be expressed as

$$\bar{H} = \int (\bar{r} \times \bar{V}_p)\, dm , \qquad (1)$$

where $\bar{r}$ is the radius vector from the origin of the rotating XYZ axes to the particle p of mass dm and $\bar{V}_p$ is the velocity of the particle p relative to inertial space.

The radius vector $\bar{r}$ is measured relative to the body fixed XYZ axes; therefore, in order to evaluate the velocity of p relative to inertial space, it is necessary to use the well-known transformation for the rate of change of any vector from fixed to rotating axes as follows:

$$V_p = \left.\frac{d\bar{r}}{dt}\right|_T = \frac{d\bar{r}}{dt} + \bar{\omega} \times \bar{r} ,$$

where

$$\bar{\omega} = P\bar{i} + Q\bar{j} + R\bar{k} .$$

Assuming the model is a rigid body, the equation reduces to

$$\bar{V}_p = \bar{\omega} \times \bar{r} ,$$

since $\bar{r}$ is then not a function of time.

Substituting this equation into Equation (1) yields

$$\bar{H} = \int \bar{r} \times (\bar{\omega} \times \bar{r})\, dm .$$

This expression is then integrated over the vehicle to obtain

$$\bar{H} = [j][.]\{\omega\} ,$$

$$[j] = [\bar{i}\ \bar{j}\ \bar{k}]$$

$$[I] = \begin{bmatrix} I_X & -J_{XY} & -J_{XZ} \\ -J_{YX} & I_Y & -J_{YZ} \\ -J_{ZX} & -J_{XY} & I_X \end{bmatrix}$$

$$\{\omega\} = \begin{bmatrix} P \\ Q \\ R \end{bmatrix} .$$

The moment acting on the vehicle is equal to the rate of change of angular momentum

$$\left.\frac{d\bar{H}}{dt}\right|_T = \frac{d\bar{H}}{dt} + \bar{\omega} \times \bar{H} = \Sigma\bar{M} \ .$$

This vector equation can be reduced to the following scalar forms:

$$\left.\begin{aligned} I_X\dot{P} + (I_Z - I_Y)RQ - J_{XZ}(\dot{R} + QP) + J_{XY}(RP - \dot{Q}) + J_{YZ}(R^2 - Q^2) &= (\Sigma M_X) \\ I_Y\dot{Q} + (I_X - I_Z)PR - J_{XY}(\dot{P} + QR) + J_{YZ}(PQ - \dot{R}) + J_{XZ}(P^2 - R^2) &= (\Sigma M_Y) \\ I_Z\dot{R} + (I_Y - I_X)QP - J_{YZ}(\dot{Q} + PR) + J_{XZ}(QR - \dot{P}) + J_{XY}(Q^2 - P^2) &= (\Sigma M_Z). \end{aligned}\right\} \qquad (2)$$

Roll pitch and yaw rates for the XYZ system may be obtained from Figure 3 as follows:

$$\begin{aligned} P &= \dot{\Phi} - \dot{\Psi}\sin\Theta \\ Q &= \dot{\Theta}\cos\Phi + \dot{\Psi}\cos\Theta\sin\Phi \\ R &= \dot{\Psi}\cos\Theta\cos\Phi - \dot{\Theta}\sin\Phi \ . \end{aligned}$$

In order to simplify the nonlinear differential equations given above to a form which facilitates analysis of the motion, vehicle symmetry will be assumed, and the motion will be restricted to small disturbances from a reference condition. Let $P = p_0 + p$, $\Psi = \psi_0 + \psi$, etc., where the zero subscripted quantities are the reference conditions and the unsubscripted lower case quantities are perturbations from this reference condition.

For the following discussion, the reference condition is selected such that $q_0 = r_0 = \theta_0 = \psi_0 = 0$ and the reference quantities p_0 and ϕ_0 are not necessarily small. Considering vehicles having symmetry about the XZ plane ($J_{xy} = J_{yz} = 0$) and neglecting products of perturbation quantities, the equations of motion become

$$\left.\begin{aligned} I_X\dot{P} - J_{XZ}(\dot{r} + qP) &= (\Sigma M)_X \\ I_Y\dot{q} + (I_X - I_Z)Pr + J_{XZ}P^2 &= (\Sigma M)_Y \\ I_Z\dot{r} + (I_Y - I_X)Pq - J_{XZ}\dot{P} &= (\Sigma M)_Z \ . \end{aligned}\right\} \qquad (3)$$

The roll, pitch and yaw rates at this condition are given as

$$\left.\begin{aligned} p_0 &= \dot{\phi}_0 \\ p &= \dot{\phi} - \dot{\psi}\sin\theta \\ q &= \dot{\theta}\cos\Phi + \dot{\psi}\cos\theta\sin\Phi \\ r &= \dot{\psi}\cos\theta\cos\Phi - \dot{\theta}\sin\Phi \ . \end{aligned}\right\} \qquad (4)$$

For models having triagonal or greater symmetry, the nonrolling coordinate system $\tilde{X}\tilde{Y}\tilde{Z}$ may be conveniently used when these axes correspond to the models' principal inertia axes. Since the body is moving with respect to the $\tilde{Y}$ and $\tilde{Z}$ axes (rotating about the $\tilde{X}$ axis), the restriction of symmetry is necessary, otherwise the moments of inertia with respect to the $\tilde{X}\tilde{Y}\tilde{Z}$ system will be time varying. For the above case, the angular momentum expression is given as

$$\bar{H} = I_X P\hat{i} + I\tilde{q}\hat{j} + I\tilde{r}\hat{k} \ ,$$

where

$$I = I_Y = I_Z$$

$$\tilde{q} = q \cos \Phi - r \sin \Phi$$

$$\tilde{r} = r \cos \Phi + q \sin \Phi$$

$$\Phi \simeq \int_0^t P(t)\, dt \ , \quad |\dot{\Phi}| >> |-\dot{\psi} \sin \theta| \ .$$

Note that, even though $\Phi = 0$ for the nonrolling coordinates, its $\tilde{X}\tilde{Y}$ plane is rotating with respect to the $X_T Y_T$ plane at the angular rate $-\dot{\psi} \sin \theta$.

The equations of motion referenced to the nonrolling coordinates are given as

$$\frac{d\bar{H}}{dt} + \bar{\Omega} \times \bar{H} = \Sigma \bar{M} \ ,$$

where

$$\bar{\Omega} = 0\hat{i} + \tilde{q}\hat{j} + \tilde{r}\hat{k} \ .$$

These equations of motion reduce to

$$\left.\begin{aligned} I_X \dot{P} &= (\Sigma M)_{\tilde{X}} \\ I\dot{\tilde{q}} + I_X P\tilde{r} &= (\Sigma M)_{\tilde{Y}} \\ I_Z \dot{\tilde{r}} - I_X P\tilde{q} &= (\Sigma M)_{\tilde{Z}} \ . \end{aligned}\right\} \qquad (5)$$

2.2.3 Aerodynamic Moments

The general procedure for expanding the aerodynamic moment relations is that developed by Bryan[2]. It is assumed that the moments are functions of the steady-state reference conditions and the instantaneous values of the disturbance velocities, control angles, and their time derivatives. A Taylor series expansion of an aerodynamic reaction yields this form. For example, the aerodynamic reaction $A = A(U, V, \ldots)$ is expressed as

$$A(U,V,\ldots) = A(u_0,v_0,\ldots) + \left(\frac{\partial A}{\partial u}\right)_0 (U - u_0) +$$

$$+ \left(\frac{\partial A}{\partial v}\right)_0 (V - v_0) + \left(\frac{\partial^2 A}{\partial u^2}\right)_0 (U - u_0)^2 +$$

$$+ \left(\frac{\partial^2 A}{\partial u \partial v}\right)_0 (U - u_0)(V - v_0) +$$

$$+ \left(\frac{\partial^2 A}{\partial v^2}\right)_0 (V - v_0^2) + \ldots \ ,$$

where

$$U = u_0 + u \ , \quad \text{etc.}$$

This expansion is linearized by neglecting products of the perturbation quantities; therefore, for the above example the linearized aerodynamic reaction becomes

$$A(U,V,\ldots) = A(u_0,v_0,\ldots) + \left(\frac{\partial A}{\partial u}\right)_0 u + \left(\frac{\partial A}{\partial v}\right)_0 v + \ldots \ .$$

Aerodynamic reactions can be expanded with respect to the variables U , V , W , P , Q , R , the control deflection angles, and time derivatives of these variables. For a given configuration, conditions of symmetry and past experience concerning relative effects of these derivatives can be used to reduce the number of derivatives needed to describe the aerodynamic moment system. For a spinning vehicle having triagonal or greater symmetry, the moment equations can be reduced to

$$M_X = M_{X0} + \left(\frac{\partial M_X}{\partial p}\right)_0 p + \left(\frac{\partial M_X}{\partial \delta^\star}\right)_0 \delta^\star \qquad (6)$$

$$M_Y = M_{Y0} + \left(\frac{\partial M_Y}{\partial v}\right)_0 v + \left(\frac{\partial M_Y}{\partial w}\right)_0 w + \left(\frac{\partial M_Y}{\partial \dot{w}}\right)_0 \dot{w} + \left(\frac{\partial M_Y}{\partial q}\right)_0 q$$

$$M_Z = M_{Z0} + \left(\frac{\partial M_Z}{\partial w}\right)_0 w + \left(\frac{\partial M_Z}{\partial v}\right)_0 v + \left(\frac{\partial M_Z}{\partial \dot{v}}\right)_0 \dot{v} + \left(\frac{\partial M_Z}{\partial r}\right)_0 r \ .$$

The term $(\partial M_Y/\partial v)_0$ in the pitch equation and the term $(\partial M_Z/\partial w)_0$ in the yaw equation are usually negligible except for the case when the vehicle is spinning rapidly. These terms are caused by the Magnus effect. They are given in a more familiar form as follows.

Let

$$\left(\frac{\partial M_Y}{\partial v}\right)_0 = M_{Yv0} \ ; \qquad \left(\frac{\partial M_Z}{\partial w}\right)_0 = M_{Zw0} \ .$$

Taking the first term as an example and assuming that it is primarily a function of P, its Taylor series expansion about the condition $P = 0$ is given as

$$M_{Yv0}(P,\dots) = M_{Yv0}(0,\dots) + \left(\frac{\partial M_{Yv0}}{\partial p}\right)(P - 0) + \dots \quad .$$

The first term on the right hand side is usually negligible; therefore, this expression may be reduced to

$$M_{Yv0}(P) = \left(\frac{\partial M_{Yv0}}{\partial p}\right) P = \left(\frac{\partial^2 M_Y}{\partial v \partial p}\right)_0 P \ .$$

Similarly,

$$M_{Zw0}(P) = \left(\frac{\partial M_{Zw0}}{\partial p}\right) P = \left(\frac{\partial^2 M_Z}{\partial w \partial p}\right)_0 P \ .$$

The pitching- and yawing-moment equations are then given as

$$M_Y = M_{Y0} + \left(\frac{\partial M_Y}{\partial w}\right)_0 w + \left(\frac{\partial M_Y}{\partial \dot{w}}\right)_0 \dot{w} + \left(\frac{\partial M_Y}{\partial q}\right)_0 q + \left(\frac{\partial^2 M_Y}{\partial v \partial p}\right)_0 Pv \qquad (7)$$

$$M_Z = M_{Z0} + \left(\frac{\partial M_Z}{\partial v}\right)_0 v + \left(\frac{\partial M_Z}{\partial \dot{v}}\right)_0 \dot{v} + \left(\frac{\partial M_Z}{\partial r}\right)_0 r + \left(\frac{\partial^2 M_Z}{\partial w \partial p}\right)_0 Pw \ . \qquad (8)$$

The terms M_{X0}, M_{Y0}, and M_{Z0} in Equations (6), (7), and (8), respectively, are the moments about the X, Y and Z axes while the model is at the reference flight condition. The reference condition is often chosen such that these terms are zero.

Equations (3) describe the motion of a model which has three degrees of freedom in rotation about a point fixed in space. Unique test equipment is required in order to obtain these motions using a captive model test technique. Two balances which have this capability are described later in Section 3.1.1. In most captive model dynamic stability tests, the model is restrained to a single degree of freedom, i.e., rotation about a single axis. An example of a typical dynamic stability balance would be a single-degree-of-freedom system using a flexure pivot. The equation of motion for a system of this type will be developed in the following discussion.

2.2.4 Single Degree of Freedom

The velocity components in the body axis for the case of a model mounted on a single-degree-of-freedom flexure pivot at an angle of attack α and oscillating symmetrically at a small angle θ are

$$\left.\begin{aligned} U &= V_\infty(\alpha + \theta) = V_\infty \cos\alpha - \theta V_\infty \sin\alpha \\ V &= 0 \end{aligned}\right|$$

$$\left.\begin{aligned} W &= V_\infty \sin(\alpha + \theta) = \theta V_\infty \cos\alpha + V_\infty \sin\alpha \\ P &= 0 \\ Q &= q = \dot{\theta}, \quad \dot{q} = \ddot{\theta} \\ R &= 0 . \end{aligned}\right\} \tag{9}$$

The reference conditions used here are those that exist when the model is at the angle of attack α. Under these conditions, Equation (2) reduces to

$$I_Y \dot{q} = (\Sigma M)_Y .$$

Only the derivation of the equation for a single degree of freedom in pitch is presented, since the derivations for oscillations in yaw and roll are similar and are treated in detail in many of the references included (see, e.g., Reference 4).

An elastic restraint is provided in the balance to aid in restoring the model to the reference attitude following a displacement. When the aerodynamic moment is expanded to include all significant terms and the restoring moment $K_1(\alpha + \theta)$ and the damping moment $C_1\dot{\theta}$ of the restraint are added to this to obtain the total moment, the equation of motion in pitch is written as

$$I_Y \dot{q} = M_{Y0} + M_u u + M_q q + M_w w + M_{\dot{w}} \dot{w} + K_1(\theta + \alpha) + C_1 \dot{\theta} ,$$

where

$$M_u = (\partial M_Y / \partial u)_0 , \qquad M_q = (\partial M_Y / \partial q)_0$$

$$M_w = (\partial M_Y / \partial w)_0 , \qquad M_{\dot{w}} = (\partial M_Y / \partial \dot{w})_0 .$$

After including the relationships for the linear and angular components of velocity (Equation (9)), the equation above reduces to the form

$$I_Y \ddot{\theta} + (-M_q - V_\infty M_{\dot{w}} \cos\alpha - C_1)\dot{\theta} +$$

$$+ (M_u V_\infty \sin\alpha - M_w V_\infty \cos\alpha - K_1)\theta - M_{Y0} + K_1\alpha = 0 . \tag{10}$$

In the undisturbed case, conditions of equilibrium give

$$M_{Y0} = K_1\alpha ,$$

and, for small values of α, Equation (10) becomes

$$I_Y \ddot{\theta} - (-M_q - V_\infty M_{\dot{w}} - C_1)\dot{\theta} + (-K_1 - M_w V_\infty)\theta = 0 . \tag{11}$$

Defining the damping-moment parameter and the restoring-moment parameter by $M_{\dot{\theta}}$ and M_{θ}, respectively, where

$M_{\dot{\theta}_a} = (Mq + V_\infty M_{\dot{w}})$,		aerodynamic
$M_{\dot{\theta}_t} = C_1$,		damping-moment parameter of elastic restraint considered as a tare
$M_{\dot{\theta}_a} = M_w V_\infty$		aerodynamic
$M_{\dot{\theta}_t} = K_1$.		static-moment parameter of elastic restraint considered as a tare.

With these definitions, Equation (11) becomes

$$I\ddot{\theta} - (M_{\dot{\theta}_t} + M_{\dot{\theta}_a})\dot{\theta} - (M_{\theta_t} + M_{\theta_a})\theta = 0 .$$

Following the procedure presented in Reference 4, similar expressions can be written for the equations of motion in the body axis for yaw and roll.

2.2.5 Stability Derivative Coefficients

The stability derivative coefficients are obtained in this section using the reference condition $\Psi_0 = \theta_0 = w_0 = v_0 = q_0 = r_0 = 0$. This is a typical condition for a symmetrical model oscillating about its zero-angle-of-attack trim. The NACA system[11] will be used here with the time constant defined as $t^* = l/u_0$. The aerodynamic moments are defined in this system as

$$M_X = \rho V_c^2 A l C_l \tag{12}$$

$$M_Y = \rho V_c^2 A l C_m \tag{13}$$

$$M_Z = \rho V_c^2 A l C_n . \tag{14}$$

where $V_c = \sqrt{(U^2 + v^2 + w^2)}$

and it is necessary that the reference length (l) be defined in half lengths; e.g., $l = d/2$, $l = b/2$, etc.

The coefficient form of the derivative $(\partial M_Y/\partial w)_0$ is obtained, using Equation (13), as follows:

$$\left(\frac{\partial M_Y}{\partial w}\right)_0 = 2\rho V_c \left(\frac{\partial V_c}{\partial w}\right)_0 A l C_{m_0} + \rho V_c^2 A l \left(\frac{\partial C_m}{\partial w}\right)_0 . \tag{15}$$

Since $(\partial V_c/\partial w) = w/V_c$, the first term on the right-hand side of Equation (15) is negligible.

The angle of attack is defined to first order (small angles of attack) as

$$\alpha = \frac{w}{u_0} ,$$

where

$$u_0 \simeq V_c .$$

Substitution of this definition into Equation (15) yields

$$\left(\frac{\partial M_Y}{\partial w}\right)_0 = \rho V_c A l C_{m\alpha} ,$$

where $$C_{m\alpha} = \left(\frac{\partial C_m}{\partial \alpha}\right)_0 .$$

The coefficient form of the derivative $(\partial M_Y/\partial q)_0$ is obtained, using Equation (13), as follows:

$$\left(\frac{\partial M_Y}{\partial q}\right)_0 = \rho V_c^2 A l \left(\frac{\partial C_m}{\partial q}\right)_0 . \tag{16}$$

The coefficient C_{mq} is defined, using the time constant and the derivative from the right-hand side of this equation, as

$$C_{mq} = \frac{1}{t^*}\left(\frac{\partial C_m}{\partial q}\right)_0 = [\partial C_m/\partial(ql/V_c)]_0 .$$

Using this definition, Equation (16) becomes

$$\left(\frac{\partial M_Y}{\partial q}\right)_0 = \rho V_c^2 A l t^* C_{mq} .$$

The remaining coefficients are obtained using techniques similar to those outlined.

Using Equations (6), (7), and (8) and the above methods for obtaining the coefficients, Equations (12), (13), and (14) can be written in the following coefficient forms, where $l = d/2$:

$$M_X = \tfrac{1}{2}\rho V_c^2 A d \left[C_{l0} + C_{lp}\left(\frac{pd}{2V_c}\right) + C_{l\delta_a}\delta^*\right]$$

$$M_Y = \tfrac{1}{2}\rho V_c^2 A d \left[C_{m0} + C_{m\alpha}\alpha + C_{m\dot{\alpha}}\left(\frac{\dot{\alpha}d}{2V_c}\right) + C_{mq}\left(\frac{qd}{2V_c}\right) + C_{mp\beta}\left(\frac{pd}{2V_c}\right)\beta\right]$$

$$M_Z = \tfrac{1}{2}\rho V_c^2 A d \left[C_{n0} + C_{np}p + C_{n\dot{\beta}}\left(\frac{\dot{\beta}d}{2V_c}\right) + C_{nr}\left(\frac{rd}{2V}\right) + C_{np\alpha}\left(\frac{pd}{2V_c}\right)\alpha\right] .$$

SECTION 3

CAPTIVE MODEL TESTING TECHNIQUE

3.1 GENERAL DESCRIPTION OF TECHNIQUE

Methods for obtaining rotary derivatives in pitch, yaw or roll involve restraint of the model in several degrees of freedom and measurement of moments required to sustain an oscillation for specified conditions of frequency and amplitude (forced oscillation technique) or measurement of model motion after it has been disturbed (free oscillation technique).

The basic units in the captive model testing system are the pivots, the support system and, in the forced oscillation technique, mechanisms for forcing the model oscillation. The pivot is a very important part of a dynamic stability test system, and the selection of the type of pivot and design will depend on several factors, some of which have a direct bearing on the quality of data that may be obtained with the system. Also of importance is the suspension system and the influence it may have on the aerodynamic measurements. Detailed descriptions of model pivots, suspension systems, and balance tare damping characteristics are presented in Sections 3.1.1 to 3.1.3.

3.1.1 Model Pivots

Pivots of various types which are employed in dynamic stability balances include ball bearings, gas bearings, knife edges, cones, and crossed flexures. The selection of a particular type pivot will depend on the system operating requirements and the environment in which it will be used. One of the most important factors that must be considered in the design of a dynamic stability balance for aerodynamic damping measurements is the damping that the system contributes to the measured wind on damping. Aerodynamic damping decreases with increased Mach number and becomes a small percentage of the measured damping at the hypersonic Mach numbers. One exception that will be discussed in Section 3.1.3 are gas bearings which generally have negligible tare damping. Because of its importance, tare damping will usually be one of the principal considerations for selection of the pivot type or bearing for roll damping balance systems.

3.1.1.1 Flexure

High pivot friction may be avoided by employing crossed flexures of the general type shown in Figure 4. These bend in such a way that the center of rotation remains at essentially a fixed position. The crossed flexure provides stiffness, which is necessary to overcome static moments on models tested at angles of attack by the free-oscillation technique. Flexure pivots are used in many applications, in particular scientific instruments, because they have many favorable characteristics. They are simple in design, yet rugged in construction for their flexibility; they do not

introduce hysteresis or backlash in the system; they do not require lubrication; and they are not susceptible to wear. Their main disadvantage is that they are not suitable for large angles of rotation because of stress considerations, especially under combined loadings. The design of flexure pivots for a particular application requires consideration of the model loads, moments, and oscillation frequency for dynamical similitude. Experience at the AEDC-VKF has shown that crossed flexures have linear stiffness characteristics and structural damping that is repeatable even though the flexure is of multipiece construction. This method of construction is desirable because the flexures can be machines as a single unit and then cut into sections for the individual flexures. The theory for design of symmetrical crossed-flexure pivots is given in References 13 through 16.

Examples of flexure pivots, including cruciform and torsion tube pivots, that have been used in various applications are shown in Figure 5. For each of these, the pivot tare damping varies inversely with the frequency of oscillation. Strain gages mounted to one member of the crossed flexure are employed to obtain a signal voltage which is proportional to the angular displacement.

For some applications, such as tests in very small tunnels or low density tunnels which have a small test core, it may be impractical to machine flexure pivots of the type shown in Figure 5. The AEDC-VKF has developed a small dynamic stability balance using a commercially available instrument flexure pivot of the type shown in Figure 6. The characteristics of this pivot were found to be repeatable and linear. Angular motion time histories are measured with an angular transducer described in Section 3.2.2.1.

3.1.1.2 Knife Edge and Cone

Knife edge and cone pivots of the type shown in Figures 7 and 8 have recently been used in dynamic stability balance systems because they are nearly frictionless.

The principal disadvantage of either the knife edge or cone pivot is that some method of restraint must be employed to hold the pivots in contact and fine adjustments are necessary to eliminate binding.

The single-degree-of-freedom knife edge pivot shown in Figure 7 was used in a single-degree-of-freedom free-oscillation balance system developed at DTMB. Here knife edges are used to constrain the model and also form the axis of rotation.

A similar technique has also been used by DTMB for a three-degree-of-freedom balance system; however, in this case, the model mounting system is a cone on the end of the sting inserted in a conical depression contact within the model (Fig. 8). The model is free to roll, pitch, and yaw about the cone and is held on the pivot by model drag. In each of these cases, model attitude is measured from photographic records of model motion.

3.1.1.3 Ball Bearing

Ball bearing pivots may be used in a dynamic stability balance system for pitch and yaw derivative measurements if high resultant model loads are to be supported and if aerodynamic damping is large so that bearing damping constitutes a small part of the

measured damping. Experience has shown that a ball bearing pivot is likely to have about two orders of magnitude higher damping than that of a flexure pivot designed to carry comparable loads. Although the ball bearing pivot has the advantage of being suitable for large angles of rotation, bearing damping is a function of the amplitude of oscillation and is often nonrepeatable. A ball bearing pivot used in an AEDC-VKF free-oscillation balance is shown in Figure 9.

Ball bearing pivots are quite frequently used in forced-oscillation balances when high amplitudes of oscillation cannot be obtained with flexure pivots. Although the bearing damping is high, its effects may be eliminated in the measurements by measuring the forcing torque on the model side of the bearings, as shown in Figure 10. For such a balance system, angular contact bearings are used with preload to eliminate free play in the bearings.

Ball bearings are used in Magnus force and moment balance systems where models are spun to high rotational speeds. In this application, bearing friction is not important since the measurements are static forces and moments in the yaw plane; however, bearing heating may be a problem at extremely high rotational speeds.

Until recently, roll-damping balance systems have been designed with ball bearings; however, new systems in development are designed with gas bearings to overcome bearing damping, wear, requirements for lubrication, and sometimes cooling. Angular motion time histories may be measured with the type of angular transducer described in Section 3.2.2.1.

3.1.1.4 Gas Bearing

Although gas film lubrication is an old concept, it is only since about 1950 that the study of gas bearings has noticeably accelerated. The reason for this is that special bearing requirements can often be best satisfied with a gas bearing. Gas bearings were used in special wind tunnel drag-force balances as early as 1956; however, they were not applied to balances for dynamic stability in pitch and yaw measurements until about 1961 (Ref. 18), and roll damping until 1964 (Ref. 19). Applications in wind tunnel testing techniques have been extensive since these early developments. This is understandable since all of the desirable features of a pivot, which include high load-carrying capability, low damping, and unlimited rotation, are combined in a gas bearing pivot; whereas flexures and ball bearing pivots have only some of these characteristics. Gas bearing pivots are used extensively for dynamic stability testing in the AEDC-VKF at hypersonic speeds where the aerodynamic damping is very low. It is difficult to measure damping accurately with a flexure pivot balance under this condition because of the high percentage of tare damping.

An example of a journal-type gas bearing pivot used in an AEDC-VKF one-degree-of-freedom dynamic stability balance for measuring pitch or yaw derivatives is shown in Figure 11. The inner or core section of the bearing is supported on each side by a sting, and the model is mounted to a pad on the outer movable ring. Supply gas, generally dry nitrogen, is supplied through the core to a radial set of orifices in the center of the bearing. Filters are provided in the core to remove foreign particles that will cause bearing fouling. A closed gas supply and return system is not used at the AEDC-VKF, since tests have shown that the small flow rates have negligible influence on base pressures and wakes. Bearings have been developed at the AEDC-VKF

with two radial rows of orifices spaced to improve the yawing-moment carrying capability. Bearings are usually designed for specific applications; however, commercial gas bearings now exist that may be used in one-degree-of-freedom balance systems. This is an important fact since design, development and fabrication of gas bearings can become very time-consuming and costly.

The gas bearing shown in Figure 11 was designed with inherent orifice compensation according to the procedure outlined in Reference 20. Analysis of this type of bearing is a problem of compressible flow with friction in three-dimensional passages that change area with loading. Treatment of this problem consisted of reducing the complex analysis of the bearing to the analysis of a simple, flat plate model. As will be shown later, these simplifying assumptions lead to a model realistic enough to yield acceptable results for design.

The gas bearing shown in Figure 11 differed from the design model of Reference 20 in the following ways: (i) the gas plenum was located in the fixed center portion of the bearing to supply gas through radial orifices to float the outer moving ring and (ii) plates were added to the ends of the bearing. These provided a self-centering feature required for proper operation and some degree of lateral restraint. In addition, the end plates were designed with shields to direct the exhaust gas toward the center of the bearing; otherwise, gas exhausting radially would impinge on the inside of the model and possibly influence the damping measurements. The bearing shown in Figure 11 is capable of carrying high radial loads; however, the lateral load capability is small, yet adequate for most purposes. Where side loads are large, additional gas supply orifices and pads should be provided on the ends.

The performance characteristics necessary for evaluating the journal gas bearing for application to dynamic stability testing include the radial load capacity, bearing pressure, and the tare damping. Curves illustrating the relationship of radial load to critical pressure are presented in Figure 12. The critical pressure is defined as the pressure loading for an outer shell eccentricity ratio of approximately 0.5 of the bearing clearance. Permissible loading is nearly a linear function of the supply pressure and agrees with the performance predicted by theory.

As noted previously, the one most desirable characteristic of the gas bearing for use in dynamic stability balance systems is the extremely low tare damping. Data on the damping of the gas bearing in Figure 11 are presented in Figure 13 as a function of frequency of oscillation and radial load. In true viscous damping, the damping moment, $M_{\dot{\theta}}\dot{\theta}$, is defined as a moment proportional to $M_{\dot{\theta}}$ which is invariant with oscillation amplitude and frequency. This was not found to be the case for the bearing when evaluated over a range of frequencies and loads at 11.5 deg oscillation amplitude. The results of the evaluation of the bearing damping presented in Figure 13 shows an inverse relationship with frequency as is the case for flexures and a dependency on radial load. The damping is in the form

$$M_{\dot{\theta}} = C\alpha^{b},$$

where C and b depend on radial load. In actual practice, these small values of tare damping are usually neglected. For example, the damping shown in Figure 13 is only 0.8% of the aerodynamic damping for a typical blunt cone re-entry configuration at Mach number 10.

Gas bearings have been used extensively in industry for application to machinery operating at high speeds where bearing friction is very important. Satisfactory operations at high rotational speeds with very low friction makes the gas bearing very attractive for use in roll-damping balance systems. Until recently, ball bearings were used exclusively; however, they have many disadvantages, such as significant tare damping, wear, lubrication requirements, and heating, that can be overcome with the use of gas bearings. A typical example of gas bearings applied to a roll-damping balance is shown in Figure 14.

Bearing pivots described up to this point only allow rotation about one axis. Many problems encountered in flight can only be investigated experimentally using a balance which has rotational freedom about three mutually perpendicular axes. A prime example of a flight phenomenon of this type would be the coupling of the rigid body pitch and roll modes. A three-degree-of-freedom balance provides this capability and in addition simultaneously performs the functions of the several one-degree-of-freedom balances as it incorporates into one balance the ability to measure pitch, yaw, and roll damping. The single-degree-of-freedom balances still have an application as they can be used to restrain the motions to pure pitch, yaw, or roll in situations where this becomes necessary.

An inherently compensated, spherical, gas journal bearing shown in Figure 15 has been developed at the AEDC-VKF for use as the pivot in a three-degree-of-freedom dynamic stability balance. The inner core of this bearing consists of four spherically surfaced pads arranged in a manner which allows the bearing to resist loads in any radial direction. Gas is supplied through an orifice located at the center of each pad. This configuration is capable of supporting maximum radial loads of 100 lb using nitrogen or 160 lb using helium. Changes in the bearing core design will allow the bearing to support radial loads of approximately 350 lb. The damping inherent in the spherical bearing, like that of the cylindrical bearings, is extremely low.

Continuous motion histories provide the data required to determine the aerodynamic derivatives. For very small flexures or bearing pivots, it is desirable to measure the motion without physically contacting the moving parts of the system. A device referred to as an angular transducer was originally developed by the AEDC-VKF for use in dynamic stability balance systems[21]. The variable reluctance angular transducer, shown mounted on a cylindrical gas bearing in Figure 11, consists of two E-cores mounted on the outer movable ring of the bearing. When the coils contained in the E-cores are excited, magnetic paths are established through the E-cores, their adjacent air gaps, and the eccentric ring. As the bearing rotates, the reluctance of the magnetic paths through the E-cores and eccentric ring remain constant, while the reluctance of the air gap changes. This change in reluctance produces an analog signal proportional to the angular displacement.

Instrumentation for the spherical gas bearing consists of three mutually perpendicular angular transducers (Fig. 15). The pitch and yaw transducers located on the forward portion of the instrument ring operate from an eccentric which is concentric in roll and eccentric in pitch and yaw, whereas the roll transducer located in the aft portion of the ring operates from an eccentric which is concentric in pitch and yaw and eccentric in roll.

Gas bearing technology is growing very rapidly, and many texts have been prepared on the methods for design and analysis (see the Bibliography). Reference 2 Vol.I, contains detailed summaries of design methods, material selection, and measurement techniques, and Vol.II is devoted to applications.

3.1.2 Suspension System

The design of the suspension system will depend for the most part on the type of model to be tested and the measurements required. Models may be generally categorized as (i) two-dimensional models which span the test section and are supported from the side walls, (ii) three-dimensional, semispan models which are mounted on a reflection plane supported by the test section side wall, and (iii) three-dimensional, full-span models which are supported by a sting, a side strut, or a magnetic suspension system. With the exception of magnetic suspension, each model mounting system presents a potential problem when being used for tests of some types of configurations, that being the influence of the support on the aerodynamic measurements. When this problem cannot be dealt with in captive model testing by proper support design or evaluation of the influence of the suspension system, free-flight testing in the wind tunnel and range, and testing with magnetic model suspension is used.

Support systems for the three types of models commonly investigated in wind tunnels may be generally grouped into two categories: (i) the wall support method for the two-dimensional and three-dimensional semispan models and (ii) the sting, strut, and magnetic suspension system support for the three-dimensional full-span and body-of-revolution models.

3.1.2.1 Wall Support

The wall support method for testing half models has the advantage that, for a given test section size, a larger model can be tested and thus a larger Reynolds number can be obtained than with a complete model. The large half model also simplifies the model construction, instrumentation installation, and routing instrumentation wires and pressure tubes out of the model through the large contact areas at the tunnel walls. Large angles of attack can be obtained with wall-supported models without introducing interferences from sting supports. In addition, measuring systems and instrumentation for dynamic stability tests of the complete model or control surfaces can be located outside the tunnel, so that equipment size is not an important factor. In many tests of wings or control surfaces, this is the only method of support that can be used to acquire dynamic stability data without altering the model contour for an internal balance. An example of a two-dimensional and three-dimensional model mounted on the tunnel walls, with equipment for measuring dynamic stability, is shown in Figures 16 and 17 to illustrate the principal advantages of the wall-support method described[23].

When models are mounted directly on the tunnel walls, the effect of the tunnel boundary-layer flow has to be considered, since it may change the flow field over the model. As noted by van der Bliek[24], the wall boundary layer influenced the lift and drag coefficient on delta wings and wing-body combinations mounted on the side walls and had a tendency to promote separation and stall near the wing root. Although similar conclusions have not been formulated for dynamic stability tests, the influence on static tests results should be sufficient to initiate concern about the influence of the test section wall boundary layer.

In order to alleviate the influence of the wall boundary layer, several methods have been used with success at subsonic speeds by various investigators. These include boundary-layer removal through porous walls or slots ahead of the model and the installation of V-shaped vortex generators on the tunnel wall ahead of the attachment. Formation of large disturbed areas on the model close to the wall may be prevented by using fences attached to the model or displacing the model from the tunnel wall by inserting shims between the model and walls. Each of these methods has the disadvantage of altering the shape of the model configuration and not completely eliminating the influence of the wall boundary layer.

Tests have shown that wall boundary-layer effects are largely eliminated by using reflection planes of the types illustrated in Figure 18. With this method, a reflection plane is introduced as the longitudinal plane of symmetry and is displaced from the wall to allow passage of the wall boundary layer flow. For some mounting methods, contouring in the flow passage may be necessary to eliminate choking of the flow and the resultant ineffectiveness of the reflection plane. The reflection plane can be fixed to the wall and the model rotated, or the model can be fixed to the plate and rotated as a unit. When the model is rotated on the reflection plate, as is generally done in dynamic stability tests, a gap must be allowed, which may introduce leakage around the model reflection-plane junction and change the local flow field. Tests of very blunt models on reflection planes will produce significant boundary-layer separations and thus alter the model flow field. Information on reflection plane design is given in Reference 26.

3.1.2.2 Sting Support

Sting supports are principally used in tests of complete vehicle configurations and are inserted into the model base through the center of the wake to minimize their influence on the model flow field. Careful attention must be given to the design of the sting to insure that it provides a stiff support; however, modification of the model contour may be necessary to accommodate the sting. Such a modification is a compromise between a small diameter sting of constant length for a distance behind the model and one which will carry the aerodynamic loads without significant movement of the pivot axis. Often the consequences of the compromise are not clear, and therefore tests are required to evaluate the influence.

Static tests[27] have shown that both the sting diameter and sting length have an influence on force and base pressure data for most configurations. Some forced-oscillation systems have shaker motors in enlarged sections of the sting support, to simplify the overall design and reduce the complexity of the driving linkages. In these cases it is important that the enlarged section be located an ample distance downstream of the model base to permit proper formation of the wake. Very few experiments have been conducted to investigate specifically the influence of the sting diameter and length on dynamic stability measurements.

A series of tests have been conducted at the AEDC-VKF (Ref. 28), over a range of Reynolds numbers, to investigate the influence of the sting diameter and length on the dynamic stability of a 10-deg half-angle cone with a flat base. To determine the relative effects of sting length, disturbances downstream of the model base were introduced by placing a 20-deg conical windshield at various stations along the sting from 0.75d to 3d. Relative interference caused by the sting diameter size was created

by repeating the tests with diameters of 0.4, 0.6, and 0.8d. The test results included dynamic stability, static stability, and base pressure data, since base pressures are very sensitive to the degree of interference that the support presents to the base flow. Representative results are shown in Figures 19, 20, 21, and 22 for Mach numbers 2.5, 3, and 4 over a range of Reynolds numbers and sting lengths using three sting diameters. Evidence of interference caused by the support length may be judged by the deviation of the base pressure ratio from the reference curve corresponding to the longest sting length ($l_s/d = 3$).

Boundary-layer transition is generally at the model base, at a Reynolds number which is slightly less than the value where the minimum base pressure occurs. An analysis of the results based on the base pressure data and schlieren photographs for $l_s/d = 3$ shows that the Reynolds number range was sufficient for a transitional and fully turbulent wake. There is evidence in the data presented in Figure 19 to confirm that some support geometry configurations can have an influence on the dynamic stability derivatives. However, it appears that if the support is designed using criteria for static force and base pressure tests[27], it is unlikely that the dynamic stability data will be influenced. This observation does not apply to configurations which have contoured bases, since these are more critical with regard to the influence of the support because the wake condition has a direct influence on the pressure distribution around the base. A further complication arises in this case because the base must be partially removed to allow movement of the model over the sting. In cases where the relative influence of the support system on damping results cannot be assessed by captive model testing, wind-tunnel, free-flight, and aeroballistic range tests are necessary to obtain comparative results.

Some examples of a very rigid sting and support for a high frequency, free-oscillation, dynamic stability balance system are shown in Figure 23 and a more conventional support for a low frequency system is shown in Figure 24.

3.1.2.3 Strut Support

Where limitations on model amplitudes are imposed by mechanical interference between the model base and sting, these may be overcome by mounting the model on a transverse rod support system so that it is free to rotate on the rod with no restraints. An example of one such system used in the AEDC-VKF 50-in. Mach 10 tunnel is shown in Figure 25. The balance, consisting of a gas-bearing pivot, model lock, and position transducer, is contained within the model; nitrogen gas for the bearing and the model position lock and instrumentation leads pass through the transverse rods.

Extension of the transverse rod into the model will affect the flow over the model primarily in the region aft of the rod and along the sides of the model. A region of flow separation will exist on the model ahead of the rod. Since the interference flow field caused by the rod will depend on the boundary-layer flow and the position of the interference on the model surface, it is to be expected that measurements obtained with a transverse rod support system will be dependent upon the oscillation amplitude and the Reynolds number of the flow. An example of such a dependence is shown in Figure 26, where data obtained with a sting support are included for comparison. It is apparent from these results, for a 10-deg half-angle cone at Mach number 10, that both Reynolds number and oscillation amplitude are important parameters. It should be noted that when the Reynolds number is large the influence of Reynolds number and amplitude disappear and the results obtained with a sting support and transverse rod support are

in agreement. However, at low Reynolds numbers, very large differences can exist in results obtained by the two methods, thus indicating significant adverse effects from the transverse rod.

The influence of the size of the transverse rod supports at Mach 5 is shown in Figure 27 for a blunt cone cylinder model with and without a base flare. A cylindrical rod and double-wedge rod were tested with roughness on the model nose to produce turbulent flow and thus to eliminate separation ahead of the base flare. The results show no significant effects caused by rod size for diameters up to 30% of the model diameter and no effects caused by rod configuration, i.e., a cylindrical rod as compared to a double-wedge rod. A significant reduction of the damping occurred when roughness and the transverse rods were eliminated for the configuration with the flared base, because of the rod wake influence on the region of separated flow ahead of the flare.

Although very few systematic investigations have been conducted to investigate the effects of transverse rod geometry on dynamic damping over a range of model configurations, Mach numbers, Reynolds numbers, and amplitudes, the data available tend to indicate that (i) rod influence becomes negligible at the high Reynolds numbers when the flow is turbulent and (ii) rod size effects are small provided the rod is small compared to the model size. Tests with transverse rod supports should be supplemented with tests employing a sting support balance system to provide comparative data at low amplitudes, where the influence of the transverse rod is most pronounced.

3.1.2.4 Magnetic Model Support

Magnetic suspension provides a means for suspending a model in a test unit without any physical support, and thereby eliminates any questions about the experimental results being influenced by the method of physical support (sting or strut). The magnetic suspension system consists of a series of electromagnets which produce magnetic fields and gradients of magnetic fields to provide forces and moments on a model. The model has a magnetic moment which may be a part of the model if a permanent magnet is used in the model construction. Other methods for providing a magnetic moment are described in Reference 29. Included in the system for control is an optical system which monitors the position of the model by light beams passing through the test section and focused onto sensors. When the system is in equilibrium, forces and moments caused by gravity, aerodynamics, and inertial effects, for the case of a moving model, balance out the applied magnetic forces and moments. Changes in model position activate the control system, and currents flow through the magnetic coils to produce forces and moments on the model to hold it in equilibrium.

A magnetic suspension system with V-magnet orientation developed at the AEDC-VKF (Ref. 30) for static force, moment, and wake measurements is shown in Figures 28 and 29. A similar system, but with L orientation of the magnets has been developed by MIT (Ref. 31) to obtain static force, moment, and dynamic stability measurements.

3.1.3 Balance Tare Damping

3.1.3.1 Description of Damping

Wind tunnel models have to be mechanically suspended on a bearing or spring to provide oscillatory motion. Exceptions to this are recent developments of magnetic model

suspension systems which have been refined to the degree that damping data have been obtained[29]. Mechanical suspension introduces damping which must be accounted for in the analysis.

Aerodynamic damping as a rule cannot be measured directly with most balance systems, since it is a part of the measured total damping; therefore it must be obtained indirectly as the difference between the total and tare damping. With gas bearing pivots this is generally not necessary, since they usually have a negligible amount of tare damping. It is customary in writing the linear differential equations expressing an oscillatory motion to assume that the total damping, which is the aerodynamic plus tare damping, is proportional to $\dot{\theta}$. Therefore the motion in pitch for a free oscillation may be expressed by

$$I_Y\ddot{\theta} - (M_{\dot{\theta}a} + M_{\dot{\theta}t})\dot{\theta} - (M_{\theta a} + M_{\theta t})\theta = 0 ,$$

where the subscript a identifies the aerodynamic term and t identifies the tare term.

The term tare damping is applied here to denote the operation of non-aerodynamic influences which, by resisting the motion and absorbing energy from the system, reduce the amplitude of motion. A constant-amplitude oscillation would continue to exist if damping forces of various kinds did not exist. Damping forces arise from the mechanical system damping, damping capacity of the materials used in the system, and air damping. Although it is convenient to classify the contributing factors in this manner in discussing tare damping as applied to dynamic stability testing, the mechanical system damping and damping capacity of the materials are inseparable in the measurements and constitute the term $M_{\dot{\theta}t}$. Air damping is important only insofar as determining the magnitude of $M_{\dot{\theta}t}$ from air-off tests.

Mechanical system damping involves distinguishable parts of the system and arises from slip and other boundary shear effects at mating surfaces, interfaces, or joints. Energy dissipation here may occur as the result of dry sliding (Coulomb friction) lubricated sliding (viscous forces) or both.

The damping capacity of materials, or material damping, refers to the energy dissipation that occurs within the material when the structure is undergoing cyclic stress or strain. These internal energy losses may be considered as being due to imperfections in the elastic properties of the material. In a truly elastic member, not only is strain proportional to stress but also, on removal of the stress, the material retraces the stress-strain relationship that existed during the application of the stress. Even if materials are stressed within the elastic limit, some energy is lost. Energy dissipation in a material during a stress cycle leads to a hysteresis loop in the stress-strain curve and the area of the loop denotes the energy lost per cycle.

Air damping results from a loss of energy caused by restrictive effects as a mass moves through a medium such as air. The damping may result from dynamic pressure, viscous effects, and vortex formation and shedding; however, the relative effects of each are not known. Theoretical studies of the viscous damping force on a sphere and cylinder oscillating in a fluid[32,33] show that each will experience forces proportional to the velocity and square root of the fluid density. Experimental air-damping data for circular and rectangular plates, cylinders, and spheres are presented in Reference 34 and show the effect of pressure, vibratory amplitude, frequency, shape, and surface

area on the air damping for models that are mounted on the end of a cantilever beam. The results show that air damping associated with plates is directly proportional to the ambient pressure and amplitude is indicative of the influence of dynamic pressure. Low amplitude results for cylinders oriented perpendicular to the plane of oscillatory motion are in agreement with a theory by Stokes[33] and are proportional to the square root of the density but show no variation with frequency.

It is preferable to design dynamic-stability balance systems in such a way that the tare damping is small compared to the aerodynamic damping. For some classes of models at hypersonic and hypervelocity speeds, where the aerodynamic damping is low, the tare damping can approach, or even exceed, the aerodynamic damping. An example of the contribution of the mechanical system and air damping relative to aerodynamic damping is shown in Figure 30. It is apparent from this example that, as the Mach number is increased, extreme care must be taken to obtain measurements of tare damping with a high degree of accuracy, so that the difference constitutes an accurate measurement of the aerodynamic damping.

3.1.3.2 Evaluation of Still-Air Damping

Mechanical and material damping can be determined by tests in still air at atmospheric pressure; however, this can introduce large errors in some cases, since the damping thus obtained includes air damping. To determine the magnitude of air damping, tests are made in a chamber of the type shown in Figure 31 to permit variation in the ambient pressure. The wind tunnel can also be used for this test; however, its environment must be free of even small amounts of airflow and turbulence. A typical set of tare damping measurements for a blunt cone model are shown in Figure 32 for a range of pressures from atmosphere to vacuum. The level of damping at a vacuum represents the mechanical system and material damping, since the air damping is essentially zero. An example of the magnitude of the air damping as a percentage of the aerodynamic damping is shown in Figure 33 for a series of model shapes. At supersonic speeds the air damping is on the order of 2 to 4%, but increases significantly with Mach number, even approaching 100% of the aerodynamic damping at Mach 10.

The necessity for accurate tare damping results has been mentioned and specific reference made to some of the sources of damping in a mechanical system, one being energy dissipation in joints of multiple piece systems. To ensure that tare damping is repeatable and consistent, a number of tare damping recordings are usually made following removal and replacement of the model and flexure or pivot system until tare damping is shown to be repeatable.

In cases where the axial and/or normal forces are large, measurements are made with the pivot loaded to determine its influence on the mechanical damping and pivot stiffness. In most cases the pivot static loading will have little effect on the tare damping characteristics.

Since the model undergoing test will oscillate at a frequency different from that of the tare damping tests at a wind-off condition, it is necessary to establish how the energy loss or tare, $M_{\dot{\theta}_t}$, at a vacuum, will vary with frequency. For flexure-type pivots Smith[35] notes that the tare damping per cycle is a constant fraction of the energy stored in the spring at the beginning of the cycle, independent of the frequency. This is equivalent to $M_{\dot{\theta}_t} = C/\omega$, which was found earlier in experiments by Welsh and Ward[36].

3.1.3.3 Damping Characteristics of Different Metals

Damping characteristics of materials exposed to cyclic stress are affected by several factors, which must be considered in the selection of materials for flexure pivots. Some of the factors are

(i) condition of the material - composition and effect of heat treatment,

(ii) state of internal stress - effect of machining and changes in stress due to cyclic motion and temperature histories,

(iii) stress imposed by service conditions - type of stress, magnitude, stress variations, and environmental conditions.

Factors which include the magnitude of the stress, stress history, and frequency may be significant at one operating condition and unimportant at another. Final selection of a material should be based on tests of a specimen in the configuration in which the material will be used and under simulated operating conditions.

It should be recognized that, in most systems where oscillations or vibrations occur, the damping introduced by the properties of the materials employed is, in general, only one factor contributing to the total damping. Nevertheless, a knowledge of the characteristics of structural materials is important and the choice of material should be guided by its damping characteristics.

Materials having a Young's modulus which ranged from 6.2×10^6 for magnesium to 28.5×10^6 lb/in.^{2} for Armco 17.4 stainless steel have been tested in the VKF to provide material damping data for use as a guide in selecting materials for flexure-pivot designs. An example of the material damping results for a range of frequencies and beam stiffnesses is shown in Figure 34. Additional information on material damping may be found in Reference 37.

3.2 DYNAMIC STABILITY DERIVATIVES - PITCH OR YAW

The basic methods for obtaining dynamic stability measurements are well known, dating back to early 1920 when British reports on the subject began to appear. It was found that aerodynamic pitch damping derivatives consisted of two parts, M_q and $M_{\dot{\alpha}}$, and experiments were devised to account for these terms separately. These experiments were successful; however, it was concluded that the technique was not satisfactory for deducing $M_{\dot{\alpha}}$ at high speeds (transonic) or high frequencies. Some modes of oscillation such as short-period damping can be evaluated satisfactorily if the sum of the damping derivatives, for example $(C_{mq} + C_{m\dot{\alpha}})$, is known, even though the separate values of C_{mq} and $C_{m\dot{\alpha}}$ are unknown. Instances may exist at supersonic speeds in which the application of test data to calculations may require the damping derivatives in some way other than the combined form; however, the general practice has been to measure the derivatives in combined form. Wind tunnel techniques that are in most general use at supersonic speeds and above can be summarized as the free-oscillation and forced-oscillation methods.

The free-oscillation method is one of the earliest used and is considered to be the simplest from the viewpoint of equipment and instrumentation. The model, restrained by a pivot, is deflected to an initial amplitude and released, and the decaying motion is observed.

With the forced-oscillation technique, a restrained model is forced to perform simple harmonic motion by means of an oscillator, transmitting forces through a linkage to a torque member which is rigidly connected to the model. Normally the structural damping of balance systems used at supersonic and hypersonic speeds is very low and the torque member stiffness is also low. This requires the system to be operated at or near its resonant frequency. In order to obtain data over a wide frequency range, the model moment of inertia or the stiffness of the structural restraint may be varied.

An alternative method that may be used for tests over a wide range of oscillation frequencies is referred to as inexorable forcing; and as the name implies, the model is driven in a controlled manner by rigid linkage.

Most forced-oscillation systems employ special instrumentation techniques which utilize a feedback control system for controlled oscillation of the model when negative damping is present. In addition, these control systems provided amplitude control for measuring positive damping.

Both free-oscillation and forced-oscillation balances may be further categorized as either small-amplitude or high-amplitude systems. A small-amplitude balance measures local values of damping and pitching moment slope, since the model oscillates at amplitudes of about one or two degrees, and is often used to obtain data at angles of attack other than zero. The balance stiffness or restoring moment for large-amplitude balances is normally zero or near zero. Forced-oscillation systems may be operated at about ±15 degrees, as compared to amplitudes which are only limited by the balance support for free-oscillation balances.

The mathematical treatment of systems with free- or forced-oscillation motion may be found in many texts; however, the methods are treated in the next section for the sake of completeness.

3.2.1 Theory

The theory for linear and non-linear one-degree-of-freedom and three-degrees-of-freedom free-oscillation systems will be treated. The forced-oscillation theory will be developed, followed by a brief treatment of local and effective values of damping and finally the aerodynamic transfer equations will be developed.

3.2.1.1 Free Oscillation (One-Degree-Of-Freedom)

The equation of motion for a body in pitch was derived in Section 2.2 and has the same general form as the equations of motion for a body in yaw and roll. For free-oscillation systems having structural stiffness, the equation of motion has the form

$$I_Y\ddot{\theta} - (M_{\dot{\theta}a} + M_{\dot{\theta}t})\dot{\theta} - (M_{\theta a} + M_{\theta t})\theta = 0 . \qquad (17)$$

After introducing new nomenclature for simplification of the derivation of the solution to Equation (17), it becomes

$$I_Y\ddot{\theta} + C\dot{\theta} + K\theta = 0 . \qquad (18)$$

The general solution of this equation describing free-oscillation motion can be written as

$$\theta = A_1 e^{r_1 t} + A_2 e^{r_2 t} , \tag{19}$$

where A_1 and A_2 are arbitrary constants and r_1 and r_2 are the roots of the characteristics equation. These are obtained as

$$r_{1,2} = -\frac{C}{2I_Y} \pm \sqrt{\left[\left(\frac{C}{2I_Y}\right)^2 - \frac{K}{I_Y}\right]} \tag{20}$$

but, since the undamped natural circular frequency is $\omega = \sqrt{(K/I_Y)}$, and letting $C/2I_Y = a$, Equation (20) becomes

$$r_{1,2} = -a \pm \sqrt{(a^2 - \omega^2)} .$$

The case of interest is $a < \omega$, where the roots are complex, representing the condition where the system will oscillate. The general solution to Equation (19) for this case is

$$\theta = A_1 e^{(a+bi)t} + A_2 e^{(a-bi)t} , \tag{21}$$

where $r_{1,2} = a \pm bi$

$$a = -c/2I_Y$$

$$b = \sqrt{\left[\frac{K}{I_Y} - \left(\frac{C}{2I_Y}\right)^2\right]} = \omega_d \quad \text{(undamped natural frequency)} .$$

Equation (21) can also be written as

$$\theta = \theta_0 e^{-(C/2I_Y)t} \cos(\omega_d \pm \phi) , \tag{22}$$

θ_0 and ϕ being arbitrary constants. Equation (22) represents a harmonic oscillation with damping. When $\cos(\omega_d t - \phi) = 1$, the envelope encompassing the points of tangency with the displacement is described by

$$\theta = \theta_0 e^{-(C/2I_Y)t} .$$

From this relationship, the logarithmic decrement $\log_e(\theta/\theta_1)$ is used to obtain the damping term C . An often used parameter for measuring the damping coefficient is the time required to damp to a particular amplitude ratio. Letting θ_1 and θ_2 represent amplitudes occurring at times t_1 and t_2 , respectively, and letting $\theta_2/\theta_1 = R$, we obtain the following equation for the damping moment:

$$C = -2I_Y f \log_e R/C_{yR} . \tag{23}$$

since $$t_2 - t_1 = C_{yR}/f .$$

From Equation (21) for the natural damped frequency, the static moment is

$$K = I_Y \omega_d^2 + I_Y (C/2I_Y)^2 \quad . \tag{24}$$

The term $I_Y(C/2I_Y)^2$ is usually very small and can be neglected.

As shown in Equations (17) and (18), the dynamic damping and static moments consist of moments due to the aerodynamics and moments produced by tares in the balance system. The tares are evaluated from wind-off measurements, and the final aerodynamic dynamic damping and static moments are given by

$$C = - M_{\dot\theta w} = - (M_{\dot\theta a} + M_{\dot\theta t})_w$$

$$M_{\dot\theta a} = (M_{\dot\theta a} + M_{\dot\theta t})_w - (M_{\dot\theta t})_v$$

$$K = - M_{\theta w} = - (M_{\theta a} + M_{\theta t})_w$$

$$M_{\theta a} = (M_{\theta a} + M_{\theta t})_w - (M_{\theta t})_v \quad .$$

where the subscripts w and v denote wind-on and vacuum conditions, respectively.

Since the structural damping moment parameter varies inversely as the frequency of oscillation, incorporation of Equations (23) and (24) along with the equations above gives

$$M_{\dot\theta a} = 2I_Y \log_e R \left[(f/C_{yR})_w - (f/C_{yR})_v \frac{f_v}{f_w} \right]$$

$$M_{\theta a} = I_Y [(\omega_d)_w^2 - (\omega_d)_v^2] \quad .$$

In cases where the balance system has no structural stiffness (systems using a gas bearing or ball bearing pivot), the tare damping may be evaluated independently of the model. Semi-empirical means may be needed to find the tare damping at the frequency and the motion axial load that will be experienced in the wind tunnel. Equation (23) is simply used to yield

$$M_{\dot\theta w} = 2I_Y f \log_e R/C_{yR} \quad .$$

The tare damping is noted as $M_{\dot\theta t}$ and

$$M_{\dot\theta a} = 2I_Y f \log_e R/C_{yR} - M_{\dot\theta t} \quad .$$

The aerodynamic stiffness is obtained from Equation (24) as

$$M_{\theta a} = I_Y \omega_w^2 \quad .$$

The derivatives, when reduced to a dimensionless form for pitching motion, become

$$C_{mq} + C_{m\dot\alpha} = M_{\dot\theta a} (2V_\infty / q_\infty A d^2)$$

$$C_{m\alpha} = M_{\theta a} / q_\infty A d \quad .$$

It should be noted that the above equations were developed for a linear model. It will be shown later, in Section 3.2.1.2, that erroneous values of damping may result if the linear equations are applied to models which have a nonlinear restoring moment. It will also be shown in Section 3.2.1.2 that Equation (22) may be generalized as

$$\theta = \theta_0(0)\left[\frac{\omega(0)}{\omega(t)}\right]^{\frac{1}{2}} e^{-(C/2I_Y)t}\cos\left[\Upsilon(t) - \phi\right] ,$$

where $\Upsilon(t) = \int \omega(t)\, dt$,

and Equation (23) now becomes

$$C = -2I_Y f \log_e\left[R(\omega_2/\omega_1)^{\frac{1}{2}}\right]/C_{yR} .$$

3.2.1.2 Effects of Nonlinearities

Many aerodynamic configurations of interest have damping rates and oscillation frequencies that vary with time. Quite often these parameters are functions of the dependent variable and its time derivatives; therefore the differential equation which describes the angular motion is nonlinear. In many cases, these nonlinearities are slight, and the amplitude-time history may be broken into intervals over which the motion is approximately exponentially damped. It has often been assumed that, by applying the linear theory over these approximately exponentially damped segments, an accurate estimate of the aerodynamic damping may be obtained. This is true only when the aerodynamic stiffness is constant. Nicholaides[38] has shown qualitatively how errors in the damping measurements can be made using this approach. In order to show this, Equation (18) will be used in the form

$$\ddot{\theta} + D_1\dot{\theta} + D_2\theta = 0 \qquad (25)$$

where

$$D_1 = D_1(\theta, \dot{\theta}, t)$$

$$D_2 = D_2(\theta, \dot{\theta}, t) .$$

Multiplying Equation (25) through by $2\dot{\theta}/D_2$ and integrating yields

$$-\theta^2\Big|_{t_1}^{t_2} = (\dot{\theta}^2/D_2)\Big|_{t_1}^{t_2} + \int_{t_1}^{t_2}\left[\dot{D}_2 + 2D_1D_2\right](\dot{\theta}/D_2)^2\, dt .$$

Assuming that t_1 and t_2 are times that peaks in the motion occur, this expression reduces to

$$\theta_1^2 - \theta_2^2 = \int_{t_1}^{t_2}\left[\dot{D}_2 + 2D_1D_2\right](\dot{\theta}/D_2)^2\, dt .$$

A dynamic stability condition is obtained from this expression as

$$[\dot{D}_2 + 2D_1D_2] > 0 .$$

For zero viscous damping ($D_1 = 0$), the convergence or divergence of the motion is dictated by the rate of change of D_2 with respect to time. Thus the variable aerodynamic stiffness term D_2 supplies a mechanism by which energy may be fed into or taken away from the system. The linear theory, Equation (18), assumes that D_2 is constant and therefore that the constant term D_1 determines the convergence or divergence of the system. One can readily see that if the linear theory is applied to a situation where D_2 is a variable, the value of D_1 obtained will be erroneous. This is true even if the linear theory is applied to the nonlinear oscillation over small approximately exponentially damped intervals. The magnitude of this error is, of course, dependent of the magnitude of $\dot{D}_2$.

When the aerodynamic nonlinearities are large, Equation (25) is very difficult to solve. Fortunately, as mentioned previously, there are many aerodynamic configurations of interest for which these nonlinearities are small. In addition, these shapes usually have damping moments that are small compared to the restoring moment. For such shapes Equation (25) may be written as

$$\ddot{\theta} + D_1(\theta,\dot{\theta},t)\dot{\theta} + [D_{20} + D_{21}(\theta,\dot{\theta},t)]\theta = \theta , \tag{26}$$

where

$$D_2 = D_{20} + D_{21}$$

$$D_{20}\theta \gg D_1\dot{\theta}$$

$$D_{20} \gg D_{21} .$$

This equation may be reduced to the van der Pol equation, which is given as

$$\ddot{\theta} + D_{20}\theta = \epsilon\hat{\phi}(\theta,\dot{\theta},t) , \tag{27}$$

where $\hat{\phi}(\theta,\dot{\theta},t)$ contains the nonlinear terms and ϵ is a small dimensionless parameter which characterizes how close the system is to a linear conservative one. For the above example,

$$\epsilon\hat{\phi}(\theta,\dot{\theta},t) = - [D_1(\theta,\dot{\theta},t)\theta + D_{21}(\theta,\dot{\theta},t)\theta] .$$

The motion may be approximated for short time intervals by the solution for a harmonic oscillator ($\epsilon = 0$) which is given as

$$\theta = \theta_0 \cos (\sqrt{D_{20}}t + \phi) .$$

Since the right-hand side of Equation (27) is small but not zero, θ_0 and ϕ are actually slowly varying functions of time.

It is shown in Reference 39 that a second-order nonlinear differential equation, like Equation (27), may be reduced to an equivalent linear second-order equation with

variable coefficients which has a first-order solution identical to that of Equation (27). This equivalent linear equation may be written as

$$\ddot{\theta} - \frac{2\dot{\theta}_{0m}}{\theta_{0m}}\dot{\theta} + [\sqrt{(D_{20})} + \dot{\phi}_m]^2\theta = 0 ,$$

where the m subscripts indicate mean values over a cycle of oscillation.

The equation above can be rewritten as

$$\ddot{\theta} + C_1(t)\dot{\theta} + C_2(t)\theta = 0 . \tag{28}$$

In order to solve this equation, the following transformation will be used:

$$\theta(t) = u(t)A(t) . \tag{29}$$

Differentiating this expression and substituting into Equation (28) yields

$$u\ddot{A} + 2\dot{u}\dot{A} + \ddot{u}A + C_1u\dot{A} + C_1\dot{u}A + C_2uA = 0 .$$

Choose u and A such that

$$2\dot{u}\dot{A} + C_1u\dot{A} = 0 . \tag{30}$$

This reduces the previous equation to

$$u\ddot{A} + \ddot{u}A + C_1\dot{u}A + C_2uA = 0 . \tag{31}$$

Dividing Equation (30) by $\dot{A}$ and integrating yields

$$u = Ke^{-\frac{1}{2}\int C_1\,dt} , \tag{32}$$

where K is the constant of integration.

Differentiating this expression and substituting into Equation (31) yields

$$\ddot{A} + B(t)A = 0 , \tag{33}$$

where

$$B(t) = [C_2 - \tfrac{1}{4}C_1^2 - \tfrac{1}{2}\dot{C}_1] .$$

According to a theorem by Winter[40], the asymptotic solution of Equation (33) is

$$A(t) = [B(t)]^{-\frac{1}{4}}[K_1 \cos \Upsilon(t) + K_2 \sin \Upsilon(t)] , \tag{34}$$

where $\Upsilon(t) = \int\sqrt{B(t)}\,dt$.

This solution applies after a finite length of time has elapsed, such that the oscillatory motion approaches being periodic.

It is interesting to note that for certain forms of $B(t)$, Equation (33) may be reduced to Bessel's differential equation.

Equations (29), (32), and (34) may be combined and manipulated algebraically to yield

$$\theta(t) = \theta(0) \left[\frac{B(0)}{B(t)}\right]^{\frac{1}{4}} e^{-\frac{1}{2}\int C_1(t)\, dt} \cos\left[\Upsilon(t) + \phi\right] , \qquad (35)$$

where $\theta(0)$ and $B(0)$ are the values of envelope amplitude and $C(t)$ respectively at $t = 0$.

For the case being considered, where C_1 varies slowly and is small compared to C_2, $B(t)$ given in Equation (33) may be reduced to

$$B = \omega^2 \simeq C_2 .$$

The following form of Equation (35) may be applied over intervals of the data where C_1 is approximately constant:

$$\theta = \theta(0) \left[\frac{\omega(0)}{\omega(t)}\right]^{\frac{1}{2}} e^{-\frac{1}{2}C_1 t} \cos\left[\Upsilon(t) + \phi\right] ,$$

where

$$\Upsilon(t) = \int_0^t \omega(t)\, dt$$

$$C_1 = C/I_Y .$$

In order to use this solution to determine C_1, ω and γ must be known as functions of time.

3.2.1.3 Free Oscillation (Three Degrees of Freedom)

Solutions of the equations of motion referenced to the nonrolling coordinates will be obtained in this section*. For this development it is assumed that the model has triagonal or greater symmetry and that the $\tilde{X}\tilde{Y}\tilde{Z}$ axes correspond to the principal inertia axes of the model. The effects of slight asymmetries of the model will be considered, i.e., asymmetries which have a negligible effect on the above assumptions.

3.2.1.3.1 Equation of Pitching and Yawing Motions

For a model of the above type rotating about a point fixed in space, Equations (5) describe the motion.

---

* These methods have been extracted from References 38 and 41.

$$I\dot{\tilde{q}} + I_X P\tilde{r} = (\Sigma M)_{\tilde{Y}} = \rho \frac{V_c^2 Ad}{2} \tilde{C}_m \tag{36}$$

$$I\dot{\tilde{r}} - I_X P\tilde{q} = (\Sigma M)_{\tilde{Z}} = \rho \frac{V_c^2 Ad}{2} \tilde{C}_n \, , \tag{37}$$

where $I = I_{\tilde{y}} = I_{\tilde{z}}$.

For motion about a point fixed in space,

$$\left.\begin{aligned} \theta &= \alpha \\ \psi &= -\beta \, . \end{aligned}\right\} \tag{38}$$

The angular rates in the nonrolling coordinate system are given as

$$\tilde{q} = q \cos \Phi - r \sin \Phi$$

$$\tilde{r} = r \cos \Phi + q \sin \Phi \, ,$$

where

$$\Phi \simeq \int_0^t P(t) \, dt \, .$$

Substituting the angular rates given in Equations (4), these expressions reduce to

$$\left.\begin{aligned} \tilde{q} &= \dot{\theta} \\ \tilde{r} &= \dot{\psi} \cos \theta \, . \end{aligned}\right\} \tag{39}$$

When the motion is restricted to small angular excursions ($\theta << 1$), Equations (39) reduce to

$$\left.\begin{aligned} \tilde{q} &= \dot{\theta} \\ \tilde{r} &= \dot{\psi} \, . \end{aligned}\right\} \tag{40}$$

Multiplying Equation (36) by i and subtracting Equation (37) from it, these equations may be combined to form a single differential equation

$$I(-\dot{\tilde{r}} + i\dot{\tilde{q}}) - iI_X P(-\tilde{r} + i\tilde{q}) = iq_\infty Ad(\tilde{C}_m + i\tilde{C}_n) \, .$$

Assuming small angular excursions and substituting the time derivatives of Equations (38) and (40) into the equation above yields

$$I(\ddot{\beta} + i\ddot{\alpha}) - iI_X P(\dot{\beta} + i\dot{\alpha}) = iq_\infty Ad(\tilde{C}_m + i\tilde{C}_n) \, .$$

The complex angle of attack may be reduced to

$$\tilde{\zeta} = \frac{\tilde{v} + i\tilde{w}}{V_c} \simeq \tilde{\beta} + i\tilde{\alpha} ,$$

where it is assumed that $\tilde{\beta} \simeq \tilde{v}/V_c$ and $\tilde{\alpha} \simeq \tilde{w}/V_c$. Substituting the time derivatives of this complex angle into the equation of motion,

$$I\ddot{\tilde{\zeta}} - iI_X P\dot{\tilde{\zeta}} = iq_\infty Ad(\tilde{C}_m + i\tilde{C}_n) . \tag{41}$$

Assuming that first-order linear aerodynamics are adequate and that the motion is described by α, β, $\dot{\alpha}$, $\dot{\beta}$, P, q, and r, the pitching- and yawing-moment coefficients are given in the body coordinates XYZ as

$$C_m = C_{m0} + C_{m\alpha}\alpha + C_{mq}\left(\frac{qd}{2V_c}\right) + C_{m\dot{\alpha}}\left(\frac{\dot{\alpha}d}{2V_c}\right) + C_{mp\beta}\beta\left(\frac{Pd}{2V_c}\right)$$

$$C_n = C_{n0} + C_{n\beta}\beta + C_{nr}\left(\frac{rd}{2V_c}\right) + C_{n\dot{\beta}}\left(\frac{\dot{\beta}d}{2V_c}\right) + C_{np\alpha}\alpha\left(\frac{Pd}{2V_c}\right) .$$

The terms C_{m0} and C_{n0} were included in this expansion of the coefficients to account for the assumed slight asymmetry of the model*. As outlined by Murphy[41], the Magnus coefficients, $C_{np\dot{\alpha}}$, $C_{mp\dot{\beta}}$, C_{npq}, and C_{mpr}, have a negligible effect on the motion; therefore they were not included.

For a missile with triagonal or greater symmetry†,

$$C_{n\beta} = -C_{m\alpha} = -C_{M\alpha}$$

$$C_{n\dot{\beta}} = -C_{m\dot{\alpha}} = -C_{M\dot{\alpha}}$$

$$C_{nr} = C_{mq} = C_{Mq}$$

$$C_{np\alpha} = C_{mp\beta} = C_{Mp\alpha} .$$

Substitute these relations into the yawing-moment equation, then multiply the result by i and add it to the pitching-moment equation to obtain

$$i(C_m + iC_n) = i(C_{m0} + iC_{n0}) + C_{M\alpha}(\beta + i\alpha) +$$

$$+ (C_{Mq} + C_{M\dot{\alpha}})(\dot{\beta} + i\dot{\alpha})\frac{d}{2V_c} + C_{Mp\alpha}(\beta + i\alpha)\hat{P} ,$$

---

* This approach was first used by Nicolaides[42] in his development of the "Tricyclic" theory.

† See References 38 and 41 for a discussion of symmetry.

where

$$\hat{P} = Pd/2V_c .$$

Substituting the complex angle of attack referenced to the body coordinates,

$$\xi \simeq \beta + i\alpha ,$$

into the above relation yields

$$i(C_m + iC_n) = i(C_{m0} + iC_{n0}) + C_{M\alpha}\xi + \\ + (C_{Mq} + C_{M\dot{\alpha}}) \frac{\xi d}{2V_c} + C_{Mp\alpha}\xi\hat{P} . \qquad (42)$$

It now becomes necessary to transform these coefficients from the body coordinates to the nonrolling coordinates. This transformation is given as

$$i(C_m + iC_n)e^{i\Phi} = i(\tilde{C}_m + i\tilde{C}_n) .$$

The transformation for the complex angle of attack is given as

$$\xi e^{i\Phi} = \tilde{\xi} .$$

This is easily proved by expanding this relation and equating real and imaginary parts as follows

$$\left(\frac{v + iw}{V_c}\right)(\cos\Phi + i \sin\Phi) = \frac{\tilde{v} + i\tilde{w}}{V_c}$$

$$\tilde{v} = v \cos\Phi + w \sin\Phi$$

$$\tilde{w} = w \cos\Phi - v \sin\Phi .$$

These relations are the nonrolling velocity components[41].

Murphy[41] used the above transformation to transform Equation (42) to the nonrolling coordinates. The result may be written as

$$i(\tilde{C}_m + \tilde{C}_n) = i(C_{m0} + iC_{n0})e^{i\Phi} + C_{M\alpha}\tilde{\xi} + \\ + (C_{Mq} + C_{M\dot{\alpha}}) \frac{\dot{\tilde{\xi}} d}{2V_c} + iC_{Mp\alpha}\tilde{\xi}\hat{P} .$$

Substituting this relation into Equation (41) results in

$$\ddot{\tilde{\xi}} + (G + iH)\dot{\tilde{\xi}} + (J + iK)\tilde{\xi} = Le^{iPt} , \qquad (43)$$

where

$$G = -\frac{q_\infty A d^2}{2V_\infty I}(C_{Mq} + C_{M\dot{\alpha}})$$

$$H = -\frac{I_X}{I}P$$

$$J = -\frac{q_\infty A d}{I}C_{M\alpha}$$

$$K = -\frac{q_\infty A d^2}{2V_\infty I}C_{Mp\alpha}P$$

$$L = i\frac{q_\infty A d}{I}(C_{m0} + iC_{n0}) \quad .$$

3.2.1.3.2 Solution for Constant Coefficients

Assuming constant coefficients, a solution to this second-order linear differential equation is given as

$$\tilde{\xi} = K_1 e^{(\lambda_1 + i\omega_1)t} + K_2 e^{(\lambda_2 + i\omega_2)t} + K_3 e^{iPt} \quad , \tag{44}$$

where

$$K_3 = -\frac{L}{\{(P - \omega_1)(P - \omega_2) + \lambda_1\lambda_2 + i[\lambda_1(P - \omega_2) + \lambda_2(P - \omega_1)]\}}$$

$$\lambda_j + i\omega_j = -\frac{(G + iH) \pm \sqrt{[G^2 + 2GHi - H^2 - 4(J + iK)]}}{2} \quad .$$

subscript j = 1 or 2 .

Using boundary conditions, the remaining constants are evaluated as

$$K_{1,2} = \frac{\dot{\tilde{\xi}} - (\lambda_{2,1} + i\omega_{2,1})(\tilde{\xi}_0 - K_3)}{\lambda_{1,2} - \lambda_{2,1} + i(\omega_{1,2} - \omega_{2,1})} \quad .$$

The solution given in Equation (44) is "Tricyclic" in that it is described by three two-dimensional vectors or arms (Fig.35). For models spinning at a constant rate, the first two rotating arms are damped, and the third is a constant amplitude rotating vector which results from the forcing function given in Equation (43). This rotating trim vector, due to the asymmetry of the model, causes the axis of symmetry of the model to rotate on an imaginary conical surface. As P increases, the magnitude of this rotating trim is decreased. For a statically stable model with sufficiently small

damping, the total angle of attack may increase as P approaches ω_1. In this case, the possibility of resonance exists only with the nutational frequency (ω_1) since the precessional frequency (ω_2) carries a sign opposite that of P (Ref.38). This will be shown later in the text.

The restrictions on the above solution are:

(i) Configurations with triagonal or greater symmetry having only slight configurational asymmetries.

(ii) First-order linear aerodynamics.

(iii) P = constant.

(iv) Small oscillation amplitudes.

If the relations for the modal damping rates and frequencies given in Equation (44) for j = 1 and 2, respectively, are first added together, then multiplied together, the following exact relationships result[41]:

$$\lambda_1 + \lambda_2 = -G = \frac{q_\infty A d^2}{2V_\infty I}\left(C_{Mq} + C_{M\dot{\alpha}}\right)$$

$$\omega_1 + \omega_2 = -H = \frac{I_X}{I} P$$

$$\lambda_1\lambda_2 - \omega_1\omega_2 = J = -\frac{q_\infty A d}{I} C_{M\alpha}$$

$$\lambda_1\omega_2 + \lambda_2\omega_1 = K = -\frac{q_\infty A d^2}{2V_\infty I} C_{Mp\alpha} P .$$

For most configurations of interest

$$\left|(-H^2 - 4J)\right| \gg \left|(G^2 + 2iGH - 4iK)\right| .$$

Therefore the expression for the modal frequencies and damping rates is approximated by

$$\lambda_j + i\omega_j \simeq -\frac{(G + iH)}{2} \pm \frac{1}{2}\left[\left\{-(H^2 + 4J)\right\} + \frac{G^2 + 2iGH - 4iK}{2i\left\{(H^2 + 4J)\right\}}\right] .$$

In order to derive the expression for the gyroscopic stability factor, only predominant aerodynamic effects are considered in this relation, which reduces it to

$$\lambda_j + i\omega_j \simeq \frac{1}{2}\left[-iH \pm \left\{-(H^2 + 4J)\right\}\right] .$$

For an aerodynamically statically unstable model, $J < 0$. It is obvious then, for this case, that unless $-(H^2 + 4J) < 0$ the motion will diverge, since $\lambda_1 > 0$. If

$H^2 > -4J$, then $\lambda_j = 0$, the constant-amplitude periodic motion results. The gyroscopic stability factor is defined as

$$S_g = \frac{-H^2}{4J} = \frac{I}{4q_\infty Ad}\left(\frac{I_X}{I}\right)^2 \frac{P^2}{C_{M\alpha}} . \tag{45}$$

The stability condition is given as

$$1/S_g < 1 .$$

Static stability is insured for all aerodynamically statically stable models ($C_{M\alpha} < 0$) and for aerodynamically statically unstable models ($C_{M\alpha} > 0$) when $S_g > 1$.

If we let

$$\tau = (1 - 1/S_g)^{-\frac{1}{2}} ,$$

then $\tau < 1$ for $C_{M\alpha} < 0$, and $\tau > 1$ for $C_{M\alpha} > 0$ when the roll rate of the model is sufficiently high to insure static stability.

The expression for the modal damping rates and frequencies is given as

$$\lambda_j + i\omega_j \simeq -\left[\frac{G}{2}(1 + \tau) \pm \frac{K\tau}{H}\right] - i\frac{H}{2}\left(1 \pm \frac{1}{\tau}\right) , \tag{46}$$

where

$$\lambda_j \simeq \left[\frac{G}{2}(1 \pm \tau) \pm \frac{K\tau}{H}\right] = \frac{q_\infty Ad^2}{2V_\infty I}\left[(C_{Mq} + C_{M\dot{\alpha}})(1 \pm \tau) \pm \frac{I}{I_X} C_{Mp\alpha}\tau\right] \tag{47}$$

$$\omega_j \simeq -\frac{H}{2}\left(1 \pm \frac{1}{\tau}\right) = \frac{I_X}{2I} P \left(1 \pm \frac{1}{\tau}\right) . \tag{48}$$

It is shown in Equation (47) that the Magnus moment tends to increase the damping of one modal vector and decrease the damping of the other. A model will, therefore, diverge when

$$\left|IC_{Mp\alpha}\tau/I_X\right| > \left|(C_{Mq} + C_{M\dot{\alpha}})(1 + \tau)\right| .$$

For a spinning model, the modal frequencies are unequal, as evidenced in Equation (48). The largest angular rate (ω_1) is known as the nutation frequency and the smaller angular rate (ω_2) is the precession frequency. The nutation frequency (ω_1) always carries the same sign as the roll rate (P); therefore, K_1 rotates in the same direction as K_3 . For an aerodynamically statically stable model ($\tau < 1$), the frequencies are unequal in sign and therefore cause the modal vectors K_1 and K_2 to rotate in opposite directions (Fig. 35). When $P = 0$, $\tau = 0$, then $\omega_1 = -\omega_2$, $\lambda_1 = \lambda_2$, and the motion is described by lines, ellipses and circles (Fig. 36). As P increases ($\tau > 0$) the motion becomes flowerlike and finally, for large P , the motion becomes like that of a fast spinning gyroscopic pendulum (Fig. 37). For an aerodynamically statically unstable

model ($\tau > 1$), the frequencies are equal in sign and therefore the modal vectors K_1 and K_2 rotate in the same direction. Motions characteristics of a fast spinning aerodynamically statically unstable model are given in Figure 38.

In order to obtain the damping rates and frequencies of the modal vectors, the usual approach is to fit the solution given in Equation (44) to the observed motion, using a least squares differential correction method. For a description of this method and its application, see References 41 and 42.

3.2.1.3.3 Solution for Varying Roll Rate

In many cases of interest, the roll rate is not constant as assumed. If the region of resonance is avoided and the roll rate is slowly varying, the solution given in Equation (44) may be used to fit the data if it is applied over intervals of the motion where P is nearly constant.

For roll rates near resonance, P is usually small enough such that $G >> H$ and $J >> K$. Roll rates varying near resonance will therefore have a negligible effect on the homogeneous solution of Equation (43). This is not true of the particular solution which undergoes drastic variations at this condition; therefore Equation (44) is not valid for this condition.

In order to investigate the problem of roll rates varying near resonance, we will rewrite Equation (43) as

$$\ddot{\underset{\sim}{\xi}} + (G + iH)\dot{\underset{\sim}{\xi}} + (J + iK)\underset{\sim}{\xi} = Le^{i\Phi(t)} , \tag{49}$$

where

$$\Phi(t) \simeq \int_0^t P(t)\, dt$$

$$G + iH = \text{constant}$$

$$J + iK = \text{constant} .$$

The complementary function of the differential equation (49) will be the same as that given in Equation (44). The task is now to obtain a particular integral. This will be accomplished using the method of variation of parameters, as Murphy did in Reference 41.

Assume the particular solution is of the form

$$\underset{\sim}{\xi}_p = A_1 e^{(\lambda_1 + i\omega_1)t} + A_2 e^{(\lambda_2 + i\omega_2)t} , \tag{50}$$

where the coefficients A_j are variable unknowns and λ_j and ω_j are known constants ($j = 1$ or 2).

Applying the method of variation of parameters results in the following two simultaneous equations:

$$\dot{A}_1 e^{(\lambda_1 + i\omega_1)t} + \dot{A}_2 e^{(\lambda_2 + i\omega_2)t} = 0 \tag{51}$$

$$\dot{A}_1(\lambda_1 + i\omega_1)e^{(\lambda_1 + i\omega_1)t} + \dot{A}_2(\lambda_2 + i\omega_2)e^{(\lambda_2 + i\omega_2)t} = Le^{i\Phi(t} \quad . \tag{52}$$

Solving Equations (51) and (52) simultaneously results in

$$\dot{A}_1 = \frac{Le^{-(\lambda_1 + i\omega_1)t + i\Phi(t)}}{(\lambda_1 - \lambda_2) + i(\omega_1 - \omega_2)}$$

$$\dot{A}_2 = \frac{Le^{-(\lambda_2 + i\omega_2)t + i\Phi(t)}}{(\lambda_2 - \lambda_1) + i(\omega_2 - \omega_1)} \quad .$$

These expressions are integrated and substituted into Equation (50). The solution to Equation (49) is then given as

$$\tilde{\xi} = K_1 e^{(\lambda_1 + i\omega_1)t} + K_2 e^{(\lambda_2 + i\omega_2)t} +$$

$$+ \frac{L\int_0^t \left[e^{(\lambda_1 + i\omega_1)(t - t_1)} - e^{(\lambda_2 + i\omega_2)(t - t_2)}\right] e^{i\int_0^{t_1} P(t)\,dt}}{\lambda_1 - \lambda_2 + i(\omega_1 - \omega_2)} \quad .$$

In order to use this solution, P must be known as a function of time.

By arbitrarily including the term $e^{\lambda_3 t}$ in the K_3 vector, the solution given as Equation (44) can be made to approximately compensate for the changes in the rolling trim angle*. This solution then does not require knowing P as a function of t and is given as

$$\tilde{\xi} = K_1 e^{(\lambda_1 + i\omega_1)t} + K_2 e^{(\lambda_2 + i\omega_2)t} + K_3 e^{(\lambda_3 + i\omega_3)t} \quad , \tag{53}$$

where $\omega_3 = P$.

It should be emphasized that the solutions obtained thus far are for slowly varying roll rates. If the roll rate is large and rapidly varying, these solutions are not applicable.

---

* This method was related to Mr L.K.Ward in a private communication with Professor Robert S.Eikenberry of the Department of Aerospace Engineering, University of Notre Dame, Notre Dame, Indiana.

3.2.1.3.4 Solution for Variable Coefficients

The effects of variable aerodynamic stiffness and damping were discussed previously in Section 3.2.1.2. In that section, the need for correcting the damping measurements for the effects of variable aerodynamic stiffness was emphasized. It was shown that, for slowly varying coefficients and small damping, a second-order nonlinear differential equation, like the homogeneous portion of Equation (49), can be reduced to a linear equation with variable coefficients and retain the same first-order solution.

For the nonlinear case ($J = J(\xi,\dot{\xi},t)$, etc.), the homogeneous portion of Equation (49) may be written correctly to first order as follows:

$$\ddot{\tilde{\xi}} + [G(t) + iH(t)]\dot{\tilde{\xi}} + [J(t) + iK(t)]\tilde{\xi} = 0 . \tag{54}$$

Murphy[41] derived a correction to the linear complementary function by assuming the following solution to Equation (54):

$$\tilde{\xi} = K_1 e^{i\phi_1} + K_2 e^{i\phi_2} , \tag{55}$$

where K_j is a variable and

$$\phi_j(t) = \int_0^t \omega_j(t)\, dt \qquad (j = 1 \text{ or } 2) .$$

This solution is similar in form to linear epicyclic complementary functions obtained for constant coefficients.

The following set of equations was obtained by substituting the first and second time derivatives of the solution (55) into Equation (54) and separating real and imaginary parts:

$$\frac{d}{dt}[\dot{K}_j/K_j] + [\dot{K}_j/K_j]^2 - \omega_j^2 + G[\dot{K}_j/K_j] - H\omega_j + J = 0 \tag{56}$$

$$\dot{\omega}_j + 2[\dot{K}_j/K_j]\omega_j + H[\dot{K}_j/K_j] + G\omega_j + K = 0 . \tag{57}$$

Since $\omega_j >> \dot{K}_j/K_j$ and $\dot{K}_j/K_j$ is slowly varying, Equation (56) may be reduced and manipulated algebraically to yield

$$\omega_j = -\frac{H}{2} \pm \sqrt{\left[\left(\frac{H}{2}\right)^2 + J\right]} . \tag{58}$$

This is essentially the same as the frequency relation obtained for constant coefficients.

Equation (57) can be rearranged to obtain

$$\dot{K}_j/K_j = \lambda_j - \frac{\dot{\omega}_j}{2\omega_j} + \frac{\dot{H}}{4\omega_j} , \tag{59}$$

where

$$\lambda_j = -\frac{1}{2}\frac{(G\omega_j + K)}{(\omega_j + H/2)}$$

$$\hat{\omega}_j = \omega_j + H/2 .$$

This relation shows that variable aerodynamic stiffness and variable roll rate both affect the convergence or divergence of the motion. If the linear theory were applied directly to motion of this type, the complete right-hand side of Equation (59) would be obtained as the damping rate.

Equation (59) is now integrated to obtain

$$K_j(t) = K_j(0)\left[\frac{H(0)^2 + 4J(0)}{H(t)^2 + 4J(t)}\right]^{\frac{1}{4}} e^{\int_0^t (\lambda_j + \dot{H}/4\hat{\omega}_j)\, dt} .$$

Using Equations (58) and (59), and the condition of slowly varying parameters, the equation above can be rewritten as

$$K_j(t) = K_j(0)\left[\frac{\omega_j(0) + H(0)/2}{\omega_j(t) + H(t)/2}\right]^{\frac{1}{2}} e^{\lambda_j t} ,$$

where it is assumed that

$$\lambda_j >> \dot{H}/\{4(\omega_j + H/2)\} .$$

Substituting this into Equation (55), the complementary function becomes

$$\tilde{\xi} = K_1(0)\left[\frac{\omega_1(0) + H(0)/2}{\omega_1(t) + H(t)/2}\right]^{\frac{1}{2}} e^{\lambda_1 t + i\phi(t)} +$$

$$+ K_2(0)\left[\frac{\omega_2(0) + H(0)/2}{\omega_2(t) + H(t)/2}\right]^{\frac{1}{2}} e^{\lambda_2 t + i\phi_2(t)} .$$

This solution may be applied over portions of the motion history where λ_j is approximately constant if $\omega_j(t)$ and $P(t)$ are known.

3.2.1.3.5 Graphic Data Reduction Method (Approximate)

A graphic data reduction method may be used to determine the modal damping rates (λ_j) and frequencies (ω_j). In order to apply this method, it is necessary to convert the tricyclic motion to epicyclic motion. This is accomplished using the roll rate history as follows:

$$\tilde{\xi} e^{-iPt} = Be^{i(\omega_1 - P)t} + Ce^{i(\omega_2 - P)t} + K_3 e^{i\Phi_0} .$$

where

$$B = K_1 e^{\lambda_1 t}$$

$$C = K_2 e^{\lambda_2 t}$$

$$K_3 e^{i\Phi_0} = \text{constant} .$$

The motion is transformed to body fixed coordinates by rotating each angle through its corresponding roll orientation (Fig. 39). This results in epicyclic motion about the point $K_3 e^{i\Phi_0}$.

At maxima of the epicyclic motion, B and C add, and at minima they subtract (Fig. 40). Using the maximum and minimum amplitude points and their corresponding times, the variation of B and C with respect to time is obtained (Fig. 41). Taking the ratio of the natural logarithms of these expressions yields

$$\left.\begin{aligned} \lambda_1 &= \frac{1}{t_2 - t_1} \log_e \left(\frac{B_2}{B_1}\right) \\ \lambda_2 &= \frac{1}{t_2 - t_1} \log_e \left(\frac{C_2}{C_1}\right) . \end{aligned}\right\} \qquad (60)$$

The modal frequencies are obtained using Figure 40 as follows:

$$\omega_1 = \frac{2\pi + \gamma}{t_2 - t_1}$$

$$\omega_2 = -\frac{(2\pi - \gamma)}{t_2 - t_1} , \qquad C_{M\alpha} < 0 .$$

Combining Equations (45), (46), and (48) with the above frequency relations, the pitching-moment slope is given as

$$C_{M\alpha_E} = \frac{I}{4q_\infty Ad} \left[\left(\frac{I_X}{I}\right)^2 p^2 - (\omega_1 - \omega_2)^2\right] .$$

Assuming the roll rate is sufficiently small that Magnus effects can be neglected, Equations (47) and (60) can be combined to yield

$$[C_{Mq} + C_{M\dot{\alpha}}]_E = \frac{2}{Ad^2} \frac{V_\infty}{q_\infty} \frac{1}{(1 + \tau)} \frac{1}{(t_2 - t_1)} \log_e \left(\frac{B_2}{B_1}\right)$$

$$[C_{Mq} + C_{M\dot{\alpha}}]_E = \frac{2}{Ad^2} \frac{V_\infty}{q_\infty} \frac{1}{(1 - \tau)} \frac{1}{(t_2 - t_1)} \log_e \left(\frac{C_2}{C_1}\right) .$$

The effect of balance tare damping on the total damping rates must be accounted for before the aerodynamic coefficients are obtained. The use of a spherical gas bearing pivot eliminates this difficulty for almost all cases of practical interest, due to its negligibly small tare damping.

3.2.1.4 Forced Oscillation

The motion of a model balance system which is rigidly suspended in an airstream and forced to oscillate in one degree of freedom (pitch) as a sinusodial function of time may be expressed as

$$I_Y\ddot{\theta} - (M_{\dot{\theta}a} + M_{\dot{\theta}t})\dot{\theta} - (M_{\theta a} + M_{\theta t})\theta = M \cos \omega t \ , \tag{61}$$

where the subscript a refers to the aerodynamic values and the subscript t refers to the tare contribution of the model balance system.

Simplifying the nomenclature by letting

$$- (M_{\dot{\theta}a} + M_{\dot{\theta}t}) = C \tag{62}$$

and

$$- (M_{\theta a} + M_{\theta t}) = K \ , \tag{63}$$

Equation (35) becomes

$$I_Y\ddot{\theta} + C\dot{\theta} + K\theta = M \cos \omega t \ . \tag{64}$$

The complete solution of this equation consists of the sum of the complementary and particular solutions. It can be shown that, when $M = 0$, the complementary solution is Equation (19) for the case of the free-oscillation system.

To solve for the particular solution which is necessary for the steady-state case after the decay of the initial transients, it is assumed that the solution is of the form

$$\theta = \theta_0 \cos (\omega t - \phi) \ ,$$

which may be expanded to yield

$$\theta = \theta_0(\cos \omega t \cos \phi + \sin \omega t \sin \phi) \ .$$

The velocity and acceleration are then found as

$$\dot{\theta} = \theta_0\omega(-\sin \omega t \cos \phi + \cos \omega t \sin \phi)$$

$$\ddot{\theta} = -\theta_0\omega^2(\cos \omega t \cos \phi + \sin \omega t \sin \theta) \ .$$

Substituting in Equation (64) and equating coefficients yields

$$\theta_0 = \frac{M}{(K - I_Y\omega^2) \cos \phi + C\omega \sin \phi}$$

$$\tan \phi = \frac{C\omega}{(K - I_Y\omega^2)} \cdot \left\{ \right. \tag{65}$$

Equation (65) shows that for constant amplitude motion, when the forcing frequency is equal to the natural frequency of the system (ϕ = 90 deg), the inertia term balances the restoring-moment term and the damping moment is precisely equal to the forcing torque,

$$C\theta_0\omega = M \ . \tag{66}$$

Under these conditions, it is only necessary to measure the forcing moment M, the angular frequency ω and the system amplitude θ_0 to measure the damping parameter C.

It is not always necessary to operate at resonance, since electronic resolvers can be used to separate the moment into components in-phase and 90 deg out-of-phase with the displacement. Application of resolvers is covered later in this section.

When operating at resonance the displacement, torque, damping and frequency are related by

$$C = M/\theta_0\omega \ .$$

Introducing the relations for C and K (Equations (62) and (63)), the aerodynamic damping moment and the equation for M_{θ_a} become

$$M_{\dot\theta_a} = (M_{\dot\theta_a} + M_{\dot\theta t})_w - (M_{\dot\theta t})_v \tag{67}$$

$$M_{\theta_a} = (M_{\theta_a} + M_{\theta t})_w - (M_{\theta t})_v \tag{68}$$

where v and w indicate the vacuum and wind-on conditions, respectively. In terms of the measured quantities, moment, amplitude and frequency

$$M_{\dot\theta_a} = \frac{1}{\omega_w}\left[\left(\frac{M}{\theta_0}\right)_w - \left(\frac{M}{\theta_0}\right)_v\right]$$

$$M_{\theta_a} = I_Y[\omega_w^2 - \omega_v^2] \ .$$

The derivatives when reduced to a dimensionless form become

$$C_{mq} + C_{m\dot\alpha} = M_{\dot\theta_a}(2V_\infty/q_\infty Ad^2)$$

$$C_{m\alpha} = M_{\theta_a}/q_\infty Ad \ .$$

A further examination can be made of the forced oscillation system with viscous damping by the use of vector diagrams which are convenient for deriving the equations used in a system having resolvers to permit testing near a resonance condition.

The equation of motion with viscous damping and an external source of energy, written earlier in the form

$$I_Y\ddot{\theta} + C\dot{\theta} + K\theta = M \cos \omega t \ , \tag{64}$$

has a particular solution that may be expressed by

$$\theta = \theta_0 \cos (\omega t - \phi) \ , \tag{69}$$

where θ_0 is the amplitude of the steady-state oscillation and ϕ the phase angle by which the motion lags the forcing moment. The angular velocity and acceleration functions, obtained from Equation (69), are given as

$$\dot{\theta} = -\omega\theta_0 \sin (\omega t - \phi) = \omega\theta_0 \cos (\omega t - \phi + \pi/2) \tag{70}$$

$$\ddot{\theta} = -\omega^2\theta_0 \cos (\omega t - \phi) = \omega^2\theta_0 \cos (\omega t - \phi + \pi) \ . \tag{71}$$

Substituting Equations (69), (70), and (71) into Equation (64) gives the following vector relation:

$$I_Y\omega^2\theta_0 \cos (\omega t - \phi) - C\omega\theta_0 \cos (\omega t - \phi + \pi/2) -$$

$$- K\theta_0 \cos (\omega t - \phi) + M \cos \omega t = 0 \ .$$

The vector relation is shown in Figure 42 for forced oscillation with viscous damping. From the diagram (Fig. 42), we obtain

$$\theta_0 = \frac{M}{\sqrt{[(K - I_Y\omega^2)^2 + (C\omega)^2]}}$$

$$\tan \phi = \frac{C\omega}{K - I_Y\omega^2} \ ,$$

which are also shown as Equations (65) in the earlier derivation. Referring to Figure 42, the system damping is

$$C = \frac{M \sin \phi}{\omega\theta_0} \ ,$$

where

$$\sin \phi = \sin (\omega t - \gamma)$$

$$= \sin \omega t \cos \gamma - \cos \omega t \sin \gamma$$

and hence

$$C = \frac{M}{\omega\theta_0} (\sin \omega t \cos \gamma - \cos \omega t \sin \gamma) \ . \tag{72}$$

The in-phase and out-of-phase moments and angles, indicated by M_r and M_i and θ_r and θ_i, respectively, in Figure 42, are related by

$$\left.\begin{aligned} \sin \omega t &= M_i/M , \qquad \sin \gamma = \theta_i/\theta_0 \\ \cos \omega t &= M_r/M , \qquad \cos \gamma = \theta_r/\theta_0 . \end{aligned}\right\} \tag{73}$$

Combining Equations (72) and (73) leads to the following relationship for the damping function:

$$C = \frac{M_i\theta_r - M_r\theta_i}{\omega(\theta_r^2 + \theta_i^2)} .$$

Introducing the relationship for C, Equation (72) becomes

$$M_{\dot\theta a} + M_{\dot\theta t} = \frac{M_i\theta_r - M_r\theta_i}{\omega(\theta_r^2 + \theta_i^2)} .$$

Since the structural damping moment parameter varies inversely with the frequency, the equation for the aerodynamic damping, Equation (67) is given as

$$M_{\dot\theta a} = \left[\frac{M_i\theta_r - M_r\theta_i}{\omega(\theta_r^2 + \theta_i^2)}\right]_w - \left[\frac{M_i\theta_r - M_r\theta_i}{\omega(\theta_r^2 + \theta_i^2)}\right]_v \frac{\omega_v}{\omega_w} ,$$

where v and w indicate vacuum and wind-on conditions.

From the vector representation shown in Figure 42(a), the equation for the static moment may be expressed as

$$\cos \phi = \cos (\omega t - \gamma) = \frac{(K - I_Y\omega^2)\theta_0}{M} \tag{74}$$

and

$$K = I_Y\omega^2 + \frac{M}{\theta_0} \cos (\omega t - \gamma) .$$

Combining Equations (73) and (74) yields

$$K = I_Y\omega^2 + \left[\frac{M_r\theta_r + M_i\theta_i}{\theta_r^2 + \theta_i^2}\right] .$$

Using Equations (73) and (74), the aerodynamic moment derivative becomes

$$M_{\theta a} = \left[I_Y\omega^2 + \left(\frac{M_r\theta_r + M_i\theta_i}{\theta_r^2 + \theta_i^2}\right)\right]_w - \left[I_Y\omega^2 + \left(\frac{M_r\theta_r + M_i\theta_i}{\theta_r^2 + \theta_i^2}\right)\right]_v .$$

In a case where the phase angle between the reference and the model displacement is zero ($\gamma = 0$, Figure 42), the resolution of the forcing moment is somewhat simplified.

From the phase diagram in Figure 42(a), we have

$$C_\omega \theta_0 = M \sin \phi$$

or

$$C = (M/C_\omega \theta_0) \sin \phi ,$$

and

$$K\theta_0 = I_Y \omega^2 \theta_0 + M \cos \phi$$

or

$$K = I_Y \omega^2 + \frac{M}{\theta_0} \cos \phi .$$

The aerodynamic derivatives now become

$$M_{\dot{\theta}a} = \left[\frac{M}{\omega\theta_0} \sin \phi\right]_w - \left[\frac{M}{\omega\theta_0} \sin \phi\right]_v \frac{\omega_v}{\omega_w}$$

and

$$M_{\theta a} = \left[I_Y \omega^2 + \frac{M}{\theta_0} \cos \phi\right]_w \left[I_Y \omega^2 + \frac{M}{\theta_0} \cos \phi\right]_v .$$

These static and dynamic derivatives may be expressed in dimensionless form as

$$C_{mq} + C_{m\dot{\alpha}} = M_{\dot{\theta}a}(2V_\infty/q_\infty A d^2)$$

$$C_{m\alpha} = M_{\theta a}(1/q_\infty A d) .$$

3.2.1.5 Effective and Local Values of Coefficients

Methods have been described for obtaining values of aerodynamic damping and aerodynamic stiffness from models in wind tunnels. In the strict sense of the word, all coefficients that are obtained from these measurements should be classified as effective coefficients (subscript E); however, if the oscillation amplitude is low ($\theta_m \simeq 1$ deg), the coefficients may be termed the instantaneous or local value (subscript L).

Effective values of the coefficients are obtained as a function of the oscillation amplitude θ as the model oscillates about its trim attitude. Local values are obtained as a function of angle of attack α, and the data are obtained with the model oscillating at small amplitudes (usually by means of a forced-oscillation balance system) at various angles of attack. There appears, however, to be some question as to the validity of this so-called local value technique for obtaining damping data and, at this writing, the question has not been satisfactorily resolved.

Redd et al.[43] have developed a method which relates the damping derivatives measured by the two methods so that derivatives can be expressed as a function of instantaneous angular displacement which is the form generally used in trajectory programs.

If the local damping coefficient $f(\theta)$ can be expressed

$$f(\theta) = A + A_2\theta^2 + A_4\theta^4 + A_6\theta^6 + A_8\theta^8 + \ldots$$

and the effective damping coefficient $f(\theta_0)$ can be expressed as

$$f(\theta_0) = C + C_2\theta_0^2 + C_4\theta_0^4 + C_6\theta_0^6 + C_8\theta_0^8 + \ldots ,$$

the coefficients are related by

$$C = A$$

$$C_2 = (1/4)A_2$$

$$C_4 = (1/8)A_4$$

$$C_6 = (5/64)A_6$$

$$C_8 = (7/128)A_8 .$$

From these equations, it can be shown that the effective damping-in-pitch coefficient over one full cycle of oscillation designated as $(C_{mq} + C_{m\dot{\alpha}})_E$ is related to the coefficient at an instantaneous angular displacement $(C_{mq} + C_{m\dot{\alpha}})_L$ by

$$(C_{mq} + C_{m\dot{\alpha}})_L = \frac{2V_\infty}{q_\infty Ad^2}\left(A + A_2\theta^2 + A_4\theta^4 + A_6\theta^6 + A_8\theta^8 + \ldots\right)$$

$$(C_{mq} + C_{m\dot{\alpha}})_E = \frac{2V_\infty}{q_\infty Ad^2}\left(A + \frac{A_2}{4}\theta_0^2 + \frac{A_4}{8}\theta_0^4 + \frac{5A_6}{64}\theta_0^6 + \frac{7A_8}{128}\theta_0^8 + \ldots\right) .$$

Therefore, if values of $(C_{mq} + C_{m\dot{\alpha}})_L$ have been determined in small amplitude forced-oscillation tests, the amplitude time history can be determined by using the logarithmic decrement relation

$$(\theta_0)_2 = (\theta_0)_1 e^{(C_{mq} + C_{m\dot{\alpha}})(q_\infty Ad^2/2V_\infty)(\Delta t/2I)} .$$

Additional details on the method and the derivation of the series coefficients are given in Reference 43.

3.2.1.6 Transfer Equations

Aerodynamic analysis frequently requires the transfer of derivatives measured at one axis location to another and may involve the transfer of derivatives along the Z as well as the X axis. Although equations for transferring results along the X axis are given in several texts and reports (Refs. 4, 10, 44 and 45), few references include equations for the case involving a transfer of results along the Z axis as well. For this reason, the derivation of the transfer equations are presented next to illustrate the procedure for the case of longitudinal stability derivatives.

The quantities referred to the initial axes location do not have subscripts, and the new axis location is designated by the subscript 1.

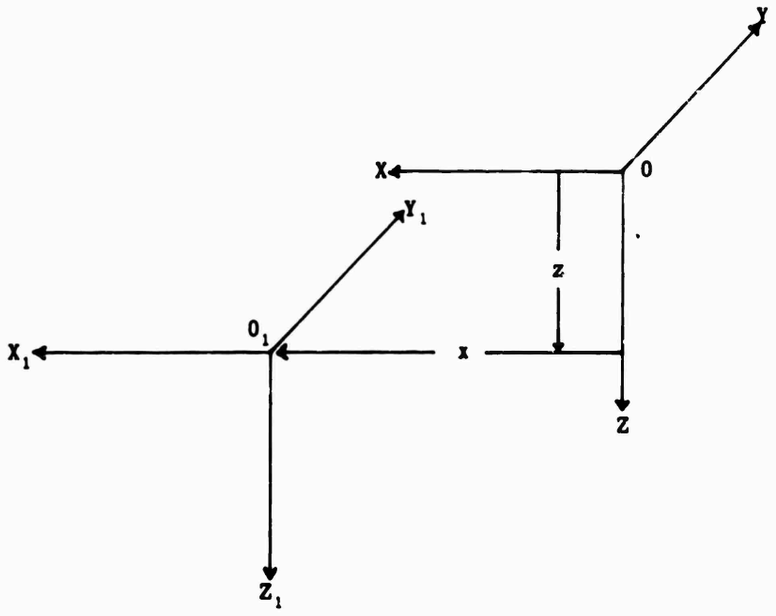

(a)

Sketch (a) shows the position of axes XYZ and $X_1Y_1Z_1$. The transfer distances x and z are positive in the senses shown in the sketch.

The equations for transferring forces and moments from axes XYZ will be derived by first writing the equations for the linear velocity components and the angular velocities. Considering the linear velocity components of 0_1, they become

$$\left.\begin{aligned} U_1 &= U + Qz \\ V_1 &= V - Pz + Rx \\ W_1 &= W - Qx \end{aligned}\right\} \qquad (75)$$

Since the axes the data are being transferred to are parallel to the initial axes, the angular velocities are

$$P_1 = P$$

$$Q_1 = Q$$

$$R_1 = R .$$

If we let the external forces and moments for the axes XYZ be designated as $(F_X F_Y F_Z)$ and $(M_X M_Y M_Z)$, respectively, the moments are given as

$$\left.\begin{aligned} M_{X1} &= M_X + F_Y z \\ M_{Y1} &= M_Y + F_Z x - F_X z \\ M_{Z1} &= M_Z - F_Y x \end{aligned}\right\} \tag{76}$$

The angular velocities and velocity components of O and O_1 parallel to the axes for disturbed motion are given by

$$\left.\begin{aligned} U &= U_0 + u, & P &= P_0 + p \\ V &= v, & Q &= Q_0 + q \\ W &= W_0 + w, & R &= R_0 + r \\ U_1 &= U_{01} + u_1, & P_1 &= P_{01} + p_1 \\ V_1 &= v_1, & Q_1 &= Q_{01} + q_1 \\ W_1 &= W_{01} + w_1, & R_1 &= R_{01} + r_1, \end{aligned}\right\} \tag{77}$$

where the subscript 0, as used for U_0, V_0, W_0, P_0, Q_0, and R_0, designates the velocity components of the center of gravity and the angular velocities in a reference steady-flight condition.

3.2.1.6.1 Stability Derivatives

The transformation equations are derived here by first expressing the force and moment component derivatives in a Taylor series expansion and employing the relationships derived for linear and angular velocities and forces and moments. It is convenient here to introduce the standard short form notation:

X,Y,Z,	Components of the external forces parallel to axes X, Y, Z.
L,M,N,	Moments about axes X, Y, Z.

3.2.1.6.2 Longitudinal Stability Derivatives

The general expansion of the aerodynamic force components along the body XZ axes and the pitching moment may be expressed as follows:

$$\left.\begin{aligned} X &= X_0 + X_u u + X_{\dot{u}}\dot{u} + X_q q + X_{\dot{q}}\dot{q} + X_w w + X_{\dot{w}}\dot{w} + \dots \\ Z &= Z_0 + Z_u u + Z_{\dot{u}}\dot{u} + Z_q q + Z_{\dot{q}}\dot{q} + Z_w w + Z_{\dot{w}}\dot{w} + \dots \\ M &= M_0 + M_u u + M_{\dot{u}}\dot{u} + M_q q + M_{\dot{q}}\dot{q} + M_w w + M_{\dot{w}}\dot{w} + \dots \end{aligned}\right\} \tag{78}$$

The terms X_0 , Z_0 , M_0 are the forces and moments for the reference steady-flight condition.

After neglecting all derivatives with respect to acceleration except $Z_{\dot{w}}$ and $M_{\dot{w}}$ and neglecting the derivative X_q , Equation (78) becomes

$$\left.\begin{aligned} X &= X_0 + X_u u + X_w w \\ Z &= Z_0 + Z_u u + Z_q q + Z_w w + Z_{\dot{w}}\dot{w} \\ M &= M_0 + M_u u + M_q q + M_w w + M_{\dot{w}}\dot{w} \end{aligned}\right\} \tag{79}$$

If we next consider the equation for the force along the body X axis, the derivatives with respect to velocities u and w for station 1 are

$$X_{u1} = \frac{\partial X_1}{\partial u_1} = \frac{\partial F_{X1}}{\partial u} = \frac{\partial X_1}{\partial u}\frac{\partial u}{\partial u_1} + \frac{\partial X_1}{\partial w}\frac{\partial w}{\partial u_1} .$$

Since $X_1 = X$,

$$X_{u1} = X_u \frac{\partial u}{\partial u_1} + X_w \frac{\partial w}{\partial u_1}$$

and, using Equations (75) and (77),

$$X_{u1} = X_u . \tag{80}$$

Similarly,

$$X_{w1} = \frac{\partial X_1}{\partial w_1} = \frac{\partial F_{X1}}{\partial w_1} = \frac{\partial X_1}{\partial u}\frac{\partial u}{\partial w_1} + \frac{\partial X_1}{\partial w}\frac{\partial w}{\partial w_1}$$

and

$$X_{w1} = X_u \frac{\partial u}{\partial w_1} + X_w \frac{\partial w}{\partial w_1}$$

and, using Equations (75) and (77),

$$X_{w1} = X_w . \tag{81}$$

By following the same procedure, it can be shown that, for the force derivatives,

$$\left.\begin{aligned} Z_{u1} &= Z_u \\ Z_{w1} &= Z_w \\ Z_{\dot{w}1} &= Z_{\dot{w}} \\ Z_{q1} &= Z_q + Z_w x - Z_u z . \end{aligned}\right\} \tag{82}$$

For the pitching-moment derivatives, neglecting $M_{\dot{w}}\dot{w}$,

$$M_{u1} = \frac{\partial M_1}{\partial u_1} = \frac{\partial M_{X1}}{\partial u_1} = \frac{\partial M_1}{\partial u}\frac{\partial u}{\partial u_1} + \frac{\partial M_1}{\partial w}\frac{\partial w}{\partial u_1} + \frac{\partial M_1}{\partial q}\frac{\partial q}{\partial u_1} .$$

Using Equations (50),

$$M_{u1} = \frac{\partial M}{\partial u}\frac{\partial u}{\partial u_1} + x\frac{\partial Z}{\partial u}\frac{\partial u}{\partial u_1} - z\frac{\partial X}{\partial u}\frac{\partial u}{\partial u_1} +$$

$$+\frac{\partial M}{\partial w}\frac{\partial w}{\partial u_1} + x\frac{\partial Z}{\partial w}\frac{\partial w}{\partial u_1} - z\frac{\partial X}{\partial w}\frac{\partial w}{\partial u_1} +$$

$$+\frac{\partial M}{\partial q}\frac{\partial q}{\partial u_1} + x\frac{\partial X}{\partial q}\frac{\partial q}{\partial u_1} .$$

After simplifying,

$$M_{u1} = M_u\frac{\partial u}{\partial u_1} + xZ_u\frac{\partial u}{\partial u_1} - zX_u\frac{\partial u}{\partial u_1} +$$

$$+ M_w\frac{\partial w}{\partial u_1} + xZ_w\frac{\partial w}{\partial u_1} - zX_w\frac{\partial w}{\partial u_1} +$$

$$+ M_q\frac{\partial q}{\partial u_1} + xZ_q\frac{\partial q}{\partial u_1} .$$

Using Equations (77),

$$M_{u1} = M_u + xZ_u - zX_u . \tag{83}$$

By following the same procedure, it can be shown that the other pitching-moment derivatives transfer equations are

$$\left.\begin{aligned} M_{w1} &= M_w + xZ_w - zX_w \\ M_{\dot{w}1} &= M_{\dot{w}} + xZ_{\dot{w}} - zX_{\dot{w}} \\ M_{q1} &= M_q + x(Z_q + M_w) - zM_u + x^2Z_w - xz(X_w + Z_u) + z^2X_u . \end{aligned}\right\} \tag{84}$$

The dimensional form of the derivatives in the transfer equations are

$$\left.\begin{aligned} X_u &= -C_A\rho_\infty VA \\ X_w &= -C_{A\alpha}\rho_\infty VA/2 \end{aligned}\right|$$

$$
\left.
\begin{aligned}
Z_u &= -C_N \rho_\infty VA \\
Z_w &= -C_{N\alpha} \rho_\infty VA/2 \\
Z_{\dot{w}} &= -C_{N\dot{\alpha}} \rho_\infty VA/4 \\
Z_q &= -C_{Nq} \rho_\infty VA/4 \\
M_u &= C_m \rho_\infty VAd \\
M_w &= C_{m\alpha} \rho_\infty VAd/2 \\
M_q &= C_{mq} \rho_\infty VAd^2/4 \\
M_{\dot{w}} &= C_{m\dot{\alpha}} \rho_\infty VAd^2/4 .
\end{aligned}
\right\} \qquad (85)
$$

After the equations are nondimensionalized, Equations (80) through (84) for transferring results at one station (XZ) to another station $(XZ)_1$ become

$$
\left.
\begin{aligned}
C_{A1} &= C_A \\
C_{A\alpha 1} &= C_{A\alpha} \\
C_{N1} &= C_N \\
C_{N\alpha 1} &= C_{N\alpha} \\
C_{N\dot{\alpha}1} &= C_{N\dot{\alpha}} \\
C_{Nq1} &= C_{Nq} + 2\frac{x}{d} C_{N\alpha} - 2\frac{z}{d} C_N \\
C_{m1} &= C_m - \frac{x}{d} C_N + \frac{z}{d} C_A \\
C_{m\alpha 1} &= C_{m\alpha} - \frac{x}{d} C_{N\alpha} + \frac{z}{d} C_{A\alpha} \\
C_{m\dot{\alpha}1} &= C_{m\dot{\alpha}} - \frac{x}{d} C_{N\dot{\alpha}} \\
C_{mq1} &= C_{mq} - \frac{x}{d} C_{Nq} + 2\frac{x}{d} C_{m\alpha} - 4\frac{z}{d} C_m - \\
&\quad - 2\left(\frac{x}{d}\right)^2 C_{N\alpha} + 2\frac{xz}{d^2} C_{A\alpha} + 4\frac{xz}{d^2} C_N - 4\left(\frac{z}{d}\right)^2 C_A .
\end{aligned}
\right\} \qquad (86)
$$

Following the same procedure, transfer equations for lateral stability derivatives may be derived.

It should be noted that the signs for the transfer distances from the initial axes location were selected as positive for transfer in the positive sense of the axes, i.e., transfer distances down and forward are positive. References are not consistent on this point, as may be seen in Reference 44 where transfer distances aft along the X axis are considered positive.

An alternative method of deriving the transfer equations for the case of transfer of the derivatives $(C_{mq} + C_{m\dot{\alpha}})$ along the X axis may be found in Reference 44. Meyer and Seredinsky[45] point out that the transfer equations normally found in the current literature are invalid at moderate to large angles of attack and where large transfer distances are involved. Transfer equations applicable to large-angle-of-attack data may be found in Reference 45. Wehrend[44] conducted an investigation at Mach 0.25 to 2.2 to test the method of computing damping-in-pitch derivatives at an arbitrary location from derivatives measured at two locations. A similar type of investigation was conducted by Nicolaides and Eikenberry[46]. These investigations showed that the transfer equations were satisfactory whether the configuration was stable or unstable.

In order to compute the damping-in-pitch derivatives at another body station from measurements at one station, the transfer equation shows that not only the damping derivatives at the initial station, but also the damping normal-force and static characteristics, must be known. Usually static stability data are known from static force tests; however, damping normal-force characteristics must be estimated. This uncertainty in the transferred data is eliminated by measuring damping-in-pitch derivatives at two body stations, which eliminates the damping normal force from the transfer equation. When this is done, the following equation is obtained using Equations (86) and letting z/d be zero:

$$C_{mq} + C_{m\dot{\alpha}} = \frac{\frac{x_1}{d}(C_{mq} + C_{m\dot{\alpha}})_2 - \frac{x_2}{d}(C_{mq} + C_{m\dot{\alpha}})_1}{\frac{x_1}{d} - \frac{x_2}{d}} - 2\frac{x_2}{d}\frac{x_1}{d}C_{N\alpha},$$

where

$$C_{N\alpha} = \frac{C_{m\alpha 1} - C_{m\alpha 2}}{\frac{x_1}{d} - \frac{x_2}{d}}.$$

The reference length l used in Reference 44 has been changed to d to be consistent with the nomenclature used throughout the report.

Damping normal-force derivatives may also be computed from damping-in-pitch measurements at two body stations from the equation

$$C_{Nq} + C_{N\dot{\alpha}} = \frac{(C_{mq} + C_{m\dot{\alpha}})_2 - (C_{mq} + C_{m\dot{\alpha}})_1 - 2\frac{x_1}{d}\frac{x_2}{d}C_{m\alpha}}{\frac{x_1}{d} - \frac{x_2}{d}} - \frac{2\left[\left(\frac{x_1}{d}\right)^2 - \left(\frac{x_2}{d}\right)^2\right]C_{N\alpha}}{\frac{x_1}{d} - \frac{x_2}{d}},$$

where

$$C_{m\alpha} = \frac{C_{m\alpha 1}\frac{d}{x_1} - C_{m\alpha 2}\frac{d}{x_1}}{\frac{d}{x_1} - \frac{d}{x_2}}.$$

The subscripts 2 and 1 on the damping derivatives refer to the station where the derivatives are measured, and the terms x_1 and x_2 refer to the distance between moment centers. The constant 2 on the static terms in the equations is valid only when the damping derivatives are based on $2V_c$.

3.2.2 Representative Systems for Tests of Complete Models

3.2.2.1 Free-Oscillation Technique

The free-oscillation testing technique, by virtue of its simplicity because complex control systems are not required, provides the experimenter with a wide latitude in the approach to balance system design.

Although the merits of the free-oscillation technique are simplicity in construction and use, which implies economy, it has some basic deficiencies. These consist of (i) the difficulty in obtaining data under conditions of dynamic instability, since the model will diverge and may damage the crossed flexures if they are amplitude limited without mechanical stops, (ii) a reduction in model angular displacement due to the static restoring moment in the pitch or yaw plane, and (iii) the inconvenience of reducing data influenced by nonlinear amplitude and frequency effects.

Different techniques have been used for displacing models mounted on a free-oscillation balance system. These generally consist of some form of (a) mechanical release from a displaced position, (b) application of a mechanical impulse, and (c) excitation at resonance and interruption of the forcing source. Methods (a) and (b) provide positive control over the initial amplitude but have the disadvantage of requiring large forces to obtain high initial amplitudes when the elastic stiffness of the flexure is large. Method (c) overcomes this difficulty but requires more complicated equipment to force the model to oscillate at resonance. Aside from using electrical excitation for resonance, excitation can be provided by using alternating air jets impinging on the inside of the model.

Many free-oscillation dynamic stability balance systems have evolved in the United States and in NATO countries to obtain information experimentally for support of vehicle development and theoretical studies. To show the basic features of most of the systems in current use, examples of some systems will be described which are designed with crossed-flexure pivots, and gas bearing pivots.

To perform dynamic stability tests at Mach numbers from 18 to 21 in the AEDC-VKF 100 in. diameter hypervelocity tunnel (Tunnel F), which has a useful run duration of about msec, a high frequency, free-oscillation balance system is used. To obtain up to about 15 cycles of data during a run, high model frequencies, minimum inertia models, and high crossed-flexure stiffness are required. A flexure system which provides a model frequency of 150 c/s at oscillation amplitudes up to ± 3 degrees is shown in Figure 43 (Ref. 47).

To displace the pivot to an initial amplitude a couple rather than a moment is used to minimize a beat oscillation that would be imposed on the oscillation envelope and reduce the total stress experienced by the pivot.

In operation, the model and pivot system is displaced to a desired amplitude by the pneumatic operation of two displacement arms which apply a couple about the pivot axis. Once the desired amplitude is reached, two cams operated by the releasing piston make contact with the displacement arms and instantaneously release the applied couple.

A low-frequency, free-oscillation, flexure pivot balance system also in use in the AEDC-VKF is shown in Figure 44 to illustrate the simplicity of the design and a method for displacing the model. Two jets located 180 deg apart are mounted to the sting just inside of the model base and are alternately supplied with high pressure air through an oscillating servo valve.

Forces generated by impingment of the jets on the inside of the model cause the model to oscillate. Amplitude is controlled by the jet pressure, and frequency is controlled by the servo valve. The model may be forced to oscillate at its natural frequency and when the required amplitude is achieved the air excitation is terminated and the model is free to oscillate.

A free-oscillation flexure pivot system developed by ONERA[45] is shown in Figure 45 to illustrate a mechanical system for displacing the model. For most flexure pivot balance systems, strain gages are bonded to the cross flexures to provide a signal output for recording the amplitude time history and model oscillation frequency.

Free-oscillation balance systems, having either ball bearings or gas bearings for the pivot, may not have mechanical stiffness to provide a restoring moment. For these systems the model is displaced by a mechanical system and released. If the tunnel has a model injection system, the model can be preset to the required amplitude, locked, and then released after injection into the airstream. An example of an AEDC-VKF free-oscillation balance system used in this mode is shown in Figure 46.

Most of the free-oscillation balance systems described thus far have been developed for use in relatively small wind tunnels. A free-oscillation balance developed by the AEDC-PWT (Ref. 49) for tests in the 16 ft transonic and supersonic tunnels is shown in Figure 49. The balance has a single vertical flexure in the center and two longitudinal flexures at the sides for a pivot. A hydraulic mechanism is provided for

initially displacing the flexure and model, and a hydraulic cylinder provides a means for locking the system. Strain gages on the flexures are used to obtain a measure of the amplitude decay history.

A free-oscillation dynamic balance system has been developed by the University of California Institute of Engineering Research to measure dynamic stability derivatives in a low density wind tunnel[50]. Figure 50 shows the components of the balance system. The model is mounted on a transverse rod supported in the vertical plane by bearings. The bearings have an electrically vibrated inner bearing race to minimize the friction and provide repeatable bearing tares. System restoring moment is provided by a quartz fiber attached to the tip of the transverse rod support. A cross shaft is mounted on the end of the transverse rod support to displace the model by the use of an electromagnet and also interrupt a beam to a photocell. One arm casts a shadow on a screen to provide direct oscillation angle measurements.

A small scale, free-oscillation, dynamic balance developed by the AEDC-VKF for tests in a small low density tunnel is shown in Figures 51 and 52. The commercial flexure pivot is 0.125 in. in diameter. The fixed portion of the pivot is supported by two supports, and the movable center portion of the flexure is clamped in the balance centerpiece. As the movable member is rotated, the air gap between it and the E-core changes to produce a change in signal level proportional to the angle.

Angular position histories for the gas bearing pivots are recorded with the E-core transducer described in Section 3.2.2.1. Aerodynamic damping from a free-oscillation system is obtained through an analysis of the record of motion recorded on magnetic tape, film, or oscillograph recordings to obtain the logarithmic decrement. Reduction of the data from a magnetic tape may be accomplished with a high speed computer to curve fit the motion data, read the peak amplitudes, and finally curve fit data in the form of log of the amplitude versus cycles of oscillation. If the data are recorded on film or an oscillograph, many manual operations are involved which are tedious and reduce the accuracy of the data reduction.

The ablation of a vehicle's thermal protection system can result in motions which have a significant effect on the vehicle performance. Study of these effects experimentally has been somewhat restricted because present capabilities of wind tunnel facilities do not provide a complete duplication of re-entry flow conditions. Ablation affects dynamic stability primarily by changes in body shape, mass distribution, and the mixing of gaseous products of ablation with the boundary layer. At the present time, study of the effects of ablation have proceeded along the lines of using low temperature ablators and porous model blowing techniques. This is desirable in a study of shape change and its effects on stability; however, the results have limited application for important parameters such as material properties and phase angle.

Mass addition, on the other hand, offers possibilities for simulating many of the important parameters and enables measurement and systematic variation of these parameters. Some of these parameters include mass injection rate, distribution, phase, wave form, gas properties, and frequency of oscillation.

LTV has pioneered the development of techniques and equipment to investigate the effects that mass addition, through porous models, has on dynamic stability. These investigations have been conducted in the LTV hypervelocity wind tunnel, which is a modified hotshot-type facility with relatively long run times (250 milliseconds at

Mach 17) at near constant flow conditions. Dynamic stability tests are conducted with a high-frequency flexure pivot balance to provide a sufficient number of cycles of oscillation for adequately determining the aerodynamic damping.

The porous model and balance developed in the investigation are shown in Figures 53 and 54. In addition to supporting and oscillating the model at the desired frequency, the flexure must provide a means of transferring injection gas from the fixed sting to the oscillating model. The flexure pivot designs shown in Figure 54 are well suited for these purposes since they provided a means for bringing gas to the model through passageways in the flexures without increasing the tare damping of the system. Relative to the rectangular flexure cross-section design, the cruciform design has greater stiffness in the axial and normal components; however, the rectangular design has the advantages of easier fabrication and longer supply passages for a given spring constant. The mass injection balance was fabricated from one piece of aluminum, and the flexures were designed to operate at very low stresses, thus ensuring low tare damping. Model motion histories are recorded with outputs from strain gages bonded to the balance flexures.

Details of the gas supply system, test procedures, and typical test results are presented in References 51 and 52.

Some of the devices that have been used in the acquisition and reduction of data to damping coefficient form are described next.

3.2.2.1.1 Dampometer

A commercial electronic apparatus which may be used to evaluate automatically the logarithmic decrement and frequency of decaying oscillations is the dampometer which was developed by Olsson and Orlik-Ruckemann[53] (Fig.55). The design of the instrument is based on the fact that a damped oscillation may be represented by a rotating vector on the screen on a cathode-ray tube; the length of the vector is proportional to the oscillation amplitude and is thus a measure of damping. The curve described by the motion of the end of the vector is a logarithmic spiral illustrated in Figure 56.

For a decaying harmonic oscillation, the input voltage to the dampometer may be written in the manner of Equation (22) as

$$E_i = E_0 e^{-(C/2I_Y)t} \cos \omega_d t$$

and the ordinate of the envelope of the harmonic oscillation is

$$E_i = E_0 e^{-(C/2I_Y)t} .$$

where voltage E_i is proportional to the length of the rotating radius vector on the cathode-ray screen.

The screen of the cathode-ray tube is covered by a circular disc, as shown in Figure 56, which has a series of radial slots equally spaced. As the spot representing the end of the vector moves in a spiral path around the screen, it passes slots in the

disc which allow light to pass to a photocell. The photocell triggers an electronic counter (damping counter) which gives the total number of slot passages, n, the vector passes in going from the outer radius r_1 to the inner radius r_2, which contains s number of radial slots.

Denoting the time at which the spot enters the slots t_1 and the time it leaves by t_2, the expression for the logarithmic decrement Δ can be derived:

$$r_1 = E_0 e^{-(C/2I_Y)t_1}$$

$$r_2 = E_0 e^{-(C/2I_Y)t_2}$$

and

$$\Delta = \pi C/I_Y\omega = s/n \log_e (r_1/r_2) .$$

The frequency of oscillation is measured with a second electronic counter by counting the number of cycles of a crystal oscillator during the period in which the damping counter is in operation from a preset number n_1 to another preset number n_2. If the frequency of the crystal oscillator is f_c and the reading of the counter n_c,

$$f = \frac{n_2 - n_1}{s} (f_c/n_c) .$$

Different discs having a range of radius ratios and number of slots are used to obtain good resolution for Δ and f. As noted in Reference 53, the dampometer can be used to obtain an accuracy of $< 2\%$ for logarithmic decrements smaller than 2; for higher values of the decrement, the accuracy decreases.

3.2.2.1.2 Travel Summation Method of Free-Oscillation Data Analysis

There may be instances when performing wind tunnel dynamic stability studies where very large amplitudes of oscillation will be of interest. In such cases, where it may be difficult to obtain an analog output of the displacement time history, a light source on the oscillating model may be used to indicate model position. Orlik-Ruckemann presents a data analysis technique[54] to obtain instantaneous reduction of free-oscillation data from this type of experimental arrangement.

In the simplest form, the experimental setup consists of an oscillating light source seen through a stationary window (Fig. 57) which is positioned such that the light source can be seen only during a portion of a cycle. The total visible travel of the light source in relation to the window is recorded by passing the light through a large number of transverse narrow slots to a photomultiplier tube to record the number of pulses.

With the travel summation method, the logarithmic decrement can be expressed as

$$\Delta = (2/s)(1 - b + b \log_e b)$$

where

$$s = 2/x_0 \sum_{n=0}^{m} (x_n - x_m) - (x_0 - x_m) \qquad (87)$$

and b is a constant with convenient values around 0.5, depending on the experimental arrangement. Equation (86) thus shows that the logarithmic decrement is simply obtained by dividing a constant by the dimensionless sum of the travel segments. By proper selection of b and a slotted window, the total error, including the approximations involved in retaining terms in the derivation of Equation (87), can be kept under 1% for most cases.

An alternative method for obtaining the logarithmic decay involves the summation of the time intervals for the consecutive cycles of oscillation during which time the light source is between x_0 and x_m. This method is less accurate than the travel summation method, because of approximations used in the derivation, but may be preferable since it permits simpler experimental apparatus. These data reduction methods are described in detail in Reference 54.

3.2.2.1.3 Logarithmic Circuit

A recording oscillograph is frequently used to record the decaying signal of model motion from a displacement pickup. These data which appear as a harmonic oscillation with damping must be replotted in terms of the logarithm of the amplitude versus a time function or cycles in order to extract the damping constant from the results. A method which effects a considerable saving in time in the analysis of the data traces consists of employing a logarithmic distorting circuit[6], which converts the exponential envelope of oscillation into a linear envelope which is proportional to the number of cycles of oscillation. The damping constant is then determined from the slope of the envelope.

3.2.2.1.4 Integration Method

Signals from displacement pickups recorded on magnetic tape may be analyzed quickly without the aid of a computer by making use of the integration method described in more detail in Reference 6. To employ the method, a series of complete cycles is selected from the magnetic tape recording and the signal is rectified and fed into an analog integrator which presents the integral as a reading R_1 on a d.c. voltmeter. The process is repeated for a second series of complete cycles to obtain the second integral represented by R_2 and, if n is the number of cycles between sample R_1 and R_2, the logarithmic decrement is given by

$$\Delta = \log_e \left(\frac{R_1}{R_2}\right) \Big/ 2n \ .$$

The integration method has the advantage of giving weight to every cycle of oscillation in the range covered, as opposed to measuring the number of cycles to damp to a given amplitude ratio. If noise exists on the displacement signal the integration method tends to reduce the effects it may have on the damping measurements.

3.2.2.1.5 Other Methods

A device called a damping trace reader has been developed by Leach[55] to measure the logarithmic decrement from oscillograph traces with about the same accuracy as for hand data reduction.

3.2.2.2 *Forced-Oscillation Technique*

Testing facilities have different requirements for dynamic stability balance systems. This naturally has resulted in the development of a variety of different systems now in use in the United States and in European countries. Space will not permit descriptions of all systems and therefore only a few representative ones will be discussed to show important features and techniques.

3.2.2.2.1 *AEDC-VKF*

Forced-oscillation dynamic stability balance systems have been developed at the AEDC-VKF for operation in three continuous flow tunnels, which cover the Mach number range from 1.5 to 12.

The dynamic balance system (Fig. 58) consists of a crossed-flexure pivot mounted on a sting and connected through a torque member and linkage to an electromagnetic shaker housed in the enlarged aft section of the sting. Details of the crossed flexures, input moment linkage, and model locking device are shown in Figure 59. The sting and shaker housing contain passages for water cooling which is necessary for tests at hypersonic speed. Cooling of the crossed flexures is accomplished through the use of cool air sprays which are turned off while data are being recorded. Water-cooled jackets which surround the crossed flexure are also used in some applications.

The VKF forced-oscillation balance is equipped with an amplitude control system which allows testing of both dynamically stable and unstable models. Testing is normally accomplished at the resonant frequency of the model balance system; however, the control system does provide a means of resolving the in-phase and out-of-phase (with model displacement) components of the forcing torque. Because of the low structural damping level of the balance and the aerodynamic damping levels present at supersonic and hypersonic speeds, the balance system is always operated at resonant or near-resonant conditions.

It was shown in Section 3.2.1.4 that when a model is oscillated at a constant amplitude and at the undamped natural resonant frequency of the system, the inertia moment exactly balances the restoring moment and the forcing moment is equal to the damping moment.

A block diagram of the control and data acquisition system utilized at the VKF system is given in Figure 60. The control system can be operated in either an open-look mode for testing dynamically stable configurations or in a closed-loop mode for testing either dynamically stable or unstable configurations. In either mode of operation the frequency of oscillation is controlled by the frequency of the reference oscillator.

Open-loop operation is obtained by using the amplified reference oscillator signal to drive the electromagnetic shaker motor. Resistance strain-gage bridges located on the input torque member and on a cross flexure (model displacement) provide analog signals of the forcing torque to the model and the model displacement. The electrical output of the bridges is amplified by a carrier amplifier to provide appropriate amplitudes of the torque and displacement signals necessary for the data acquisition system.

The closed-loop mode of operation operates on the amplified error principle. The reference signal and the displacement signal, which is phase-shifted approximately 90 degrees, are compared in a difference amplifier. This difference or error signal is amplified and used to drive the shaker motor. The error signal will remain in phase with the reference signal for all conditions requiring a positive application of torque. If the model is aerodynamically unstable, the error signal will be 180 degrees out of phase with the reference signal and a negative torque will be supplied to the model.

Due to high frequency vibration in the wind tunnels, signal conditioning is required to remove the noise from the torque and displacement signals before recording on the data acquisition system. Two bandpass filters tuned to the frequency of the reference oscillator are provided. The filters and other frequency-sensitive circuits track with the frequency selected by the reference oscillator. The output of the bandpass filters is amplified to provide the current necessary for the recording instruments.

The data acquisition system consists of an oscillograph, resolvers, on-line data system, analog magnetic tape system, and Beckman 210 analog-to-digital converter system. The torque and displacement signals are applied to the inputs of all the recording instruments and to an oscilloscope displaying a Lissajous pattern. The Lissajous pattern provides an indication of the 90 degree phase angle relationship between these two signals necessary to the condition of resonance of the model balance system.

Under certain tunnel conditions, and for certain model configurations, it is beneficial to operate at a frequency displaced from the resonant frequency. The resolver system is utilized to determine the in-phase and quadrature components of the forcing torque with respect to the model displacement.

The in-phase component is obtained by multiplying the torque and displacement signal with an analog multiplier. The quadrature component is obtained by phase-shifting the torque signal 90 degrees and then multiplying the phase-shifted signal with the displacement signal. The output signals of the multipliers contain a d.c. component and a double frequency component. By filtering out the double frequency component, a d.c. value is obtained which is proportional to the in-phase and quadrature torque components.

The in-phase torque component is zero at resonance, and the quadrature component is a maximum value. A d.c. voltmeter is utilized to monitor the in-phase component and serves as an indication of a resonance condition. Both torque components are recorded on analog magnetic tape, the Beckman 210 converter, and the on-line data system.

Data recording systems utilized for forced-oscillation testing are the oscillograph, analog magnetic tape, Beckman 210 converter, and on-line data system. The oscillograph and analog magnetic tape provide permanent recordings of the data as obtained in the wind tunnel. The Beckman 210 analog-to-digital converter provides digital conversion of the analog data and records the digital values on magnetic tape, which is then processed by a high speed computer to obtain final data.

Reduced data are desirable, and in some cases necessary, while the test is in progress. The on-line data handling system provides immediate examination of the damping derivatives Here the term on-line signifies that the test data are fed directly from test instruments into a computer. Therefore, the on-line data system includes obtaining analog representation of parameters to be measured, conversion of

these parameters to equivalent digital values, accumulation in a digital computer, computations of the data, and the presentation of the calculated data in derivative form in a data tabulation. A block diagram of the on-line data system is shown in Figure 61. A console containing all of the control systems, resolvers, and part of the on-line data system is shown in Figure 62.

Included in the console is an oscilloscope for monitoring the torque and displacement signals in either normal or Lissajous patterns to determine the resonant condition. An oscilloscope is also used to set up both the automatic control system and the resolver network, and to monitor the reference signal, error signal, or output voltage to the shaker motor. A root-mean-square and peak-reading voltmeter is used to monitor the output voltage and thus the amount of power or watts being delivered to the shaker motor. It can also be used to obtain either root-mean-square or peak voltage of the torque and displacement signals. The ratio of these signal peaks is used to determine the damping derivatives.

The complete resolver system mounted in the console includes all the amplifiers, filters, etc., required for resolving the in-phase and out-of-phase torque components. One centerscale d.c. voltmeter is used to read the in-phase component of the torque resolver network. Additional information on the system is given in Reference 56.

3.2.2.2.2 AEDC-PWT

The forced-oscillation balance system in use in the AEDC-PWT is shown in Figure 63. The balance has a bearing pivot with a hydraulic-controlled mechanism capable of producing a controlled pitching motion to the model. Angular displacement is sensed by strain gages on the flexure pivot, and the moment is measured between the pivot and the actuating mechanism.

The constant amplitude, sinusoidal oscillation is controlled by feedback systems in which the displacement signals are compared with a command signal, and frequency is controlled by the hydraulic pump motor speed. Figure 64 is a block diagram showing the control and readout instrumentation. Oscillation amplitude and frequency are selected by settings on a two-phase oscillator which is used as a phase reference for model motion and input moment. Deviations from a set amplitude generate an error signal which is amplified and results in a system drive signal.

In addition to in-phase signals, the two-phase oscillator also generates an out-of-phase signal which leads the in-phase signal by 90 degrees. The in-phase and out-of-phase oscillator signals provide readout gage excitations for the moment gage and position gage to form a sinusoidal oscillation of the four readout gage outputs about a d.c. level.

Each gage output wave form is integrated over a number of cycles, the a.c. component is averaged out, and the d.c. component remains as a signal datum. Model position and applied torque are proportional to the signal data and when used with a phase diagram provide relationships for determining the dynamic stability and static stability derivatives. The system readouts are fed to a computer for data reduction and display of the aerodynamic derivatives in tabular or graphical form while the test is in progress.

The basic theory, description of the physical components, theory of the control and readout system, and derivation of the associated stability parameters are presented in References 57 and 58.

3.2.2.2.3 NASA-LRC

The forced-oscillation balance system used by NASA-LRC is shown in a exploded and assembled view in Figure 65. Sketches of the balance system are presented in Figures 66 and 67. Sinusoidal, constant-amplitude motion about an oscillation axis is produced by a mechanical Scotch yoke and crank which is driven by a variable-frequency electric motor in the downstrean portion of the sting. The stiff strain-gaged beam located between the model attachment bulkhead and pivot axis is used to measure the forcing moment required to oscillate the model. Because of its location the signal output is not influenced by the friction or mechanical play in the system. Model displacement is measured with a strain-gaged cantilever beam mounted between the fixed sting and the oscillating model support. Springs of different stiffnesses are used to provide a range of resonant frequencies.

Outputs from the displacement and forcing-moment strain gages pass through coupled sine-cosine resolvers which are geared to the drive shaft and thus rotate at the fundamental drive frequency (Fig.66). Oscillation frequency is measured with a signal generator coupled to the drive shaft. In operation the resolvers transform the moment and amplitude functions into orthogonal components which are measured with d.c. microammeters. From these components the resultant applied moment, displacement, and phase angle are found and, with the oscillation frequency, the aerodynamic static and damping moments are computed. A block diagram of the electronic circuit used to measure the applied moment is shown in Figure 68 and a similar circuit is used to measure the angular displacement.

Use is made of automatic digital equipment to acquire data quickly and eliminate operator errors due to incorrect manual recording or reading. All of the system variables are automatically digitized, and a high speed computer is used to perform the data reduction and present results in coefficient form.

A complete description of the system electrical relations and methods involved in the operation and data reduction are found in References 59 and 60.

3.2.2.2.4 RAE-Bedford

The forced-oscillation testing technique has been employed by the RAE, Bedford, in the development of a system for measuring stability derivatives and damping derivatives due to angular velocity in roll and yaw on sting-mounted models[62]. Derivatives can be obtained for motion in vertical or horizontal translation (heave or sideslip); however, it is noted in Reference 62 that the apparatus was not designed for this purpose and the accuracy of the measurements is less than that required for most tests. Emphasis in the design has been toward a small size system that can be used for testing slender wings of fiber glass construction.

In some respects the balance system is similar to those described in Section 3.2.2.1 in that the model is mounted on a sting by means of a flexure pivot allowing one degree of freedom in rotation. Continuous excitation at or near the resonant frequency of the system is provided by a moving-coil permanent-magnet vibration generator mounted on the sting and coupled to a driving rod passing through the sting.

A schematic arrangement of various parts of the balance for yaw-sideslip oscillation is shown in Figure 69. The balance is mounted on the end of a sting by means of a

flexure pivot to allow rotation. A view of the flexure pivot and cylindrical section of the balance which mounts inside of the model is shown in Figure 69, and photographs are presented in Figure 70. Included in the flexure pivot assembly is the drive linkage to convert the longitudinal force in the driving rod into a couple acting between the end of the sting and the model.

The balance for measuring oscillation in roll is illustrated schematically in Figure 69. The unit is of one-piece construction and is instrumented with yaw and roll accelerometers. The system has one degree of freedom, and excitation in roll is provided by applying torque through the driving rod by means of linkage from the vibration generator.

Although the flexure pivot is located near the center of pressure of the wing models, in order to avoid large deflections under steady aerodynamic loads, the flexibility of the sting will allow some translation of the pivot axis which may be appreciable for some cases. To allow for displacement of the pivot axis, for example, when measuring pitching derivatives, heaving derivatives are measured by exciting a vertical oscillation (which will be accompanied by some angular movement) and measuring the changes in natural frequency, excitation force, and angular movement.

The motion of the model on the balance system consists of a pitching component, generated in part by the rotation of the model about the flexure pivot and in part by the bending of the end of the sting. These two components are present in different proportions in the two natural modes of the system. The pitching mode includes a certain amount of heave motion of the pivot axis, and the heave mode includes an appreciable amount of pitching motion and similarly for yaw and sideslip.

As was noted in Reference 62, it may not be obvious how an exciting couple acting between the model and the end of the sting can produce no deflection. The reason is that in the natural mode of oscillation in heave, for example, there is a certain amount of relative angular movement between the model and the end of the sting (even when there is no pitching component in the oscillation). It is thus possible for the excitation couple to feed energy into the system in this model.

The analysis of the system is simplified by treating the system as having two degrees of freedom with two natural modes of vibration - one predominantly pitching and the other predominantly heaving. The heaving derivatives appear as a by-product of the analysis to obtain the damping-in-pitch derivatives. Yawing derivatives are measured in the same manner, with sideslip derivatives appearing as a by-product.

The basic measurements made with the balance system include (i) the excitation frequency which is measured by an electronic counter, (ii) the excitation force which is measured in terms of the exciter current, and (iii) the balance displacements which could be obtained as measurements of strains or relative displacements; accelerometers were selected for the design since they are not affected by steady loads and are comparatively free from interactions.

The balance is designed (Fig. 70) with strain gages mounted on sections for measuring static forces and moments, except for rolling moment which is more conveniently measured with the flexure unit designed for roll oscillations.

The automatic measuring and recording equipment developed by the RAE for experiments concerned with oscillatory derivative is a digital amplitude and phase measuring system (DAPHNE). It was designed to use the wattmeter method[6] to resolve the input signals into in-phase and quadrature components, and accurate measurements of frequency are made with an electronic counter.

3.2.2.2.5 NASA-ARC

A method and a balance system is described in Reference 63 for measuring the lateral and dynamic stability derivatives. The features of the system include single-degree-of-freedom oscillations which are used to obtain components of pitch, yaw, and roll by varying the axis of oscillation. Amplitude control is achieved with a velocity feedback loop. The system is equipped with a system of strain gage data processing in which electronic analog computer elements are used in measuring the amplitude and phase position. Moment derivatives which arise from angular motions can be measured with the balance system. These include the rotary damping derivatives C_{np}, $C_{mq} + C_{m\dot{\alpha}}$, and $C_{nr} - C_{n\dot{\beta}}$; the cross derivatives C_{np} and $C_{lr} - C_{l\dot{\beta}}$; and the displacement derivatives $C_{m\alpha}$, $C_{m\beta}$ and $C_{l\beta}$.

The forced-oscillation system has two oscillation mechanisms - one for pure pitching or yawing motion in which the oscillation axis is perpendicular to the longitudinal axis of the sting, and one for combined rolling and pitching or rolling and yawing in which the axis of oscillation is inclined 45 degrees to the longitudinal axis of the sting. The electromagnetic shaker is housed in an enlarged section of the sting downstream of the model and connected to the flexure pivots by push rods. Strain gages were used to measure the oscillation amplitude and supply inputs to the analog computer.

The theory of the system operation, feedback control, analog computing system, and description of the apparatus is presented in Reference 63.

3.2.2.2.6 University of Michigan

Results obtained at hypersonic and hypervelocity speeds have shown the importance of the reduced frequency of oscillation. With the use of the free-oscillation testing technique, the frequency of oscillation can be varied only by changing either the moment of inertia or the flexure spring constant. Thus coverage of a wide range of frequencies requires several time-consuming changes in the test equipment.

The University of Michigan has developed an electromagnetic, forced-oscillation method which enables a range of oscillation frequencies to be investigated with ease[64]. The method utilizes the principle of the moving coil galvanometer. An alternating current, passing through a coil embedded within the test model, interacts with a static magnetic field imposed by a coil system mounted in one plane of the test section. This causes the model to oscillate in a sinusoidal manner following the existing torque but out of phase with it. From the phase lag of the motion relative to the existing moment and wind-on and wind-off results, it is possible to determine the aerodynamic damping.

A schematic view of the test setup showing the external coil is presented in Figure 71. A circular exciter coil was mounted coaxially within the Plexiglas model which was mounted on a cruciform flexure pivot shown in Figure 72.

The methods have been used for measuring the position of the model. One of the methods utilized the output of the strain gage bridge shown in Figure 72 and the other was based on the response of a second circular coil within the exciter coil located in the model. As the model oscillates in the magnetic field, an electromotive force is induced in the secondary coil and may be used for sensing the cone position. Although this technique has been successful, it has the drawback that the data reduction procedure is very lengthy, which may preclude on-line reduction. Use of strain gages to measure the model position eliminates the difficulties associated with the two-coil techniques.

The technique of electromagnetic excitation and using the phase angle to determine the damping has limitations which may prohibit its use for some configurations. Although the structural damping was small, the phase angle measurements at Mach number 2.5 on a 25 degree half-angle cone were less than one degree, which makes accurate measurements of aerodynamic damping at this and higher Mach numbers very difficult but not impossible. Improvements in the accuracy of the damping measurements will result if the model size is increased, the pivot axis is moved as far forward as possible, and a gas bearing is used to eliminate amplitude restrictions and structural damping due to the flexure. In addition the gas bearing would eliminate sting vibrations that influence damping measurements. Details on the instrumentation, data reduction procedures, and sample test results obtained with electromagnetic excitation are presented in Reference 64.

3.2.2.3 Magnetic Model Suspension System

Systems for captive model aerodynamic testing require support of the model by use of a sting into the model base region, a side-mounted strut, or even thin wires. Each of these techniques may introduce interference effects which can in some cases have a significant influence on the results. Support interference effects must be studied experimentally to gain some idea of the magnitude of the influence, since the problem has not been reduced to theoretical analysis.

Magnetic suspension of wind tunnel models provides one means for eliminating the influence of the support system. The first successful suspension of a wind tunnel model that enabled the measurement of interference-free drag was accomplished at ONERA, France, in 1957 (Ref. 65). Since that time, several laboratories in France, England, and the United States have been engaged in the development of magnetic suspension systems for different purposes. The potential for magnetic suspension is very great when it is considered that not only is it an interference-free support system, but it is a balance system for static forces and moments and dynamic measurements, since model motion can be controlled.

For example, control signals may be introduced into a feedback control circuit to produce model motion without alteration of the basic system. In principle, models can be subjected to rigidly forced motion either in sinusoidal or random modes or rotational motion with the translational degrees of freedom fixed. With the latter mode of operation, dynamic damping data in pitch or yaw are obtained by either the free- or forced-oscillation techniques. Roll damping measurements may be made on axisymmetric and finned bodies by using the spin decay technique.

The development of magnetic suspension systems has progressed very rapidly in the past several years; however, it has not reached the stage that the suspension systems compete favorably with the more conventional techniques for obtaining static and dynamic

stability data. Magnetic suspension systems are, however, used routinely for wake studies and some drag measurements. Although research to develop techniques for making dynamic stability measurements with a magnetic model suspension system is in the formative stages, the status of the work accomplished to date is briefly summarized to point out the major areas of development. Treatment of the equations of motion and data reduction have been omitted, since each depends more or less on the specific system; these topics are covered in the references.

The suspension system in use at the Gas Dynamics Laboratory at Princeton University[66] was developed to support models for experimental research on hypersonic wakes of axisymmetric bodies. Since the configurations of interest ranged from spheres to slender bodies, a three-degree-of-freedom system and a one-point suspension was used (Fig. 73). The system is mounted vertically to use the gravity force to oppose drag, to help the magnetic suspension. Models are made with ferrite spheres as the magnetic element to be acted on by the magnetic field. A conical model with a ferrite sphere embedded in the body is shown in Figure 74. When only spheres are tested, the ferrite is used without any other material. Although the Princeton system is not used for dynamic stability measurements, such data can be obtained with the system and model shown in Figure 74 by making use of the free-oscillation technique, provided position sensing is incorporated in the system for model motion histories. Completely free rotational model motion is also possible with the balance system developed by the University of Virginia[67], provided position sensing is incorporated.

The MIT magnetic model suspension system described in Reference 31 and shown in Figure 75 has been used to obtain dynamic stability data from wind tunnel measurements at supersonic speeds. The forced-oscillation technique was employed to measure damping-in-pitch derivatives on a model undergoing a forced motion by measuring the change in the phase of the motion. Use of this technique requires that the slope of the aerodynamic moment curve, M_θ, be known and sinusoidal motion imposed by the forcing function. Although no attempt was made[31] to measure damping due to plunging, a method is described in the reference whereby such measurements could be obtained.

The RAE magnetic model suspension system in use at Mach 9 is shown in schematic form in Figure 76, and a view of the system installed in the tunnel is shown in Figure 77. The system, now in the final stages of development, was designed to measure static forces and moments and dynamic stability. Additional details on the system may be found in References 68 and 69.

The magnetic suspension system at Southampton University[70, 71] makes use of three horseshoe-shaped electromagnets and one hollow solenoid-like coil for control of the model in six degrees of freedom; the model itself contains a permanent magnet. A schematic arrangement of these magnets is shown in Figure 78, and a model subjected to a forced oscillation in roll while suspended in the six-component balance is shown in Figure 79. The system has been designed for the measurement of aerodynamic derivatives, and emphasis has been placed on tests of winged models which requires proper control over the model roll attitude. Although there are several different methods that have been investigated for controlling model roll attitude, shaped cores within the model have been investigated most extensively. The usual practice in magnetic suspension systems is to have a magnetic core arranged to lie along the model axis. These cores are generally circular in cross section and thus do not impart any resistance to disturbances in roll. However, if the core is constructed with a noncircular cross section, the core will adopt one or more preferred attitudes when suspended in the field of the

model supporting magnet B shown in Figure 78. As pointed out in Reference 71, a model containing a shaped core can be induced to run as a synchronous motor by varying currents to the lateral magnets; however, the model would have to be spun up to the synchronous speed to allow lock on. Speeds greater than 1000 r.p.m. have been produced on a 0.75 in. diameter body of revolution at the University of Southampton. This technique could be used for measuring roll derivatives.

Reference should be made to Reference 29 for information on magnets, optics systems, control circuits, operating techniques, equations of motion, data reduction, and problem areas.

3.2.3 Representative Systems for Tests of Control and Lifting Surfaces

Methods for experimentally obtaining dynamic stability data on models of missiles and aircraft may also be applied to investigations of the aerodynamic characteristics of control surfaces, such as rudders, elevators, and ailerons. Although aerodynamic theory has been developed to analyze control surface behavior, recourse to experimental verification is necessary because of nonlinear effects which may be a function not only of amplitude and frequency but also of Reynolds number as associated with flow separation ahead of the control surface.

Experimental investigations to date have been designed primarily to measure the aerodynamic characteristics (hinge moment and damping) of control surfaces oscillating at transonic and low supersonic speeds where the theories show a strong influence of oscillation frequency and Mach number[72].

Since the specific details on the design of the model control surface and dynamic balance system will depend on the ingenuity of the designer, no attempt will be made to treat detailed problems peculiar to a particular system. Reference will, however, be made to typical systems to describe the general techniques that may be used to obtain control surface damping and hinge-moment data. Representative systems for obtaining damping data on lifting surfaces are also presented.

3.2.3.1 Free- and Forced-Oscillation Techniques

The methods employed and the data reduction, in general, are the same as those described in Section 3.2.1 for the free- and forced-oscillation techniques applied to control surfaces and half models. Applications of these techniques to a control surface mounted on the trailing edge of a triangular wing (Fig. 80) are presented in Reference 73. The control surface was attached to the wing by means of a flat spring running the full length of the control surface. Excitation was supplied with a torque motor mounted in the model, and control surface position was measured with strain gages mounted on cross flexures. These were used to increase the natural frequency of the system. To operate in the forced-oscillation mode, the control surface was driven at the resonant frequency of the system where the torque required to sustain a given amplitude of oscillation is directly proportional to the damping of the control surface. Thus the damping could be calculated from a measurement of the armature current of the torque motor.

For the free-oscillation tests, the system was driven at the resonant frequency of the system to a given amplitude. The armature circuit of the torque motor was then opened and the ensuing decay in amplitude was measured to obtain the damping from the log decrement.

Although oscillating at resonance to obtain the initial displacement has the advantage that the torque to deflect the control surface is small, it has the disadvantage of increasing the mass moment of inertia of the system. Initial amplitudes for free-oscillation motion may be obtained with a static or impulsive deflection of the surface to the desired amplitude, but this technique has the disadvantage that the localized loading may lead to some distortion of the control surface.

Forced-oscillation systems used for damping measurements, or as a means to achieve initial amplitudes, generally require considerably more space compared to the requirements for the free-oscillation system with a static displacement mechanism and therefore are restricted to large models. Orlik-Ruckemann[74] has applied the forced oscillation technique to obtain initial amplitudes for free-oscillation tests on small aerodynamic control surfaces by developing an experimental apparatus for use with half models. The apparatus for elevator oscillation tests on a half-airplane model is shown in Figures 81 and 82. In operation, the control surface is oscillated by a pair of driving coils to a desired amplitude and at the resonance frequency of the oscillating system and then the circuit is interrupted to allow a free oscillation. For this design, the control surface motion is measured by strain gages located on the control surface hinges which are, in this case, cantilever beams. The signal from the strain gages, which is proportional to the angular displacement of the control surface, was processed with a dampometer to obtain the characteristics of the oscillation, and thus the aerodynamic data.

Martz[75] has used the free-oscillation technique on rocket-powered free-flight models to obtain hinge-moment characteristics for a full-span, trailing-edge control surface on a delta wing. This same technique can also be used in wind tunnel tests. The control surface was mounted to the wing through a cantilever-type flexure hinge which was instrumented with strain gages to measure the control surface deflection. Initial displacement of the control surface was achieved by plucking periodically at the root chord by means of a motor-driven cam shown in Figure 83.

Orlik-Ruckemann and Laberge[25] have used electromagnetic excitation for free-oscillation dynamic tests on a series of delta wings. An example of the system is shown in Figure 84. This system[76] has been developed to the stage that its operation is completely automatic, that is, the output signal from the model suspension, which is a strain-gaged cruciform elastic member, and the input signal to the electromagnetic oscillator form a closed-loop circuit in which the frequency is automatically adjusted to the natural frequency of the system. After the circuit is interrupted, the model oscillates freely; data are recorded on the dampometer, and the cycle is again repeated. This automatic feature allows acquisition of a large amount of data within a short period of time and is particularly useful for blowdown tunnels which operate for very short time periods where manual adjustment of instrumentation is not possible without reducing the amount of data that may be acquired. A schematic block diagram of the system control and data acquisition in shown in Figure 85.

A half-model, fixed-amplitude, derivative measurement system used in the Aerodynamic Research Laboratory of Hawker Siddeley Dynamics Ltd. is shown in Figure 86. The system

is described in detail in Reference 23. The apparatus provides measurements of the wing and control surface derivatives due to models performing sinusoidal motion in pitch and vertical translation. A nonresonant method is used to reduce the electronic and mechanical system complexity.

The balance system is built on a nominally rigid platform which is connected to earth by three supports and force detecting transducers. Angular, simple harmonic motion is achieved with a variant of the well-known Scotch Yoke mechanism which converts constant angular motion into linear harmonic motion. This motion is then imparted through linkage to the model shaft. The model is driven by an electric motor through a variable speed gear box so that the frequency may be varied between 5 and 25 cycles per second at amplitudes of 2 degrees.

The oscillating system is inertia balanced so that the difference between the wind-on and wind-off transducer outputs in terms of amplitude and phase relationship with respect to model motion are measured for oscillations about two model axes. In-phase and quadrature components are resolved from these measurements to give the stiffness and damping derivatives due to pitch and plunge.

3.3 DYNAMIC ROLL DERIVATIVES

As a vehicle having aerodynamic lifting and control surfaces rolls about its longitudinal axis with an angular velocity P, points on the surfaces follow a helix path. Variations in spanwise local angle of attack of the vehicle aerodynamic surfaces alter the local normal and drag force loading distribution and inclination of the lift vector. In the case of a winged vehicle having tail surfaces, rolling at various rates produces a change in symmetry of the trailing vortex sheet, and thus influences the aerodynamic characteristics of the tail surface. These factors have an influence on derivatives due to rolling.

3.3.1 Theory

3.3.1.1 Free Rotation

The damping-in-roll derivative, C_{l_p}, can be measured using the free-rotation method where the model is free to rotate under the influence of an initial rolling velocity, and the subsequent decay in the roll rate is measured. Another version of the free rotation technique consists of forced continuous rotation by a known moment imparted by deflecting a model fin.

Although some of the equations describing free rotation are included in Section 3.2.1.3, the derivation is included here for completeness and in a different format. For a freely spinning axisymmetric body, the differential equation of the free-rolling motion may be derived by equating the rate of change of the angular momentum to the applied damping moment:

$$I_x \dot{P} = M_{x_p} P \,. \tag{88}$$

where the roll-damping moment, $M_{x_p} P$, consists of the contribution due to aerodynamic damping and the tare damping due to friction in the bearing system. It is assumed here that these moments are linear functions of angular velocity. The mechanical damping

is evaluated by a series of roll-decay tests in a vacuum and the results are subtracted from the wind-on data to obtain the aerodynamic roll damping. In applying this method, the tacit assumption is made that the decay mechanism during the vacuum tests is associated entirely with friction damping and is not dependent on aerodynamic loading and model dynamics. With tare damping included, Equation (88) becomes

$$I_X\dot{P} = [(M_{Xp})_a + (M_{Xp})_t]P \ . \tag{89}$$

This equation is a linear differential equation of the first order with the solution

$$P = Ae^{Ct} \ , \tag{90}$$

where A is a constant of integration and

$$C = \frac{(M_{Xp})_a + (M_{Xp})_t}{I_X} = \frac{M_{Xp}}{I_X} \ .$$

The roll-damping-moment parameter may be obtained by taking the logarithm of the ratio of the solution (90) at any two points, 1 and 2, of the P versus t history as follows:

$$M_{Xp} = \frac{I_X \log_e (P_2/P_1)}{(t_2 - t_1)} \ .$$

For an exponentially damped system of the type described in Equation (90), M_{Xp} may be determined using the above relation over any time interval $(t_2 - t_1)$ of the P versus t history. If the damping-moment parameter is not constant, as assumed in Equation (90), the P versus t curve deviates from being exactly exponentially damped. For cases where this deviation is not large, the above solution may be applied over portions of the P versus t history which are approximately exponentially damped.

The aerodynamic portion of the total damping-moment parameter is determined as follows:

$$(M_{Xp})_a = I_X \left\{ \left[\frac{\log_e (P_2/P_1)}{t_2 - t_1} \right]_w - \left[\frac{\log_e (P_2/P_1)}{t_2 - t_1} \right]_v \right.$$

In coefficient form, the roll-damping derivative may be written as

$$C_{lp} = \partial C_l / \partial (pd/2V) = (M_{Xp})_a (2V_\infty / q_\infty A d^2) \ .$$

The spin decay technique can be used to determine both the roll-damping moment and the aerodynamic rolling moment due to deflected model fins, grooves in the model surface, etc. For a finned model, the equation of motion is obtained by modifying Equation (89) as follows:

$$I_X\dot{P} = M_{Xp}P + M_{X\delta^*}\delta^* \ . \tag{91}$$

where $M_{X\delta^*}\delta^*$ is the rolling moment due to fin deflection δ^*.

For simplicity in the derivation, no distinction will be made here between aerodynamic damping moments and damping moments due to friction, since the wind-off corrections for tare damping may be introduced in the final equations. The solution for Equation (91), where P_i is the initial rolling velocity and t_i is the initial time is given as

$$M_{X_p}P + M_{X\delta^\star}\delta^\star = (M_{X_p}P_i + M_{X\delta^\star}\delta^\star)e^{(M_{X_p}/I_X)(t-t_0)} . \tag{92}$$

For the steady-state roll condition, $\dot{p} = 0$ and $P = P_s$, Equation (91) yields

$$P = -(M_{X\delta^\star}/M_{X_p})\delta^\star . \tag{93}$$

Using this, Equation (66) becomes

$$P - P_s = (P_i - P_s)e^{(M_{X_p}/I_X)(t-t_0)} .$$

Here again, taking the logarithm of the ratio of the above solution at any two points, 1 and 2, of the P versus t history yields

$$M_{X_p} = I_X \log_e [(P_2 - P_s)/(P_1 - P_s)]/(t_2 - t_1) . \tag{94}$$

If the roll-rate history deviates from being exponentially damped, the solution (94) may be applied over intervals near the steady-state condition (P_s) which are approximately exponentially damped.

The definitions of the roll-damping coefficient derivative, C_{l_p}, and the rolling-moment coefficient derivative due to fin deflection, $\delta^\star$, are respectively

$$C_{l_p} = \partial C_l / \partial(Pd/2V) = (M_{X_p})_a(2V_\infty/q_\infty Ad^2) \tag{95}$$

$$C_{l\delta^\star} = \partial C_l/\partial\delta^\star = M_{X\delta^\star}/q_\infty Ad . \tag{96}$$

Substituting Equation (93) into Equation (95),

$$C_{l_p} = [I_X/(t_2 - t_1)][2V_\infty/q_\infty Ad^2] \log_e [(P_2 - P_s)/(P_1 - P_s)]$$

and, from Equations (93) and (96),

$$C_{l\delta^\star} = -(P_s/\delta^\star)(d/2V_\infty)C_{l_p} .$$

The steady-state rolling velocity is the asymptotic value achieved over a period of time. Bearing friction is evaluated by obtaining air-off roll histories under vacuum conditions, and the value of M_{X_p} measured under these conditions is subtracted from the values obtained during tunnel air-on conditions.

3.3.1.2 Forced Rotation

Derivatives due to rolling, such as C_{l_p}, may be measured using the method of forced rotation which is similar to the forced-oscillation method. A steady rolling

motion is imparted to the model by means of a drive system, and the damping in roll can be measured between the drive system and model. Since $\dot{p} = 0$ for steady rolling motion, the roll-damping moment is given by

$$M_{Xp} = - M_X/P_s \ ,$$

where M_X is the input torque and P_s is the steady-state roll velocity. In coefficient form, the roll-damping derivative is given as

$$C_{lp} = - 2M_X V_\infty / P_s q_\infty A d^2 \ .$$

As was noted in Section 3.1.3, tare damping due to friction in the system is evaluated with air-off tests to obtain a correction for the air-on data.

Another version of the forced-rotation technique which is convenient for obtaining the derivatives C_{lp} and C_{np} is the method of forced oscillation in roll at constant amplitude with freedom to respond in yaw. The equations of motion for yaw and roll which describe the motion are derived in Reference 77. Because they are for a very specialized case, they are not presented here; however, the system will be described in Section 3.3.2.

3.3.2 Representative Systems

3.3.2.1 Free Rotation

A system used by NOL[78], which has a roll drive system external to the model, is shown in Figure 87. The motor drive consists of a sliding vane air motor which is coupled to the sting by a magnetic clutch. After the model is up to speed, the clutch is released and the decay history recorded by a transistor-type tachometer. Since the roll damping is influenced by the bearing system, special consideration is given to bearings design to minimize friction and thus improve the accuracy of the system. Gas bearings discussed in Section 3.1.1.4 are particularly well suited for this application because of the small friction in relation to ball bearings[79].

The external bearing and drive system (Fig. 88) has the advantage that it can be easily used on small models and models of various sizes and shapes. The disadvantage is that, because of its location, the gas bearing must be designed for moment as well as radial load.

The AEDC-VKF free-rotation, roll-damping system, which is located within the model, is shown in Figure 89. The model rotates on a gas bearing and is driven up to speed with an air turbine. After the model has been driven to the required spin rate, an air-activated clutch is released and the model is free to rotate. Rotational speed is measured with a magnetic pickup.

The magnetic model suspension systems described in Section 3.2.2.3 may be used to obtain damping-in-roll measurements not influenced by the presence of a support system. This is done by forcing the model to roll at a known rate, using an alternating current for generating the roll forcing function. Damping in roll is determined from the logarithmic decrement following termination of the roll forcing function. The wind-off data includes eddy current damping, which must be subtracted from the wind-on roll-damping measurements.

3.3.2.2 Forced Rotation

An example of a system[80] for forced, continuous-rotation, damping-in-roll tests is shown in Figure 90. The balance has an electric motor which drives the model through a planetary gear system. The stationary ring gear mounted in the gear system is restrained from rotation by an instrumented cantilever beam. Torque to overcome model aerodynamic damping and friction damping in the system is proportional to the restraint provided by the ring gear. Tests in a vacuum provide tare values for correcting the wind-on data.

A two-degree-of-freedom system, in which oscillations in roll are forced, has been used by NASA to obtain rolling derivatives and directional stability and damping-in-yaw data[77]. The system has been used for yaw amplitudes up to 2 degrees and forced at oscillation frequencies up to 20 c/s. A schematic and pictorial representation of the system is shown in Figures 91 and 92 to illustrate the modes of model motion. By use of flexures and ball bearings, the model is allowed two angular degrees of freedom - rolling and yawing - rolling being a forced oscillation and yawing being free. Harmonic, forced oscillation in roll is produced by means of rotary motion of an eccentric and oscillatory motion of the drive flexure indicated in Figure 91. Variations in the amplitude of the oscillatory rolling motion are provided by the amount of eccentricity in the drive system. It is transmitted to the torque tube, which is supported at the front end by roll flexures and the aft end by a ball bearing. Thus the only contact between the model and the support structure is through the roll flexure system. This was necessary because of the need to avoid the undesirable damping characteristics of ball bearings.

Strain gages in the system at locations shown in Figure 92 are used to measure angular roll and yaw positions of the model, and the roll input torque applied to the model to maintain forced oscillations in roll at a constant amplitude. The amplitudes and phase angles of the strain gage outputs are obtained by passing the signals through a sine-cosine resolver located at the drive motor and gear driven by the motor shaft. The resolver outputs are directly proportional to the in-phase and out-of-phase components of the strain gage signals. By vectorial summation of these quantities, oscillation amplitudes are obtained as well as the relationships necessary to determine the forcing torque and yaw position phase angles. An electronic counter operated by a portion of the oscillating, roll position, strain gage signal is used to measure oscillation frequency.

With the model rigidly restrained against motion in yaw, measurements of the roll position, torque required for constant amplitude roll oscillations and the roll-input-torque phase angle are made at various frequencies by means of the resolvers. These data, obtained for both wind-on and wind-off (near vacuum) conditions, provide $C_{l_p} + \alpha C_{l_{\dot{\beta}}}$ at zero angle of attack and C_{l_β} at angles of attack.

With the model unrestrained against yawing motion, the model is oscillated in roll at the yaw natural frequency to increase the yawing amplitude. When the desired amplitude is attained, the drive motor is stopped abruptly and the time history of the decaying yawing motion is recorded. Wind-on and wind-off data provide $C_{n_r} - C_{n_{\dot{\beta}}}$ and C_{n_β}.

Although the system can be operated in two degrees of freedom to obtain cross derivatives $C_{lr} - C_{l\dot{\beta}}$ and $C_{l\beta}$, the experience related in Reference 77 indicates that, where the system was used in this mode, the results were unreliable.

The detailed derivations and data reduction equations used with this system for measuring dynamic lateral stability derivatives are presented in Reference 77.

3.4 MAGNUS EFFECT

The "Magnus force and moment", "Magnus effect", and "Magnus characteristics" are synonymous terms which are given to the aerodynamic forces and moments that result in the plane perpendicular to the flow when a body is spinning in the cross flow produced at angles of attack. The name, Magnus, was given to the phenomenon in honor of the Berlin physicist, Professor G.Magnus, who around 1850 proved with a series of experiments the existence of a Magnus force[81]. Luchuk[82] gives a thorough historical account of the Magnus effect.

Magnus force data have become more important with the more general use of spin to produce stabilization and to overcome manufacturing asymmetries of finned projectiles. Dynamic instability may result on a spinning projectile if the Magnus moment becomes too large[83]. Also, the usual assumption that Magnus effects may be neglected because the spin rate is small is sometimes erroneous[84].

3.4.1 Types of Magnus Forces

There are several different types of Magnus forces and moments produced by various aerodynamic mechanisms. The different Magnus effects are usually classified as those caused by the body, by canted fins, by driven fins, by base pressure, and by vorticity from forward wing panels acting on the tail surfaces. These different types of Magnus effects will be discussed briefly and, where practical, illustrated sketches are given (Fig.93).

The body Magnus effect at low angles of attack is caused by the shifting of the thicker boundary layer on the leeward side in the direction of the spin[85] (Fig.93(a)). Thus the body shape is effectively altered and is asymmetric. At large angles of attack where the leeward side flow is separated, the spin shifts the separated portion to an asymmetric shape (Fig.93(b)). The body Magnus force both at small and large angles of attack is in the negative Y direction for positive (clockwise looking upstream) spin rates. Generally, the force acts on the rear part of the body.

On positive-spinning canted fins (Fig.93(c)) at an angle of attack, each fin, as it rotates through the leeward side, will lose part of its force because of the blanketing of the fin by the leeward wake[86]. At small angles of attack there will be a net negative side force which will tend back toward zero as the angle of attack is increased. Also on canted fins, there is a Magnus moment, which has been pointed out by Benton[87], caused by the axial component of fin normal force.

On driven fins at zero cant angle, each fin loses part of its lift distribution as it rotates through the leeward wake (Fig.93(d)). Thus there is a net side force in the positive Y direction[86].

A Magnus moment can be established on the fins, caused by unequal fin base pressures. This moment is small and can only exist if the boundary layer on the fins is laminar. Platou[84] gives a thorough explanation of this fin base pressure effect.

Benton[88] shows that wing-tail interference can cause large Magnus effects on a finned missile whose wings are deflected into an aileron setting. Basically, the side loads are caused by the vortices from the wind interacting with the tail surfaces.

3.4.2 Test Procedure

Determining the Magnus effects by wind tunnel tests necessitates the measurement of the loads on the model while it is spinning at an angle of attack. It is a well-known fact, as illustrated in Figure 94 (Ref.89), that the Magnus effects are dependent on the spin parameter (Pb/2V). Therefore, in addition to the usual parameters such as Mach number, Reynolds number, and model attitude, the spin parameter (Pb/2V) must also be monitored.

The spin parameter for the ground tests must be matched with the full-scale flight tests. For most wind tunnel facilities, and especially high Mach numbers, the model size is small, and the velocity is much lower than flight velocity because enthalpy is not simulated. Therefore much higher roll rates are required for the wind tunnel model than for the full-scale vehicle to properly simulate the flight spin parameter. These required high model roll rates, as will be noted later, often introduce special problems in the experimental work.

Tests by Platou[89] at Mach 2 at angles of attack up to 5 degrees showed that the Magnus force increased with grit size (Fig.95). Other investigations[84, 90] also have shown that the Magnus effects are dependent on the nature of the boundary layer, i.e. whether it is laminar, turbulent, or transitional. Therefore, since it is usually not possible to keep the Reynolds number of the ground tests the same as the full-scale flight test because of tunnel limitations, additional consideration of the influence of Reynolds number and boundary layer transition, to aid in the application of ground test results to flight data, is required.

The test method employed usually depends on the drive system of the test unit. The different test units will be discussed in a later section. For a motor drive system, the data can be recorded at the various angles of attack while holding the rotational speed constant, or the speed range can be covered for each angle of attack. With a turbine drive system, the data can be recorded continuously as the spin decays while holding other test conditions constant. In the blowdown tunnels, where the data recording time is limited, data have been recorded while increasing the rotational speed with the turbine[91]. When using the "power-up" technique, careful examination should be made to ensure that the data are not influenced by the air exhaust from the turbine.

Problems arise because of gyroscopic effects when data are taken continuously while varying the angle of attack with the model spinning. Although attempts have been made to eliminate the gyroscopic forces present by corrective data reduction[82], it is best to avoid this test technique if possible because of the uncertainty involved.

3.4.3 Representative Systems and Drive Units

Basically, the majority of the Magnus force test systems have the model mounting on ball bearings whose inner races are fixed to an inner shell which mounts directly

or indirectly to a four-component balance. A drive unit, either an electrical motor or an air turbine, is used to spin the model and normally is an integral part of the system enclosed by the model. Tachometer units, consisting of permanent magnets mounted on the rotating unit and a wire-wound pole mounted on the stationary portion of the assembly, are usually used to measure the model spin rates. As the model rotates, the combination provides a signal which is proportional to the spin rate. Typical systems for conducting Magnus force tests are shown in Figures 96 to 100.

Rotational speeds on the order of 100,000 r.p.m. are sometimes required to simulate the full-scale flight spin rate arameter ($Pb/2V_\infty$). Such speeds are very difficult, if not impossible, to achieve with a reasonable size electric motor. Motors which are available, consistent with model size and power requirements, are very expensive and require positive internal cooling. Cooling provides added complications to the system because of routing the coolant lines. If the motor is the connecting link between the balance and model, extreme care must be taken to ensure that the coolant and power lines are not stiff enough to take some load off the balance or to create small interference side loads that would influence the accuracy of the data. Also, with large motors some unbalance in the rotor may create vibration problems. However, for large models with fins which have high damping characteristics, the variable frequency motors are often the best system and frequently simplify the design.

A typical Magnus force test installation[92], using an electric drive motor, is shown in Figure 96. The electric motor and gear box is an integral part of the model and is the connecting link between the stationary balance and the rotating model through a flexible coupling at the upstream end. The inner shell mounted to the balance supports the two ball bearings on which the model rotates.

High model spin rates, not generally available with electric drive motors, have been obtained by NOL, BRL, and WADD through the use of an air turbine housed within the model. The air turbines can be made smaller than commercially available electric motors, and weights are a fraction of those for equivalent electric motors, thus eliminating low resonant frequencies which can interfere with strain gage measurements. Also, they are more versatile for designing in that there is no direct linkage required as with an electric motor where there must be a direct drive between model and motor. Procedures for design of small air turbines for Magnus force balances are given in Reference 93.

Magnus force test systems utilizing air turbine drive units are shown in Figures 97 to 100. For the systems shown in Figures 97 to 99, the model is mounted on ball bearings which transmit loading to a strain gage balance, whereas in the system shown in Figure 100 a gas bearing is used for model support. All of these have the air turbine near the base of the model, with the air exhausting out of the model base into the wake region. Some designs have been developed where the turbine is forward of the balance and a return loop is used for the air exhaust. The return loop system has the advantage that tests can be made while increasing speed with the turbine without fear of an effect of the air exhaust on the Magnus measurements. However, the turbine, when enclosed for the return loop, is out of necessity smaller for a given size model, and therefore will produce less torque. In addition, problems may arise when air is passed through the center of the balance because of the changing balance temperature, thus reducing the accuracy of the data.

The system shown in Figure 98 is a design used by WADD and is similar to one developed by BRL. Rotational speeds up to 90,000 r.p.m. have been obtained with this unit. The rotating assembly, consisting of the model shell, turbine assembly, and tachometer permanent magnets, mounts on two ball bearings which support the model on a strain gage balance. More detailed information on this system may be found in Reference 94.

The system shown in Figure 99 is used in the AEDC-VKF supersonic and hypersonic tunnels. The model mounts on ball bearings on an inner shell which fits over the balance. The turbine is at the rear of the balance and, after it has powered the model to the required spin rate, it can be disconnected from the model by a sliding clutch. The balance is a four-component moment type incorporated in the system as a separate unit. Thus, different capacity balances can easily be used without changing the other parts of the system.

An air bearing has been used by NOL in the system shown in Figure 100 to provide either a Magnus force or roll-damping test capability with the same balance equipment without modifications. The model is spun up with an air turbine drive, and when the required spin rate has been achieved, the turbine drive is disconnected from the model by an air-operated clutch. Magnus measurements are made with a four-component balance which is interchangeable to provide different load capabilities. This balance is more complex than one normally used with a ball bearing support, since supply air for the gas bearing and balance coolant must be routed through the balance.

3.4.3.1 Bearings

A critical factor in the rotating model Magnus force measuring system is the bearings, since they must in some cases be capable of withstanding rotational speeds of 100,000 r.p.m. or more. It is a general practice to mount the bearings so that they are subjected to a thrust load at all times. This preload confines the ball rotation to one axis and prevents brinelling of the races that could occur from dynamic axial movement. Temperature rises in bearings result from operation at high speeds and these should be monitored to given an indication of the bearing performances.

Bearings used in the WADD Magnus force balance system are run at 10,000 and 20,000 r.p.m. and temperatures are continuously monitored until the temperature levels off. A plateau in temperature at the forward end of the support strut is an indication that the bearings are in good condition and that the balls have worn a track cycle.

Temperatures are continually monitored during tests, and excessive rises above about 150°F indicate that the bearings should be disassembled, rinsed in solvent, and regreased. Experience indicates that bearing temperatures much above 150°F signal the onset of freezing of the bearing assembly.

As noted earlier, the Magnus force system shown in Figure 98 was designed by WADD using much of the experience from BRL. A series of tests was made by WADD to extend the use of the BRL developed bearings to rotational speeds considerably above the 40,000 to 50,000 r.p.m. specified by the manufacturer as the upper limit.

Bearing failures were generally found to occur when the inner race temperatures reached 200 to 250°F. Because of the heat generated, carbon particles from the lubricant and phenolic retainer were produced, and under some conditions the carbon particles

scored the races, produced additional heat, and ultimately caused failure. This problem was overcome by a conditioning procedure devised by WADD (Ref.94) which consisted of bearing run in to seat the balls and also form a glazed surface on the phenolic retainer at critical contact points.

Lubrication of bearings is dependent for the most part on the type of operation they will be subjected to. For intermittent service, where the bearings are allowed to cool, lubrication consists of light applications of Aircraft and Instrument Grease, MIL-G-25760 and a few drops of Instrument Lubricating Oil, MIL-L-6085A. No grease seals are used, since a portion of the grease remains on the bearings for intermittent operations. Conditioning of the bearing in this manner has resulted in a life span of 10 to 50 runs with cleaning between every 10 to 20 spinups.

Continuous operation at high rotational speeds of 70,000 to 90,000 r.p.m. requires continuous bearing cooling to prevent excessive heating and bearing freeze up. The WADD system shown in Figure 98 was designed with a bleed line from the main air supply to provide cooling air to the bearings. Reduction of the front bearing temperature was effectively achieved; however, cooling of the rear bearing was ineffective. The bearing temperatures are shown in Figure 101 for various throttle value settings on the air cooling air supply. Although this method of cooling is effective, it reduced the number of runs between lubrications because the lubricant was carried away with the cooling air. A final development in the system included mist lubrication by an alemite system to maintain lubrication while cooling the bearings. Details of the lubrication system are shown in Figure 102.

Bearings with phenolic retainers were used exclusively in the WADD Magnus force system[98], since these were found to possess the best properties for rapid accelerations and high speeds. Radial-type ball bearings provided the best combination with the inner race spring-loaded. A precision bearing with controlled minimum play was used for the front bearing and a class 3 bearing for the rear bearing. Stainless steel bearings were used at the rear station because the rear bearing operated at higher temperatures and greater dissipation of heat was achieved with stainless steel bearings.

3.4.3.2 Model Construction

Dynamic conditions can exist at high rotational speeds which render Magnus force data unreliable, increase bearing wear, cause fouling in the air turbine drive system, and also reduce turbine performance. These adverse conditions may be eliminated or minimized by dynamic balancing of the model. The balancing should be done carefully and to a high degree of accuracy, since only a very small unbalance can significantly influence the accuracy of the data.

The ideal model is one with low weight and high strength and designed to maintain good fits regardless of temperature gradients, normal loading, and spin rates. A material combination used frequently is 75ST aluminum and heat-treated stainless steel. This combination has low weight and high strength, and good fits may be maintained. It is particularly important that a minimum of parts be used and that all mating parts be made to close tolerances, so that dynamic balancing will not be required after each assembly.

3.4.3.3 Strain Gage Balance

Four-component strain gage balances are required to record forces and moments generated in the pitch and yaw planes by model spin. Since Magnus forces are at the maximum 1/10 to 1/20 of the normal force and can be much smaller, the Magnus balance must be stiff enough to withstand large normal-force loads while at the same time maintain the sensitivity required to accurately measure the small side loads. NOL developed a balance with eccentric side beams so that when the balance is subject to yaw loads a secondary bending moment is induced in the eccentric column which acts as a mechanical amplifier[79]. An AEDC-VKF balance of this type is shown in Figure 103(b). The AEDC-VKF balance has a normal force to side force capacity ratio of 10. Balances have also been developed which have extremely small outrigger side beams that act as pure tension members. Normal force to side force capacities up to 25 have been obtained with this design (Fig. 103(a)).

Satisfactory results can be obtained with the forementioned methods utilizing conventional wire strain gages. However, an attractive method for improvement of Magnus force measurements is to use semiconductor strain gages as substitutes for wire-wound gages. Wire gages have a gage factor of 2, whereas semiconductor gage factors are on the order of 60 to 200. Utilization of semiconductor strain gages would produce voltage outputs 30 to 100 times greater than the conventional wire gages, since the voltage output for a given stress is directly proportional to the gage factor.

The feasibility of using semiconductor strain gages for Magnus force measurements has been investigated by Platou of BRL[96]. Results from these investigations show that the semiconductor strain gage is very sensitive to temperature. These adverse effects can be diminished by temperature compensation provided factory matched gages are used in each bridge. In addition, the usual precautions in mounting, bonding, and soldering connections should be strictly adhered to for good performance. An example of the increased sensitivity obtained using semiconductor strain gages is shown in Figure 104.

3 5 PRESSURE MEASUREMENTS

Most of the interest in the last 20 years or more has been in the development of instrumentation for measuring total forces and moments on a model rather than local values. However, some efforts have been directed toward measuring forces and moments on segmented wings at supersonic speeds[97,98] to obtain section static aerodynamic characteristics. Distributions of forces and moments, as well as the total loading, are of considerable value, especially to validate theories. Detailed study of aerodynamic damping may be enhanced by knowledge of local loading especially for the cases of models having flow separations, boundary layer transition which varies with angle of attack, and models constructed with low temperature ablation simulators releasing gas to the boundary layer.

Measurements of detailed pressure distributions on an oscillating model and integration of the distributions provide a means to obtain local loading relative to the motion of the model and in-phase and quadrature lift and moment.

With the exception of some unreported tests at AEDC-VKF on an 8-degree cone at Mach 4 and measurements of pressure distributions on an oscillating wedge at Mach 1.4 and 1.8 (Ref. 99), most of the experimental work[100-102] has been conducted at low subsonic

and transonic speeds. The authors reporting on these tests have described the transducer installations, test techniques, and data reduction in detail, and therefore their work has been used liberally in preparing the following sections.

3.5.1 Transducer Installation

The most important considerations in developing a system for measuring pressures on an oscillating model are the transducer characteristics and installation.

Some of the desirable characteristics for a transducer to measure time-varying pressures on oscillating models, in addition to resolving power are[103, 104]:

(a) Transducer outputs should be insensitive to the inertia loads imposed under oscillatory conditions.

(b) Transducer outputs should be linear with applied pressure.

(c) The transducer should be small to allow installation of several units spaced for adequate coverage and installation close to the measuring point to avoid a lag in response.

(d) The resonant frequencies of the transducer components should be well above the frequency range for pressure measurements.

(e) The diameter of the pressure receiver should be smaller than the half wave length of the pressure wave.

(f) The transducer should be insensitive to environmental temperature change.

In practice, there may not be one transducer with characteristics which embody all of these requirements for a particular application, and therefore a practical design must be developed with the sacrifice of some of the desirable features. In all cases, however, the transducer should be selected giving major weight to both high resolving power and high frequency response.

The next important consideration following selection of a transducer using these guidelines is the installation. The method of installation is governed to a large extent by the size and geometry of the model and the transducer response characteristics. The transducer should be located near enough to the surface to accurately measure rapidly varying pressures. Ideally, it is most desirable to have the transducer diaphragm right at the measuring point to have zero tube length and transducer volume. This, however, is not very feasible for most installations, and, therefore, the transducer must be connected to the pressure orifice by a connecting tube. Transducers used are usually the differential-pressure type which require a reference pressure system on one side of the transducer diaphragm.

Connecting tubing between the orifice and transducer must be selected with proper regard to the important variables - namely frequency response and phase shift.

3.5.2 Pressure System Response

In the range of typical tubing lengths ranging from 0.1 to 6 in., tubing diameters ranging from 0.015 to 0.125 in. and transducer volumes from 0.01 to 0.1 cubic in., Davis[104] notes that the viscous and thermal effects predominate, with a dependency on

the frequency of oscillation. An example of the magnitude pressure response and phase angle variation with frequency from Reference 104 is presented in Figure 105 to illustrate these effects.

A method is presented by Davis[104] for calculating the dynamic response of a system and phase angle for a sinusoidal pressure input. The assumptions used in the formulation, based on the work of References 105, 106 and 107, include

(a) constant pressure over the tube cross section,

(b) constant pressure over the gage volume,

(c) laminar flow throughout the system,

(d) small pressure perturbations.

The expression for the pressure at the transducer or gage is given by

$$\frac{p_m}{p_i} \simeq \frac{1}{1 - \frac{V_g}{V_t}\frac{l^2\omega^2}{c^2} + i\omega\frac{V_g}{V_t}\frac{8\mu l^2}{\bar{p}r^2}} .$$

This equation should only be used as a rough guide, since the pressure system has been represented by a differential equation with frequency-dependent coefficients. Exact characteristics of a pressure system should be determined by calibration.

3.5.3 Calibration Technique

Calibration of a transducer tubing system which is to be used for unsteady pressure measurements is necessary because of the numerous uncertainties which exist in the analytical treatment.

The dynamic response calibration of a pressure transducer and tubing system is characterized by frequency response curves such as those in Figure 105 showing magnitude and phase angle. Specialized calibration equipment is necessary for calibrations which must be made over a wide range of frequencies. Techniques for calibrating microphones are directly applicable to calibration of pressure transducers and are used here to outline general specifications for pressure transducer calibration equipment[104, 108].

(i) The pressure oscillation amplitude should be constant over long periods and at different frequencies and easily variable over the range of interest.

(ii) The frequency of oscillation should be continuously variable over the frequency range of interest.

(iii) Local conditions such as mean pressure and temperature should be variable over the range of interest and known.

(iv) The wave form of the pressure oscillation should be relatively free of harmonics.

(v) The calibration equipment should have a standard pickup near the point of measurement.

For dynamic calibrations at frequencies of 25 c/s and lower, a system of the type shown in Figure 106 will provide a sinusoidal, oscillating pressure. Oscillation of the pump plunger by motion of the motor drive cam pressurizes the diaphragm and produces an oscillating pressure input to the transducer. The phase lag between the pressure application and transducer response is determined from components of the transducer output in phase and in quadrature with the motion of the plunger. The mean pressure in the calibration may be adjusted for the pressure range of interest.

For frequencies between 10 and 100 c/s, a piston-type calibrator may be used; however, at higher frequencies up to 5000, Davis[104] recommends a cam-type pulsator of the type shown in Figure 107. The pulsator chamber is supplied with high pressure air which exits through an opening controlled by the rotating cam. The space between the cam and the exit is adjusted until the wave form is sinusoidal. Reference pressure gages and the transducer and tube system to be calibrated are mounted to sense the pressure within the chamber of the pulsator.

REFERENCES

1. Lanchester, F.W. — *Aerodonetics*. Constable, London, 1908.

2. Bryan, G.H. — *Stability in Aviation*. MacMillan, 1911.

3. Durand, W.F. (Editor) — *Aerodynamic Theory*. Vol.V., Div.N, Springer, Berlin, 1934-1936.

4. Valensi, J. — *A Review of the Techniques of Measuring Oscillatory Aerodynamic Forces and Moments on Models Oscillating in Wind Tunnels in Use on the Continent*. AG 15/P6, Papers presented at the Fifth Meeting of the AGARD Wind Tunnel and Model Testing Panel, Scheveningen, Netherlands, May 3-7, 1954.

5. Arnold, Lee — *Dynamic Measurements in Wind Tunnels*. AGARDograph 11, August 1955.

6. Bratt, J.B. — *Wind-Tunnel Techniques for the Measurement of Oscillatory Derivatives*. ARC R&M 3319, ARC 22 146, August 1960.

7. Dayman, B., Jr — *Free-Flight Testing in High-Speed Wind Tunnels*. AGARDograph 113, March 1966.

8. Ames Research Center Staff — *Ballistic-Range Technology*. AGARDograph in preparation.

9. Orlik-Ruckemann, K. — *Methods of Measurement of Aircraft Dynamic Stability Derivatives.* Nationa' Research Council, Canada, LR-254, July 1959.

10. Perkins, C.D. Hage, R.F. — *Airplane Performance, Stability and Control.* John Wiley, New York, 1949.

11. Etkin, B. — *Dynamics of Flight.* John Wiley, New York, 1959.

12. Babister, A.W. — *Aircraft Stability and Control.* Pergamon Press, 1961.

13. Eastman, F.S. — *Flexure Pivots to Replace Knife Edges and Ball Bearings.* University of Washington Experimental Station Bulletin No.86, November 1935.

14. Eastman, F.S. — *The Design of Flexure Pivots.* Journal of the Aeronautical Sciences, Vol.5, No.1, November 1937, pp.16-21.

15. Young, W.E. — *Investigation of the Cross-Spring Pivot.* Journal of Applied Mechanics, Vol.XI, No.2, June 1944, pp.A113-A120.

16. Wittrick, W.H. — *The Theory of Symmetrical Crossed Flexure Pivots.* Council for Scientific and Industrial Research, Division of Aeronautics Report SM 108, January 1948, ATI 37 720.

17. O'Neill, E.B. Phillips, K.A. — *A Comparison of Damping-in-Pitch Derivatives Obtained through Different Experimental Techniques.* David Taylor Model Basin, May 1966, Private Communication.

18 Hodapp, A.E. — *Evaluation of a Gas Bearing Pivot for a High Amplitude Dynamic Stability Balance.* AEDC-TDR-62-221, December 1962, AD 290 948.

19. Regan, F.J. Horanoff, E. — *Wind Tunnel Model Support Using a Gas Bearing.* NOL TR-65-14.

20. Richardson, H.H. — *Static and Dynamic Characteristics of Compensated Gas Bearings.* ASME Transactions, Vol.80, October 1958, pp.1503-1509.

21. Welsh, C.J. et al. — *Dynamic Stability Tests in Hypersonic Tunnels and at Large Model Amplitudes.* AEDC-TR-59-24, December 1959, AD 229516.

22 Mechanical Technology, Inc., (Edited by N.F.Rieger) — *Design of Gas Bearings.* Vols. I and II, 1966.

23 Hall, G.Q., Osborne, L.A. — *Description of the HSD Cov. Half-Model Oscillating Derivative Measurement Rig.* Hawker Siddeley Dynamics, Coventry, ARL Report 64/10.

24. van der Bliek, J.A. — *Notes on Half-Model Testing in Wind Tunnels.* AGARD Report 298, 1959.

25. Orlik-Ruckemann, K.J. Laberge, J.G. — *Static and Dynamic Longitudinal Stability Characteristics of a Series of Delta and Sweptback Wings at Supersonic Speeds.* National Research Council, Canada, LR-396, January 1966.

26. Ormerod, A.O. — *An Investigation of the Disturbances Caused by a Reflection Plate in the Working-Section of a Supersonic Wind Tunnel.* ARC R&M 2799, RAE Report Aero 2084, November 1950.

27. Whitfield, J.D. — *Critical Discussion of Experiments on Support Interference at Supersonic Speeds.* AEDC-TN-58-30, August 1958, AD 201108.

28. Uselton, B.L. — *Investigation of Sting Support Interference Effects on the Dynamic and Static Stability Characteristics of a 10-deg Cone at Mach Numbers 2.5, 3.0 and 4.0.* AEDC-TDR-64-226, November 1964, AD 450 660.

29. Daum, F.L. — *Summary of ARL Symposium on Magnetic Wind Tunnel Model Suspension and Balance Systems.* ARL 66-0135, July 1966.

30. Crain, C.D. et al. — *Design and Initial Calibration of a Magnetic Suspension System for Wind Tunnel Models.* AEDC-TR-65-187, September 1965, AD 470 147.

31. Chrisinger, J.E. et al. — *Magnetic Suspension and Balance System for Wind Tunnel Application.* Journal of the Royal Aeronautical Society, Vol.67, November 1963, pp.717-724.

32. Lamb, Sir Horace — *Hydrodynamics.* Sixth Edition, Dover Publications, New York, 1945.

33. Stokes, G.G. — *On the Effect of Internal Friction of Fluids on the Motion of Pendulums.* Transactions, Cambridge Philosophical Society, Vol.IX, Pt.II, 1951, pp.8-106.

34. Stephens, D.G. Scavullo, M.A. — *Investigation of Air Damping of Circular and Rectangular Plates, a Cylinder, and a Sphere.* NASA TN D-1865, April 1965.

35. Smith, T.L. — *Dynamic Stability Measurements.* Memorandum Report 1352, June 1961.

36. Welsh, C.J. Ward, L.K. — *Structural Damping in Dynamic Stability Testing.* AEDC-TR-59-5, February 1959, AD 208 776.

37. Demer, L.J. — *Bibliography of the Material Damping Field.* WADC Technical Report 56-180, June 1956.

38. Nicolaides, J.D. — *Missile Flight and Astrodynamics.* US Bureau of Weapons, Department of the Navy, TN-100A, 1959-61.

39. Cunningham, W.J. — *Introduction to Nonlinear Analysis.* McGraw-Hill, New York, 1958.

40. Winter, Aurel — *The Schwarzian Derivative and the Approximation Method of Brillouin.* Quarterly of Applied Mathematics, Vol.XVI, No.1, April 1958, pp.82-86.

41. Murphy, C.H. — *Free Flight Motion of Symmetric Missiles.* BRL Report 1216, July 1963.

42. Nicolaides, J.D. — *On the Free Flight Motion of Missiles Having Slight Configurational Asymmetries.* BRL Report 858, June 1953 and IAS Preprint 395, 1952, AD 26405.

43. Redd, B.; Oslen, D.M.; Barton, R.L. — *Relationship Between the Aerodynamic Damping Derivatives Measured as a Function of Instantaneous Angular Displacement and the Aerodynamic Damping Derivatives Measured as a Function of Oscillation Amplitude.* NASA TN D-2855, June 1965.

44. Wehrend, W.R. Jr — *An Experimental Evaluation of Aerodynamic Damping Moments of Cones with Different Centers of Rotation.* NASA TN D-1768, March 1963.

45. Meyer, R.C.; Seredinsky, V. — *Longitudinal Axis Transfer Relations Applicable to Large Angle-of-Attack Dynamic Data.* Grumman Report ADR 01-07-63.1.

46. Nicolaides, J.D.; Eikenberry, R.F. — *Dynamic Wind-Tunnel Testing Techniques.* AIAA Paper 66-752, AIAA Aerodynamic Testing Conference, Los Angeles, California, September 21-23, 1966.

47. Urban, R.H. — *A Dynamic Stability Balance for Hypervelocity (Hotshot) Tunnels.* AEDC-TR-65-222, October 1965, AD 472707.

48. Vaucheret, Xavier; Broussaud, Pierre — *Dispositif d'Oscillations Libres Pour Souffleries à Rafales.* (Free-Oscillation Device for Intermittent Wind Tunnels), La Recherche Aérospatiale No.107, Juillet-Aout, 1965, pp.49-52.

49. Dubose, H.C. — *Static and Dynamic Stability of Blunt Bodies.* AGARD Report 347, April 1961.

50. Maas, W.L. — *Experimental Determination of Pitching Moment and Damping Coefficients of a Cone in Low Density, Hypersonic Flow.* University of California, Technical Report HE-150-190.

51. Stalmach, C.J. Jr; Moore, D.R.; Lindsey, J.L. — *Stability Investigations During Simulated Ablation in a Hypervelocity Wind Tunnel - Including Phase Control.* LTV Report 2-59740/5R-2192, April 1965.

52. Moore, D.R.
Stalmach, C.J. Jr
Pope, T.C.
Dynamic Stability Wind-Tunnel Tests of a 10° Cone with Simulated Ablation at $M_\infty = 17$. AIAA Paper 66-757, AIAA Aerodynamic Testing Conference, September 21-23, 1966.

53. Olsson, C.O.
Orlik-Ruckemann, K.J.
An Electronic Apparatus for Automatic Recording of the Logarithmic Decrement and Frequency of Oscillation in the Audio and Sub-Audio Frequency Range. The Aeronautical Research Institute of Sweden, FFA Report 52, February 1954.

54 Orlik-Ruckemann, K.J.
Travel Summation and Time Summation Methods of Free-Oscillation Data Analysis. Technical Note, AIAA Journal, Vol.I, No.7, July 1963, pp.1698-1700.

55. Leach, R.N.
A Slide Rule Type of Device to Measure Logarithmic Decay Times as Presented by Oscillograph Records. Sandia Corporation SC-4418 (RR), March 1960.

56. Welsh, C.J.
Hance, Q.P.
Ward, L.K.
A Forced-Oscillation Balance System for the von Karman Gas Dynamics Facility 40-by 40-Inch Supersonic Tunnel. AEDC-TN-61-63, May 1961, AD 257 380.

57. Riddle, C.D.
A Description of a Forced-Oscillation Balance. AEDC-TDR-62-68, May 1962, AD 276105.

58. McKee, M.L.
A Description of the Control and Readout System for a Forced-Oscillation Balance. AEDC-TDR-62-69, June 1962, AD 277453.

59. Kilgore, R.A.
Averett, B.T.
A Forced-Oscillation Method for Dynamic Stability Testing. Proceedings AIAA Aerodynamic Testing Conference, Washington, DC, March 9-10, 1964, pp.59-62, (Journal of Aircraft, Vol.I, September-October 1964, pp.304-305).

60. Braslow, A.L.
Wiley, H.G.
Lee, C.Q.
A Rigidly Forced Oscillation System for Measuring Dynamic-Stability Parameters in Transonic and Supersonic Wind Tunnels. NASA TN D-1231, March 1962.

61. Bielat, R.P.
Wiley, H.G.
Dynamic Longitudinal and Directional Stability Derivatives for a 45° Sweptback-Wing Airplane Model at Transonic Speeds. NASA TM X-39, August 1959.

62. Thompson, J.S.
Fail, R.A.
Oscillatory Derivative Measurements on Sting Mounted Wind Tunnel Models. RAE Report Aero 2668, July 1962.

63. Beam, B.H.
A Wind Tunnel Test Technique for Measuring the Dynamic Rotary Stability Derivatives at Subsonic and Supersonic Speeds. NACA Report 1258, 1956.

64. Roos, F.W.
Kuethe, A.M.
Application of an Electromagnetic Method to Dynamic Stability Measurements. ARL 66-0135, July 1966. Summary of ARL Symposium on Magnetic Wind Tunnel Model Suspension and Balance Systems, by F.L.Daum.

65. Tournier, M.
Laurenceau, P.
Suspension Magnétique d'une Maquette en Soufflerie. La Recherche Aéronautique, No.59, Juillet-Aout, 1957, pp.21-26.

66. Zapata, R.N.
Dukes, T.A.
The Princeton University Electromagnetic Suspension System and Its Use as a Force Balance. ARL 66-0135, July 1966. Summary of ARL Symposium on Magnetic Wind Tunnel Model Suspension and Balance Systems, by F.L.Daum.

67. Phillips, W.M.
The Measurement of Low Density Sphere Drag with a University of Virginia Magnetic Balance. ARL 66-0135, July 1966. Summary of ARL Symposium on Magnetic Wind Tunnel Model Suspension and Balance Systems, by F.L.Daum.

68. Wilson, A.
Luff, B.
The Development, Design and Construction of a Magnetic Suspension System for the RAE 7 in. x 7 in. (18 x 18 cm) Hypersonic Wind Tunnel. ARL 66-0135, July 1966. Summary of ARL Symposium on Magnetic Wind Tunnel Model Suspension and Balance Systems, by F.L.Daum.

69. Crane, J.F.W.
Preliminary Wind Tunnel Tests of the RAE Magnetic Suspension System and a Discussion of Some Drag Measurements Obtained for a 20° Cone, ARL 66-0135, July 1966. Summary of ARL Symposium on Magnetic Wind Tunnel Model Suspension and Balance Systems, by F.L.Daum.

70. Judd, M.
Goodyer, M.J.
Some Factors in the Design of Magnetic Suspension Systems for Dynamic Testing. ARL 66-0135, July 1966. Summary of ARL Symposium on Magnetic Wind Tunnel Model Suspension and Balance Systems, by F.L.Daum.

71. Goodyer, M.J.
The Theoretical and Experimental Performance of Roll Control Elements in the Six Component Magnetic Wind Tunnel Balance. ARL 66-0135, July 1966. Summary of ARL Symposium on Magnetic Wind Tunnel Model Suspension and Balance Systems, by F.L.Daum.

72. Martin, D.J.
Thompson, R.F.
Martz, C.W.
Exploratory Investigation of the Moments on Oscillating Control Surfaces at Transonic Speeds. NACA RM L55E31b, August 1955.

73. Reese, D.E. Jr
Carlson, W.C.
An Experimental Investigation of the Hinge-Moment Characteristics of a Constant-Chord Control Surface Oscillating at High Frequency. NACA RM A55J24, December 1955.

74. Orlik-Ruckemann, K.J.
Some Data on Elevator Damping and Stiffness Derivatives on a Delta Wing Aircraft Model at Supersonic Speeds. National Research Council, Canada report, 1959.

75. Martz, C.W. — *Experimental Hinge Moments on Freely Oscillating Flap-Type Control Surfaces.* NACA RM L56G20, October 1956.

76. Orlik-Ruckemann, K.J. — *Measurement of Aerodynamic Damping and Stiffness Derivatives in Free Oscillating with Automatically Recycled Feedback Excitation.* National Research Council, Canada, Report LR-246, June 1959.

77. Lessing, H.C.; Fryer, T.B.; Mead, M.H. — *A System for Measuring the Dynamic Lateral Stability Derivatives in High-Speed Wind Tunnels.* NACA TN 3348, December 1954.

78. Regan, F.J. — *Roll Damping Moment Measurements for the Basic Finner at Subsonic and Supersonic Speeds.* NAVORD Report 6652, March 1964.

79. Regan, F.J.; Horanoff, E. — *Wind Tunnel Model Support Using a Gas Bearing.* US Naval Ordnance Laboratory, White Oak, Maryland, NOL TR 65-14, in publication.

80. Volluz, R.J. — *Wind Tunnel Instrumentation and Operation.* Handbook of Supersonic Aerodynamics, Section 20, NAVORD Report 1483 (Vol.6).

81. Magnus, Gustav — *Ueber die Abweichung der Geschosse.* Abhandlungen der Berliner Akademie, 1852.

82. Luchuk, W. — *The Dependence of the Magnus Force and Moment on the Nose Shape of Cylindrical Bodies of Fineness Ratio 5 at a Mach Number of 1.75.* NAVORD Report 4425, April 1957.

83. Nicolaides, John D.; MacAllister, Leonard C. — *A Review of Aeroballistic Range Research on Winged and/or Finned Missiles.* TN 5, 1954, Bureau of Ordnance, Dept. of the Navy, Washington, DC, AD 95 044.

84. Platou, A.S. — *Magnus Characteristics of Finned and Nonfinned Projectiles.* AIAA Journal, Vol.3, No.1, January 1965, pp.83-90.

85. Martin, J.C. — *On Magnus Effects Caused by the Boundary Layer Displacement Thickness on Bodies of Revolution at Small Angles of Attack.* BRL Report 870, June 1955.

86. Platou, A.S. — *The Magnus Force on a Finned Body.* BRL Report 1193, March 1963.

87. Benton, E.R. — *Supersonic Magnus Effect on a Finned Missile.* AIAA Journal, Vol.2, No.1, January 1964, pp.153-155.

88. Benton, E.R. — *Wing-Tail Interference as a Cause of "Magnus" Effects on a Finned Missile.* Journal of the Aerospace Sciences, Vol.29, No.11, November 1962, pp.1358-1367.

89. Platou, A.S. — *The Magnus Force on a Short Body at Supersonic Speeds.* BRL Report 1062, January 1959. AD 212 064.

90. Nicolaides, J.D.; Brady, J.J. — *Magnus Moments on Pure Cones in Supersonic Flight.* NAVORD Report 6183, January 1959.

91. Greene, J.E. — *A Summary of Experimental Magnus Characteristics of a 7 and 5-Caliber Body of Revolution at Subsonic Through Supersonic Speeds.* NAVORD Report 6110, August 1958.

92. Uselton, J.C. — *Investigation of the Magnus Effects and the Effects of Unsymmetrical Leeward Vortex Patterns on a High Fineness Ratio Model at Mach Numbers 3 and 5.* University of Tennessee, Master of Science Thesis, August 1966.

93. Cornett, R. — *Design of a Miniature High-Speed Air Turbine for Spinning Wind-Tunnel Models.* NAVORD Report 4206, 1956.

94. Parobek, D.M. — *Development of Wind Tunnel Models, Instruments, and Techniques for Trisonic Magnus Force Testing at High Spin Rates and for the Angle of Attack Range of 0 to 180 deg.* WADD TR-60-213, August 1960.

95. Curry, W.H.; Reed, J.F. — *Measurement of Magnus Effects on a Sounding Rocket Model in a Supersonic Wind Tunnel.* AIAA Paper 66-754, AIAA Aerodynamic Testing Conference, Los Angeles, California, September 21-23, 1966.

96. Platou, A.S.; Ricci, H.A. — *Wind Tunnel Tests of Solid State Strain Gages.* BRL, September 1964, private communication.

97. Pate, S.R.; Jones, J.H. — *Investigations of the Air Load Distributions on a Stabilizing Fin at Mach Numbers 1.5, 2.0 and 2.5.* AEDC-TN-61-167, December 1961, AD 268 858.

98. Wasson, H.R.; Mehus, T.E. — *A Segmented Wing Test Technique for Obtaining Spanwise Load Distributions of Wings.* AIAA Paper 66-768, AIAA Aerodynamic Testing Conference, Los Angeles, California, September 21-23, 1966.

99. Martuccelli, J.R. — *Measurements of Pressure Distributions on an Oscillating Wedge in Supersonic Flow.* MIT Aeroelastic and Structures Research Laboratory, Technical Report 71-2, October 1958.

100. Rainey, A.G. — *Measurement of Aerodynamic Forces for Various Mean Angles of Attack on an Airfoil Oscillating in Pitch and on Two Finite-Span Wings Oscillating in Bending with Emphasis on Damping in the Stall.* NACA Report 1305, 1957. (Supersedes NACA-TN-3643).

101. Molyneux, W.G.
Ruddlesden, F.
A Technique for the Measurement of Pressure Distributions on Oscillating Aerofoils with Results for a Rectangular Wing of Aspect Ratio 3.3. CP 233, ARC 18, 018, June 1955.

102. Greidanus, J.H.
van de Vooren, A.I.
Bugh, H.
Experimental Determination of the Aerodynamic Coefficients of an Oscillating Wing in Incompressible Two-Dimensional Flow. National Luchtvaartlaboratorium, Amsterdam, Reports 101, 102, 103 and 104, 1952.

103. Li, Y.T.
High-Frequency Pressure Indicators for Aerodynamic Problems. NACA TN 3042, November 1953.

104. Davis, E.L. Jr
The Measurement of Unst ady Pressures in Wind Tunnels. AGARD Report 169, March 1958.

105. Mason, W.P.
Electromechanical Transducers and Wave Filters. van Nostrand, New York, 1942.

106. Delio, G.J.
Schwent, G.V.
Cesaro, R.S.
Transient Behavior of Lumped-Constant Systems for Sensing Gas Pressures. NACA TN 1988, December 1949.

107. Taback, I.
The Response of Pressure Measuring Systems to Oscillating Pressures. NACA TN 1819, February 1949.

108. Beranek, L.L.
Acoustic Measurements. John Wiley, New York, 1949.

BIBLIOGRAPHY

Instrumentation

1. Aigrain, P.R.
Williams, E.M.
Theory of Amplitude-Stabilized Oscillators. Proceedings of the IRE, Vol. 36, No. 1, January 1948.

2. Bratt, J.B.
Wight, K.C.
Tilly, V.J.
The Application of a "Wattmeter" Harmonic Analyser to the Measurement of Aero-Dynamic Damping for Pitching Oscillations. ARC R&M 2063, May 1942, ATI 50985.

3. Lightfoot, J.R.
White, C.E.
Special Applications of Strain-Gage Balances Used in the Supersonic and Hypersonic Wind Tunnels at the US Naval Ordnance Laboratory. AGARD Report 8, February 1956.

4. Queijo, M.J.
et al.
Preliminary Measurements of the Aerodynamic Yawing Derivatives of a Triangular, a Swept, and an Unswept Wing Performing Pure Yawing Oscillations, with a Description of the Instrumentation Employed. NACA RM L55L14, April 1956.

Gas Bearings

1. Dudgeon, E.H.
   Lowe, I.R.G.
   A Theoretical Analysis of Hydrostatic Gas Journal Bearings. National Research Council, Canada, Report MT-54, August 1965.

2. Grassam, N.S.
   Powell, J.W.
   Gas Lubricated Bearings. Butterworths, London, 1964.

3. Grinnell, S.K.
   Richardson, H.H.
   Design Study of a Hydrostatic Gas Bearing with Inherent Compensation. Transactions, ASME. Vol.79, No.1, January 1957, pp.11-21.

4. Gross, W.A.
   Gas Film Lubrication. John Wiley, New York, 1962.

5. Pinkus, O.
   Sternlicht, B.
   Theory of Hydrodynamic Lubrication. McGraw-Hill, New York, 1961.

6. Tang, I.C.
   Gross, W.A.
   Analysis and Design of Externally Pressurized Gas Bearings. Transactions, ASLE, Vol.5, 1962, pp.261-284.

Tare Damping

1. Baker, W.E.
   Allen, H.J.
   The Damping of Transverse Vibrations of Thin Beams in Air. BRL R 1033, October 1957, AD 158 393.

2. Crandall, S.H.
   On Scaling Laws for Material Damping. NASA TN D-1497, December 1962.

3. Entwistle, K.M.
   The Damping Capacity of Metals. Paper from the Physical Examination of Metals, 1960, pp.487-558.

4. Gemant, Andrew
   The Problem of Reduction of Vibrations by Use of Materials of High Damping Capacity. Journal of Applied Physics, Vol.15, January 1944.

5. Hatfield, W.H.
   Stanfield, G.
   Rotherham, L.
   The Damping Capacity of Engineering Materials. Firth-Brown Research Laboratory, Sheffield, May 1942.

6. Jensen, J.W.
   Damping Capacity - Its Measurement and Significance. US Department of the Interior, Bureau of Mines, Rolla, Missouri, 1959, Report of Investigation 5441 (Unclassified).

7. Kennedy, C.
   Measuring the Coulomb and Viscous Components of Friction. Instruments, Vol.15, October 1942, pp.404-410.

8. Lazan, B.J. — *Damping Properties of Materials and Material Composites.* Applied Mechanics Review, Vol.15, No.2, February 1962.

9. Lazan, B.J. — *The Damping Properties of Materials and Their Relationship to Resonant Fatigue Strength of Parts.* General Electric Company, Report R55GL129, January 1955.

10. Lazan, B.J. et al. — *Dynamic Testing of Materials and Structures with a New Resonance-Vibration Exciter and Controller.* WADC Technical Report 52-252, December 1952.

11. Maringer, R.E. — *Damping Capacity of Materials.* Battelle Memorial Institute, Columbus, Ohio, December 30, 1965, RSIC Report 508 (Unclassified).

12. Podnieks, E.R. Lazan, B.J. — *Analytical Methods for Determining Specific Damping Energy Considering Stress Distribution.* WADC TR 56-44, June 1957, AD 130 777.

13. Robertson, J.M. Yorgiadis, A.J. — *Internal Friction in Engineering Materials.* Journal of Applied Mechanics, Vol.13, No.3, September 1946, pp.A173-A182.

14. Thorn, R.P. — *Built-In-Damping.* Machine Design, November 25, 1965, and December 9, 1965.

15. Ting-Sui Ke — *Experimental Evidence of the Viscous Behavior of Grain Boundaries in Metals.* Physics Review, Vol.71, 1947, pp.533-546.

16. Ting-Sui Ke — *Internal Friction of Metals at Very High Temperatures.* Journal of Applied Physics, Vol.21, 1950, pp.414-419.

17. Tsobkallo, S.O. Chelnokov, V.A. — *New Method for the Determination of True Damping of Oscillations in Metals.* Zhurnal Tekhnickeskoi Fiziki, Vol.24, No.3, March 1954, pp.499-510.

18. Ungar, E.E. Hatch, D.K. — *High-Damping Materials.* Product Engineering, April 17, 1961, pp.42-56.

19. von Heydekampf, G.S. — *Damping Capacity of Materials.* ASTM Proceedings, Vol.31, Part II, 1931, pp.157-171.

20. Walsh, D.F. Jensen, J.W. Rowland, J.A. — *Vibration Damping Capacity of Various Magnesium Alloys.* US Department of the Interior, Bureau of Mines, Rolla, Missouri, 1962, Report of Investigation 6116 (Unclassified).

Derivatives Due to Pitch and Rate of Pitch-Theory

1. *A General Investigation of Hypersonic Stability and Control Under Trimmed Flight Conditions.* Flight Sciences Laboratory, Inc., Buffalo, New York, R-63-011-104, June 1964, AD 434 304.

2. Acum, W.E.A. *Note on the Effect of Thickness and Aspect Ratio on the Damping of Pitching Oscillations of Rectangular Wings Moving at Supersonic Speeds.* ARC CP 151, 1953.

3. Acum, W.E.A. *The Comparison of Theory and Experiment for Oscillating Wings.* ARC CP 681, 1963.

4. Alden, L.H.
Schindel, L.H. *The Lift, Rolling Moment, and Pitching Moment on Wings in Nonuniform Supersonic Flow.* Journal of the Aeronautical Sciences, Vol. 19, No. 1, January 1952, p. 7.

5. Allen, H.J. *Estimation of the Forces and Moments Acting on Inclined Bodies of Revolution of High Fineness Ratio.* NACA RM A9126, November 1949.

6. Allen, H.J.
Perkins, E.W. *A Study of Effects of Viscosity on Flow Over Slender Inclined Bodies of Revolution.* NACA Report 1048, 1951.

7. Allen, H.J. *Motion of a Ballistic Missile Angularly Misalined with the Flight Path Upon Entering the Atmosphere and Its Effect Upon Aerodynamic Heating, Aerodynamic Loads, and Miss Distance.* NACA TN 4048, October 1957.

8. Bobbitt, P.J.
Malvestuto, F.S. Jr *Estimation of Forces and Moments Due to Rolling for Several Slender-Tail Configurations at Supersonic Speeds.* NACA TN 2955, July 1953.

9. Bourcier, M. *Application de la Méthode Asymptotique au Calcul des Dérivées Aérodynamiques de Stabilité en Hypersonique pour un Cône Circulaire.* ONERA, Note Technique No. 97, 1966.

10. Brown, C.E.
Adams, M.C. *Damping in Pitch and Roll of Triangular Wings at Supersonic Speeds.* NACA Report 892, 1948.

11. Charwat, A.F. *The Stability of Bodies of Revolution at Very High Mach Numbers.* Jet Propulsion, Vol. 27, No. 8, Part 1, August 1957, pp. 866-871.

12. Chester, W. *Supersonic Flow Past Wing-Body Combinations.* Aeronautical Quarterly, Vol. IV, August 1953, p. 287.

13. Coakley, T.J.
Laitone, E.V.
Maas, W.L. *Fundamental Analysis of Various Dynamic Stability Problems for Missiles.* Institute of Engineering Research, University of California. Berkeley, California, Series No. 176, Issue No. 1, June 1961, AD [illegible]9 127.

14. Corning, G. — *The Pitch-Yaw-Roll Coupling Problem of Guided Missiles at High Angles of Pitch.* NAVWEPS 7383, 1961.

15. Cunningham, H.J. — *Total Lift and Pitching Moment on Thin Arrowhead Wings Oscillating in Supersonic Potential Flow.* NACA TN 3433, May 1955.

16. Fink, M.R.; Carroll, J.B. — *Hypersonic Static and Dynamic Stability of Wing-Fuselage Configurations.* United Aircraft Corporation Research Laboratory, C910188-17, January 1965.

17. Dorrance, W.H. — *Nonsteady Supersonic Flow About Pointed Bodies of Revolution.* Journal of the Aeronautical Sciences, Vol. 18, No. 8, August 1951, pp. 505-511.

18. Fink, M.R. — *Hypersonic Dynamic Stability of Biconic Bodies.* United Aircraft Corporation, Research Laboratory, Conn., UAR-E20, March 21, 1965.

19. Fink, M.R. — *Hypersonic Dynamic Stability of Sharp and Blunt Slender Cones.* United Aircraft Corporation, Research Laboratory, Conn. UAR-C111, July 1964.

20. Fink, M.R. — *A Shock-Expansion Method for Calculation of Hypersonic Dynamic Stability.* United Aircraft Corporation, Research Laboratory, Conn., C-910188-4, March 1964.

21. Friedrich, H.R.; Dore, F.J. — *The Dynamic Motion of a Missile Descending Through the Atmosphere.* Journal of the Aeronautical Sciences, Vol. 22, September 1955, pp. 628-632.

22. Garner, H.C. — *Numerical Aspects of Unsteady Lifting Surface Theory at Supersonic Speeds.* ARC CP 398.

23. Garner, H.C.; Acum, W.E.A. — *Proposed Application of Linearized Theoretical Formulae to General Mechanized Calculations for Oscillating Wings at Supersonic Speeds.* NPL Aero. Report 388, 1959.

24. Garner, H.C.; Acum, W.E.A.; Lehrian, D.E. — *Comparative Calculations of Supersonic Pitching Derivatives Over a Range of Frequency Parameter.* ARC CP 591, 1962.

25. Garrick, I.E.; Rubinow, S.I. — *Theoretical Study of Air Forces on an Oscillating or Steady Thin Wing in a Supersonic Main Stream.* NACA Report 872, 1947.

26. Gilmore, A.; Seredinsky, V.; MacKenzie, D. — *Investigation of Dynamic Stability Derivatives of Vehicles Flying at Hypersonic Velocity.* Grumman Aircraft Engineering Corporation, ASD-TDR-62-460, September 1963, AD 421 874.

27. Harmon, S.M. — *Stability Derivatives at Supersonic Speeds of Thin Rectangular Wings with Diagonals Ahead of Tip Mach Lines.* NACA Report 925, 1949.

28. Harmon, S.M. Jeffreys, I. — *Theoretical Lift and Damping In Roll of Thin Wing with Arbitrary Sweep and Taper at Supersonic Speeds, Supersonic Leading and Trailing Edges.* NACA TN 2114, May 1950.

29. Harris, G.Z. — *The Calculation of Generalised Forces on Oscillating Wings in Supersonic Flow by Lifting Surface Theory.* Royal Aircraft Establishment, Technical Report 65078, 1965.

30. Henderson, A. Jr — *Pitching-Moment Derivatives* C_{mq} *and* $C_{m\dot{\alpha}}$ *at Supersonic Speeds for a Slender-Delta-Wing and Slender-Body Combination and Approximate Solutions for Broad-Delta-Wing and Slender-Body Combinations.* NACA TN 2553, December 1951.

31. Hjelte, F. — *Methods for Calculating Pressure Distributions on Oscillating Wings of Delta Type at Supersonic and Transonic Speeds.* KTH Aero TN 39, Stockholm, 1956.

32. Jones, A.L. Alksne, A. — *The Damping Due to Roll of Triangular Trapezoidal, and Related Plan Forms in Supersonic Flow.* NACA TN 1548, March 1948.

33. Jones, W.P. — *Aerofoil Oscillations at High Mean Incidences.* ARC R&M 2654, 1948.

34. Jones, W.P. — *Oscillating Wings in Compressible Subsonic Flow.* ARC R&M 2855, October 1951, (ARC 14,336).

35. Jones, W.P. — *Summary of Formulae and Notations Used in Two-Dimensional Derivative Theory.* ARC R&M 1958, August 1941.

36. Jones, W.P. — *Supersonic Theory for Oscillating Wings of Any Planform* ARC R&M 2655, 1948.

37. Jones, W.P. — *The Calculation of Aerodynamic Derivative Coefficients for Wings of Any Planform in Non-Uniform Motion.* ARC R&M 2655, 1948.

38. Jones, W.P. — *The Influence of Thickness-Chord Ratio on Supersonic Derivatives for Oscillating Aerofoils.* ARC R&M 2679, 1947

39. Kelly, H.R. — *The Estimation of Normal-Force, Drag, and Pitching-Moment Coefficients for Blunt-Based Bodies of Revolution at Large Angles of Attack.* Journal of the Aeronautical Sciences, Vol.21, August 1954, pp.549-555.

40. Kind, R.J.
Orlik-Ruckemann, K.J.
Stability Derivatives of Sharp Cones in Viscous Hypersonic Flow. National Research Council, Canada, Report LR-427, 1965; also AIAA Journal, Vol.4, No.8, 1966, pp.1469-1471.

41. Labrujere, H.E.
Determination of the Stability Derivatives of an Oscillating Axisymmetric Fuselage in Supersonic Flow. NLL TN W.13, Amsterdam, 1960.

42. Laitone, E.V.
Effect of Acceleration on the Longitudinal Dynamic Stability of a Missile. ARS Journal, Vol.29, February 1959, p.137.

43. Lawrence, H.R.
Flax, A.H.
Wing-Body Interference at Subsonic and Supersonic Speeds-Survey and New Developments. Journal of the Aeronautical Sciences, Vol.21, May 1954, pp.289-324.

44. Lawrence, H.R.
Gerger, E.H.
The Aerodynamic Forces on Low Aspect Ratio Wings Oscillating in an Incompressible Flow. Journal of the Aeronautical Sciences, Vol.19, November 1952, pp.769-781.

45. Lehrian, Doris E.
Calculation of Stability Derivatives for Oscillating Wings. ARC R&M 2922, February 1953. (ARC 15,695).

46. Lehrian, Doris E.
Calculation of Stability Derivatives for Tapered Wings of Hexagonal Planform Oscillating in a Supersonic Stream. ARC R&M 3298, 1963.

47. Lehrian, Doris E.
Smart, G.
Theoretical Stability Derivatives for a Symmetrically Tapered Wing at Low Supersonic Speeds. ARC CP 736, 1965.

48. Lighthill, M.J.
Oscillating Airfoils at High Mach Number. Journal of the Aeronautical Sciences, Vol.20, June 1953, pp.402-406.

49. Malvestuto, F.S. Jr
Hoover, Dorothy M.
Lift and Pitching Derivatives of Thin Sweptback Tapered Wings with Streamwise Tips and Subsonic Leading Edges at Supersonic Speeds. NACA TN 2294, February 1951.

50. Malvestuto, F.S. Jr
Hoover, Dorothy M.
Supersonic Lift and Pitching Moment of Thin Sweptback Tapered Wings Produced by Constant Vertical Acceleration, Subsonic Leading Edges and Supersonic Trailing Edges. NACA TN 2315, March 1951.

51. Malvestuto, F.S. Jr
Margolis, K.
Theoretical Stability Derivatives of Thin Sweptback Wings Tapered to a Point with Sweptback or Sweptforward Trailing Edges for a Limited Range of Supersonic Speeds. NACA Report 971, (Supersedes NACA TN 1761), 1950.

52. Malvestuto, F.S. Jr
Margolis, K.
Ribner, H.S.
Theoretical Lift and Damping in Roll at Supersonic Speeds of Thin Sweptback Tapered Wings with Streamwise Tips, Subsonic Leading Edges, and Supersonic Trailing Edges. NACA Report 970, 1950.

53. Mangler, K.W. — *A Method of Calculating the Short-Period, Longitudinal Stability Derivatives of a Wing in Linearised Unsteady Compressible Flow.* ARC R&M 2924, June 1952, (ARC 15,316).

54. Martin, J.C. Diederich, M.S. Bobbitt, P.J. — *A Theoretical Investigation of the Aerodynamics of Wing-Tail Combinations Performing Time Dependent Motions at Supersonic Speeds.* NACA TN 3072, May 1954.

55. Martin, J.C. Margolis, K. Jeffreys, I. — *Calculation of Lift and Pitching Moments due to Angle of Attack and Steady Pitching Velocity at Supersonic Speeds for Thin Sweptback Tapered Wings with Streamwise Tips and Supersonic Leading and Trailing Edges.* NACA TN 2699, June 1952.

56. Mathot, F. — *Formules Newtoniennes de Détermination des Dérivées Aérodynamiques de Corps Coniques ou Sphériques.* La Recherche Aérospatiale, No.111, 1966.

57. McIntosh, S.C. Jr — *Hypersonic Flow Over an Oscillating Wedge.* AIAA Journal, Vol.3, March 1965, pp.433-440.

58. Miles, J.W. — *On Damping-In-Pitch for Delta Wings.* Journal of the Aeronautical Sciences, Vol.16, September 1949, pp.574-575.

59. Miles, J.W. — *On Harmonic Motion of Wide Delta Airfoils at Supersonic Speeds.* NOL TM RRB 36, February 1950.

60. Miles, J.W. — *On the Low Aspect Ratio Oscillating Rectangular Wing in Supersonic Flow.* Aeronautical Quarterly, Vol.IV, August 1953, p.231.

61. Miles, J.W. — *The Application of Unsteady Flow Theory to the Calculation of Dynamic Stability Derivatives- and Appendixes A-C.* North American Aviation Report AL-957, September 1950, ATI 98 956.

62. Miles, J.W. — *Unsteady Supersonic Flow Past Slender Pointed Bodies.* US Naval Ordnance Test Station, China Lake, California, NAVORD Report 2031, May 1953, AD 14 999.

63. Milliken, W.F. Jr — *Dynamic Stability and Control Research.* Cornell Laboratory, Incorporated (presented at Third Anglo-American Aeronautical Conference of the RAES-IAS, Brighton, England, September 3-14, 1951). Report CAL-39.

64. Milliken, W.F. Jr — *Progress in Dynamic Stability and Control Research.* Journal of the Aeronautical Sciences, Vol.14, September 1947, pp.493-519.

65. Morikawa, G. — *Supersonic Wing-Body Lift.* Journal of the Aeronautical Sciences, Vol.18, April 1951, pp.217-228.

66. Morikawa, G. — *Supersonic Wing-Body-Tail Interference.* Journal of the Aeronautical Sciences, Vol. 19, May 1952, pp. 333-340.

67. Mueller, R.K. — *The Graphical Solution of Stability Problems.* Journal of the Aeronautical Sciences, Vol. 4, June 1937, pp. 324-331.

68. Munch, J. — *An Example for the Practical Calculation of Supersonic Flow Fields Past Oscillating Bodies of Revolution by a Method Due to Sauer.* AFOSR TN 58-881, August 1958.

69. Platzer, M.F.; Hoffman, G.H. — *Quasi-Slender Body Theory for Slowly Oscillating Bodies of Revolution in Supersonic Flow.* NASA TN D-3440, June 1966.

70. Neumark, S. — *Two-Dimensional Theory of Oscillating Aerofoils with Application to Stability Derivatives.* RAE Report Aero 2449, ARC 14,889, 1951.

71. Nielsen, J.N. — *Supersonic Wing-Body Interference.* California Institute of Technology Thesis, 1951.

72. Nielsen, J.N.; Kaattari, G.E. — *The Effects of Vortex and Shock-Expansion Fields on Pitch and Yaw Instabilities of Supersonic Airplanes.* Institute of the Aeronautical Sciences, Preprint 743, 1957.

73. Ohman, L.H. — *A Surface Flow Solution and Stability Derivatives for Bodies of Revolution in Complex Supersonic Flow.* Part I: *Theory and Some Representative Results.* National Research Council, Canada, Report LR-418, 1964.

74. Ohman, L.H. — *A Surface Flow Solution and Stability Derivatives for Bodies of Revolution in Complex Supersonic Flow.* Part II: *Results for Two Families of Bodies of Revolution for* $1.1 \leq M \leq 5$. National Research Council, Canada, Report LR-419, 1964.

75. Orlik-Ruckemann, K.J. — *Effect of Wave Reflections on the Unsteady Hypersonic Flow Over a Wedge.* AIAA Journal, Vol. 4, No. 10, 1966.

76. Orlik-Ruckemann, K.J. — *Stability Derivatives of Sharp Wedges in Viscous Hypersonic Flow.* National Research Council, Canada, Report LR-431, 1965; also (slightly extended) AIAA Journal, Vol. 4, No. 6, 1966, pp. 1001-1007.

77. Orlik-Ruckemann, K.J.; Crowe, C. — *Comparison of Various Experimental and Theoretical Results for Static and Dynamic Longitudinal Stability Derivatives of Some Wing-Body Configurations at Supersonic Speeds.* NAE Laboratory Report (to be published).

78. Pitts, W.C.; Nielsen, J.N.; Kaattari, G.E. — *Lift and Center of Pressure of Wing-Body-Tail Combinations at Subsonic, Transonic and Supersonic Speeds.* NACA Report 1307, 1957.

79. Platzer, M.F. — *A Note on the Solution for the Slowly Oscillating Body of Revolution in Supersonic Flow.* George C.Marshall Space Flight Center, MTP-AERO-63-28, April 23, 1963.

80. Quinn, B.P. — *Blast Wave Effects on the Pitching of Blunt Cones.* Paper 37, Vol.II, Proceedings of the 13th Annual Air Force Science and Engineering Symposium, Arnold Engineering Development Center, Arnold Air Force Station, Tennessee, September 1966.

81. Ribner, H.S. Malvestuto, F.S. Jr — *Stability Derivatives of Triangular Wings at Supersonic Speeds.* NACA Report 908, 1948.

82. Richardson, J.R. — *A Method for Calculating the Lifting Forces on Wings (Unsteady Subsonic and Supersonic Lifting-Surface Theory).* ARC R&M 3157, April 1955, ARC 18,622.

83. Sacks, A.H. — *Aerodynamic Forces, Moments and Stability Derivatives for Slender Bodies of General Cross Section.* NACA TN 3283, November 1954.

84. Sauerwein, H. — *Application of the Piston Analogy to the Calculation of Stability Derivatives for Pointed Axially Symmetric Bodies at High Mach Numbers.* AVCO Corporation, RAD-TM-61-40, October 1961.

85. Seredinsky, V. — *Derivation and Application of Hypersonic Newtonian Impact Theory to Wedges, Cones and Slab Wings Including the Effects of Angle of Attack, Shielding and Bluntness.* Grumman Aircraft Engineering Corporation Report XAR-A-42, April 1962

86. Smith, H.B. Beasley, J.A. Stevens, A. — *Calculations of the Lift Slope and Aerodynamic Center of Cropped Delta Wings at Supersonic Speeds.* RAE TN Aero 2697, 1960.

87. Spahr, J.R. — *Contribution of the Wing Panels to the Forces and Moments of Supersonic Wing-Body Combinations at Combined Angles.* NACA TN 4146, January 1958.

88. Stanbrook, A. — *The Lift-Curve Slope and Aerodynamic Center Position of Wings at Supersonic and Subsonic Speeds.* RAE TN Aero 2328, 1954.

89. Statler, I.C. — *Dynamic Stability at High Speeds from Unsteady Flow Theory.* Journal of the Aeronautical Sciences, Vol.17, April 1950, pp.232-242.

90. Temple, C. — *The Representation of Aerodynamic Derivatives.* ARC R&M 2114, March 1945.

91. Thelander, J.A. — *Aircraft Motion Analysis.* US Air Force Flight Dynamics Laboratory, FDL-TDR-64-70, March 1965.

92. Thomas, H.H.B.M. — *Estimation of Stability Derivatives (State of the Art).* RAE TN Aero 2776, 1961; also ARC CP 664, and AGARD Report 339.

93. Thomas, H.H.B.M.; Ross, A.J. — *The Calculation of the Rotary Lateral Stability Derivatives of a Jet-Flapped Wing.* ARC R&M 3277, January 1958.

94. Thomas, H.H.B.M.; Spencer, B.F.R. — *The Calculations of the Derivatives Involved in the Damping of the Longitudinal Short Period Oscillations of an Aircraft and Correlation with Experiment.* RAE Report Aero 2561, 1955.

95. Tobak, M. — *Damping In Pitch of Low-Aspect-Ratio Wings at Subsonic and Supersonic Speeds.* NACA RM A52L04a, April 1953.

96. Tobak, M. — *On Nonlinear Longitudinal Dynamic Stability.* Presented to the AGARD Flight Mechanics Panel, Cambridge, England, September 20-23, 1966.

97. Tobak, M. — *On the Use of the Indicial Function Concept in the Analysis of Unsteady Motions of Wings and Wing-Tail Combinations.* NACA Report 1188, 1954.

98. Tobak, M.; Allen, H.J. — *Dynamic Stability of Vehicles Traversing Ascending or Descending Paths Through the Atmosphere.* NACA TN 4275, July 1958.

99. Tobak, M.; Pearson, W.E. — *A Study of Nonlinear Longitudinal Dynamic Stability.* NASA TR R-209, September, 1964.

100. Tobak, M.; Wehrend, W.R. — *Stability Derivatives of Cones at Supersonic Speeds.* NACA TN 3788, September 1956.

101. Treadgold, D.A. — *A Review of Methods of Estimation of Aircraft Longitudinal Stability Derivatives at Supersonic Speeds.* RAE TN Aero 2415, 1955.

102. van Dyke, M.D. — *On Second-Order Supersonic Flow Past a Slowly Oscillating Airfoil.* Readers' Forum, Journal of the Aeronautical Sciences, Vol. 20, January 1953, p. 61.

103. van Dyke, M.D. — *Supersonic Flow Past Oscillating Airfoils Including Nonlinear Thickness Effects.* NACA TN 2982, July 1953.

104. Watkins, C.E. — *Air Forces and Moments on Triangular and Related Wings with Subsonic Leading Edges Oscillating in Supersonic Potential Flow.* NACA TN 2457, September 1951.

105. Watkins, C.E. — *Effect of Aspect Ratio on the Air Forces and Moments of Harmonically Oscillating Thin Rectangular Wings in Supersonic Potential Flow.* NACA TN 2064, April 1950.

106. Watkins, C.E. — *Effect of Aspect Ratio on the Air Forces and Moments of Harmonically Oscillating Thin Rectangular Wings in Supersonic Potential Flow.* NACA Report 1028, 1951.

107. Watkins, C.E. — *Effect of Aspect Ratio on Undamped Torsional Oscillations of a Thin Rectangular Wing in Supersonic Flow.* NACA TN 1895, June 1949.

108. Watkins, C.E. Berman, J.H. — *Air Forces and Moments on Triangular and Related Wings with Subsonic Leading Edges Oscillating in Supersonic Potential Flow.* NACA Report 1099, 1952.

109. Watts, P.E. — *Notes on the Estimation of Aircraft Lateral Stability Derivatives at Supersonic Speeds.* RAE TN Aero 2414, 1955.

110. Wood, R.M. Murphy, C.H. — *Aerodynamic Derivatives for Both Steady and Non-Steady Motion of Slender Bodies.* BRL MR 880, April 1955.

111. Wylly, A. — *A Second-Order Solution for an Oscillating, Two-Dimensional, Supersonic Airfoil.* RAND Corporation Report, 1951.

Derivatives Due to Pitch and Rate of Pitch-Experiment

1. Akatnov, N.I. Sabaitis, Iu. I. — *Measurement of Pitching-Moment Derivatives by a Self-Excited Oscillation Method.* Zhurnal Tekhnickeskoi Fiziki, Vol. 26, No. 9, 1956. Translated in "Soviet Physics". Vol. 1, No. 9, 1957, pp. 1986-1993.

2. Babineaux, T.L. et al. — *The Influence of Shape on Aerodynamic Damping of Oscillatory Motion During Mars Atmosphere Entry and Measurement of Pitch Damping at Large Oscillation Amplitudes.* TR-32-380, February 28, 1963.

3. Beam, B.H. — *A Wind-Tunnel Test Technique for Measuring the Dynamic Rotary Stability Derivatives Including the Cross Derivatives at High Mach Numbers.* NACA TN 3347, January 1955.

4. Beam, B.H. — *The Effects of Oscillation Amplitude and Frequency on the Experimental Damping in Pitch of a Triangular Wing Having an Aspect Ratio of 4.* NACA RM A52G07, September 1952.

5. Bird, K D. — *Dynamic Stability Testing in a Hypersonic Shock Tunnel.* July 16-17, 1963.

6. Bratt, J.B. — *A Note on Derivative Apparatus for the NPL 9½ Inch High Speed Tunnel.* ARC CP 269, January 1956.

7. Bratt, J.B. Chinneck, A. — *Information Report on Measurements of Mid-Chord Pitching Moment Derivatives at High Speeds.* ARC 10,710, July 1947, ATI 105 207.

8. Bratt, J.B. — *The Measurement of Oscillatory Aerodynamic Forces.* AGARD Wind Tunnel Panel, September 1953.

9. Bratt, J.B. Scruton, C. — *Measurements of Pitching Moment Derivatives for an Aerofoil Oscillating About the Half-Chord Axis.* ARC R&M 1921, November 1938.

10. Bratt, J.B. Wight, K.C. — *The Effect of Mean Incidence, Amplitude of Oscillation, Profile and Aspect Ratio on Pitching Moment Derivatives.* ARC R&M 2064, June 1945.

11. Bratt, J.B. Wight, K.C. Chinneck, A. — *Free Oscillations of an Aerofoil About the Half-Chord Axis at High Incidences, and Pitching Moment Derivatives for Decaying Oscillation.* ARC R&M 2214, September 1940, ARC 4711.

12. Broll, C. — *Essais en Régime Instationnaire Effectués au Centre d'Essais de Modane-Avrieux.* (Unsteady Flow Testing at the ONERA Test Centre at Modane). La Recherche Aérospatiale, No. 100, 1964.

13. Clay, J.T. Walchner, O. — *Nose Bluntness Effects on the Stability Derivatives of Cones in Hypersonic Flow.* Vol. I, Paper 8, Transactions of the Second Technical Workshop on Dynamic Stability Testing. Held at the Arnold Engineering Development Center, Arnold Air Force Station, Tennessee, April 20-22, 1965.

14. Clunies, D.A. Stiles, H.W. Jr — *An Investigation of the Feasibility of a Method of Obtaining Data from Which the Stability Derivatives* $C_{m\alpha}$ *and* C_{mq} *can be Separated.* BSc Thesis, Aeronautical Engineering Department, Massachusetts Institute of Technology, May 1957.

15. Colosimo, D.D. — *The Effects of Mass-Transfer on the Dynamic Stability of Slender Cones.* CAL Report 141, May 1965.

16. Dat, R. Destuynder, R. — *Détermination des Coefficients Aérodynamiques Instationnaires sur une Aile Delta de Mach 1.35.* ONERA NT 52, 1959.

17. Daughaday, H. Duwaldt, F. Statler, I. *Measurement of Dynamic Stability Derivatives in the Wind Tunnel, Part II, Evaluation of Testing Techniques.* WADC TR 57-274, May 1957.

18. Fink, M.R. Carroll, J.B. *Hypersonic Static and Dynamic Stability of Wing-Fuselage Configurations.* United Aircraft Corporation Research Laboratory, C910188-17, January 1965.

19 Fink, M.R. *Hypersonic Dynamic Stability of Biconic Bodies.* United Aircraft Corporation, Report UAR-E20, March 12, 1966.

20. Fink, M.R. *Hypersonic Dynamic Stability of Sharp and Blunt Slender Cones.* United Aircraft Corporation Research Laboratory, Conn., UAR-C111, July 1964.

21. Fink, M.R. *A Shock-Expansion Method for Calculation of Hypersonic Dynamic Stability.* United Aircraft Corporation, Conn., C-910188-4, March 1964, AD 436 694.

22. Fink, M.R. Carroll, J.B. *Calculations of Hypersonic Dynamic Stability.* United Aircraft Corporation, Conn., C-910188-8, June 1964, AD 442 280.

23. Fischer, L.R. *Experimental Determination of the Effects of Frequency and Amplitude of Oscillation on the Roll-Stability Derivatives for a 60° Delta-Wing Airplane Model.* NASA TN D-232, March 1960.

24. Foster, D.J. Haynes, G.W. *Rotary Stability Derivatives from Distorted Models.* Journal of the Royal Aeronautical Society, Vol.60, September 1956, pp.623-624.

25. Gilmore, A. Seredinsky, V. MacKenzie, D. *Investigation of Dynamic Stability Derivatives of Vehicles Flying at Hypersonic Velocity.* Grumman Aircraft Engineering Corporation. ASD-TDR-62-460. September 1963, AD 421 874.

26. Grimes, J.H. Jr Casey, J.J. *Dynamic Stability Testing with Ablation at Mach 14 in a Long Duration Wind Tunnel.* Proceedings, AIAA Aerodynamic Testing Conference, Washington, DC, March 9-10, 1964.

27. Hall, G.Q. Osborne, L.A. *A Control Surface Oscillating Derivative Measurement Rig for Use with Half Wing Models Having Swept Hinge Lines.* Hawker-Siddeley Dynamics, Coventry, ARL TN 205.

28. Hall, G.Q. Osborne, L.A. *Supersonic Derivative Measurements on the Planforms of the MoA.* Flutter and Vibration Committee's First Research Programme. Hawker-Siddeley Dynamics, Coventry, ARL Report 63/10.

29. Hall, G.W.
Osborne, L.A. — *Transonic and Supersonic Derivative Measurements on the Planforms of the MoA.* Flutter and Vibration Committee's First Research Programme. Hawker-Siddeley Dynamics, Coventry, ARL Report 64/9.

30. Hoop, H.H. — *A Summary of Experimental Pitch Damping Coefficients for the Pershing Re-Entry Body.* AOMC RG-TM-61-49, December 19, 1961.

31. Holway, H.P.
Herrera, J.G.
Dayman, B. — *A Pneumatic Model Launcher for Free-Flight Testing in a Conventional Wind Tunnel.* TM 33-177, July 30, 1964.

32. Jaffe, P.
Prislin, R.H. — *Effect of Boundary Layer Transition on Dynamic Stability Over Large Amplitudes of Oscillation.* TR 32-841, March 7, 1966. AIAA Paper 64-427, Vol.3, No.1, June 1964. Spacecraft Journal, January 1966.

33. LaBerge, J.G. — *Dynamic Tests on a Cone in Hypersonic Helium Flow.* NAE Laboratory Memorandum (unpublished), March 1963.

34. LaBerge, J.G. — *Effect of Flare on the Dynamic and Static Moment Characteristics of a Hemisphere-Cylinder Oscillating in Pitch at Mach Numbers from 0.3 to 2.0.* National Research Council, Canada, Report LR-295, 1961.

35. Maloy, H.E. Jr — *A Method for Measuring Damping-in-Pitch of Models in Supersonic Flow.* BRL Report 1078, July 1959.

36. Molyneux, W.G. — *Measurement of the Aerodynamic Forces on Oscillating Aerofoils.* Aircraft Engineering, Vol.28, No.323, January 1956, pp.2-10.

37. Moore, J.A. — *Experimental Determination of Damping in Pitch of Swept and Delta Wings at Supersonic Mach Numbers.* NACA RM L57G10a, September 1957.

38. O'Neill, E.B. — *A Free-Flight Method for Studying the Dynamic Behavior of Missiles at Transonic Speeds.* Proceedings of Seventh Navy Symposium on Aeroballistics, 7-9 June 1956

39. Orlik-Ruckemann, K.J. — *A Method for Obtaining the Damping in Pitch and Yaw in a Supersonic Wind Tunnel, etc.* KTH F1 134, Stockholm, 1952.

40. Orlik-Ruckemann, K.J. — *A Method for Obtaining the Damping in Pitch Derivatives of Wings at Supersonic Speeds from Free Oscillation Tests with Half Models.* FFA Ae 273, Stockholm, 1952.

41. Orlik-Ruckemann, K.J. — *Measurement of Aerodynamic Damping and Stiffness Derivatives in Free Oscillation with Automatically Recycled Feedback Excitation.* National Research Council, Canada, LR-246, June 1959.

42. Orlik-Ruckemann, K.J. — *Quadratic Effects of Frequency on Aerodynamic Derivatives.* AIAA Journal, Vol. 2, No. 8, 1964, pp. 1507-1509.

43. Orlik-Ruckemann, K.J. — *Some Applications of the Free-Oscillation Techniques for Measuring Stability Derivatives.* Seminar on Wind-Tunnel Techniques and Aerodynamics, KTH, Stockholm, 1954.

44. Orlik-Ruckemann, K.J. Crowe, C. — *Comparison of Various Experimental and Theoretical Results for Static and Dynamic Longitudinal Stability Derivatives of Some Wing-Body Configurations at Supersonic Speeds.* National Research Council, Canada, Laboratory Report (to be published).

45. Orlik-Ruckemann, K.J. LaBerge, J.G. — *Oscillatory Experiments in a Helium Hypersonic Wind Tunnel.* National Research Council, Canada,. Report LR-335, 1962; also "Advances in Hypervelocity Techniques", Plenum Press, New York, 1962, pp. 187-210.

46. Orlik-Ruckemann, K.J. LaBerge, J.G. — *Static and Dynamic Longitudinal Stability Characteristics of a Series of Delta and Sweptback Wings at Supersonic Speeds.* National Research Council, Canada, LR-396, January 1966.

47. Platzer, M.F. Hoffman G.H. — *Quasi-Slender Body Theory for Slowly Oscillating Bodies of Revolution in Supersonic Flow.* NASA TN D-3440, June 1966.

48. Pope, T.C. Stalmach, C.J. Jr — *Preliminary Investigation of the Effects of Mass-Injection on Dynamic Stability at* M = 17 . Ling-Temco-Vought, LTV Report 2-59740-/3R-479, October 1963.

49. Pugh, P.G. Woodgate, L. — *Measurements of Pitching Moment Derivatives for Blunt Nosed Aerofoils Oscillating in Two-Dimensional Supersonic Flow.* ARC R&M 3315, 1963.

50. Scherer, M. — *Mesure des Dérivées Aérodynamiques en Ecoulement Transsonique et Supersonique.* Communication présentée au IVème Congrés Aéronautique Européen à Cologne. ONERA publication No. 104, Septembre 1960.

51. Scruton, C. Woodgate, L. Lapworth, K.C. — *Measurement of Pitching Moment Derivatives for Aerofoils Oscillating in Two-Dimensional Supersonic Flow.* ARC R&M 3234, 1962.

52. Scruton C. Woodgate, L. Maybrey, J.F. — *Measurement of the Pitching Moment Derivatives for Rigid Tapered Wings of Hexagonal Planform Oscillating in Supersonic Flow.* ARC R&M 3294, 1962.

53. Scruton, C. et al. — *Measurements of the Pitching Moment Derivatives for Rigid Wings of Rectangular Planform Oscillating About the Wing-Chord Axis in Supersonic Flow.* ARC CP 594, 1962.

54. Seredinsky, V. — *Derivation and Application of Hypersonic Newtonian Impact Theory to Wedges, Cones and Slab Wings Including the Effects of Angle of Attack, Shielding and Bluntness.* Grumman Aircraft Engineering Corporation, Report XAR-A-42, April 1962.

55. Shantz, I. — *The Measurements of Damping-in-Pitch in the NOL Wind Tunnels.* Presented at the Fourth Navy Symposium on Aeroballistics, Naval Proving Ground, Dahlgren, Virginia, 1957.

56. Shantz, I. Groves, R.T. — *Dynamic and Static Stability Measurements of the Basic Finner at Supersonic Speeds.* NAVORD Report 4516, January 1960.

57. Sibley, G.O. — *Dynamic Stability Tests of AGARD Models HB-1 and HB-2 in a Blowdown Tunnel at Mach 5.4.* VKI PR 65-141, June 1965.

58. Smith, T.L. — *Dynamic Stability Measurements.* BRL M 1352, June 1961.

59. Stalmach, C.J. Jr Cooksey, J.M. — *Simulation of Rocket Power Effect on Vehicle Stability and Measurements of Aerodynamic Damping in a Hypervelocity Wind Tunnel.* IAS Paper 62-24, presented at the 30th Annual IAS Meeting, New York, January 1962 Also published in Aerospace Engineering, Vol.21, No.3, 1962.

60. Stalmach, C.J. Jr Moore, D.R. Lindsey, J.L. — *Stability Investigation During Simulated Ablation in a Hypervelocity Wind Tunnel, Including Phase Control.* Sing-Temco-Vought, LTV Report 2-59740/5R-2192, April 1965.

61. Thompson, J.S. Fail, R.A. — *Oscillatory Derivative Measurements on Sting-Mounted Wind-Tunnel Models: Method of Test and Results for Pitch and Yaw on a Cambered Ogee Wing at Mach Numbers up to 2.6.* RAE Report Aero 2668, 1962; also ARC R&M 3355.

62. Thompson, J.S. Fail, R.A. — *Measurements of Oscillatory Derivatives at Mach Numbers up to 2.6 on a Model of a Supersonic Transport Design Study (Bristol Type 198).* RAE Technical Report 64,048, 1964; also ARC CP 815.

63. Thompson, J S. Fail, R.A. — *Oscillatory Derivative Measurements on Sting-Mounted Wind Tunnel Models at RAE Bedford.* RAE Technical Report 66,197, 1966.

64. Tobak, M. — *Damping in Pitch of Low-Aspect-Ratio Wings at Subsonic and Supersonic Speeds.* NACA RM A52L04a, April 1953.

65. Tobak, M. Reese, D.E. Jr Mean, B.H. — *Experimental Damping in Pitch of 45° Triangular Wings.* NACA RM A50J26, 1950.

66. van de Vooren, A.I. — *Measurements of Aerodynamic Forces on Oscillating Aerofoils.* NLL Report MP 100, May 1954. Presented at the 5th Meeting of the AGARD Wind Tunnel and Model Testing Panel, Scheveningen, Netherlands, May 1954.

67. Vaucheret, X. — *Dépouillement d'Oscillations Libres d'un Corps de Rentrée Présentant un Cycle Limite.* (Processing the Free Oscillations of a Re-Entry Body Presenting a Limit-Cycle.) La Recherche Aérospatiale, No. 104, 1965.

68. Vaucheret, X. — *Méthode Pratique de Dépouillements d'Oscillations Libres à un Degré de Liberté, en Présence d'une Force de Rappel Discontinue.* (Practical Processing Method for One-Degree-of-Freedom Free-Oscillations with a Discontinuous Restraining Force.) La Recherche Aérospatiale, No. 89, 1962.

69. Vaucheret, X. — *Stabilité Dynamique sur Maquettes d'Avions par la Méthode des Oscillations Libres.* Presented at AGARD Fluid Mechanics Panel, Cambridge, September 1966.

70. Walchner, O.; Sawyer, F.M.; Koob, S.J. — *Dynamic Stability Testing in a Mach 14 Blowdown Wind Tunnel.* Journal of Spacecraft and Rockets, Vol. 1, No. 4, 1964, pp. 437-439.

71. Walker, H.J.; Ballantyne, Mary B. — *Pressure Distribution and Damping in Steady Pitch at Supersonic Mach Numbers of Flat Swept-Back Wings Having All Edges Subsonic.* NACA TN 2197, October 1950.

72. Wehrend, W.R. Jr — *An Experimental Evaluation of Aerodynamic Damping Moments of Cones with Different Centers of Rotation.* NASA TN D-1768, March 1963.

73. Welsh, C.J.; Clemens, P.L. — *A Small-Scale Forced-Oscillation Dynamic Balance System.* AEDC-TN-58-12, June 1958. AD 157 143.

74. Wiley, H.G. — *The Significance of Nonlinear Damping Trends Determined for Current Aircraft Configurations* Presented at the AGARD Flight Mechanics Panel, Cambridge, England, September 20-23, 1966

75. Woodgate, L.; Maybrey, J.F.M.; Scruton, C. — *Measurements of the Pitching Moment Derivatives for Rigid Tapered Wings of Hexagonal Planform Oscillating in Supersonic Flow.* ARC R&M 3294, 1963.

76. Wright, B.R.; Kilgore, R.A. — *Aerodynamic Damping and Oscillatory Stability in Pitch and Yaw of Gemini Configurations at Mach Numbers from 0.50 to 4.63* NASA TN D-3334, March 1966.

Derivatives Due to Yaw and Rate of Yaw

1. Fisher, L.R.
   Fletcher, H.S.
   Effect of Lag of Sidewash on the Vertical-Tail Contribution to Oscillatory Damping in Yaw of Airplane Models. NACA TN 3356, January 1955.

2. Fisher, L.R.
   Wolhart, W.D.
   Some Effects of Amplitude and Frequency on the Aerodynamic Damping of a Model Oscillating Continuously in Yaw. NACA TN 2766, September 1952.

3. Malvestuto, F.S. Jr
   Theoretical Supersonic Force and Moment Coefficients on a Sideslipping Vertical-and Horizontal-Tail Combination with Subsonic Leading Edges and Supersonic Trailing Edges. NACA TN 3071, March 1954.

4. Margolis, K.
   Bobitt, P.J.
   Theoretical Calculations of the Pressures, Forces, and Moments at Supersonic Speeds Due to Various Lateral Motions Acting on Thin Isolated Vertical Tails. NACA Report 1268, 1956.

5. Margolis, K.
   Elliott, M.H.
   Theoretical Calculations of the Pressures, Forces, and Moments Due to Various Lateral Motions Acting on Tapered Sweptback Vertical Tails with Supersonic Leading and Trailing Edges. NASA TN D-383, August 1960.

6. Margolis, K.
   Sherman, W.L.
   Hannah, M.E.
   Theoretical Calculation of the Pressure Distribution, Span Loading, and Rolling Moment Due to Sideslip at Supersonic Speeds for Thin Sweptback Tapered Wings with Supersonic Trailing Edges and Wing Tips Parallel to the Axis of Wing Symmetry. NACA TN 2898, February 1953.

7. Martin, J.C.
   Malvestuto, F.S. Jr
   Theoretical Forces and Moments Due to Sideslip of a Number of Vertical Tail Configurations at Supersonic Speeds. NACA TN 2412, September 1951.

8. Purser, P.E.
   An Approximation to the Effect of Geometric Dihedral on the Rolling Moment Due to Sideslip for Wings at Transonic and Supersonic Speeds. NACA RM L52B01, April 1952.

9. Queijo, M.J.
   et al.
   Preliminary Measurements of the Aerodynamic Yawing Derivatives of a Triangular, a Swept, and an Unswept Wing Performing Pure Yawing Oscillations, with a Description of the Instrumentation Employed. NACA RM L55L14, April 1956.

10. Robinson, A.
    Hunter-Tod, J.H.
    The Aerodynamic Derivatives with Respect to Sideslip for a Delta Wing with Small Dihedral at Zero Incidence at Supersonic Speeds. ARC R&M 2410, December 1947, ARC 11,322.

11. Sherman, W.L.
Margolis, K. *Theoretical Calculations of the Effects of Finite Sideslip at Supersonic Speeds on the Span Loading and Rolling Moment for Families of Thin Sweptback Tapered Wings at an Angle of Attack.* NACA TN 3046, November 1953.

Magnetic Suspension for Aerodynamic Testing

1. *Magnetic Suspension of Wind Tunnel Models.* The Engineer, Vol. 210, No. 5463, October 7, 1960, pp. 607-608.

2. *Magnetic Suspension Replaces Mechanical Support of Wind Tunnel Models.* Electronic Design News, Vol. 6, No. 7, July 1961, pp. 13-15.

3. Baron, L.A. *The Design and Construction of an Automatic Control System for a Wind-Tunnel Magnetic Suspension System.* MIT Thesis, Massachusetts Institute of Technology, Cambridge, Mass., June 1960.

4. Clemens, P.L.
Cortner, A.H. *Bibliography: The Magnetic Suspension of Wind Tunnel Models.* AEDC-TDR-63-20, February 1963, AD296400.

5. Chrisinger, J.E. *An Investigation of the Engineering Aspects of a Wind Tunnel Magnetic Suspension System.* MIT Thesis, MIT TR 460, May 1959, AD 221294.

6. Chrisinger, J.E.
et al. *Magnetic Suspension and Balance System for Wind Tunnel Application.* Journal of the Royal Aeronautical Society, Vol. 67, No. 635, November 1963, pp. 717-724.

7. Copeland, A.B.
Covert, E.E.
Stephens, T. *Recent Advances in the Development of a Magnetic Suspension and Balance System for Wind Tunnels (Part III).* ARL-65-114, June 1965.

8. Copeland, A.B.
Tilton, E.L. III *The Design of Magnetic Models for Use in a Magnetic Suspension and Balance System for Wind Tunnels.* ARL-65-113, June 1965.

9. Covert, E.E.
et al. *Recent Advances in the Development of a Magnetic Suspension and Balance System for Wind Tunnels (Part II).* ARL-64-36, March 1964.

10. Covert, E.E.
Tilton, E.L. III *Calibration of a Magnetic Balance System for Drag, Lift, and Pitching Moment.* Massachusetts Institute of Technology, Aerophysics Laboratory, Cambridge, Mass., May 1963.

11. Covert, E.E.
Tilton, E.L. III *Further Evaluation of a Magnetic Suspension and Balance System for Application to Wind Tunnels.* ARL-63-226, December 1963, AD 427 810.

12. Covert, E.E.
Tilton, E.L. III
Recent Advances in the Development of a Magnetic Suspension and Balance System for Wind Tunnels. ARL-63-235, December 1963.

13. Desmet, E.
Suspension Magnétique ONERA – Essai d'Application a l'Etude des Oscillations de Lacet d'un Corps Fusele. (The ONERA Magnetic Suspension System – Test of Application to the Study of Oscillations of a Body in Yaw.) ONERA NT 10/1579 AP, Office National d'Etudes et de Recherches Aéronautiques, Chatillonsous-Bagneux (Seine), Paris, France.

14. Desmet, E.
Rosset,
Characteristiques et Notice d'Emploi de la Suspension Magnétique Destinée aux Soufflerles S.19 et S.8. (Characteristics and Review of the Use of the Magnetic Suspension System Intended for Wind Tunnels S.19 and S.8.) ONERA NT 9/1579 AP, Office National d'Etudes et de Recherches Aéronautiques, Chatillon-sous-Bagneux (Seine), Paris, France.

15. Fosque, H.S.
Miller, G.H.
An Electromagnetic Support Arrangement with Three-Dimensional Control, Part II: Experimental. Report UVA/ORL-04-58-TR-3, Presented at 4th Conference on Magnetism and Magnetic Materials, Philadelphia, Pennsylvania, November 17-20, 1958.

16. Hensel, R.W.
Recent Developments in Wind-Tunnel Testing Techniques at Transonic and Supersonic Speeds. Journal of Spacecraft and Rockets, Vol.1, No.5, September-October 1964, pp.449-463, also AEDC-TR-65-75, June 1965.

17. Jenkins, A.W. Jr
Parker, H.M.
An Electromagnetic Support Arrangement with Three-Dimensional Control, Part I: Theoretical. Report UVA/ORL-04-58-TR-1, Presented at 4th Conference on Magnetism and Magnetic Materials, Philadelphia, Pennsylvania, November 17-20, 1958.

18. Laurenceau, P.
Etude, Réalisation et Mise au Point d'une Suspension de Maquette Aérodynamique par Action Magnétique pour une Petite Soufflerie. (Design, Construction and Operation of a Magnetic Suspension System for Aerodynamic Models in a Small Wind Tunnel.) ONERA NT 2/1579 AP, Office National d'Etudes et de Recherches Aéronautiques, Chatillon-sous-Bagneux (Seine), Paris, France.

19. Laurenceau, P.
La Suspension Magnetique des Maquettes. (The Magnetic Suspension of Models.) ONERA Discussion Technique AP, Office National d'Etudes et de Recherches Aéronautiques, Chatillon-sous-Bagneux (Seine), Paris, France, Juin 1956.

20. Laurenceau, P.
Desmet, E.
Adaptation de la Suspension Magnétique des Maquettes aux Soufflerie s S.19 et S.8. (Adaptation of the Magnetic Suspension of Models to Wind Tunnels S.19 and S.8.) ONERA NT 7/1579 AP, Office National d'Etudes et de Recherches Aéronautiques, Chatillon-sous-Bagneux (Seine), Paris, France, Janvier 1957.

21. Matheson, L.R.
Some Considerations for Design and Utilization of Magnetic Suspension. Aerodynamics Fundamental Memo No.84, General Electric Missile and Space Vehicle Department, Philadelphia, Pennsylvania, May 1959.

22. Mirande, J.
Mesure de la Résistance d'un Corps de Révolution, à $M_0 = 2.4$ *, au Moyen de la Suspension Magnétique ONERA.* (Measurement of the Drag of a Body of Revolution, at $M = 2.4$, by Means of the ONERA Magnetic Suspension System.) No.70, Office National d'Etudes et de Recherches Aéronautiques, Mai-Juin 1959, p.24.

23. Nelson, W.
Trachtenberg, A.
Grundy, A. Jr
An Apparatus for the Study of High Speed Air Flow Over a Freely Suspended Rotating Cylinder. WADC TR 57-338, AD 142127, December 1957.

24. Parker, H.M.
May, J.E.
Nurre, G.S.
An Electromagnetic Suspension System for the Measurement of Aerodynamic Characteristics. OSR-2294, AST-4443-106-62U, University of Virginia, Charlottesville, Virginia, March 1962.

25. Scott, J.E. Jr
May, J.E.
Laboratory Investigation of the Basic Nature of Low Density Gas Flow at High Speeds, Annual Report for the Period 1 January 1960 to 31 December 1960. University of Virginia, Charlottesville, Virginia, January 1960, AST-4435-109-61U.

26. Stephens, T.
Methods of Controlling the Roll Degree of Freedom in a Wind Tunnel Magnetic Balance, Part I: Production of Rolling Moments. ARL 65-242, December 1965.

27. Tilton, E.L.
et al.
The Design and Initial Operation of a Magnetic Model Suspension and Force Measurement System. ARL-63-16, August 1962.

28. Tilton, E.L.
Schwartz, S.
Static Tests on the Magnetic Suspension System. MIT AR Memo 399, Massachusetts Institute of Technology, Naval Supersonic Laboratory, Cambridge, Mass., July 1959.

29. Tournier, M.
Dieulesaint, E.
Laurenceau, P.
Etude, Réalisation et Mise au Point d'une Suspension de Maquette Aérodynamique par Action Magnétique pour une Petite Soufflerie. (Design, Construction and Operation of a Magnetic Suspension System for Aerodynamic Models in a Small Wind Tunnel.) ONERA NT 1/1579 AP, Office National d'Etudes et de Recherches Aéronautiques, Chatillon-sous-Bagneux (Seine), Paris, France.

30. Tournier, M.
Laurenceau, P.
Perfectionnements à la Suspension Magnétique des Maquettes. (Improvements in the Magnetic Suspension of Models.) ONERA NT 5/1579 AP, Office National d'Etudes Recherches Aéronautiques, Chatillon-sous-Bagneux (Seine), Paris, France, Decembre 1956.

31. Tournier, M.
Laurenceau, P.
Dubois, G.
La Suspension Magnétique ONERA. (The ONERA Magnetic Suspension System.) Conférence on Premier Symposium International sur l'Aérodynamique et l'Aérothermique des Gas Rarefiés, Nice, France, 2-5 Juillet 1958. Office National d'Etudes et de Recherches Aéronautiques, Chatillon-sous-Bagneux (Seine), Paris, France, Pergamon Press, London.

32. Zapata, R.N.
Dukes, T.
An Electromagnetic Suspension System for Spherical Models in a Hypersonic Wind Tunnel. Report 682, Gas Dynamics Laboratory, Princeton University, Princeton, New Jersey, July 1964.

Derivatives Due to Rate of Roll

1. Allwork, P.H.
Continuous Rotation Balance for Measurement of Yawing and Rolling Moments in a Spin. ARC R&M 1579, November 1933.

2. Bennett, C.V.
Johnson, J.L.
Experimental Determination of the Damping in Roll and Aileron Rolling Effectiveness of Three Wings Having 2°, 42°, and 62° Sweepback. NACA TN 1278, May 1947.

3. Boatright, W.B.
Wind-Tunnel Measurements of the Dynamic Cross Derivative $C_{lr} - C_{l\dot{\beta}}$. *(Rolling Moment Due to Yawing Velocity and to Acceleration in Sideslip) of the Douglas D-558-II Airplane and its Components at Supersonic Speeds Including Description of the Technique.* NACA RM L55H16, November 1955.

4. Bobbitt, P.J.
Linearized Lifting-Surface and Lifting-Line Evaluations of Sidewash Behind Rolling Triangular Wings at Supersonic Speeds. NACA Report 1301, 1957.

5. Bobbitt, P.J.
Malvestuto, F.S. Jr
Estimation of Forces and Moments Due to Rolling for Several Slender-Tail Configurations at Supersonic Speeds. NACA TN 2955, July 1953.

6. Brown, C.E.
Adams, M.C.
Damping in Pitch and Roll of Triangular Wings at Supersonic Speeds. NACA Report 892, 1948.

7. Brown, C.E.
Heinke, H.S. Jr
Preliminary Wind-Tunnel Tests of Triangular and Rectangular Wings in Steady Roll at Mach Numbers of 1.62 and 1.92. NACA TN 3740, June 1956.

8. Conlin, L.J.
Orlik-Ruckemann, K.J.
Comparison of Some Experimental and Theoretical Data on Damping-In-Roll of a Delta-Wing-Body Configuration at Supersonic Speeds. National Research Council, Canada, LR-266, December 1959.

9. Darling, J.
Roll Damping of the Spinner Finner Model at Mach 2.49. NAVORD Report 4502, 1958.

10. Evans, J.
Fink, P
Stability Derivatives – Determination of l_p by Free Oscillations. Australian Council for Aeronautics, Report ACA-34, April 1947.

11. Evans, J.
Fink, P
Stability Derivatives – Determination of l_p by Free Rolling. Australian Council for Aeronautics, Report ACA-35 May 1947.

12. Fra[illegible]s, [illegible]
Application of a Simplified Lifting-Surface Theory to the Prediction of the Rolling Effectiveness of Plain Spoiler Ailerons at Subsonic Speeds. NACA RM A54H26a, December 1954.

13. Goodman, A.
Adair, G.H.
Estimation of the Damping in Roll of Wings Throughout the Normal Flight Range of Lift Coefficient. NACA TN 1924, July 1949.

14. Goodman, A.
Fisher, L.R.
Investigation at Low Speeds of the Effect of Aspect Ratio and Sweep on Rolling Stability Derivatives of Untapered Wings. NACA Report 968, 1950.

15. Greene, J.E.
An Investigation of the Rolling Motion of Cruciform-Fin Configurations. NAVORD 6262, 1958.

16. Hannah, M.E.
Margolis, K.
Span Load Distributions Resulting from Constant Angle of Attack, Steady Rolling Velocity, Steady Pitching Velocity, and Constant Vertical Acceleration for Tapered Sweptback Wings with Streamwise Tips, Subsonic Leading Edges and Supersonic Trailing Edges. NACA TN 2831, December 1952.

17. Harmon, S.M.
Martin, J.C.
Theoretical Calculations of the Lateral Force and Yawing Moment Due to Rolling at Supersonic Speeds for Sweptback Tapered Wings with Streamwise Tips, Supersonic Leading Edges. NACA TN 2156, July 1950.

18. Harmon, S.M.
Jeffreys, I.
Theoretical Lift and Damping in Roll of Thin Wings with Arbitrary Sweep and Taper at Supersonic Speeds, Supersonic Leading and Trailing Edges. NACA TN 2114, May 1950.

19. Jones, A.L.
Alksne, A.
The Damping Due to Roll of Triangular, Trapezoidal, and Related Plan Forms in Supersonic Flow. NACA TN 1548, March 1948.

20. Lockwood, V.E.
Damping-In-Roll Characteristics of a 42.7 Sweptback Wing as Determined from a Wind-Tunnel Investigation of a Twisted Semispan Wing. NACA RM L9F15, August 1949.

21. Lomax, H.
Heaslet, M.A.
Damping-In-Roll Calculations for Slender Sweptback Wings and Slender Wing-Body Combinations. NACA TN 1950, September 1949.

22. MacLachlan, R.
Letko, W.
Correlation of Two Experimental Methods of Determining the Rolling Characteristics of Unswept Wings. NACA TN 1309, May 1947.

23. Margolis, K.
Theoretical Calculations of the Lateral Force and Yawing Moment Due to Rolling at Supersonic Speeds for Sweptback Tapered Wings with Streamwise Tips, Subsonic Leading Edges. NACA TN 2122, June 1950.

24. Martin, J.C.
Gerber, N.
On the Effect of Thickness on the Damping in Roll of Airfoils at Supersonic Speeds. BRL Report 843, January 1953.

25. Martina, A.P.
Method for Calculating the Rolling and Yawing Moments Due to Rolling for Unswept Wings With or Without Flaps or Ailerons by Use of Nonlinear Section Lift Data. NACA TN 2937, May 1953.

26. McDearmon, R.W.
Wind-Tunnel Investigation of the Damping in Roll of the Douglas D-558-II Research Airplane and Its Components at Supersonic Speeds. NACA RM L56F07. September 1956.

27. McDearmon, R.W.
Jones, R.A.
Wind-Tunnel Investigation of Damping in Roll at Supersonic Speeds of Triangular Wings at Angles of Attack. NACA RM L56F13a, September 1956.

28. Michael, W.H. Jr
Analysis of the Effects of Wing Interference on the Tail Contributions to the Rolling Derivatives. NACA Report 1086, 1952.

29. Pinsker, W.J.G.
A Semi-Empirical Method for Estimating the Rotary Rolling Moment Derivatives of Swept and Slender Wings. ARC CP 524, 1959.

30. Polhamus, E.C.
A Simple Method of Estimating the Subsonic Lift and Damping in Roll of Sweptback Wings. NACA TN 1862, April 1949.

31. Queijo, M.J.
Jaquet, B.M.
Calculated Effects of Geometric Dihedral on the Low-Speed Rolling Derivatives of Swept Wings. NACA TN 1732, October 1948.

32. Ribner, H.S. — *On the Effect of Subsonic Trailing Edges on Damping in Roll and Pitch of Thin Sweptback Wings in a Supersonic Stream.* NACA TN 2146, August 1950.

33. Sandahl, C.A.; Strass, H.K.; Piland, R.O. — *The Rolling Effectiveness of Wing-Tip Ailerons as Determined by Rocket-Powered Test Vehicles and Linear Supersonic Theory.* NACA RM L50F21, August 1950.

34. Scherrer, R.; Dennis, D.H. — *Damping in Roll of a Missile Configuration with a Modified Triangular Wing and a Cruciform Tail at a Mach Number of 1.52.* NACA RM A51A03, March 1951.

35. Shantz, I.; Schermerhorn, V.L. — *Roll Damping Moment Measurements for the Basic Finner at Subsonic and Supersonic Speeds.* NAVORD Report 6652, Unpublished.

36. Shue, G.L.; Long, J.E. — *A Technique of Measuring Damping in Roll and Rolling Moment of a Missile from Wind-Tunnel Investigations.* Proceedings of the Bureau of Ordnance Symposium on Aeroballistics, NAVORD R-1651, November 1950.

37. Tucker, W.A.; Piland, R.O. — *Estimation of the Damping in Roll of Supersonic Leading Edge Wing-Body Combinations.* NACA TN 2151, July 1950.

38. Walker, H.J.; Ballantyne, Mary B. — *Pressure Distribution and Damping in Steady Roll at Supersonic Mach Numbers of Flat Swept-Back Wings with Subsonic Edges.* NACA TN 2047, March 1950.

Magnus Force

1. Ahlborn, F. — *Der Magnus Effekt in Theorie and Wirklichkeit.* Zeitschrift fur Fluztechnik und Motor Luftschiffahrt, December 28, 1929, pp.642-653, (Translated in NACA TM 567.)

2. Benton, E.R. — *Aerodynamic Origin of the Magnus Effect on a Finned Missile.* Ph.D thesis presented to the Division of Engineering and Applied Physics of Harvard University, Cambridge, Mass., December 1960.

3. Betz, A. — *Der Magnus Effekt, die Grundlaze der Flettnerwalze.* Zeitschrift des Versins Deutscher Ingenieure, January 3, 1925. (Translated in NACA TM 310, April 1925.)

4. Bolz, R.E. — *Dynamic Stability of a Missile in Rolling Flight.* Journal of the Aeronautical Sciences, Vol.19, No.6, June 1952, pp.395-403.

5. Buford, W.E. — *Magnus Effect in the Case of Rotating Cylinders and Shell.* BRL MR 821, July 1954.

6. DeGrafft, W.E. — *Wind Tunnel Investigation of the Forces and Moments Acting on a Cruciform Finned Model with Fixed and Freely Spinning Tail Assemblies at a Mach Number of 2.0.* NOL TR-63-79, April 1963.

7. Fowler, R.H. et al. — *The Aerodynamics of a Spinning Shell.* Phil. Trans. Roy. Soc. of London, Vol.221, December 3, 1920, pp.295-387.

8. Greene, J.E. — *Static Stability and Magnus Characteristics of the 5-Caliber and 7-Caliber Army-Navy Spinner Rocket at Low Subsonic Speeds.* NAVORD Report 3884, 1954.

9. Hall, R.T. — *The Lift and Drag on a Rotating Cylinder in Supersonic Crossflow.* NAVORD Report 6039, January 1960, AD 232 567.

10. Heald, R.H. et al. — *Aerodynamic Characteristics of a Rotating Model of the 5.0-Inch Spin-Stabilized Rocket Model 32.* BuOrd TN 37, June 1957.

11. Kelly, H.R. — *An Analytical Method for Predicting the Magnus Forces and Moments on Spinning Projectiles.* NOTS-TM-1634, August 1954, AD 40 564.

12. Kelly, H.R. Thacker, G.R. — *The Effect of High Spin on the Magnus Force on a Cylinder at Small Angles of Attack.* NAVORD Report 5036, February 1956.

13. Kert, R.H. — *An Elementary Treatment of the Motion of a Spinning Projectile About its Center of Gravity.* BRL Report 85, 1937.

14. Krahn, E. — *Magnus Effects on Cylinders in Cross Flow.* Presented at the Fourth Navy Symposium on Aeroballistics, Naval Proving Ground, Dahlgren, Virginia, 1957.

15. Luchuk, W. Sparks, W. — *Wind Tunnel Magnus Characteristics of the 7-Caliber Army-Navy Spinner Rocket.* NAVORD Report 3813, 1954.

16. Murphy, C.H. Jr — *Criteria for the Generalized Dynamic Stability of a Rolling Symmetric Missile.* Journal of the Aeronautical Sciences, Vol.24, October 1957, Readers' Forum, pp.773-774.

17. Platou, A.S. — *The Magnus Force on a Rotating Cylinder in Transonic Cross Flows.* BRL Report 1150, September 1961.

18. Platou, A.S. Steinberg, J. — *The Magnus Characteristics of a 30 mm Aircraft Bullet.* BRL R 994, September 1956.

19. Purser, P.E.
Stevens, J.E.
Exploratory Rocket Flight Tests to Investigate the Use of a Freely Spinning Monoplane Tail for Stabilizing a Body. NACA RM L52I05a, October 1952.

20. Regan, F.J.
Horanoff, E.V.
Wind Tunnel Magnus Measurements at the Naval Ordnance Laboratory. AIAA Paper 66-753, AIAA Aerodynamic Testing Conference, September 21-23, 1966.

21. Sieron, T.R.
On the "Magnus Effects" of an Inclined Spinning Shell at Subsonic and Transonic Speeds. WADD Technical Report 60-212, 1960.

22. Sieron, T.R.
The Magnus Characteristics of the 20 mm and 30 mm Projectiles in the Trisonic Speed Range. WADC Technical Note 59-520, October 1959.

23. Stone, G.W.
The Magnus Instability of a Sounding Rocket. AIAA Paper No. 66-62, AIAA 3rd Aerospace Sciences Meeting, New York, January 24-26, 1966.

24. Thorman, H.C.
Boundary Layer Measurements on an Axisymmetric Body with Spin and Yaw. Guggenheim Aeronautical Laboratory, California Institute of Technology, Report on Army Contract DA-04-495-ORD-481, November 1957.

25. Wolff, E.B.
Koning, C.
Tests for Determining the Effect of a Rotating Cylinder Fitted into the Leading Edge of an Airplane Wing. NACA TM 354, March 1926.

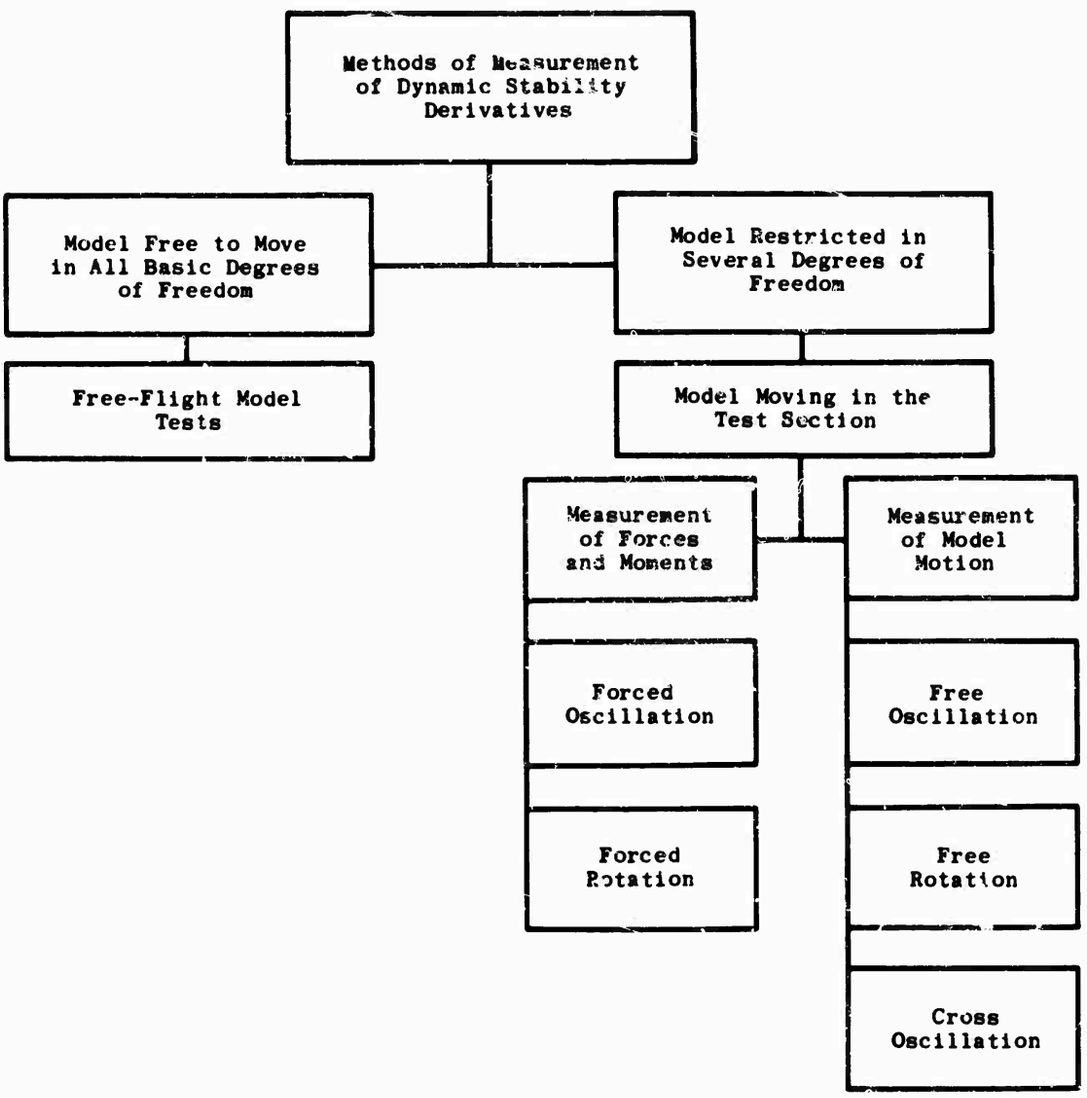

Fig. 1 Methods of measuring dynamic stability derivatives

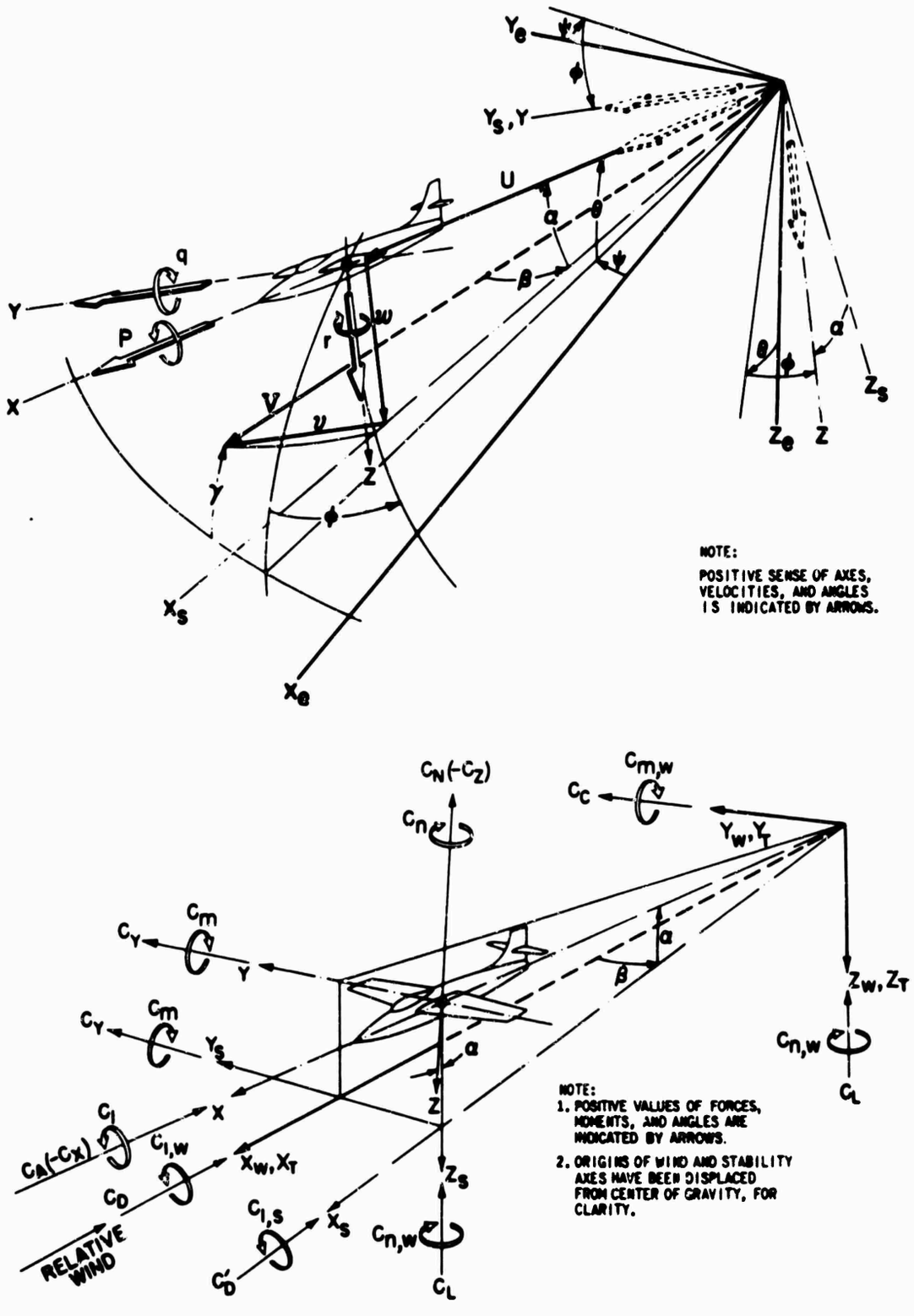

Fig. 2 Axes systems

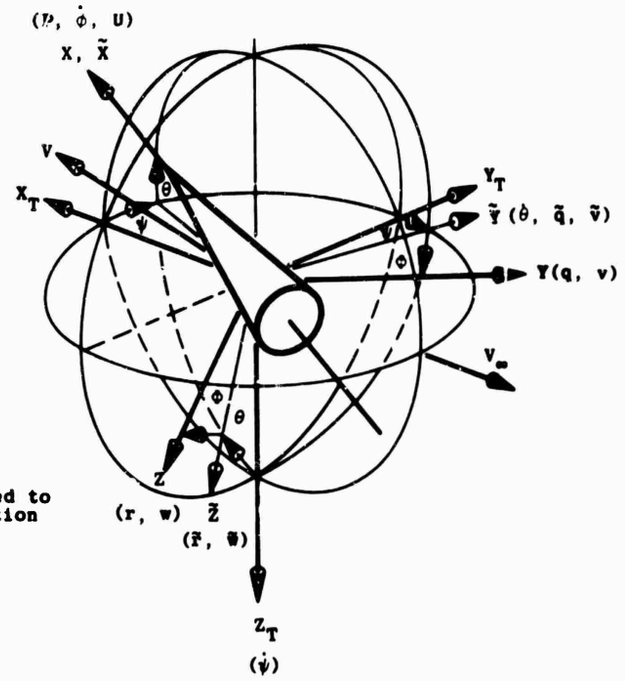

Note: Model Orientation Referenced to the Symmetric Flight Condition

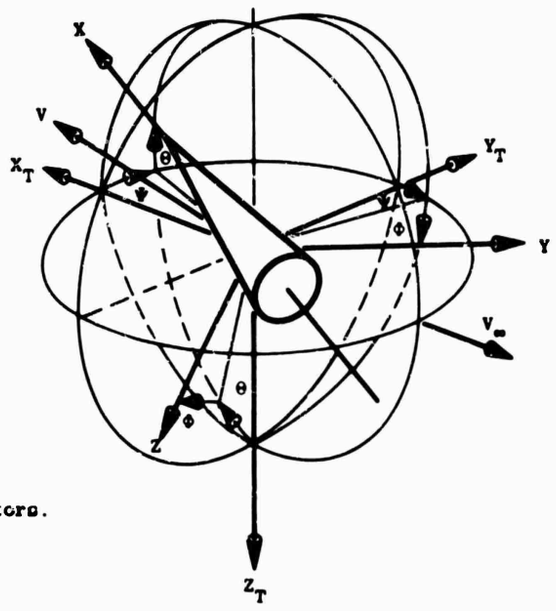

Note: Quantities given in parenthesis are vectors.

Fig. 3 Orientation of coordinate systems

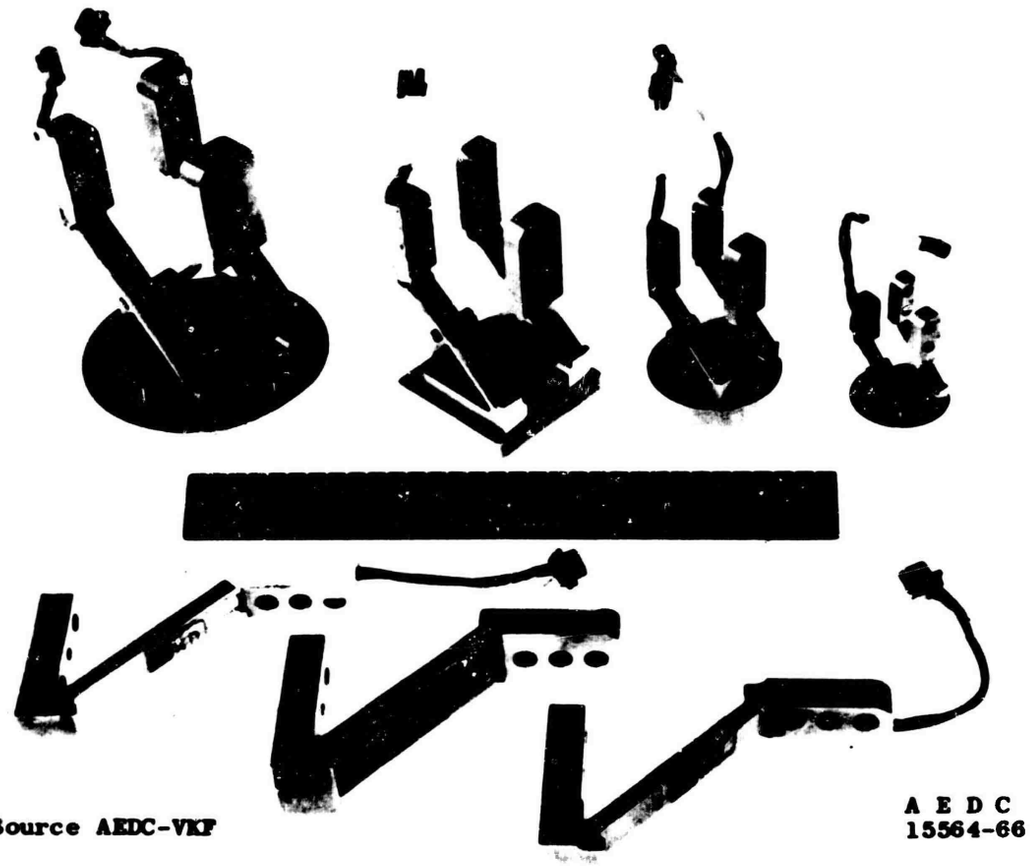

Fig. 4 Multipiece crossed flexures

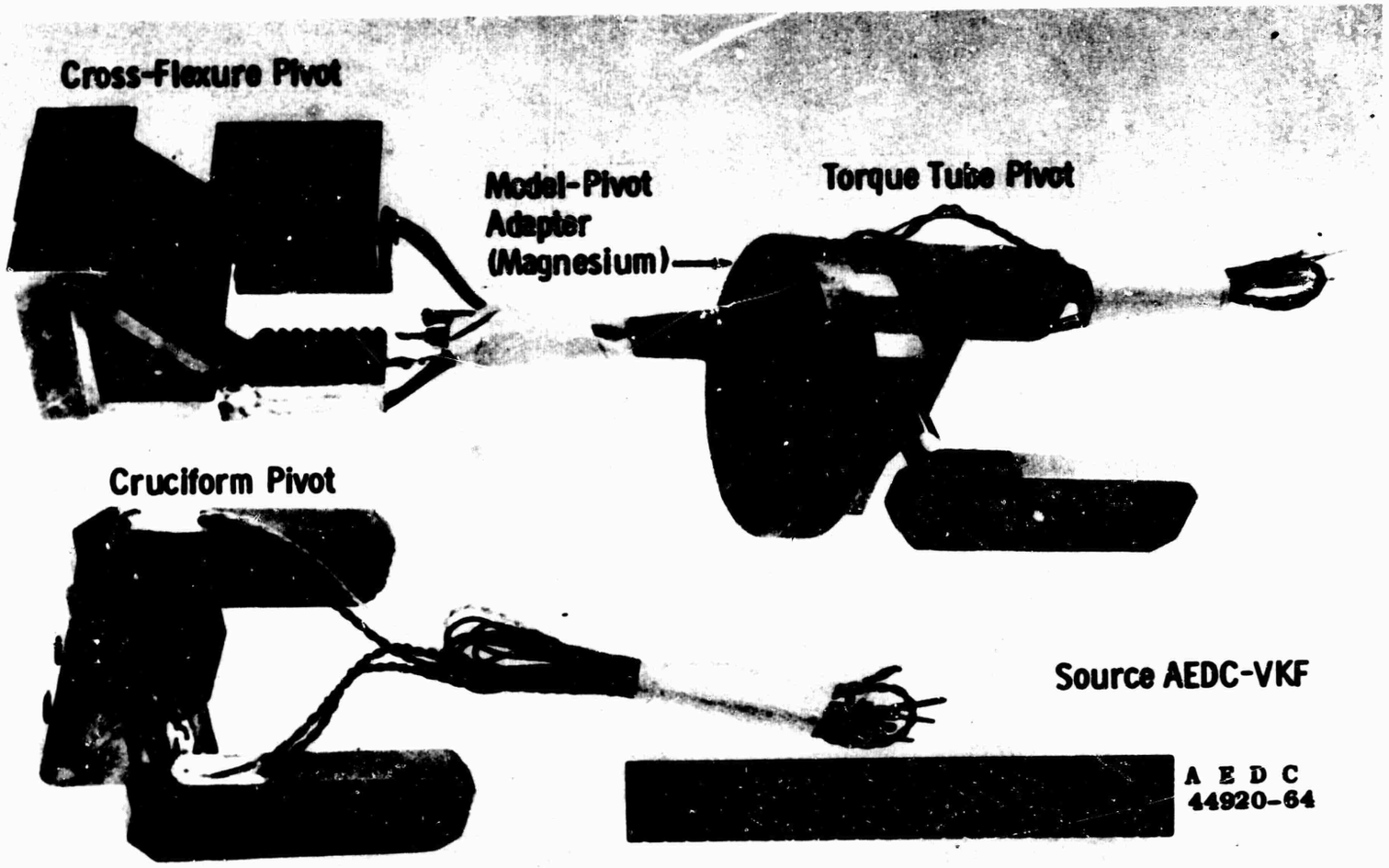

Fig. 5 Cross-flexure, cruciform and torque tube pivots

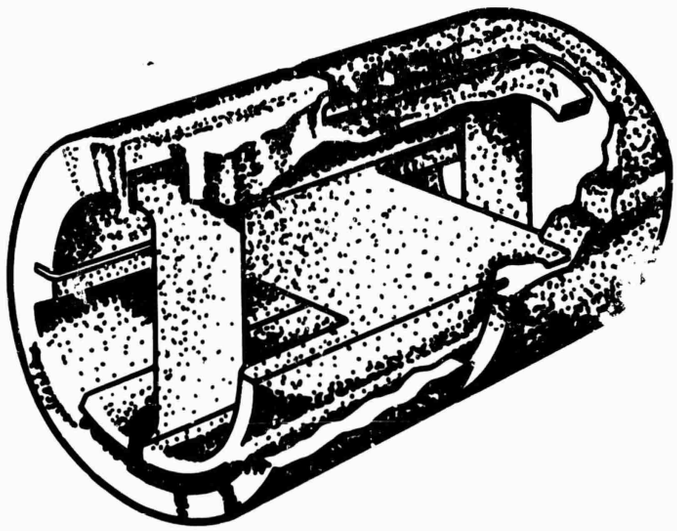

Cantilever Support

All dimensions are in inches.

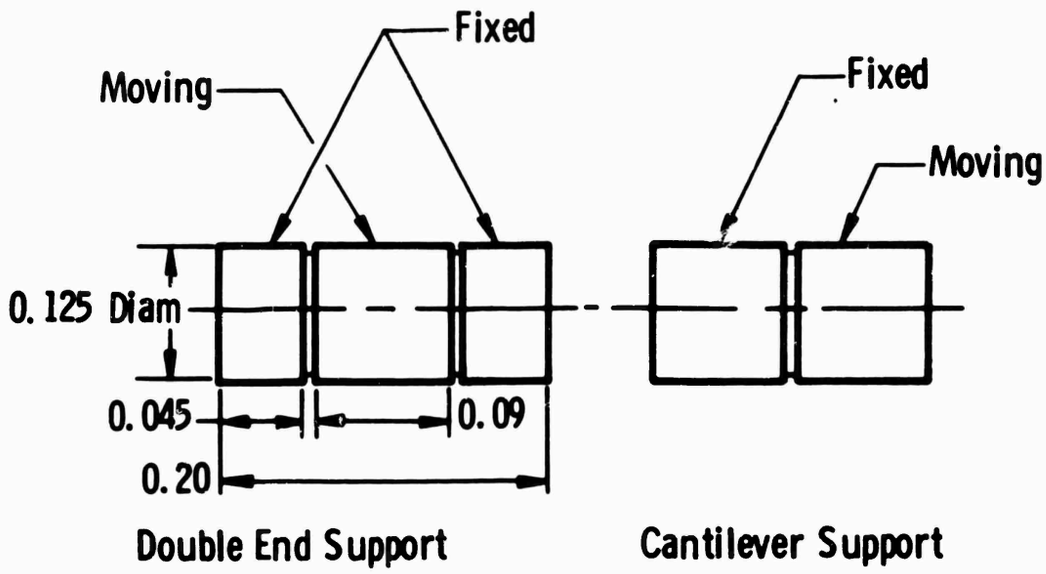

Fig.6 Small scale instrument flexure pivot

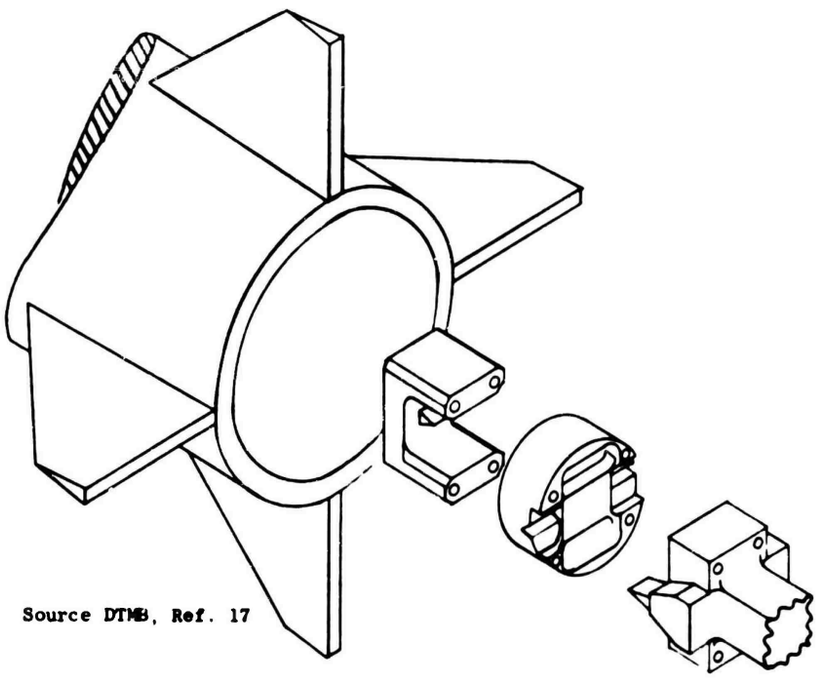

Fig. 7 Knife edge pivot

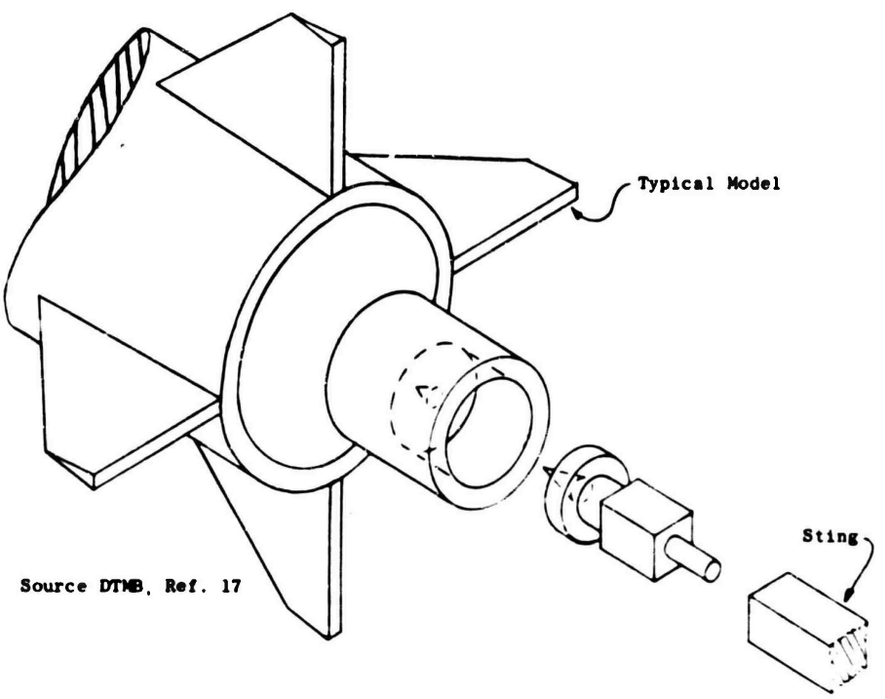

Fig. 8 Cone pivot - three degrees of freedom

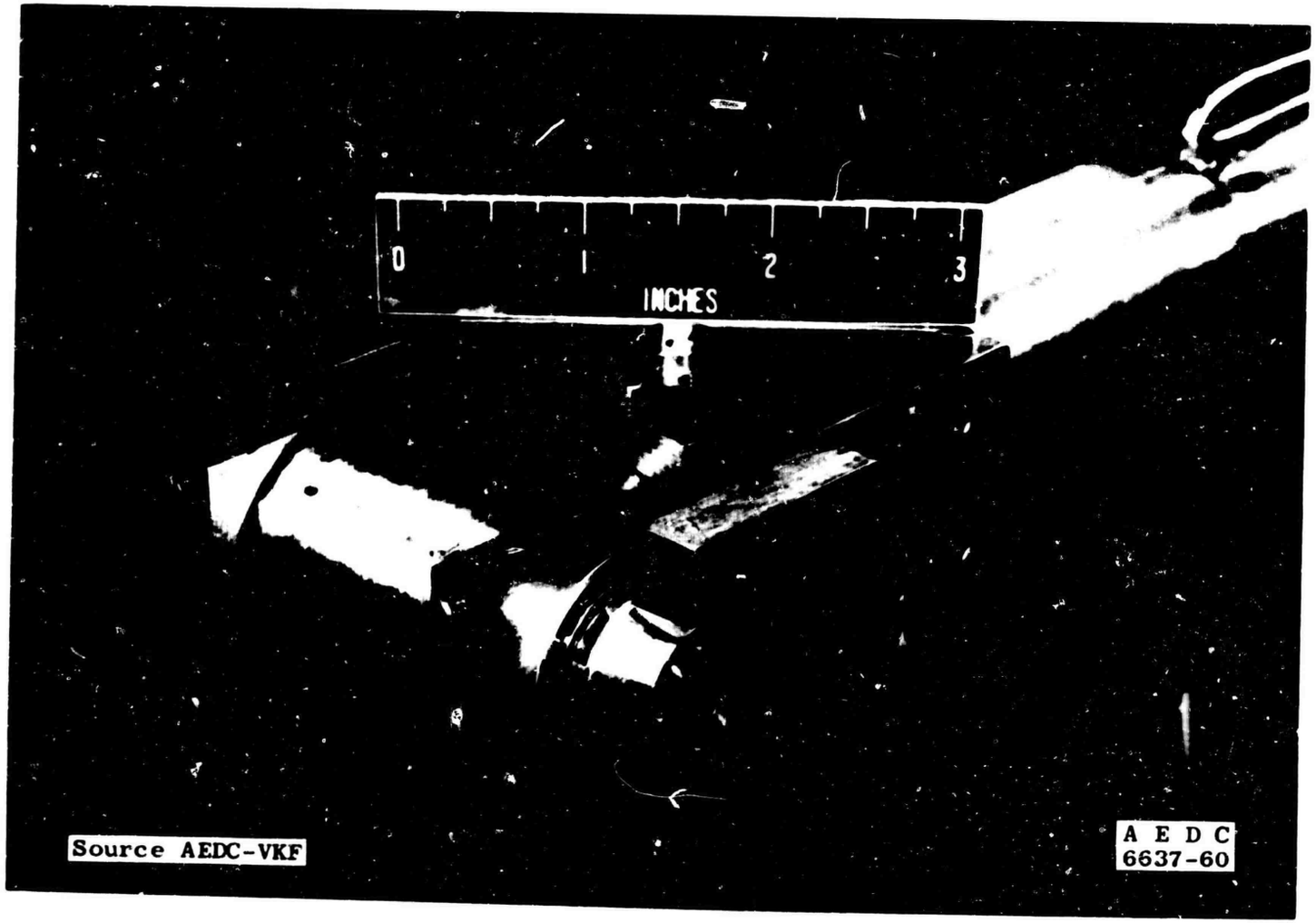

Fig. 9 Ball bearing pivot

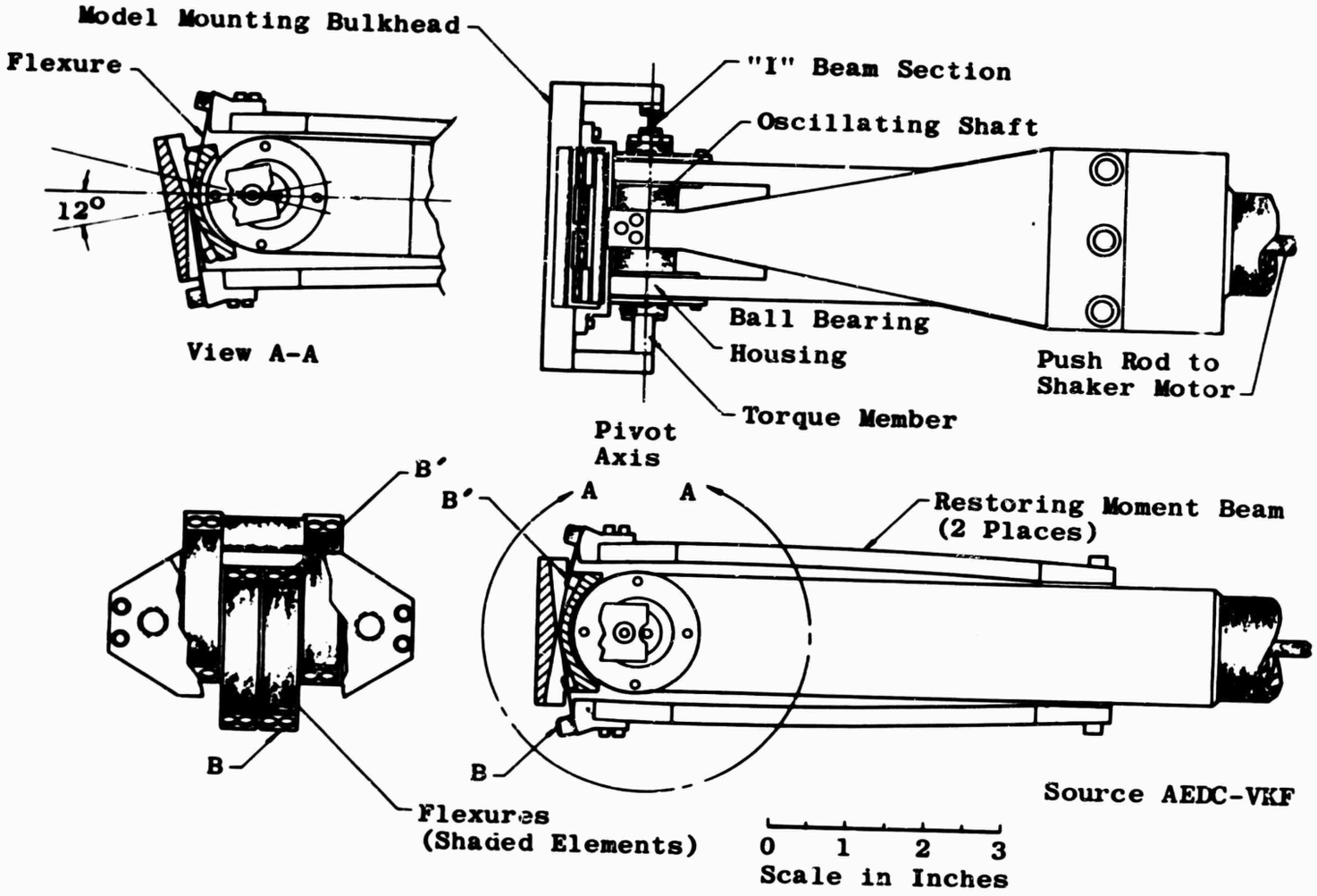

Fig. 10 High amplitude forced oscillation balance with ball bearing pivot

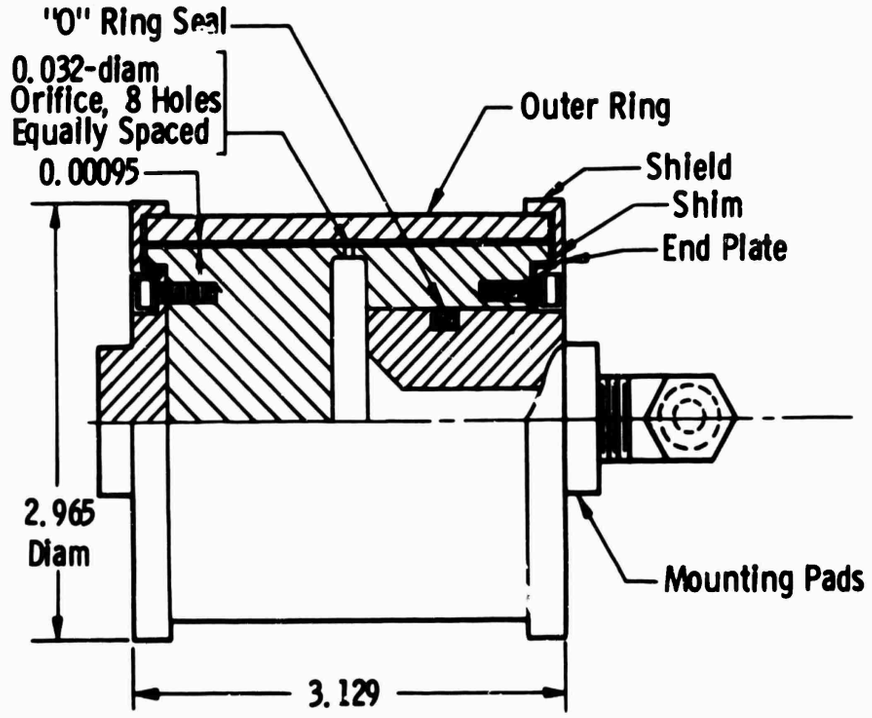

All dimensions are in inches.

Source AEDC-VKF, Ref. 19

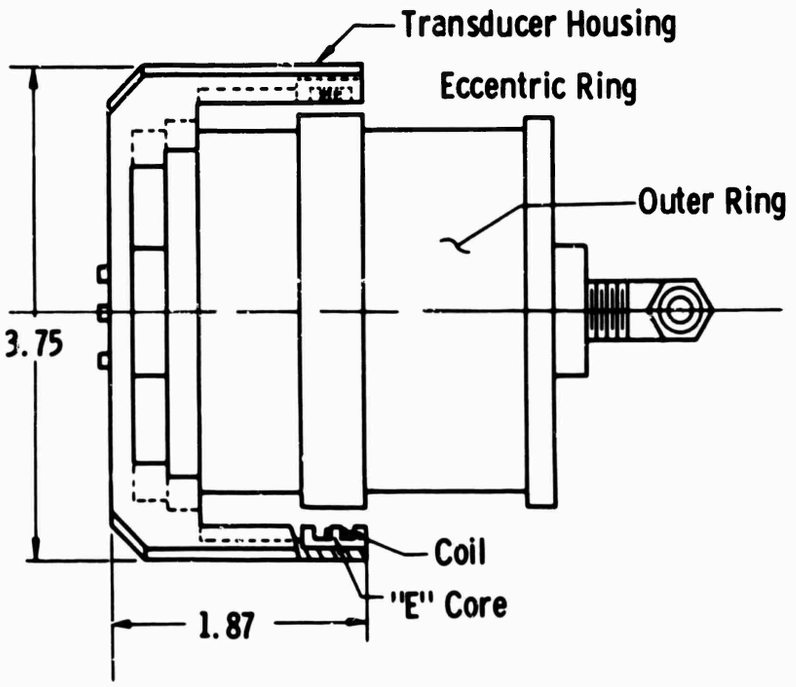

Fig. 11 Gas bearing pivot

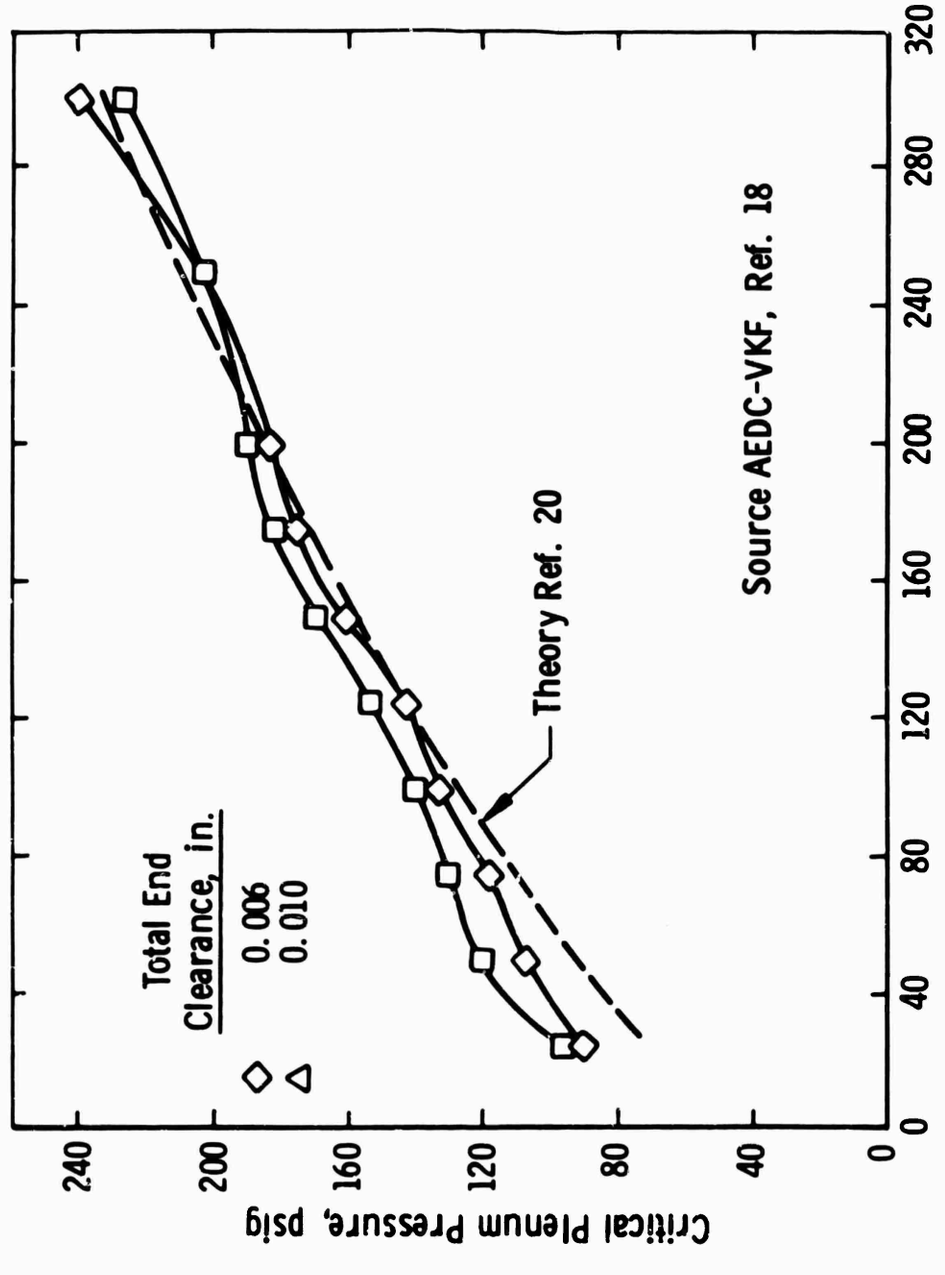

Fig. 12 Gas bearing load characteristics

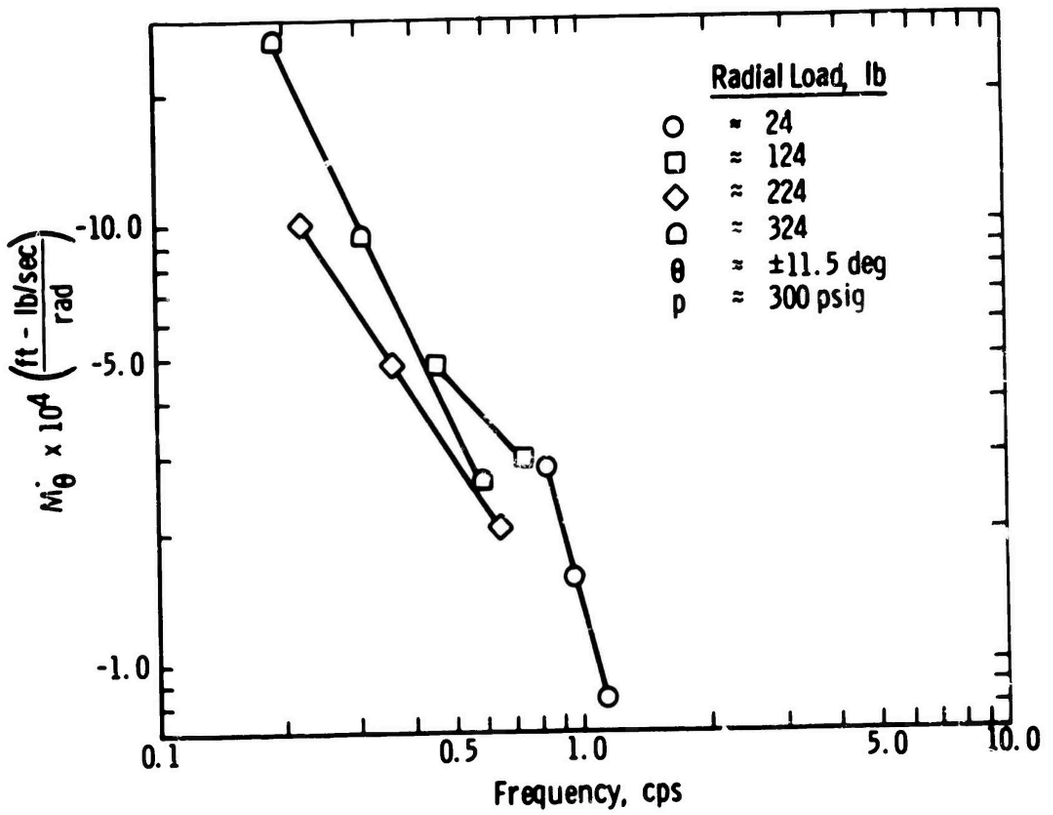

Source AEDC-VKF, Ref. 18

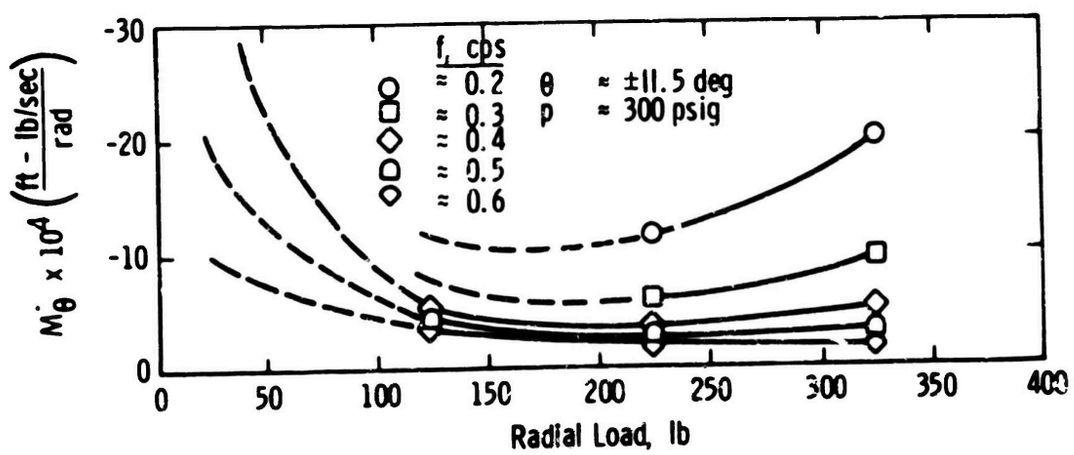

Fig. 13 Damping characteristics of AEDC-VKF gas bearing

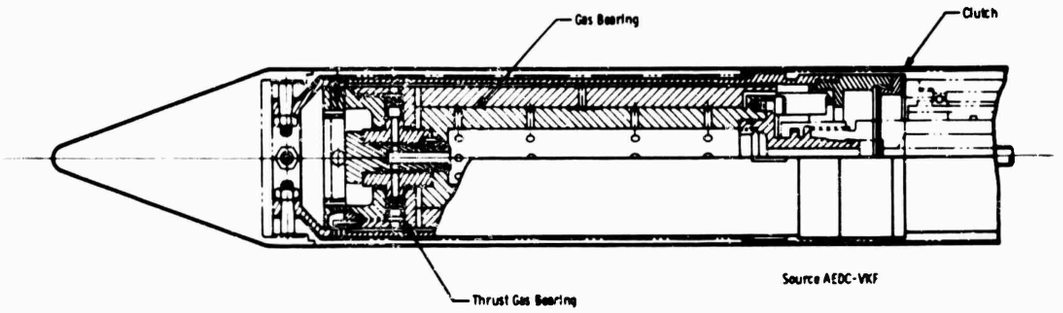

Fig. 14 Gas bearing for roll-damping system

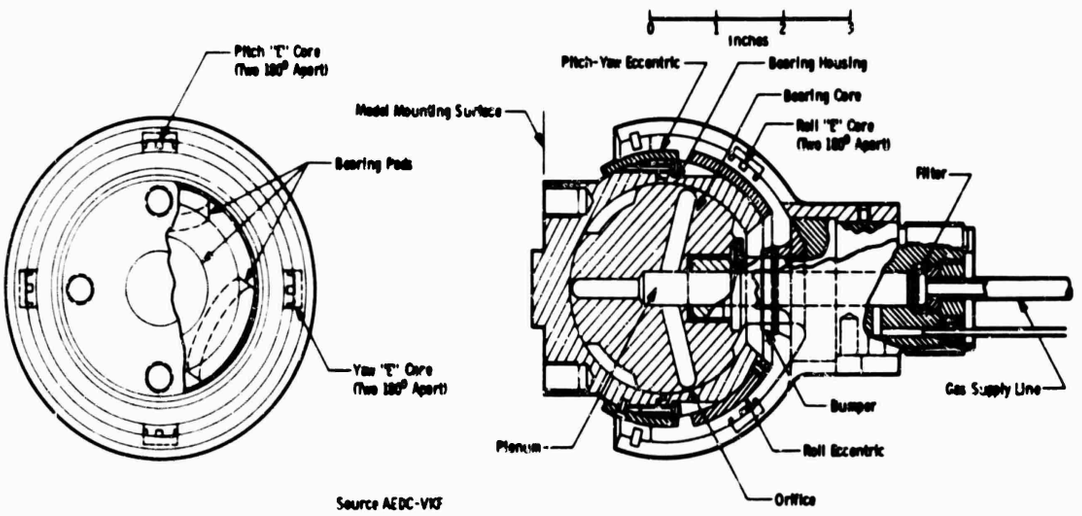

Fig. 15 Spherical gas bearing

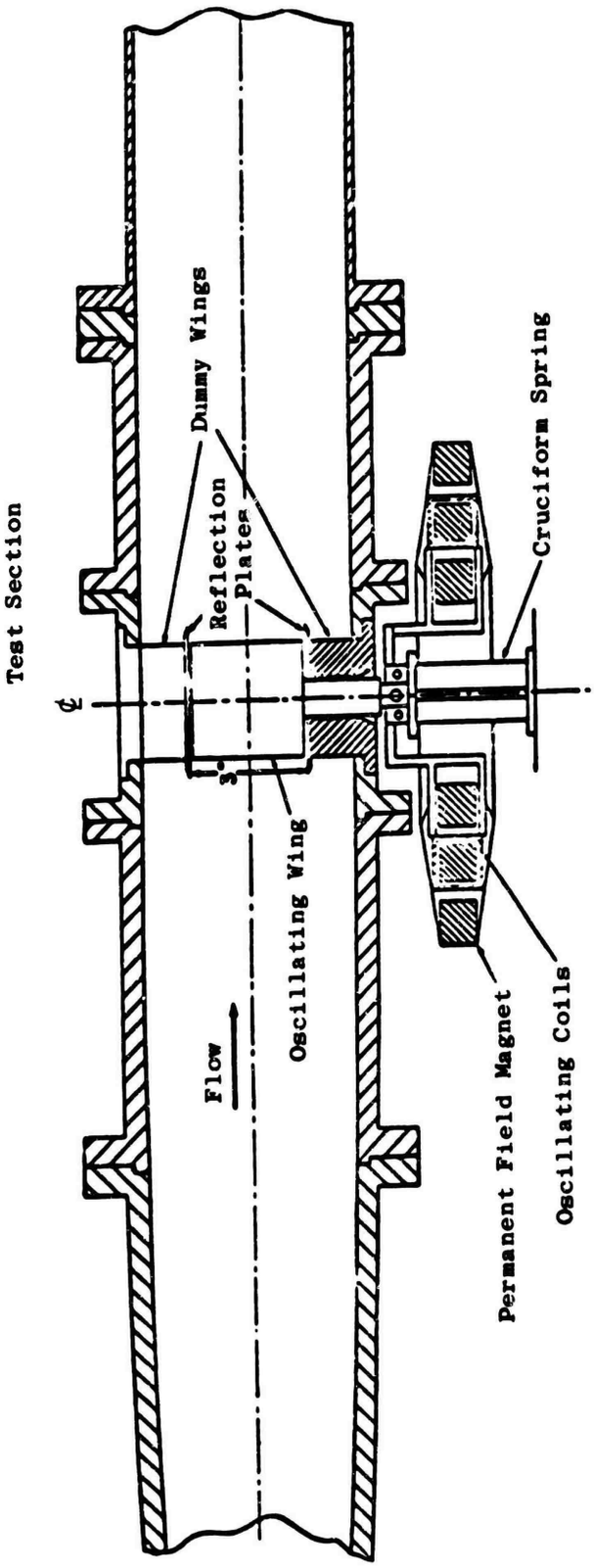

Fig. 16 Two-dimensional oscillatory apparatus

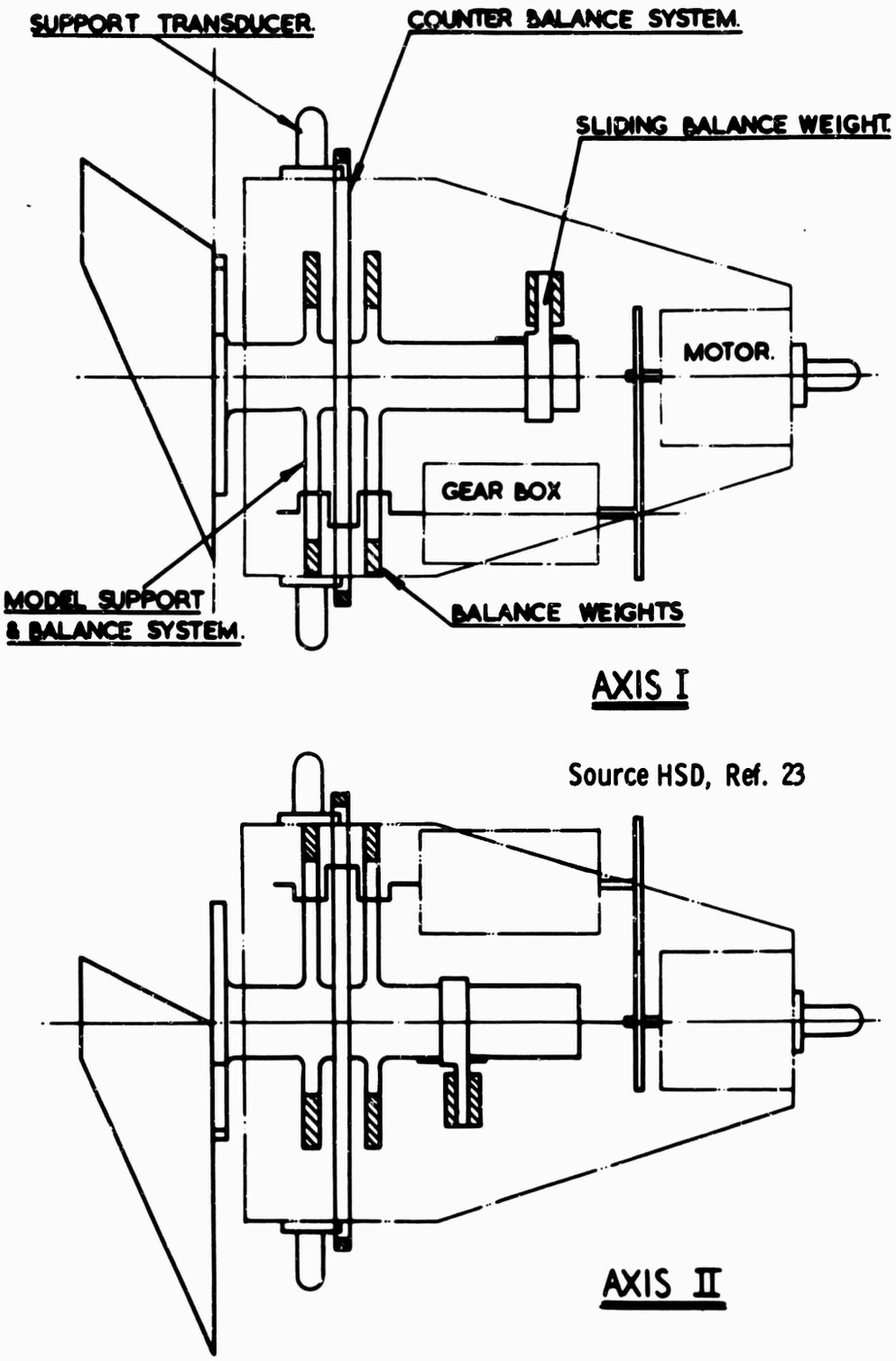

Fig. 17 Half-model oscillating rig

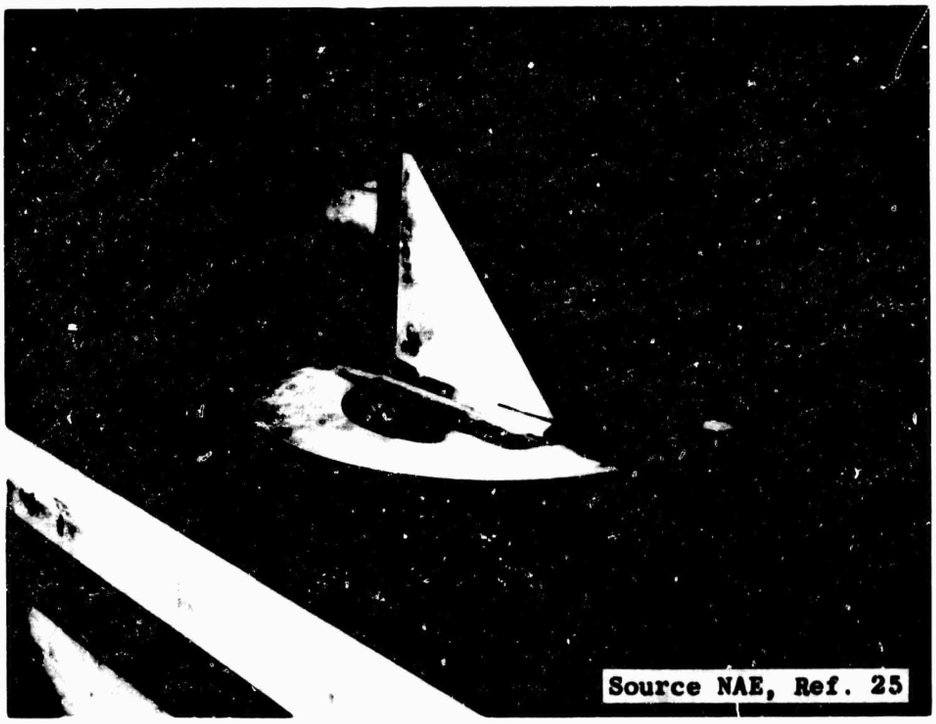

Fig. 18 Half-models and reflection planes

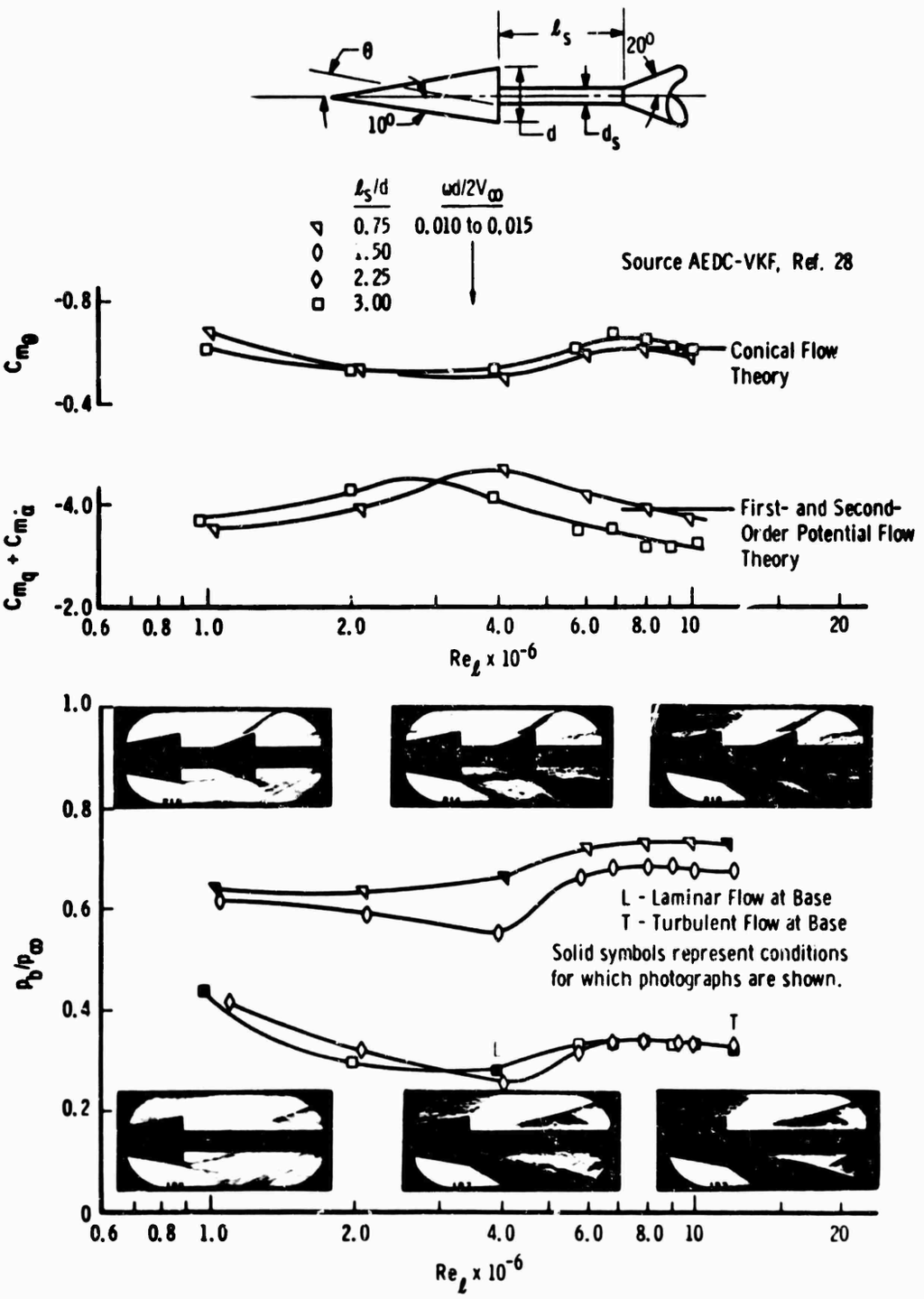

(a) $M_\infty = 2.5$, $d_s/d = 0.4$, $\alpha = \pm 2$ deg

Fig. 19 Support interference effects

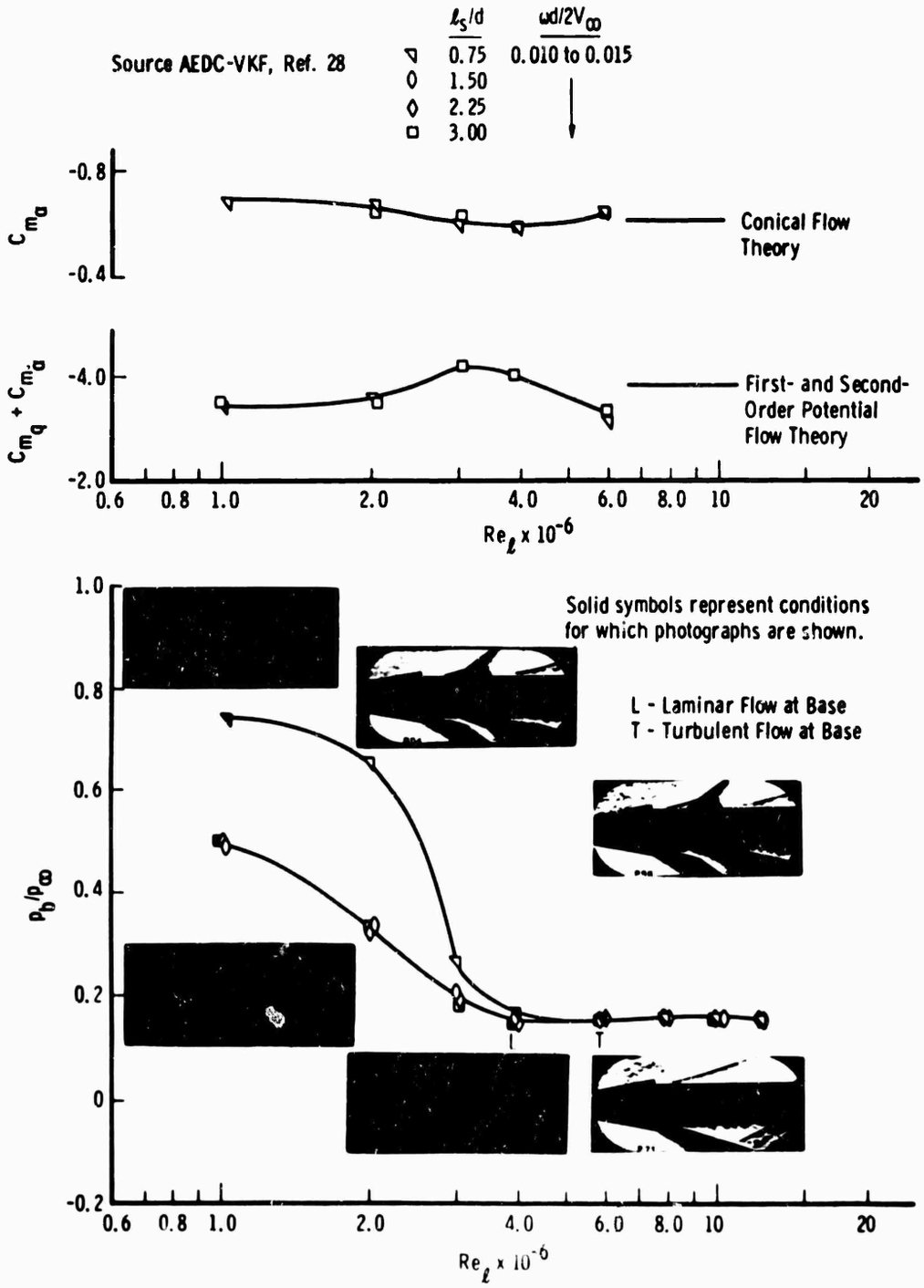

(b) $M_\infty = 2.5$, $d_s/d = 0.8$, $\alpha = \pm 1.5$ deg

Fig. 19 Support Interference effects

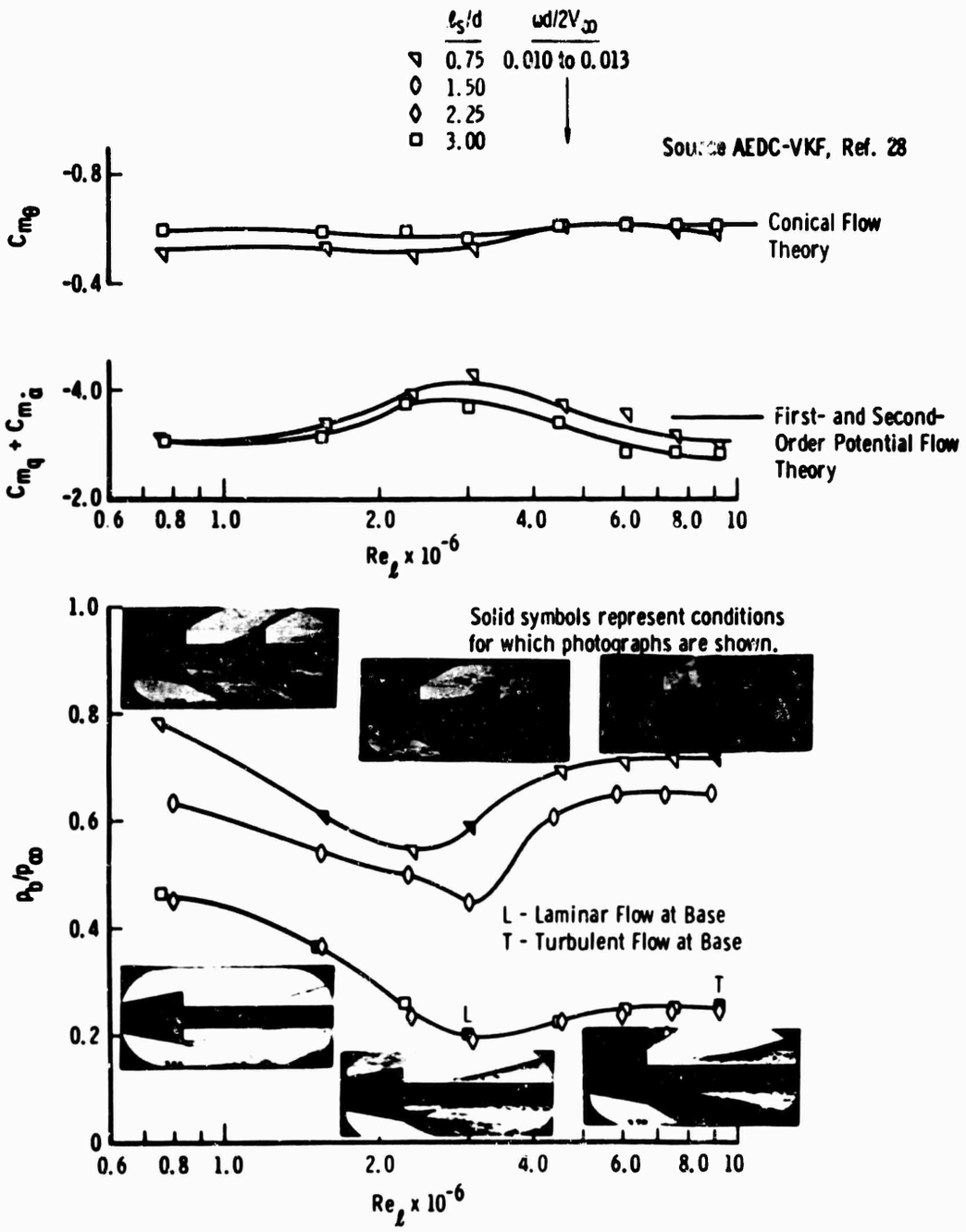

(a) $M_\infty = 3$, $d_s/d = 0.4$, $\alpha = \pm 2$ deg

Fig. 20 Support interference effects

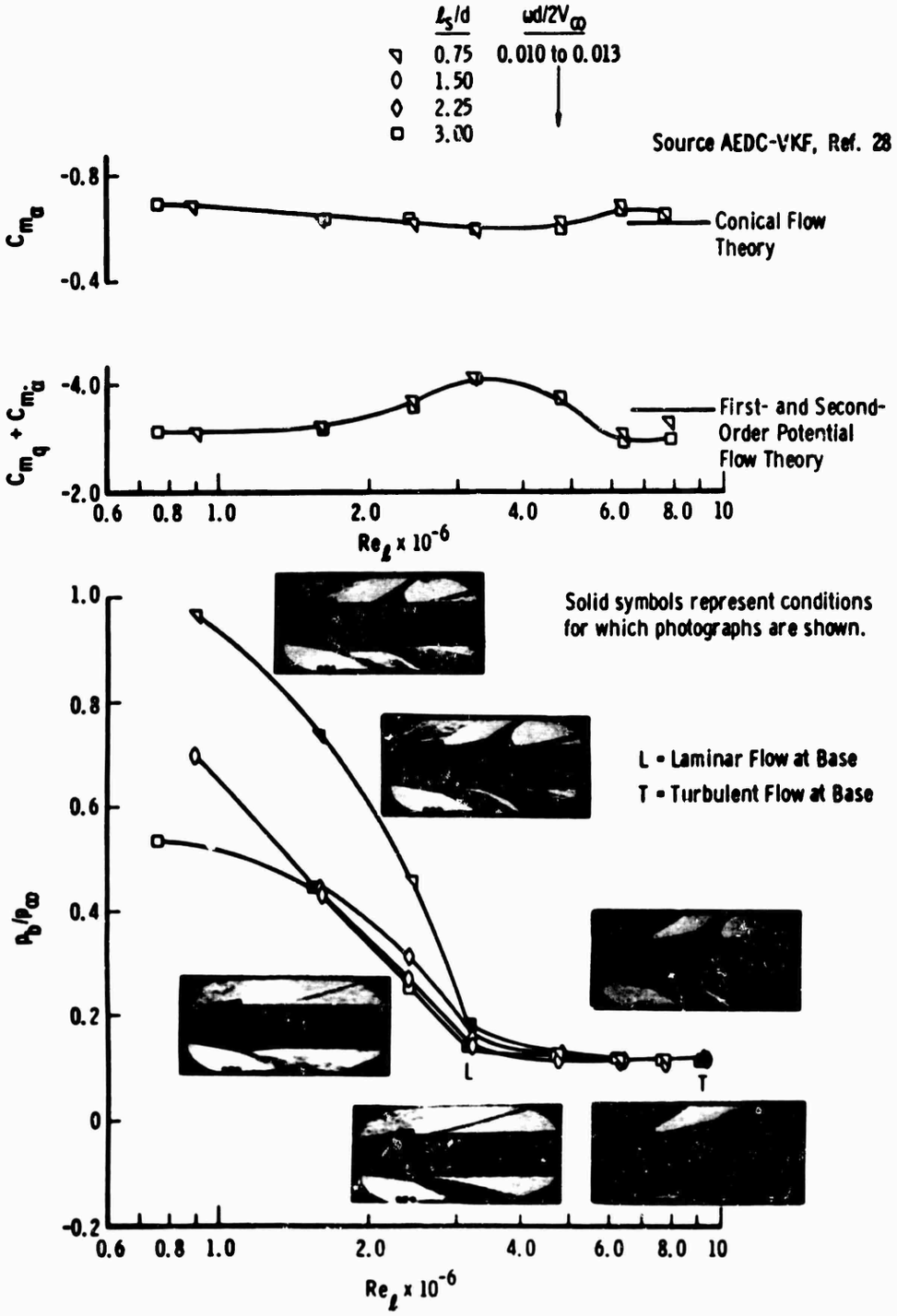

(b) $M_\infty = 3$, $d_s/d = 0.8$, $\alpha = \pm 1.5$ deg

Fig. 20 Support interference effects

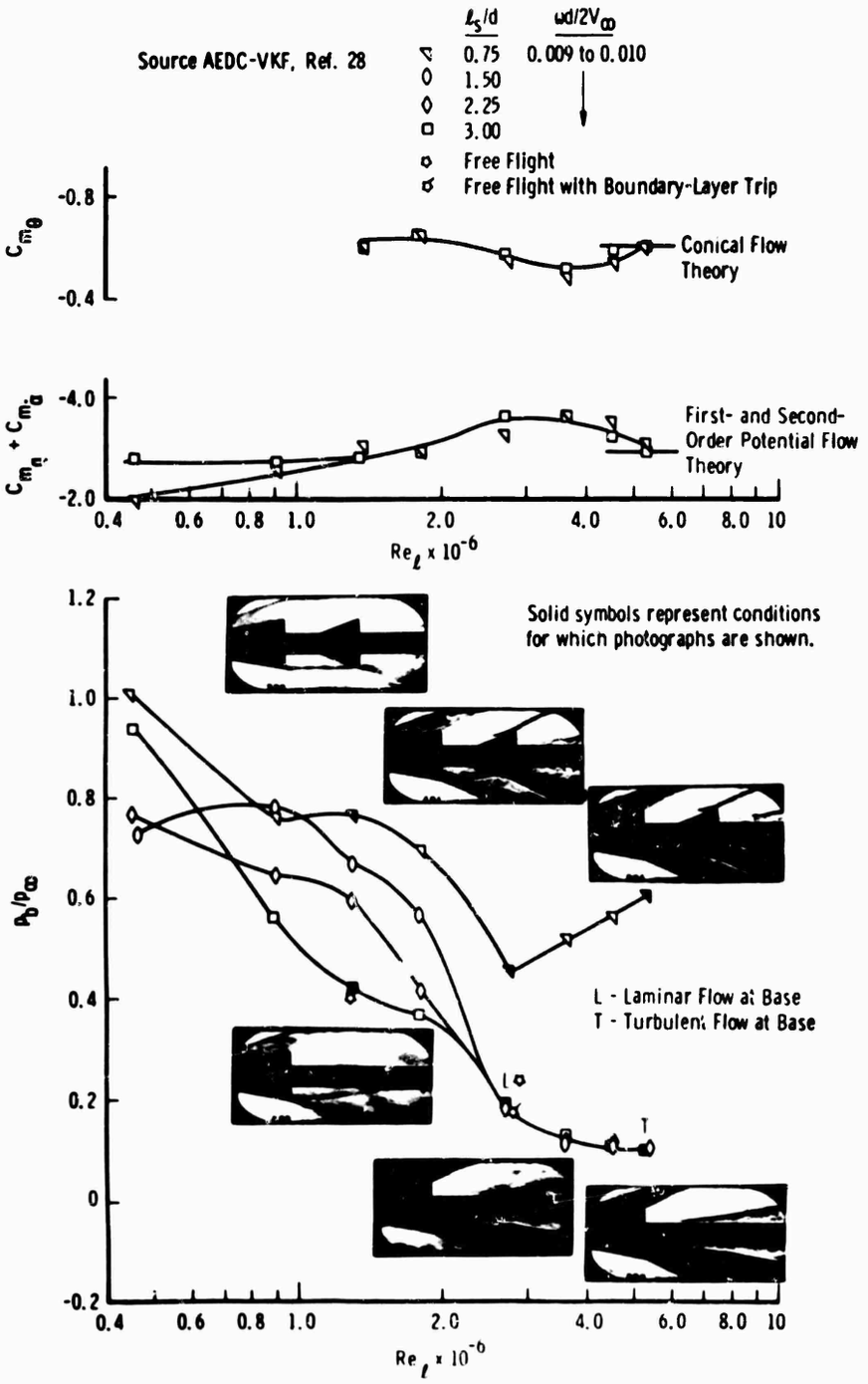

(a) $M_\infty = 4$, $d_s/d = 0.4$, $\alpha = \pm 2$ deg

Fig. 21 Support interference effects

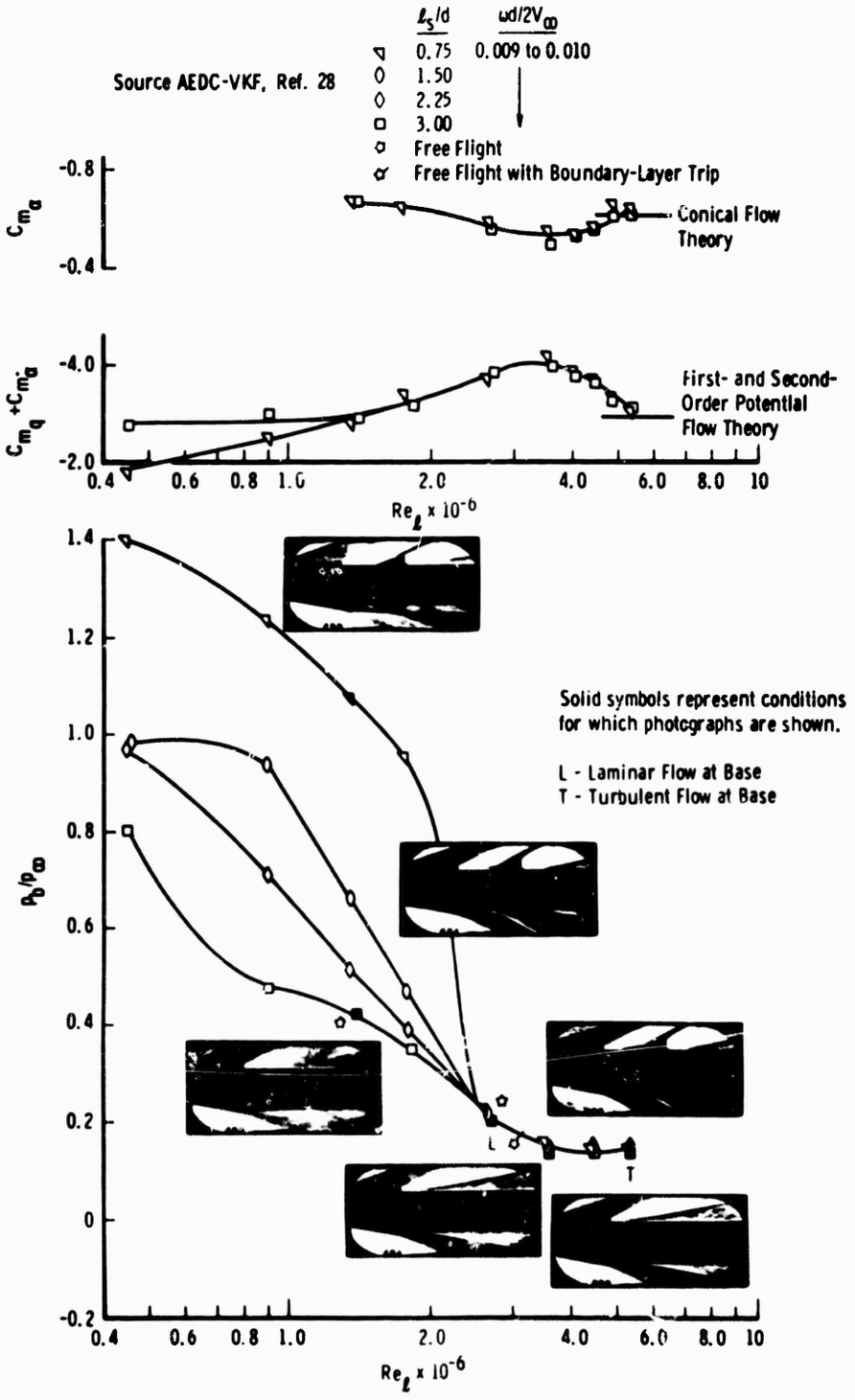

(b) $M_\infty = 4$, $d_s/d = 0.8$, $\alpha = \pm 1.5$ deg

Fig. 21 Support interference effects

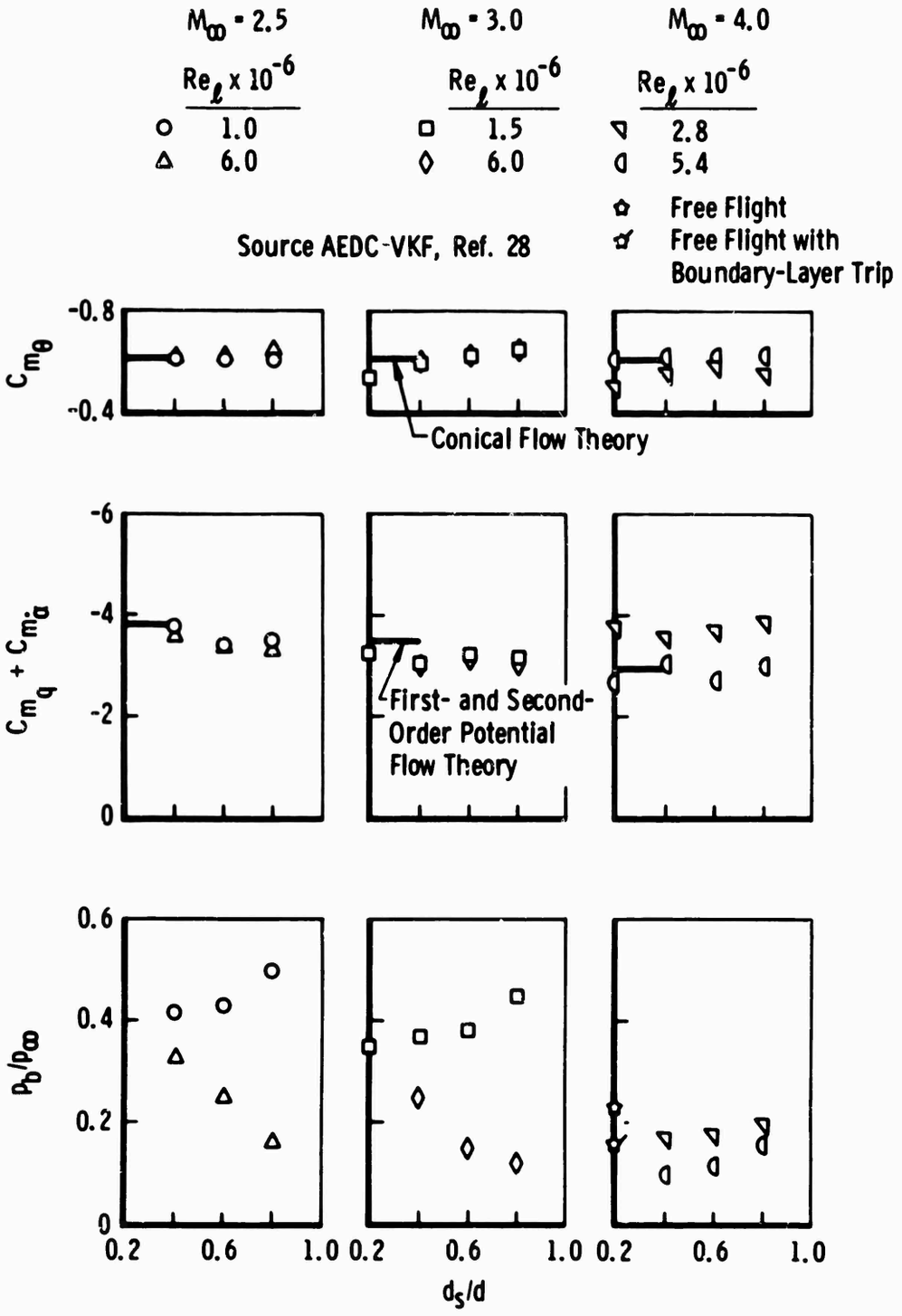

Fig. 22 Variation of static and dynamic stability coefficient and base pressure ratio with sting diameter for $l_s/d = 3$

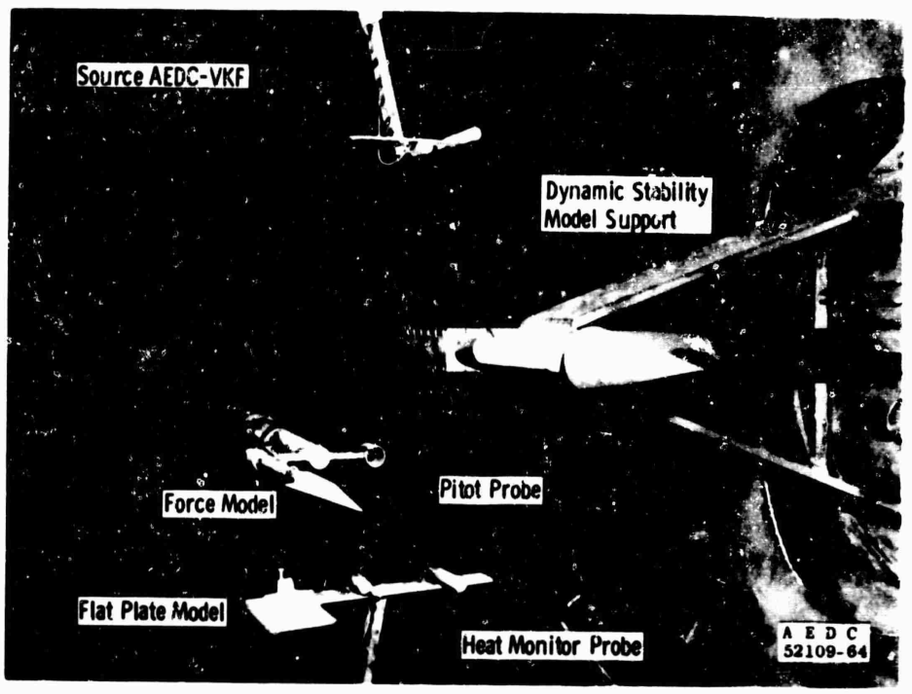

Fig. 23 Model balance and support assembly for Hotshot (AEDC-VKF tunnel F) tunnel

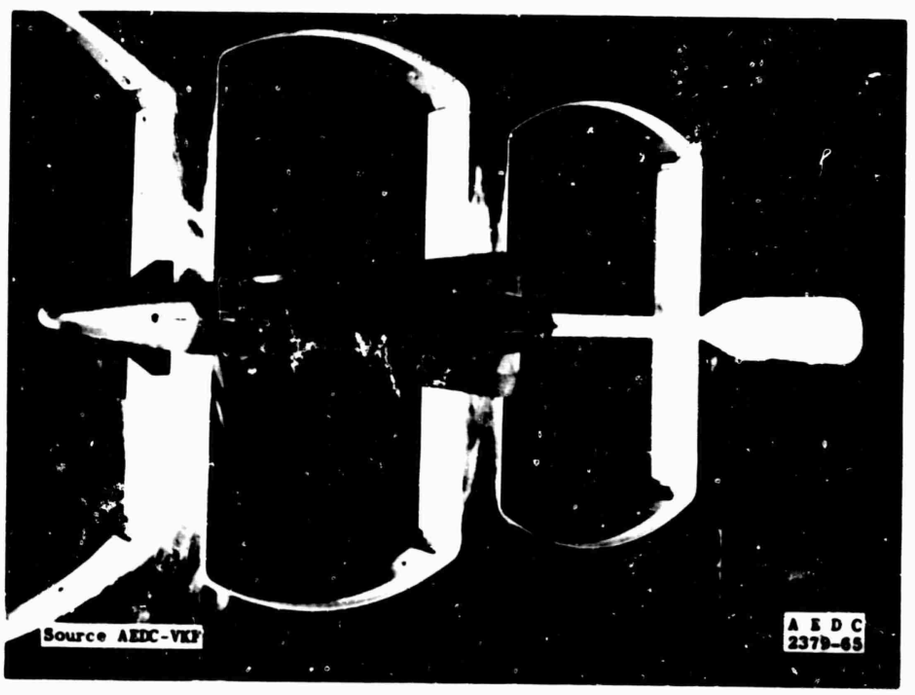

Fig. 24 Free oscillation balance system

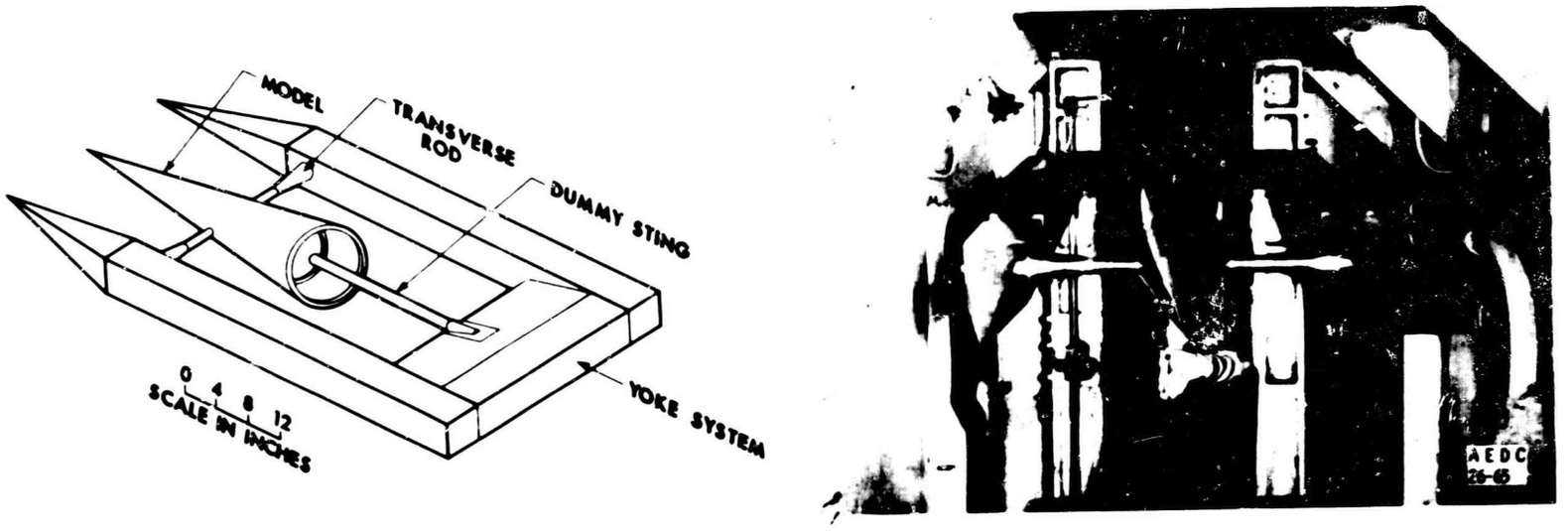

Source AEDC-VKF

Fig. 25 Transverse rod and yoke system installed in test section tank

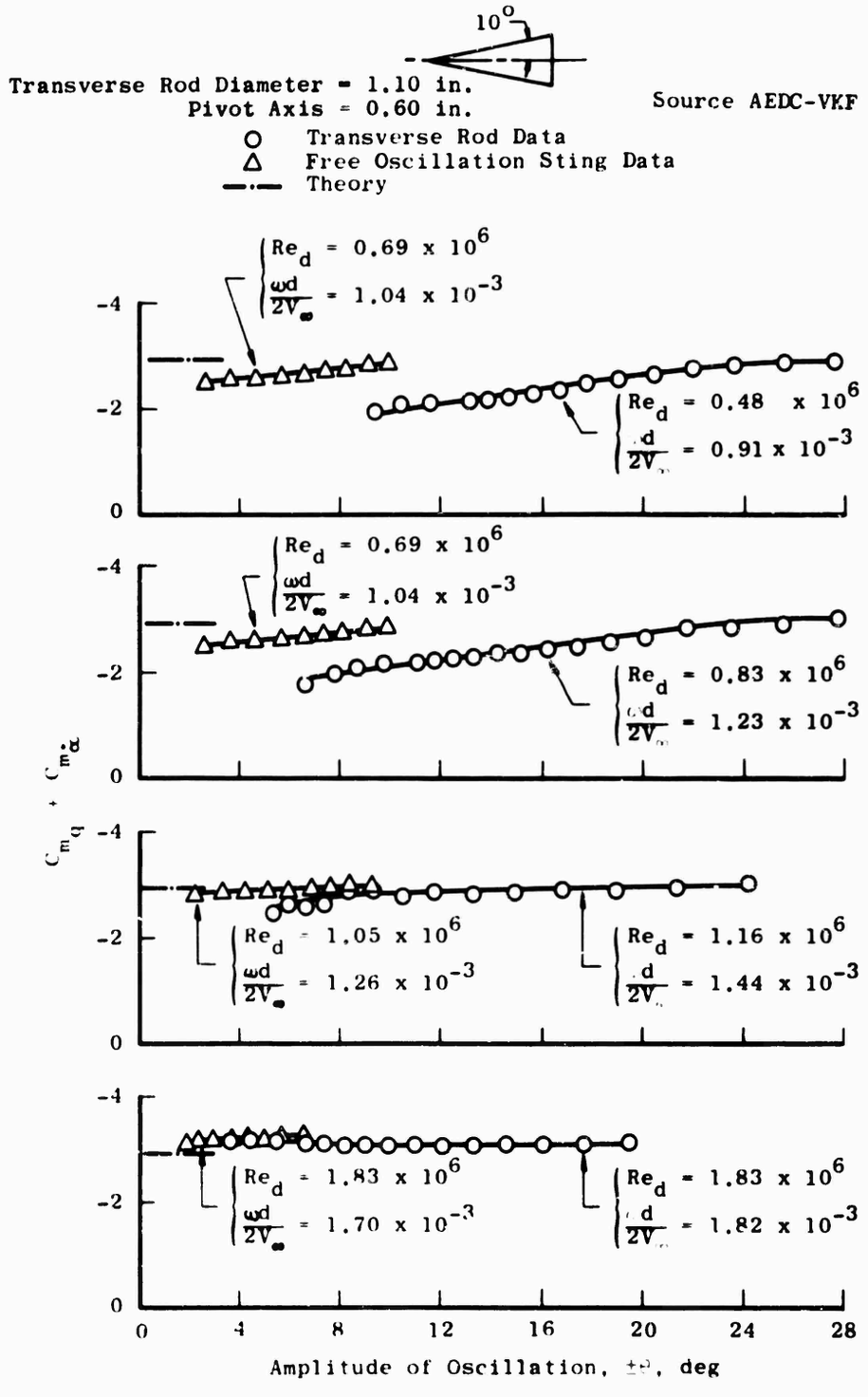

Fig. 26 Dynamic stability derivatives versus amplitude of oscillation, Mach 10

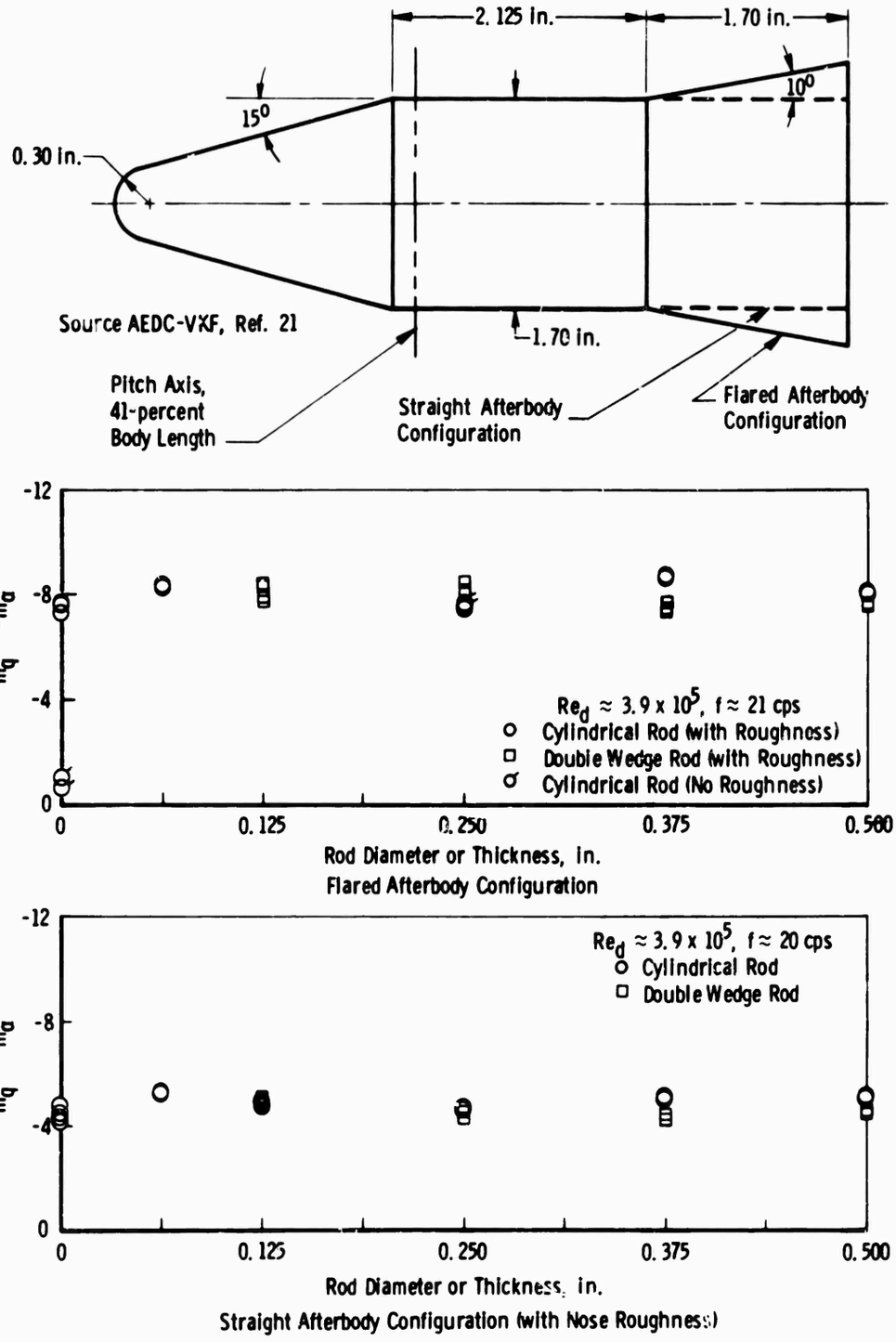

Fig. 27 Damping derivatives for the flared and straight afterbody configurations measured in conjunction with a series of simulated transverse rod configurations, forced oscillation tests, amplitude 1.5 deg, Mach 5

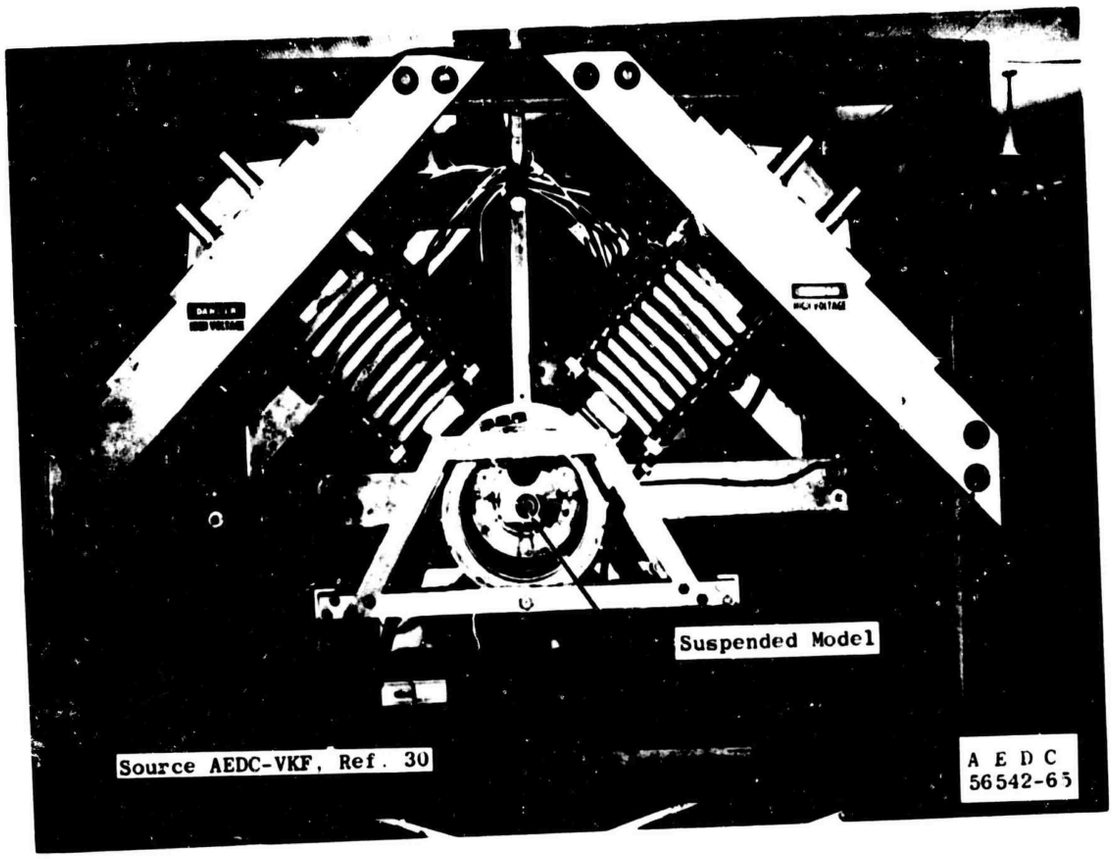

Fig. 28 Magnetic suspension system, end view

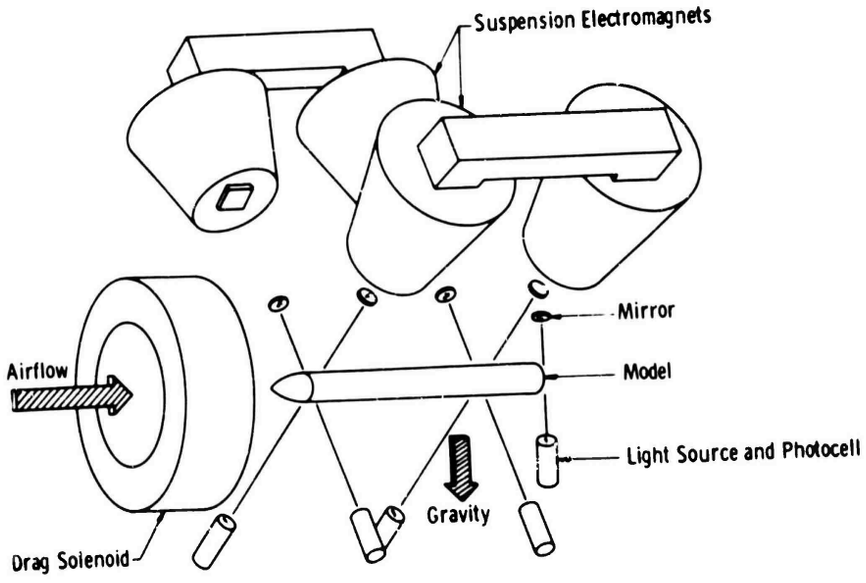

Fig. 29 Basic "V" configuration magnetic suspension system

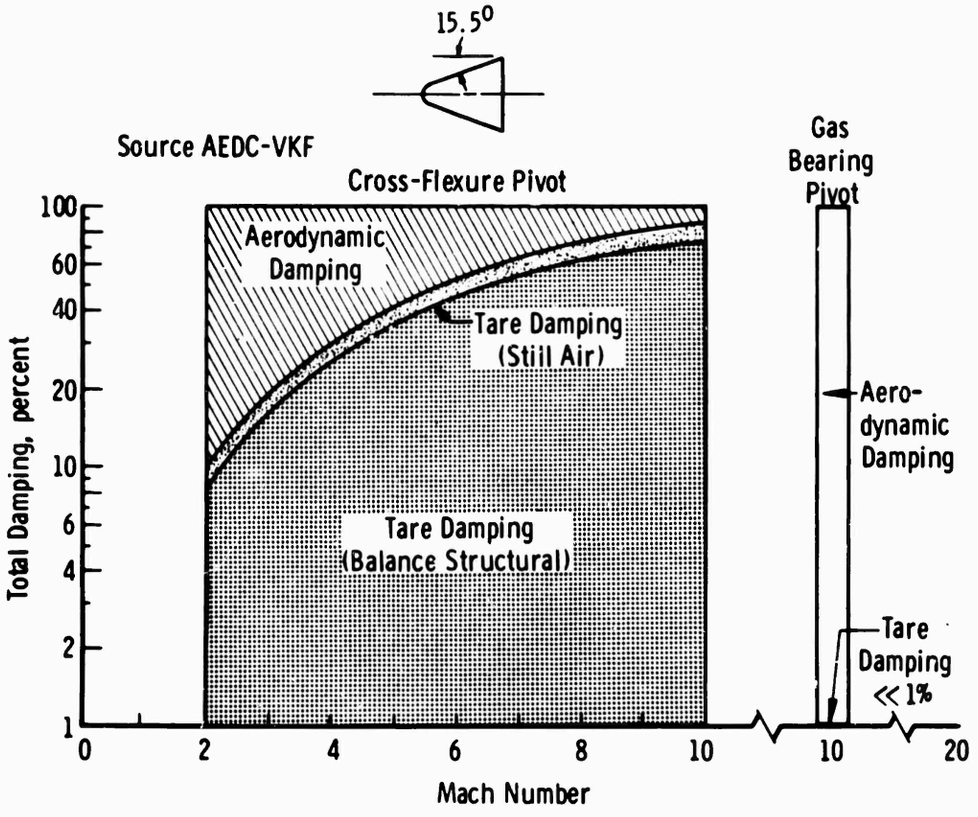

Fig. 30 Contribution of aerodynamic, still-air, and structural damping to total damping

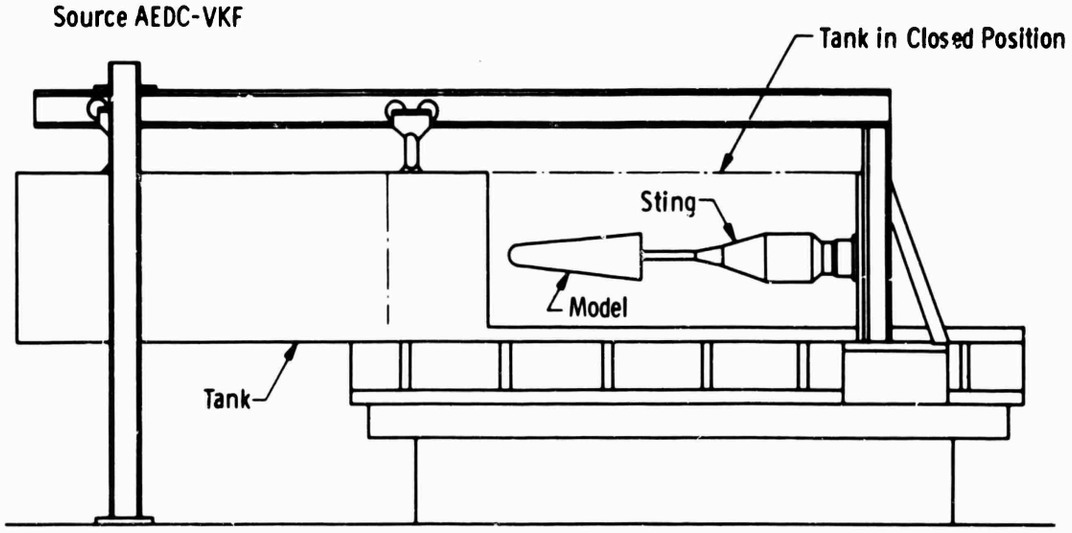

Fig. 31 Sketch of the vacuum system used to evaluate still-air damping

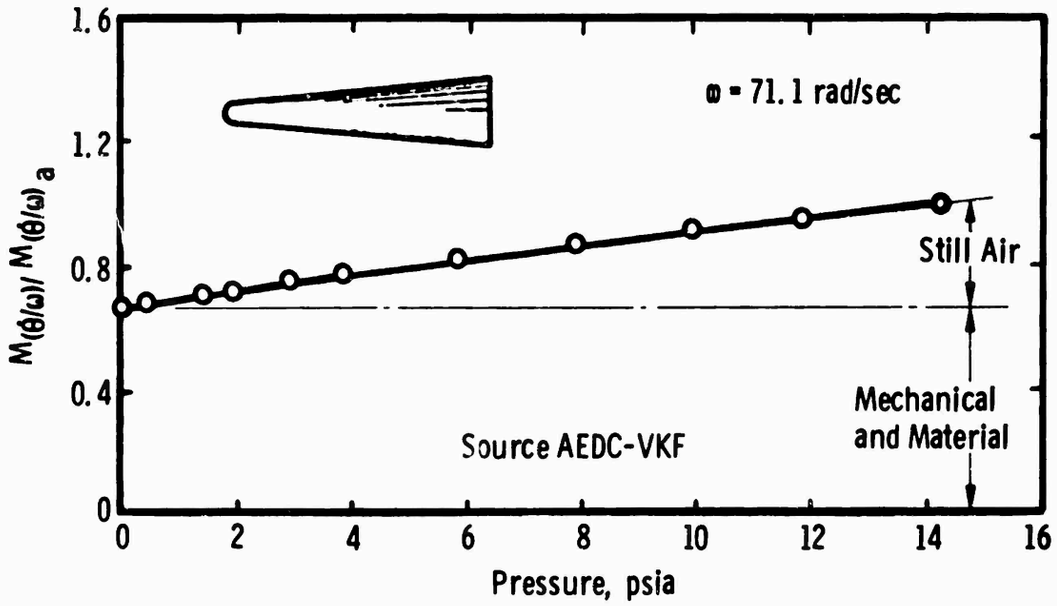

Fig. 32 Variation of structural damping with static pressure

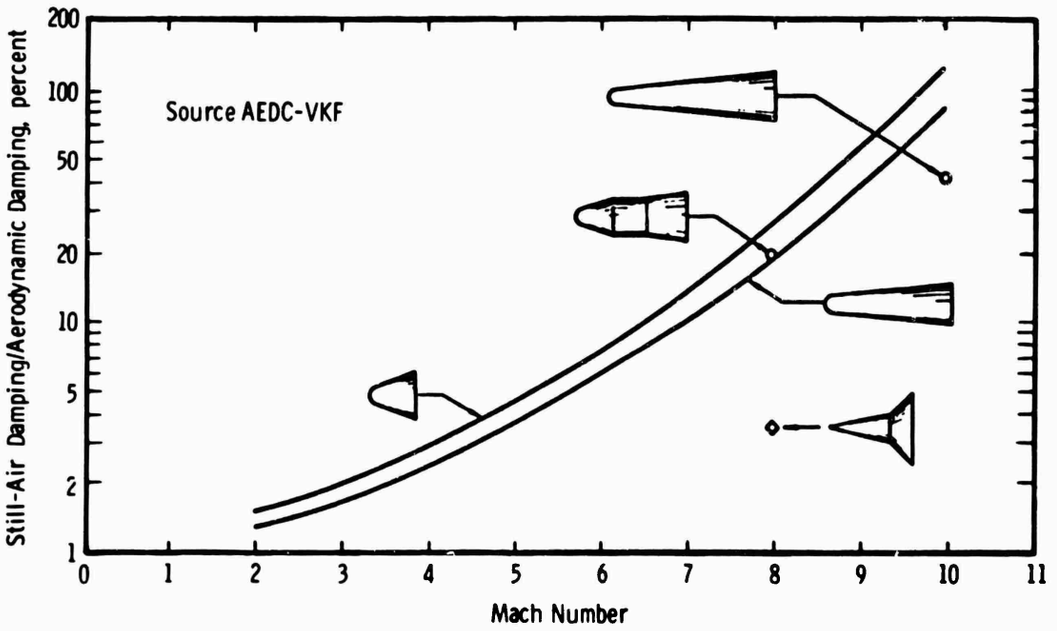

Fig. 33 Variation of the ratio of model still-air damping to model aerodynamic damping with Mach number

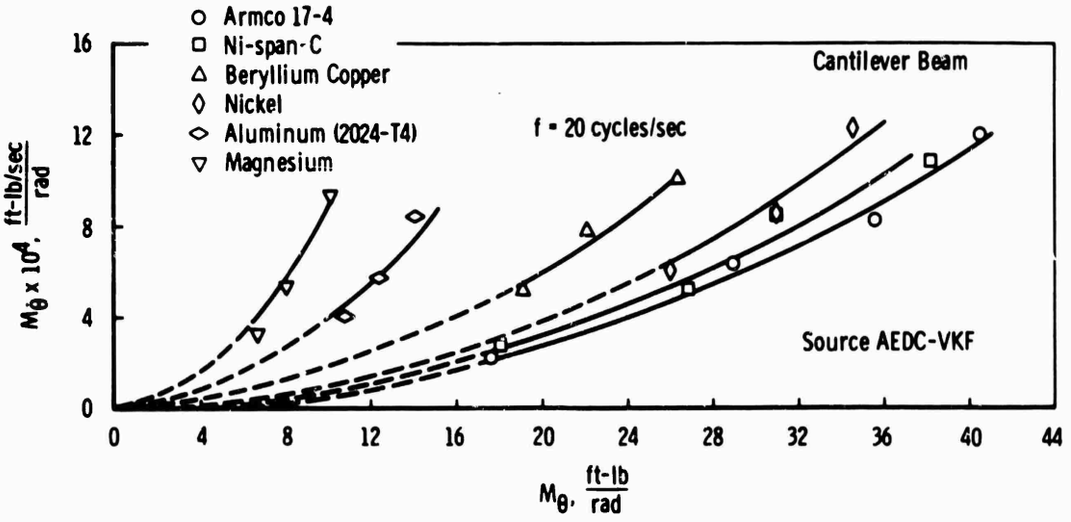

Fig. 34 Variation of the angular viscous-damping-moment parameter with angular restoring-moment parameter

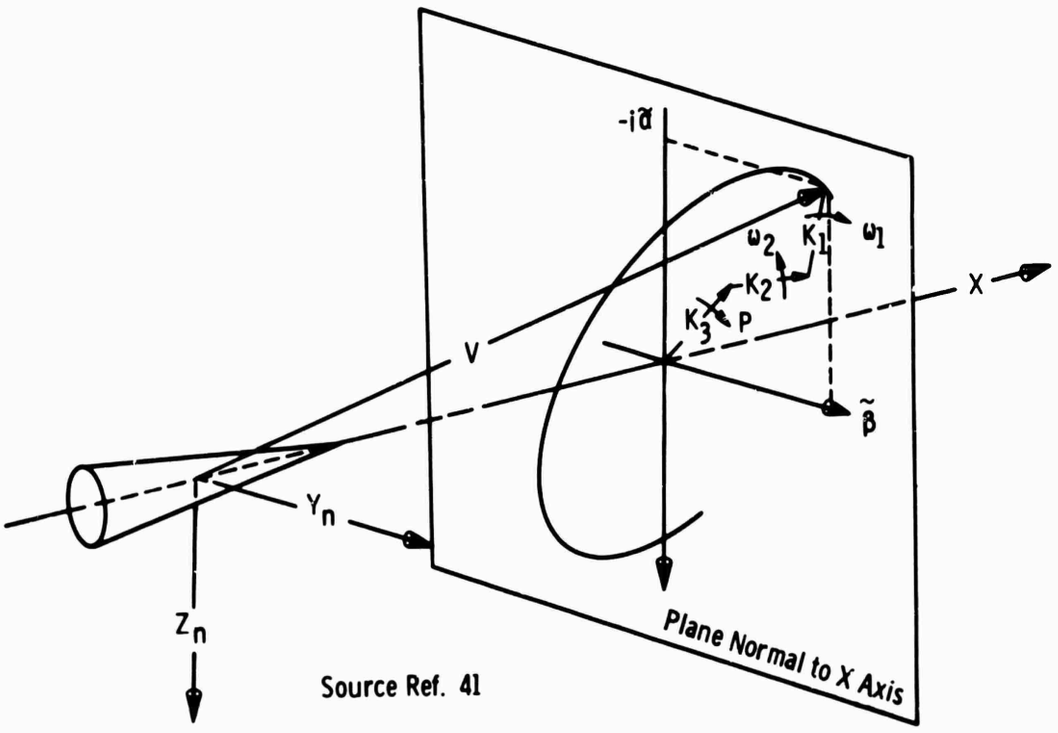

Fig. 35 Tricyclic pitching and yawing

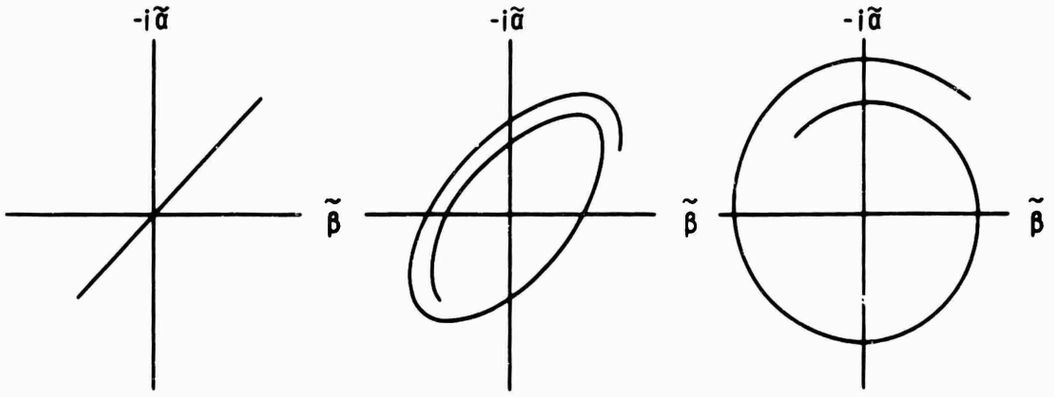

Source Ref. 41

Fig. 36 Typical free flight epicyclic pitching and yawing motions of a nonrolling statically stable symmetrical missile

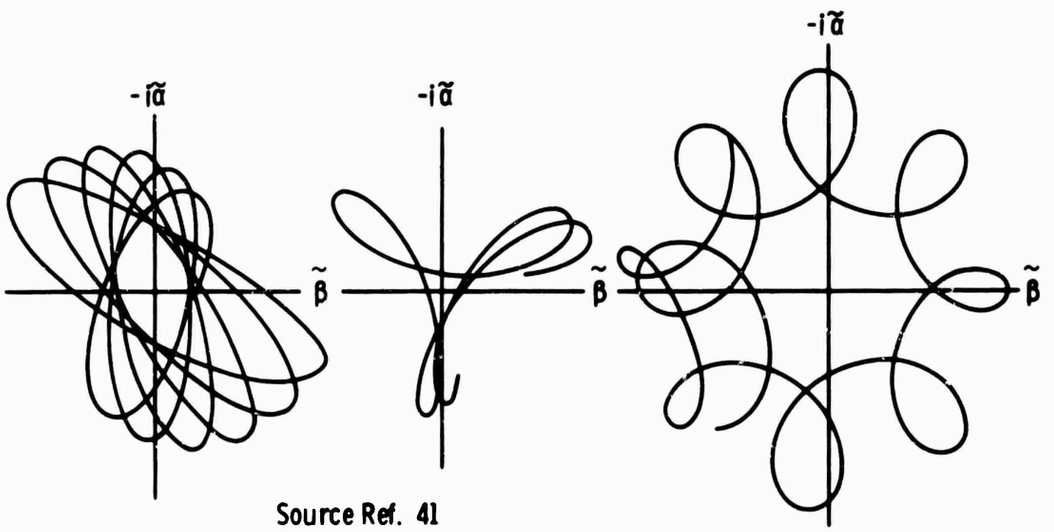

Source Ref. 41

Fig. 37 Typical free flight epicyclic pitching and yawing motions of a rolling statically stable symmetrical missile

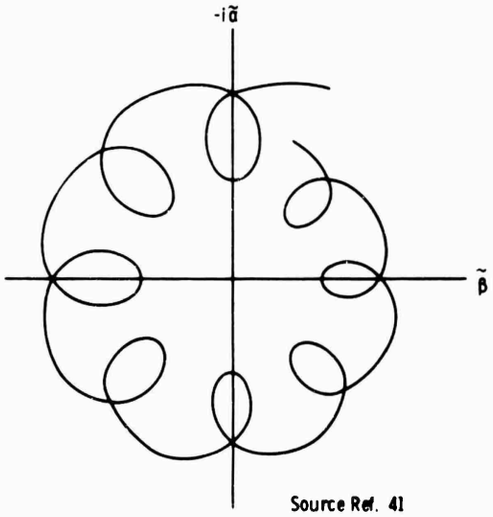

Fig. 38 Typical free flight pitching and yawing motion of rapidly rolling statically unstable symmetrical missile

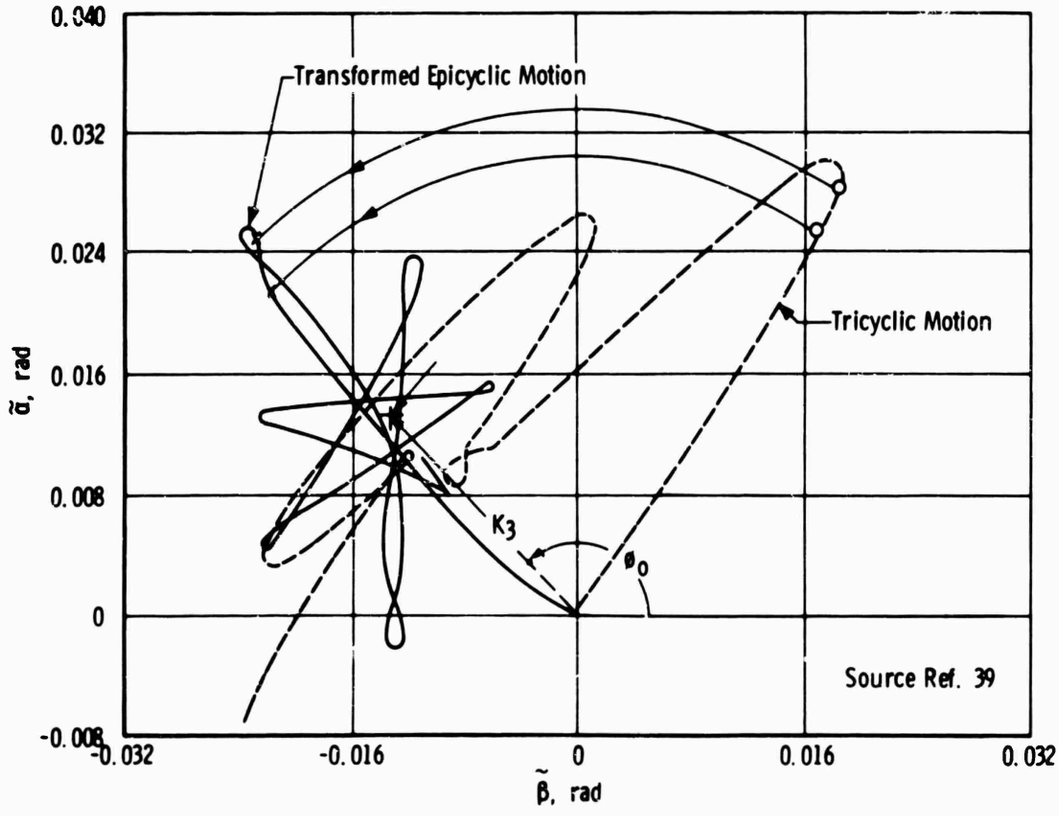

Fig. 39 Motion transformation

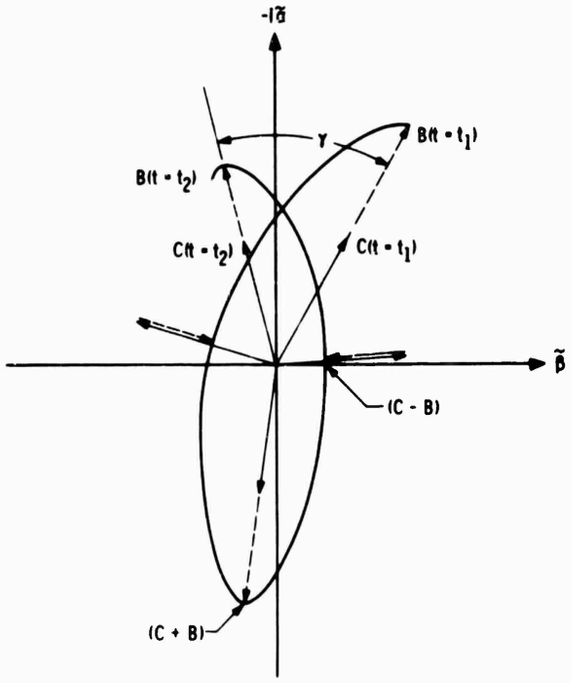

Fig. 40 Complex angular motion

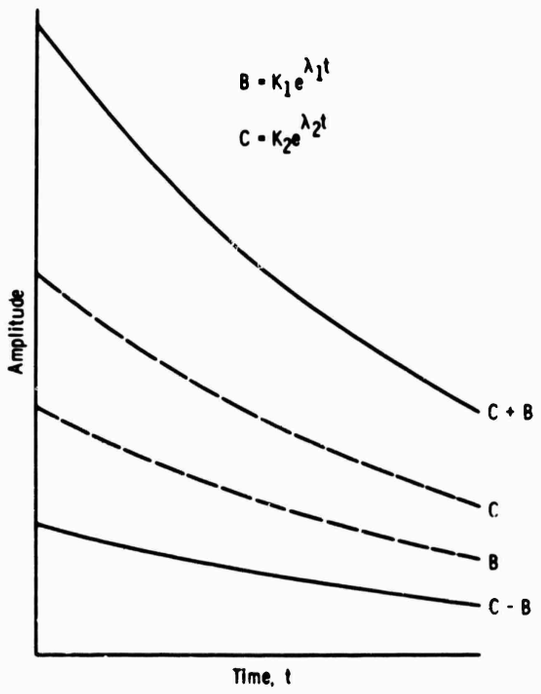

Fig. 41 Exponential decay of the modal vectors

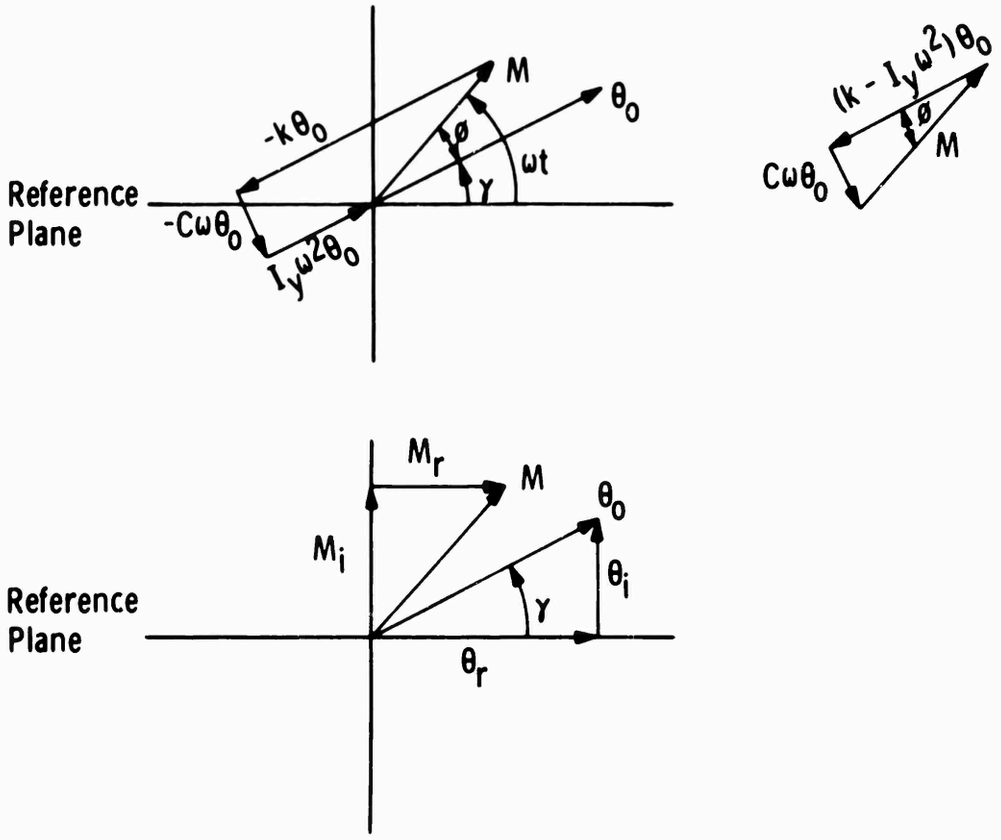

Forced Oscillation Off of Resonance

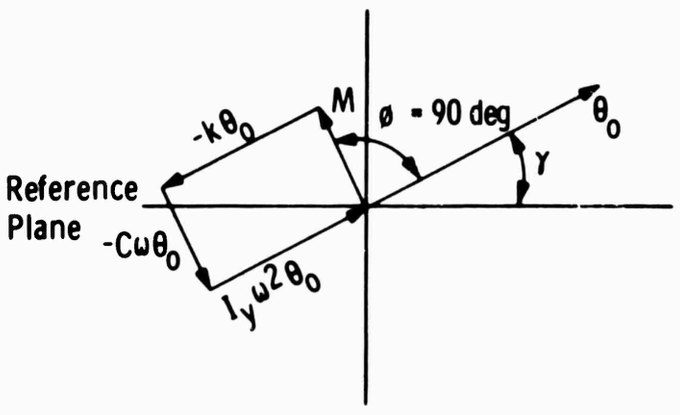

Forced Vibration at Resonance

Fig. 42 Phase diagram

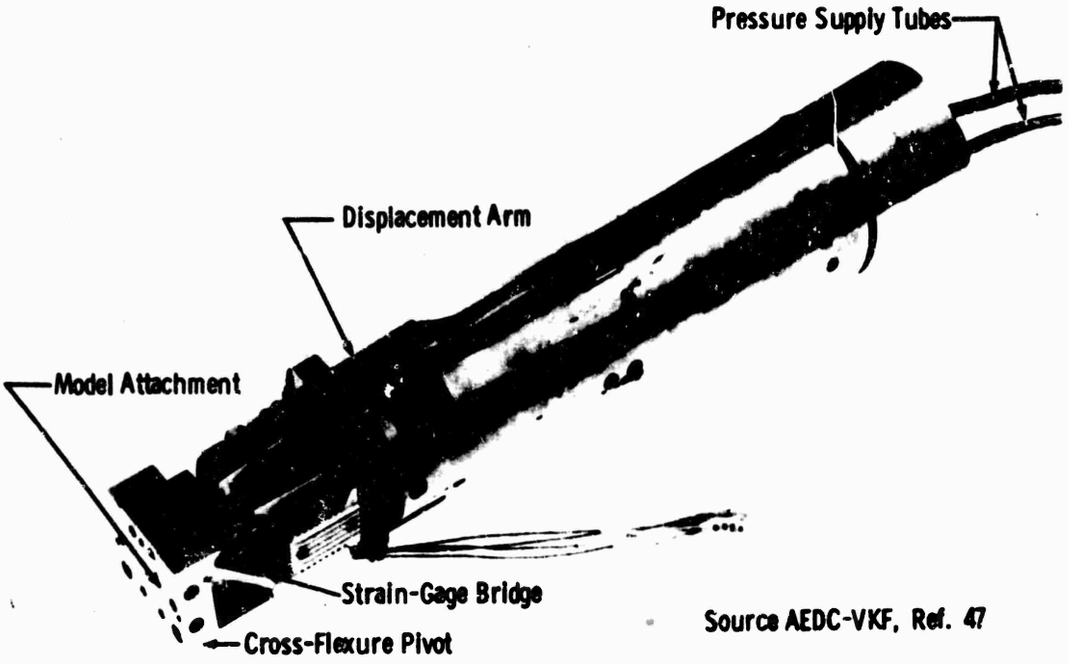

Fig. 43 High frequency free oscillation balance for Hotshot tunnel tests

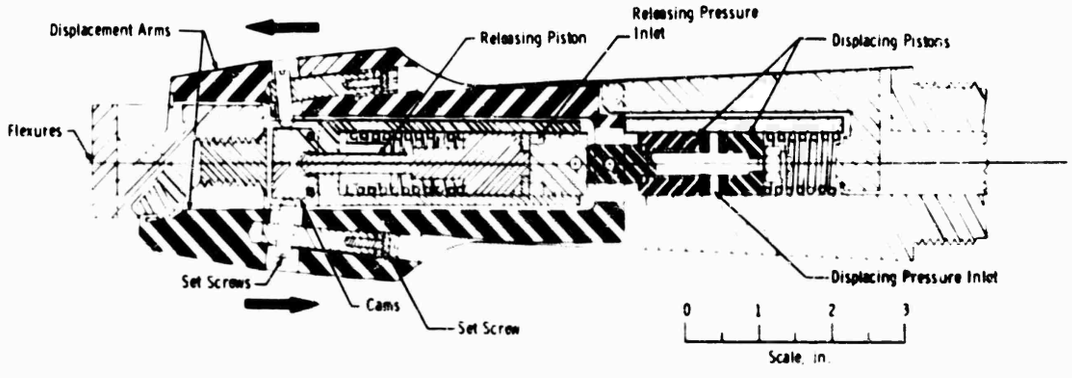

Fig. 43 Continued

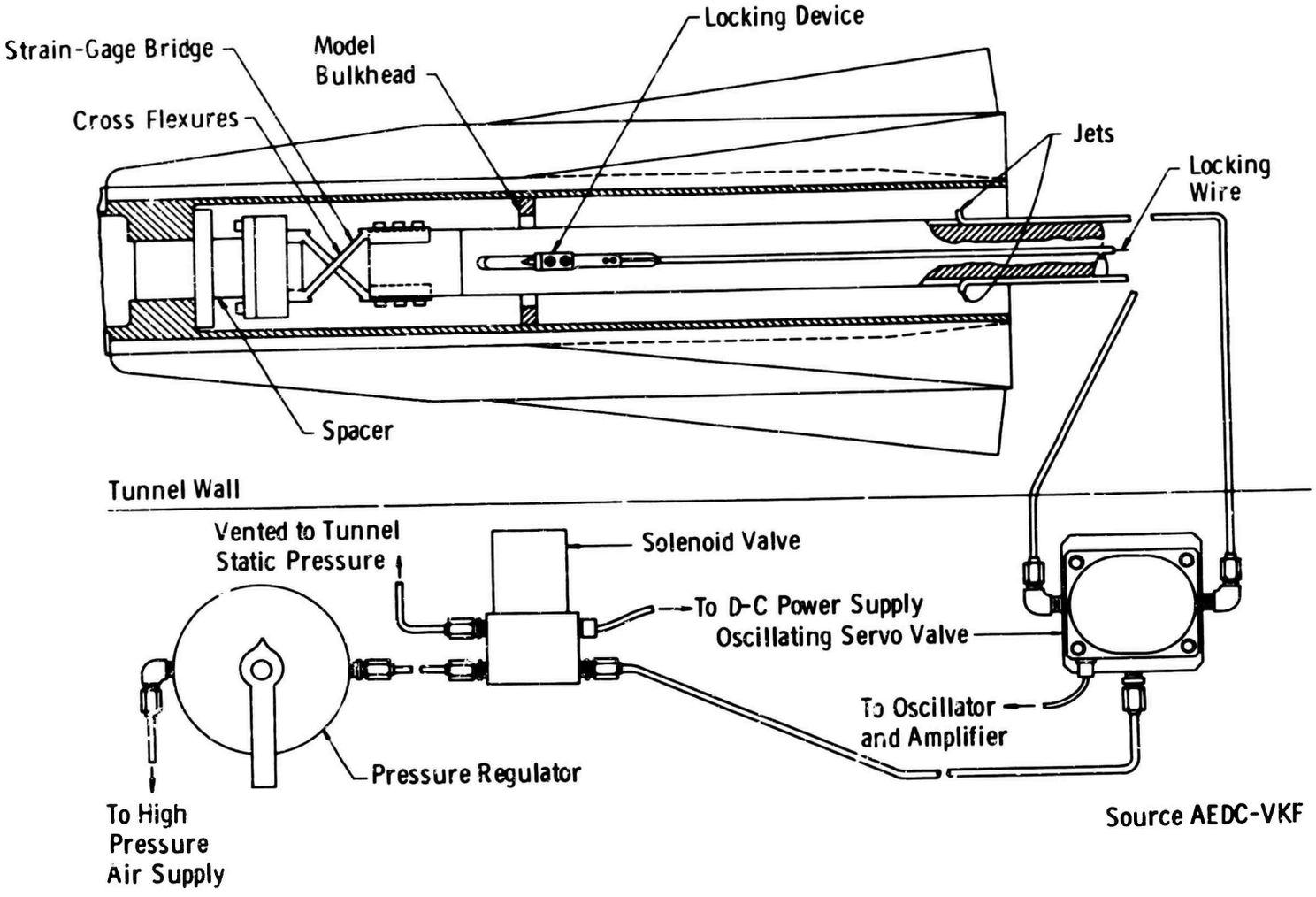

Fig. 44 Model displacement system

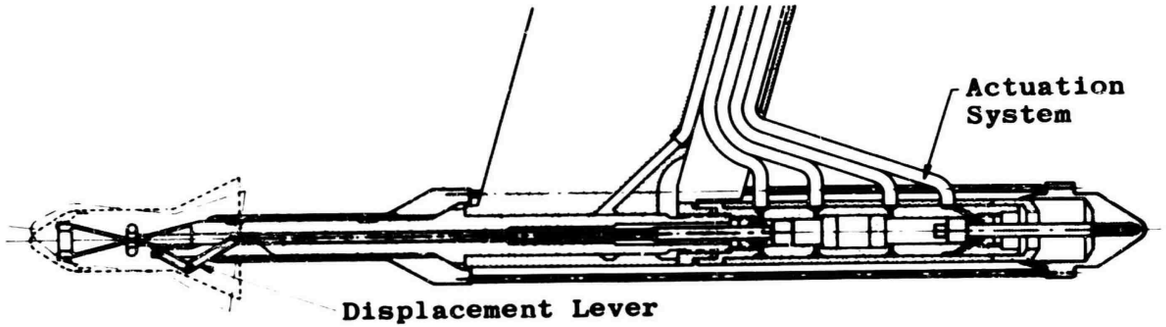

Source ONERA, Ref. 47

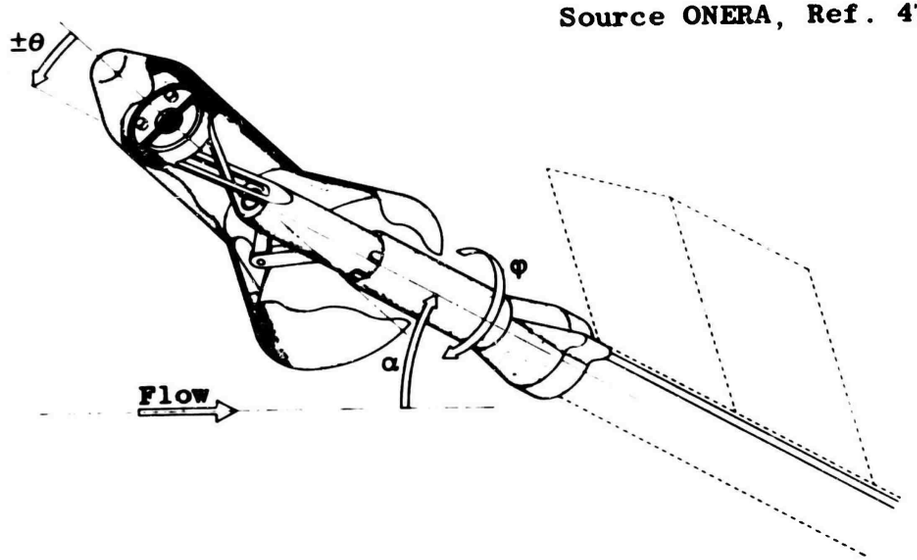

Fig. 45 Free oscillation balance and displacement mechanism

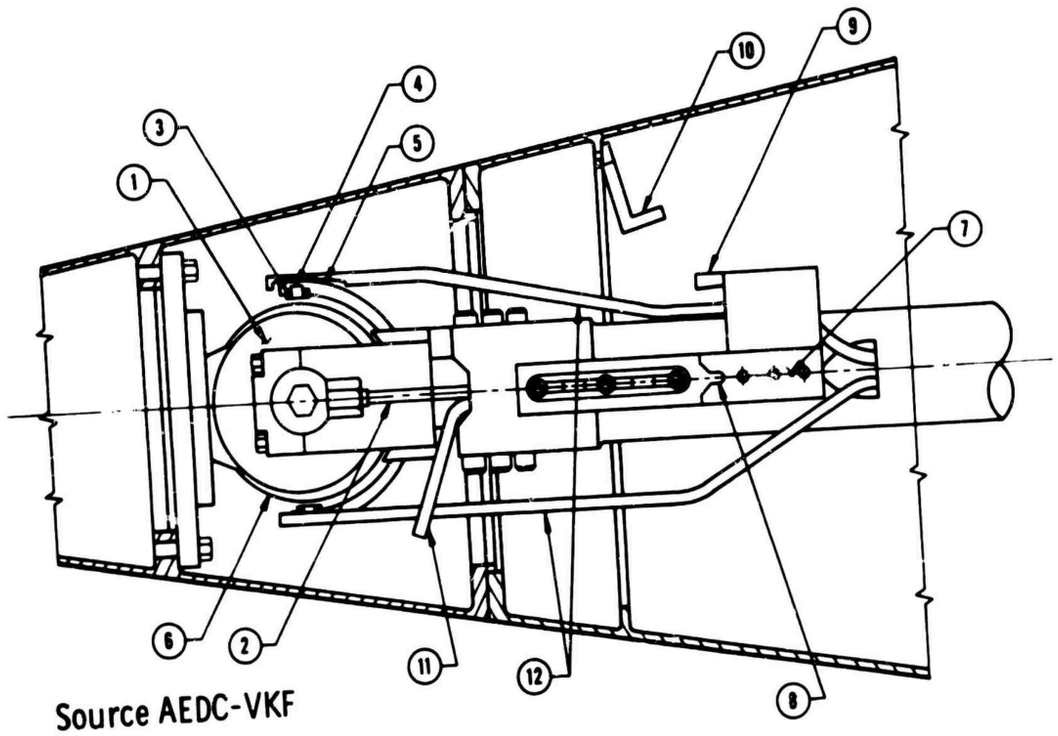

Source AEDC-VKF

Item No.	Description	Item No.	Description
1	Gas Bearing	7	Locking Assembly
2	Bearing Gas Inlet	8	Trim Lock
3	Coil	9	Displacement Arm Lock
4	"E" Core	10	Model Displacement Arm
5	"E" Core Housing	11	Model Displacement Air Line
6	Eccentric	12	Cooling Air Lines

Fig. 46 Large amplitude (±15 deg), free oscillation balance

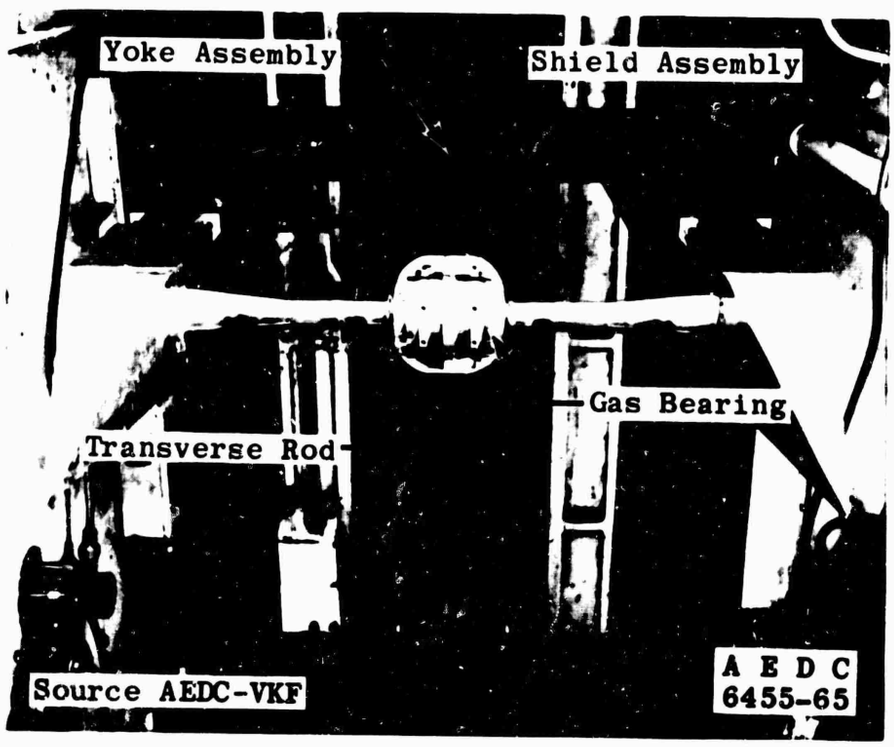

Fig. 47 Free-oscillation transverse rod balance

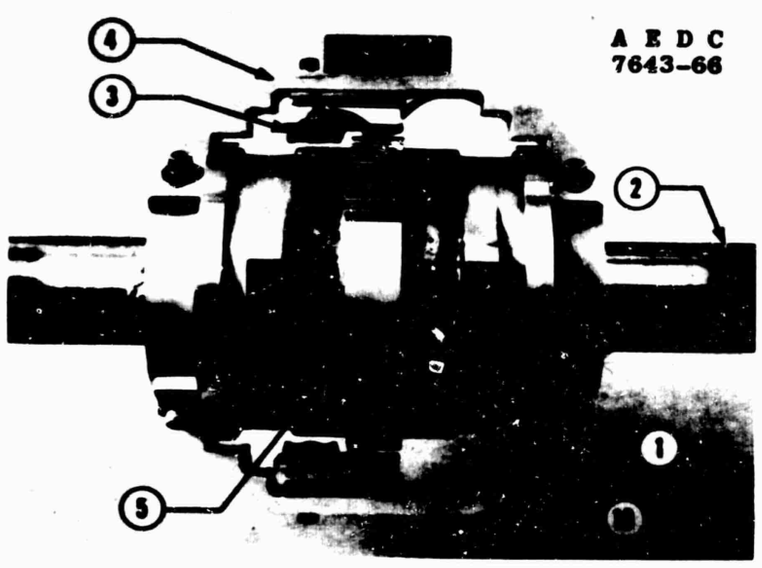

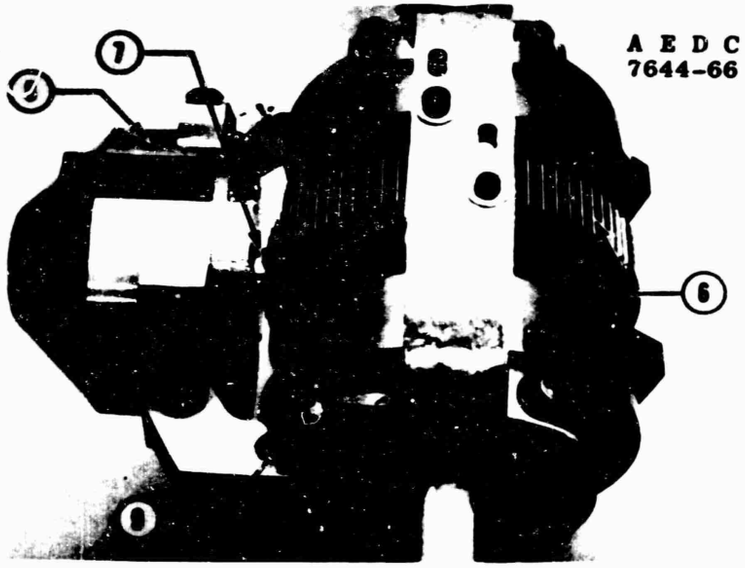

Source AEDC-VKF

Item No.	Description	Item No.	Description
1	Gas Bearing	6	Gear Rack
2	Transverse Rod	7	Air Actuated Piston
3	"E" Core	8	Lock Housing for Air Piston
4	"E" Core Mounting Bracket	9	Lock Actuating Air Line
5	Eccentric	10	Model Mounting Pad

Fig. 48 Photographs of the free-oscillation (±35 deg) transverse rod balance

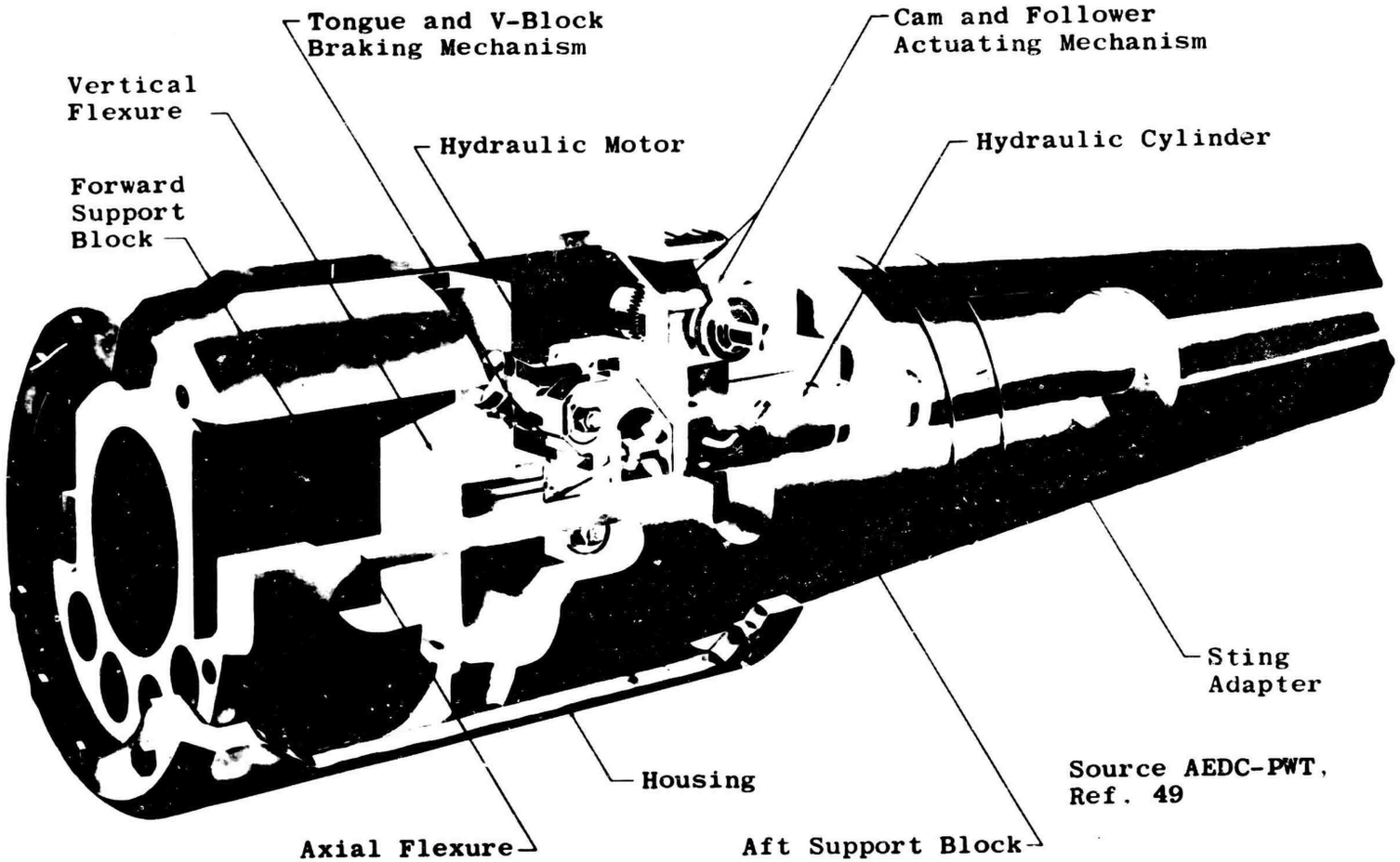

Fig. 49 Free-oscillation balance

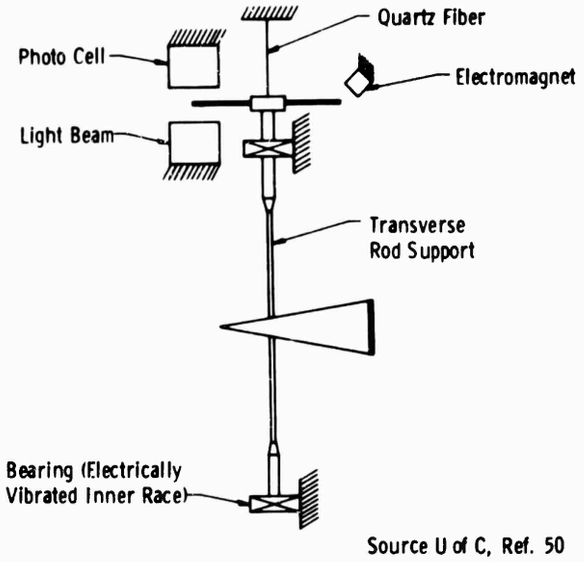

Fig. 50 Transverse rod balance for low density hypersonic flow tunnel

A E D C
43852-66
43851-66

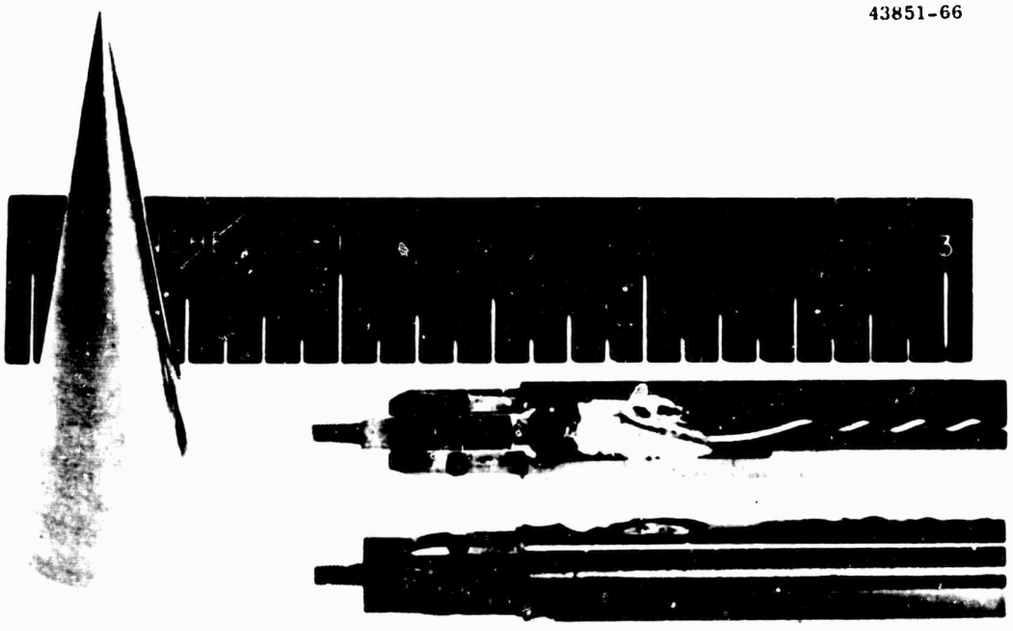

Source AEDC-VKF

Fig. 51 Photograph of the assembled balance

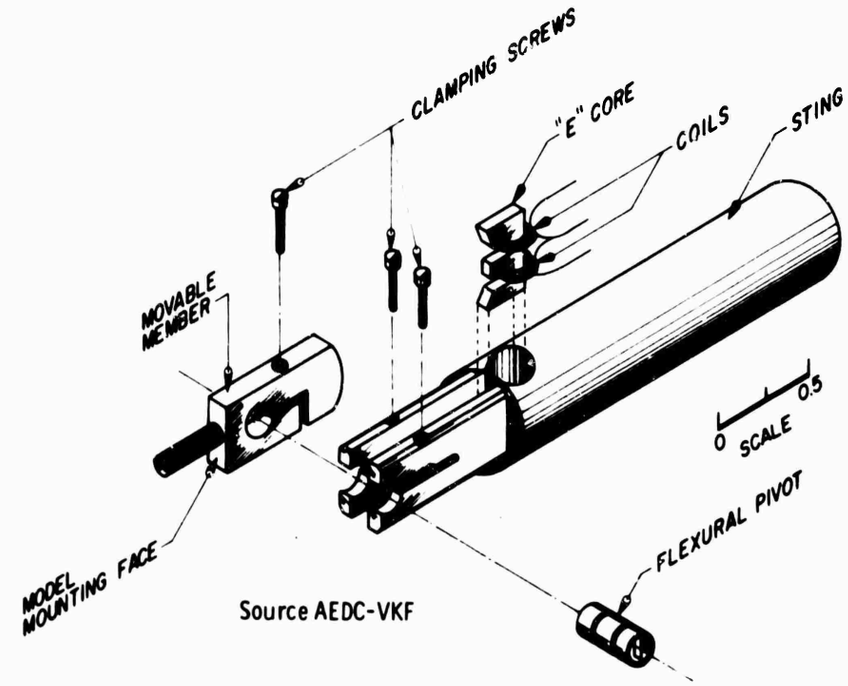

Fig. 52 Small scale free-oscillation balance

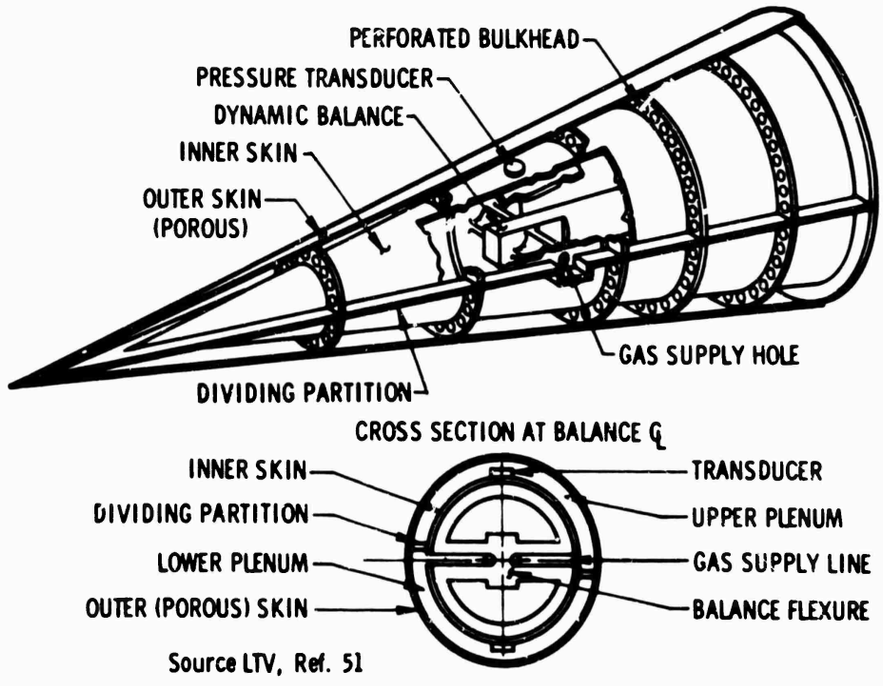

Fig. 53 Basic mass injection balance and porous model

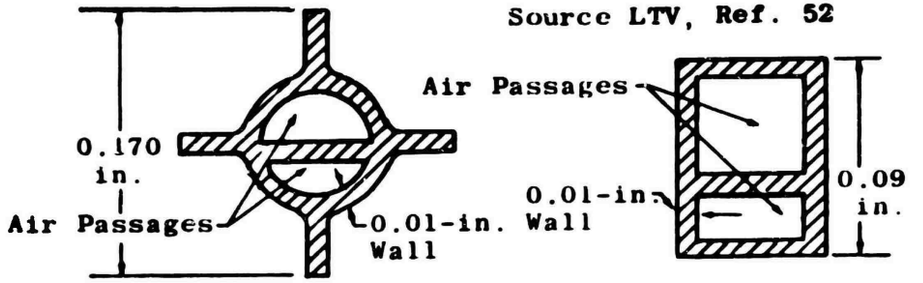

Designs of Dynamic Balance Pivot Cross Section

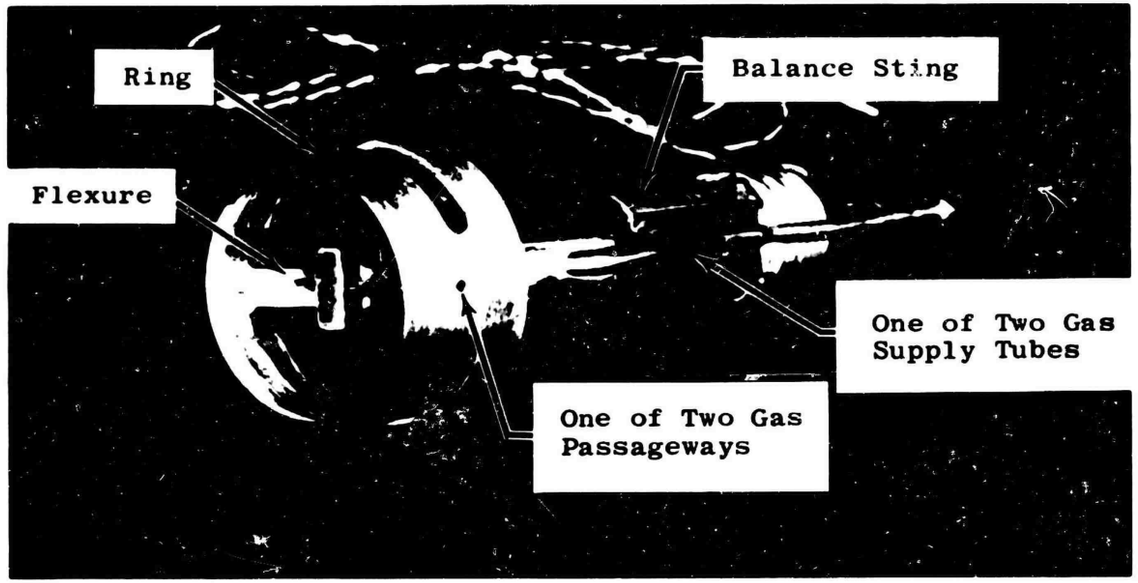

Fig. 54 Dynamic stability balance suitable for gas injection

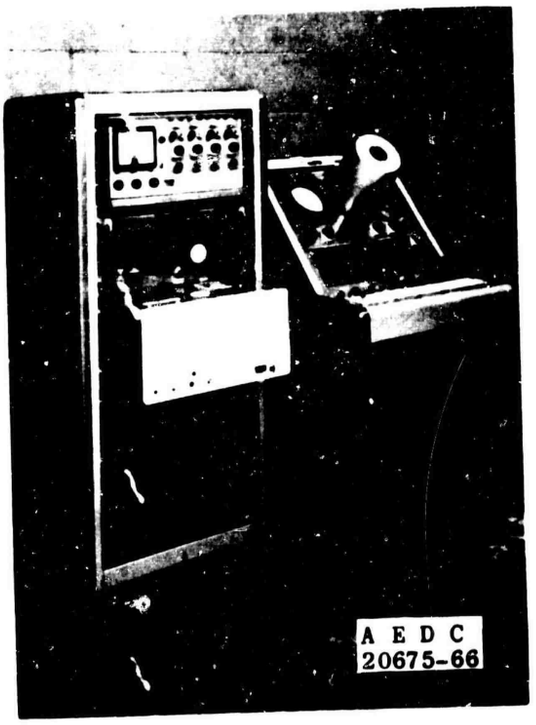

Fig. 55 Oltronix dampometer

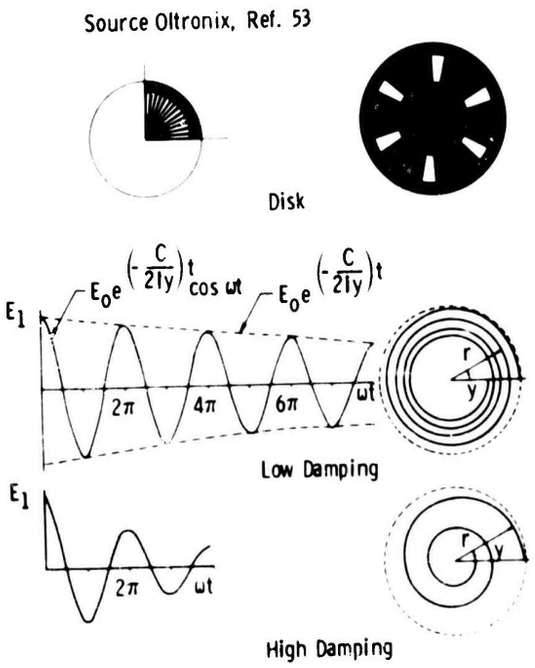

Fig. 56 Typical calibrated slotted disks and principle of dampometer operation

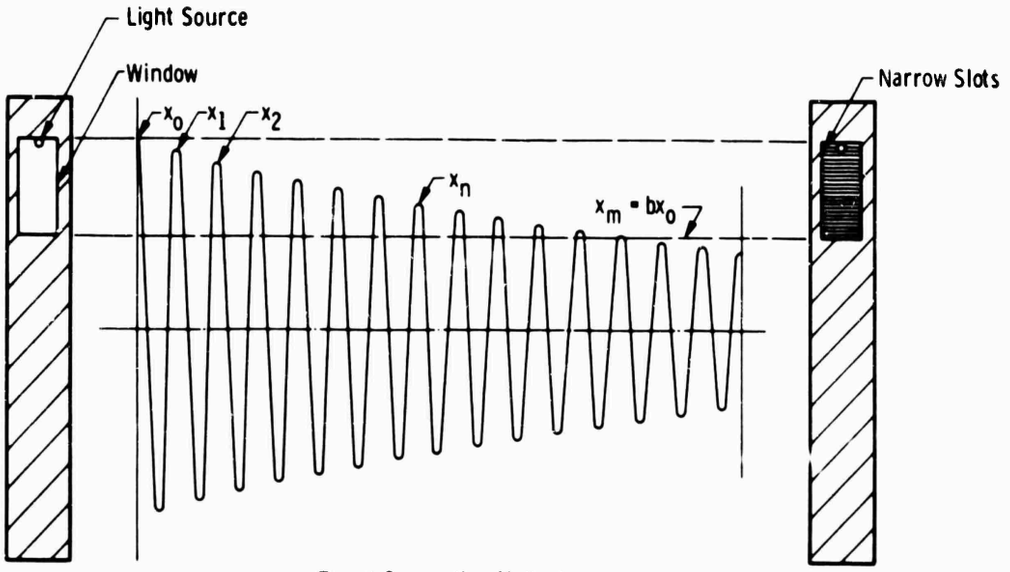

Travel Summation Method

$$\Delta = \frac{2}{s}(1 - b + b \ln b)$$

$$s = \frac{2}{x_0} \sum_{0}^{m} (x_n - x_m) - (x_0 - x_m)$$

Source NAE, Ref. 54

Fig. 57 Free-oscillation data reduction

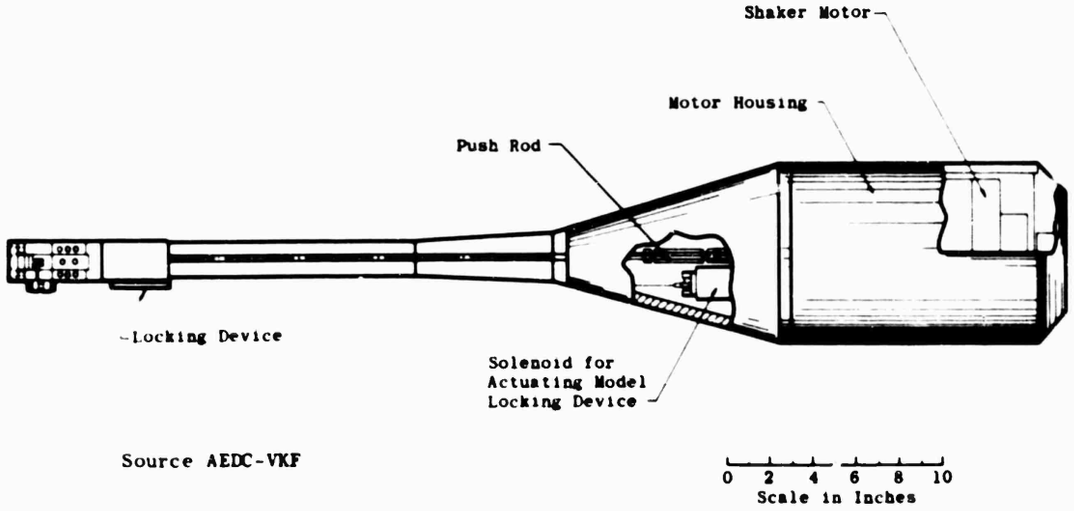

Source AEDC-VKF

Fig. 58 Sting balance assembly of the forced oscillation balance system

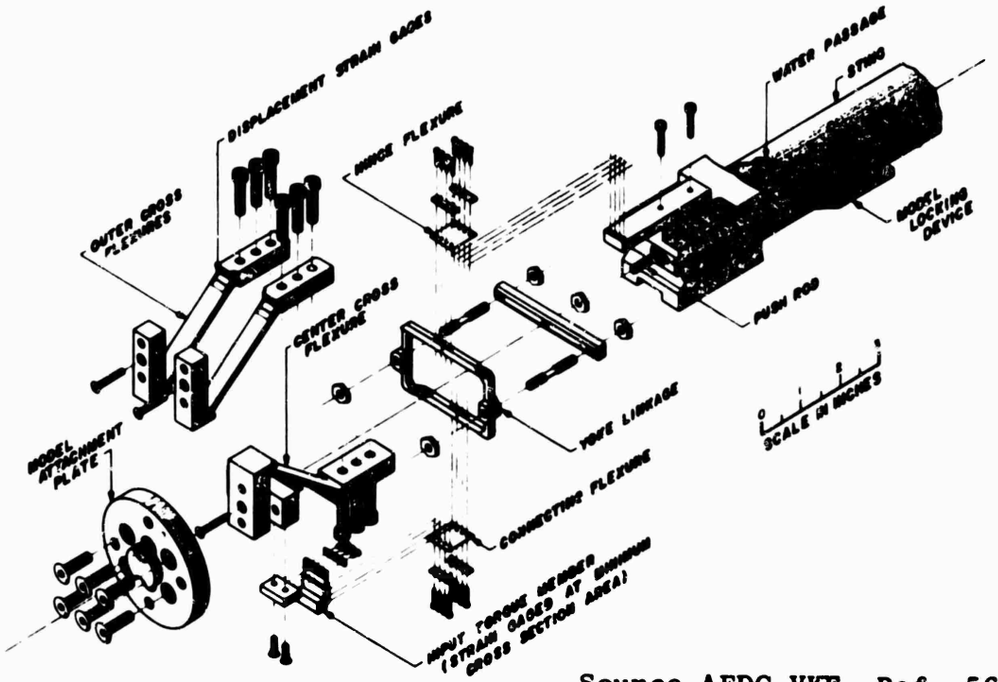

Source AEDC-VKF, Ref. 56

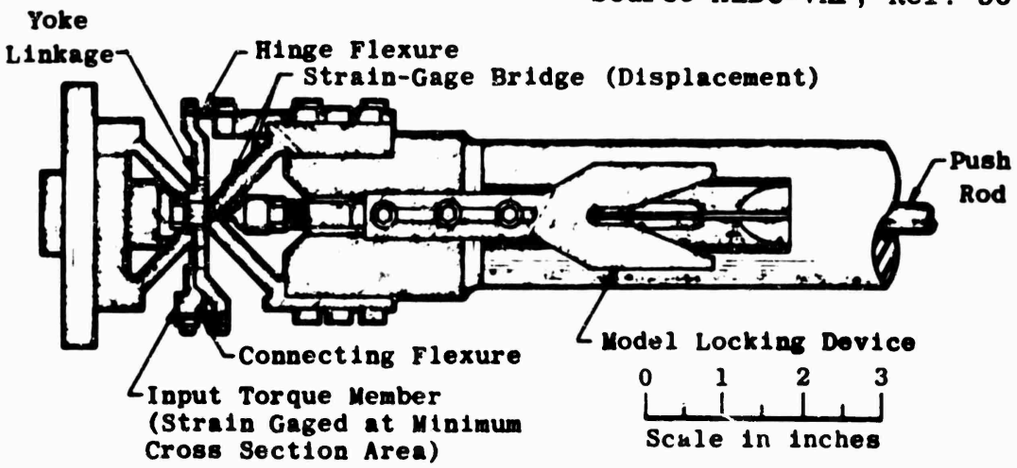

Fig. 59 Small amplitude (±3 deg), forced oscillation balance

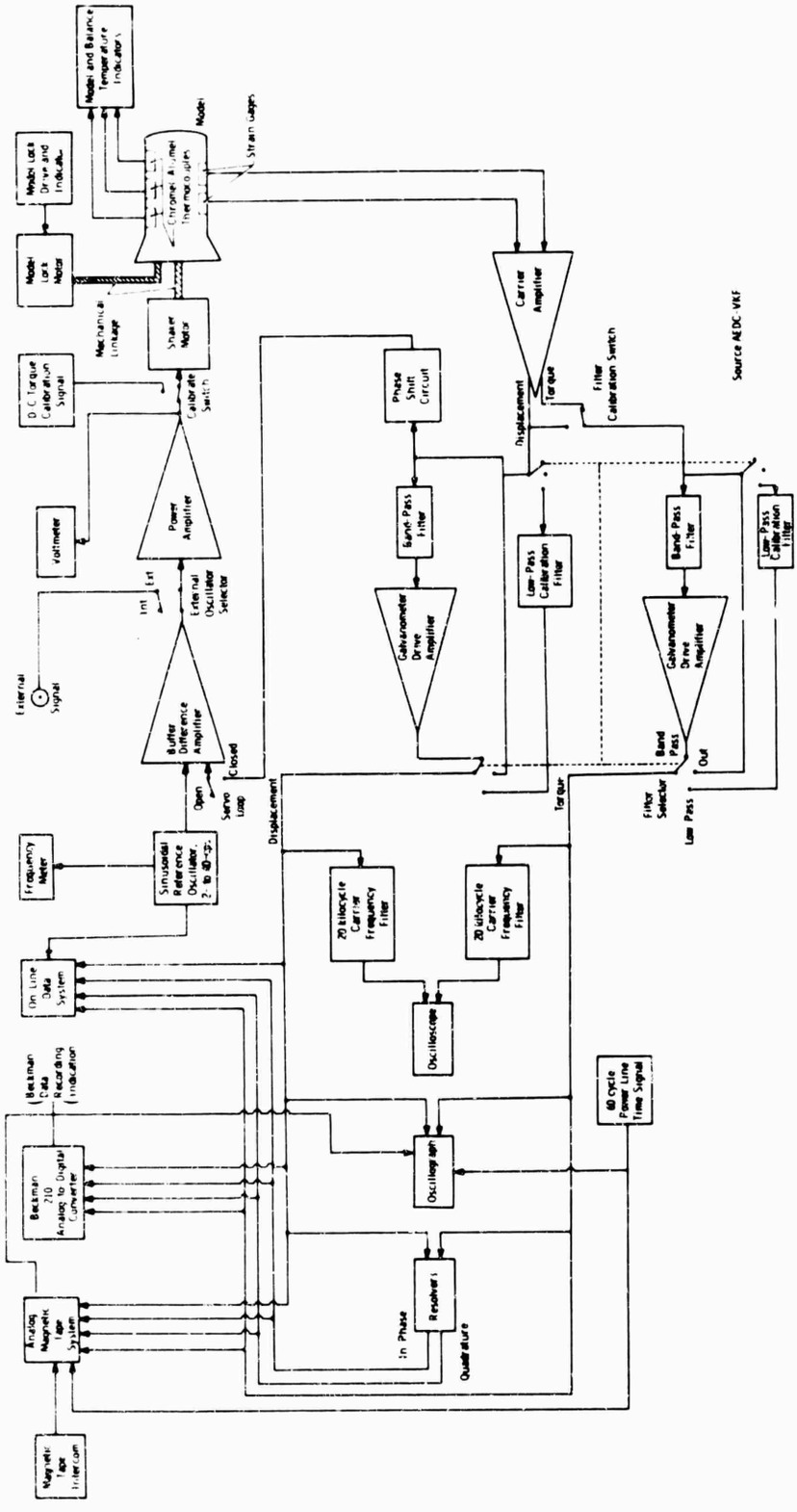

Fig. 60 Dynamic stability control and readout system

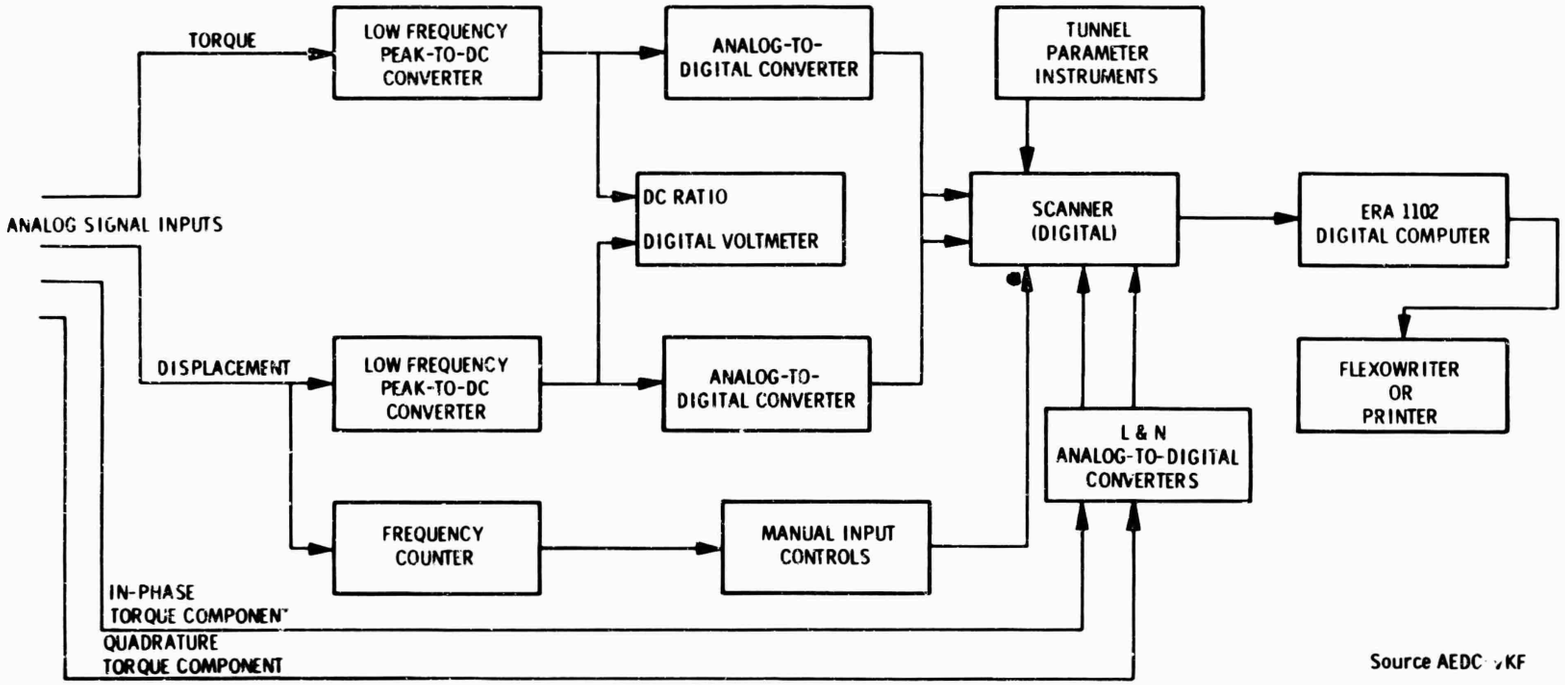

Fig 31 On-line data system for forced-oscillation dynamic stability testing

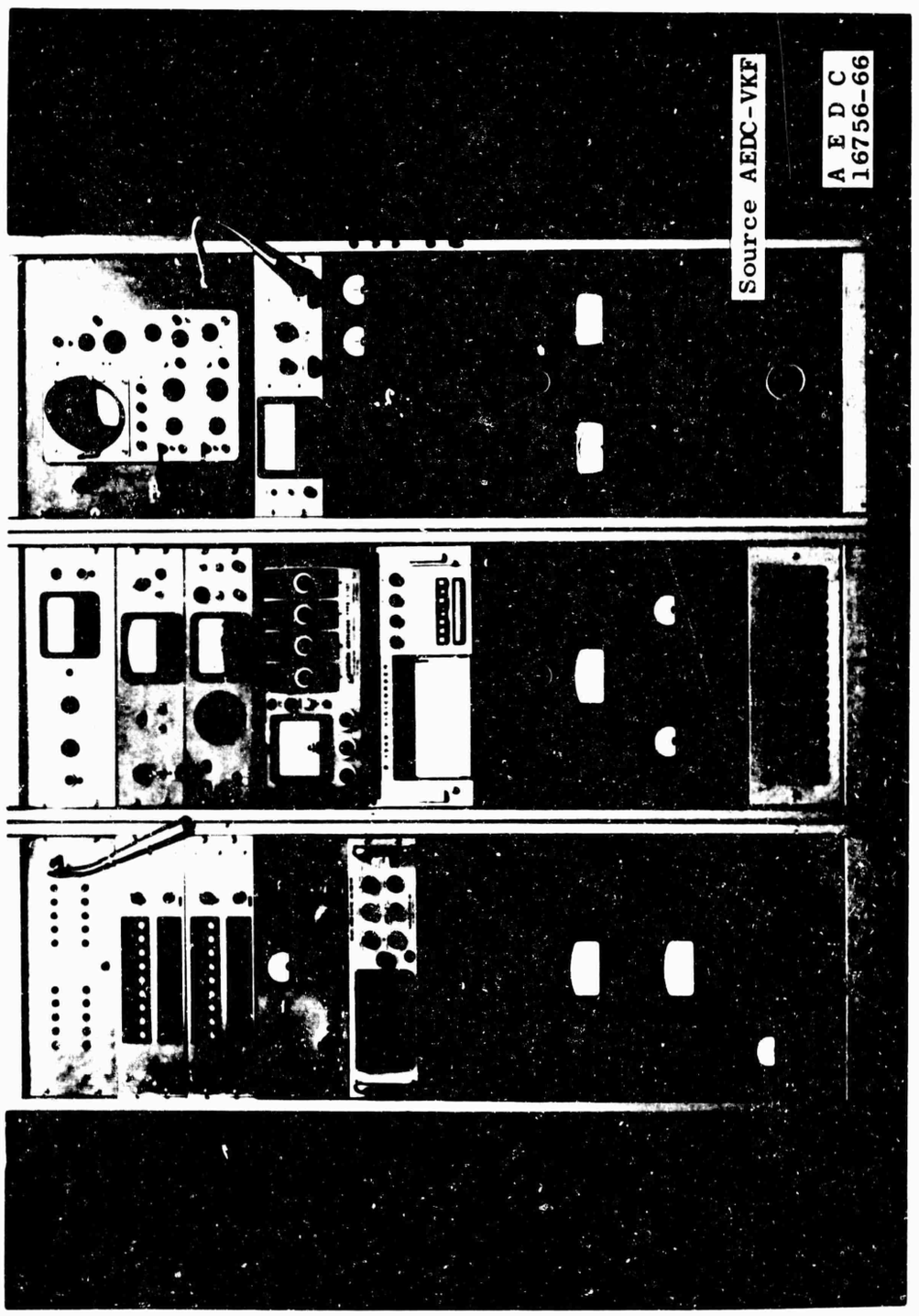

Fig. 62 Control panel for forced-oscillation system

Source AEDC-PWT, Ref. 57

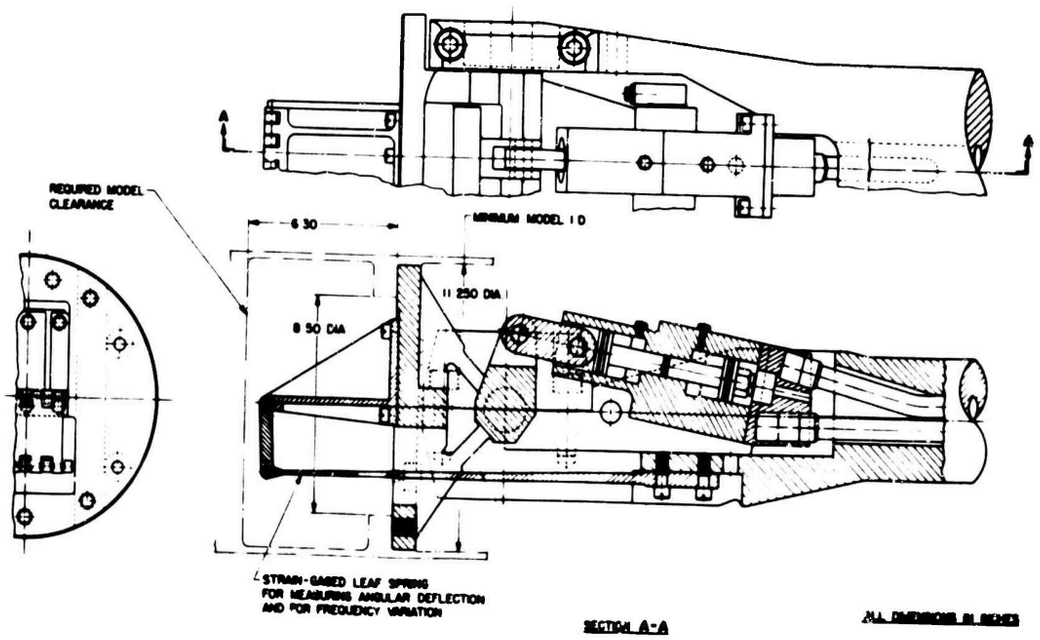

Fig. 63 Forced-oscillation balance

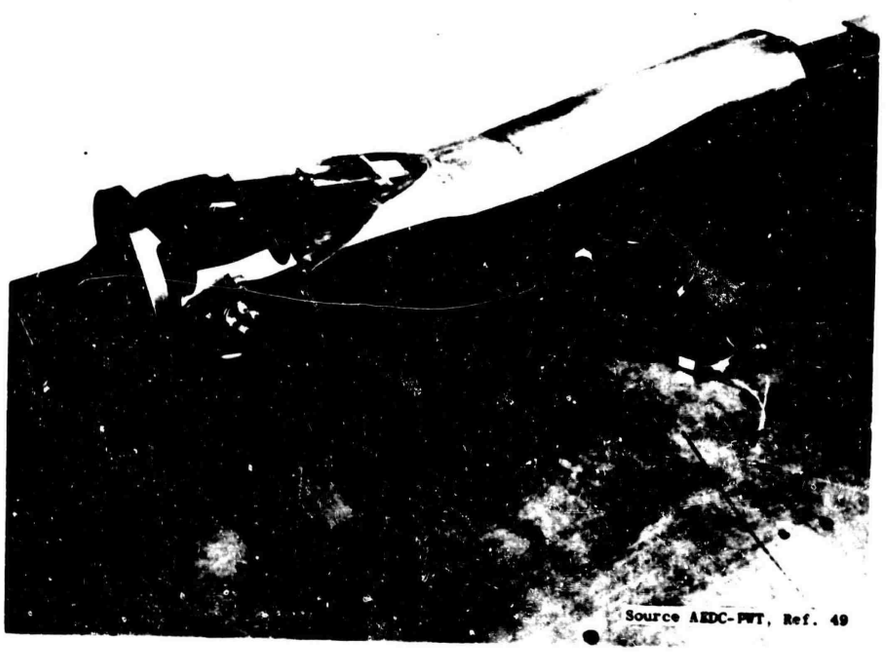

Fig. 63 Continued

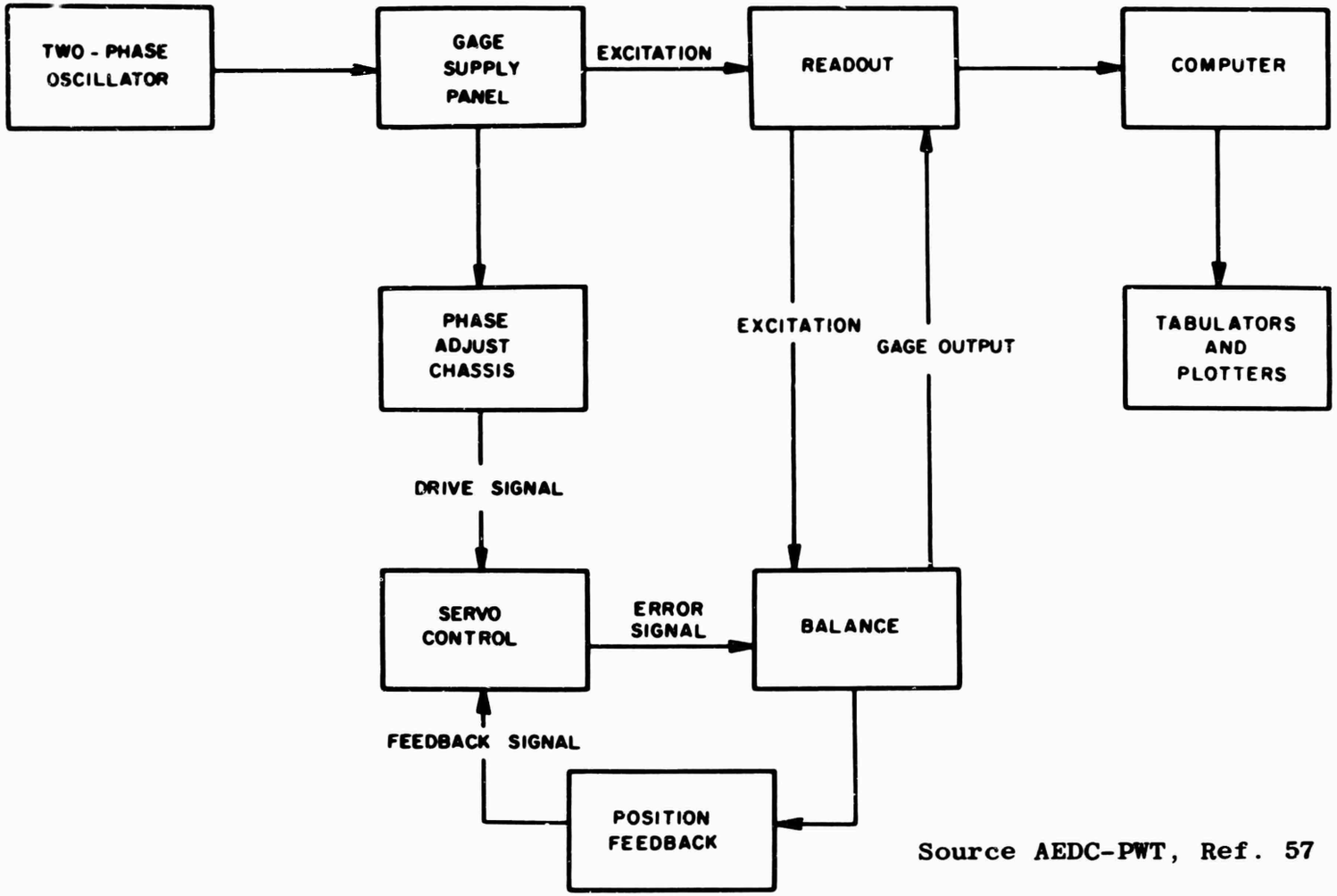

Fig. 64 System block diagram for forced-oscillation balance

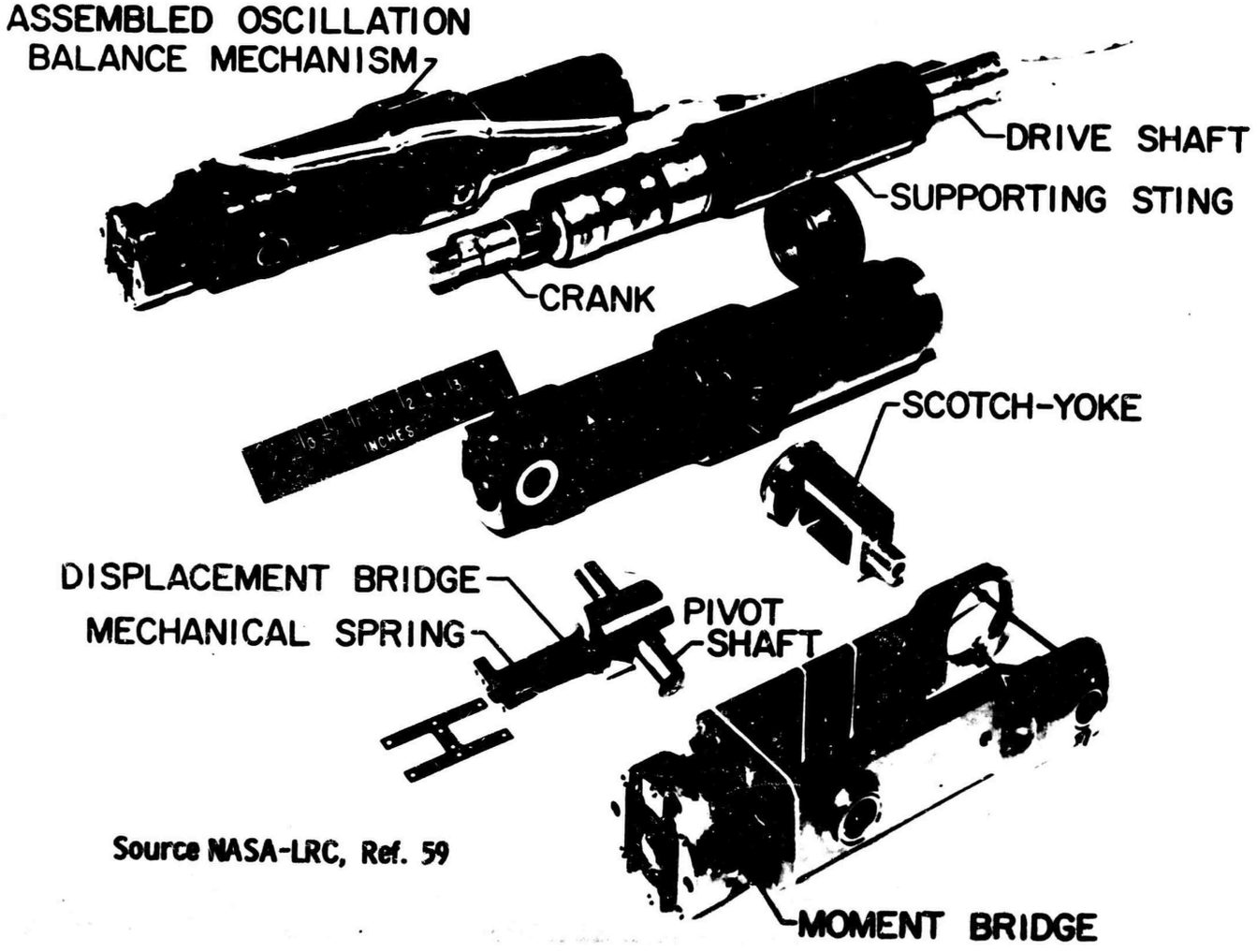

Fig. 65 Photograph of the forward portion of the forced-oscillation balance mechanism

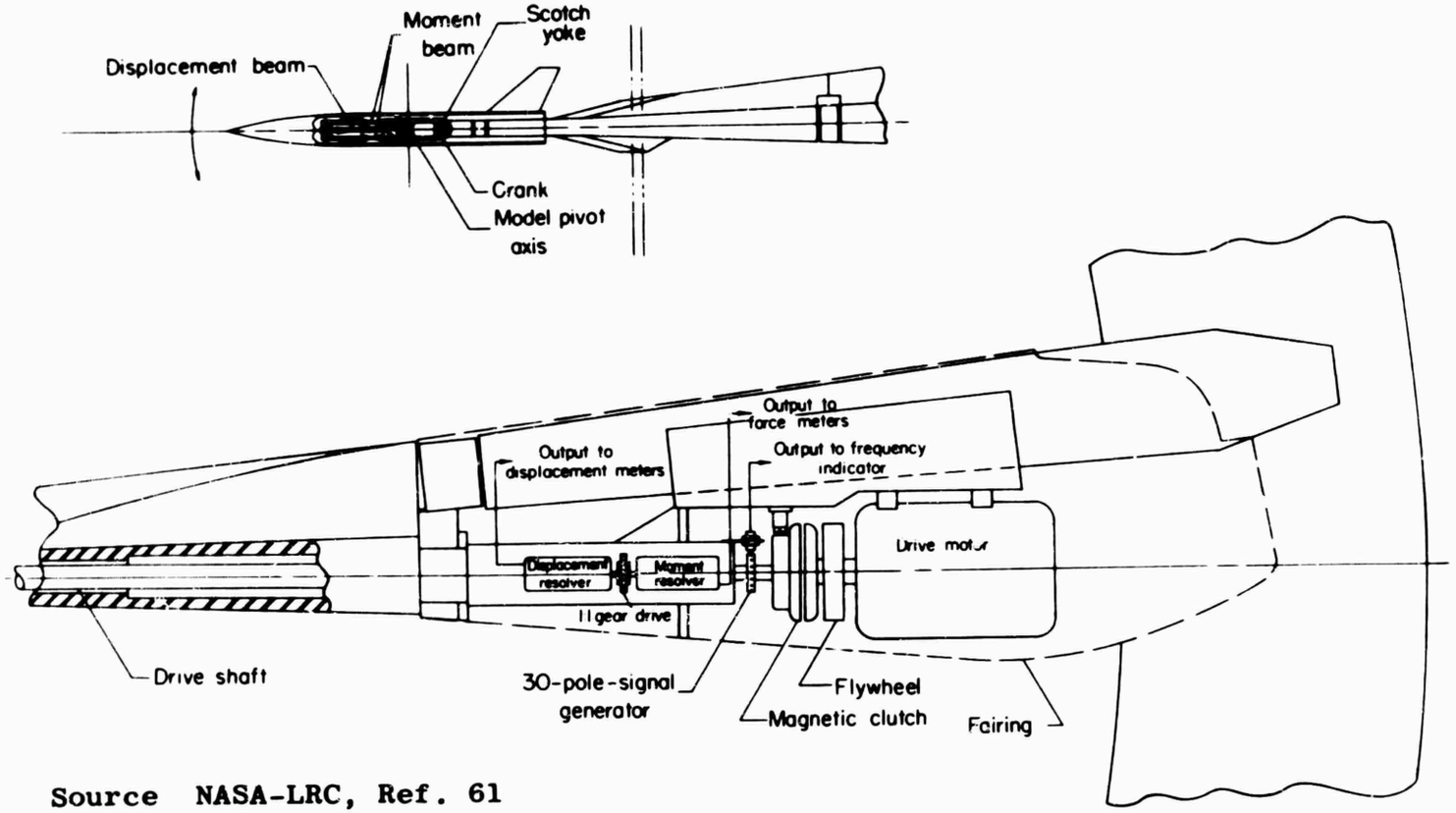

Source NASA-LRC, Ref. 61

Fig. 66 Schematic view of model and driving-system components

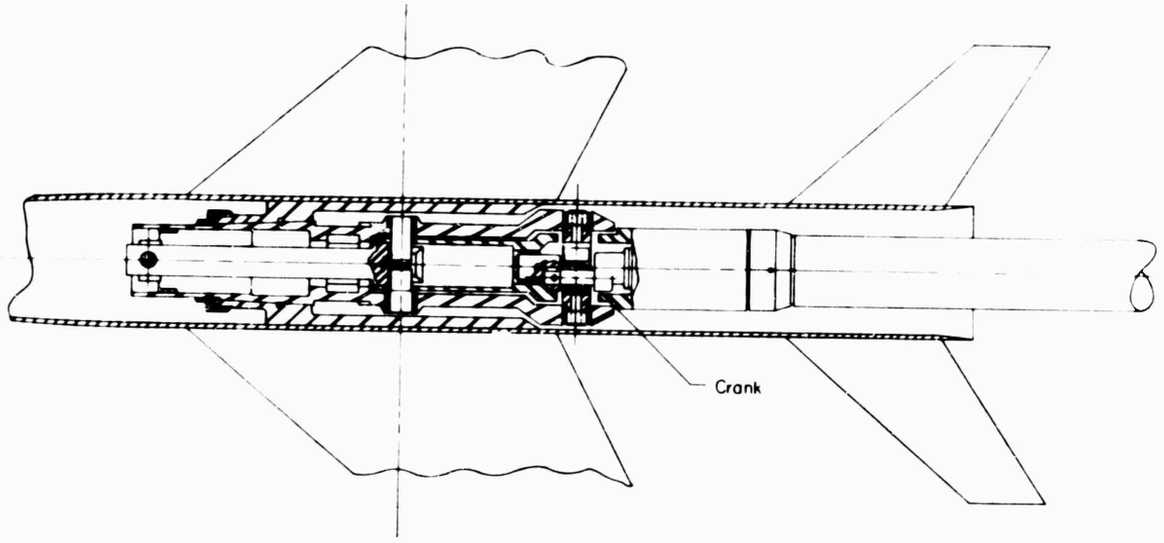

Source NASA-LRC, Ref. 61

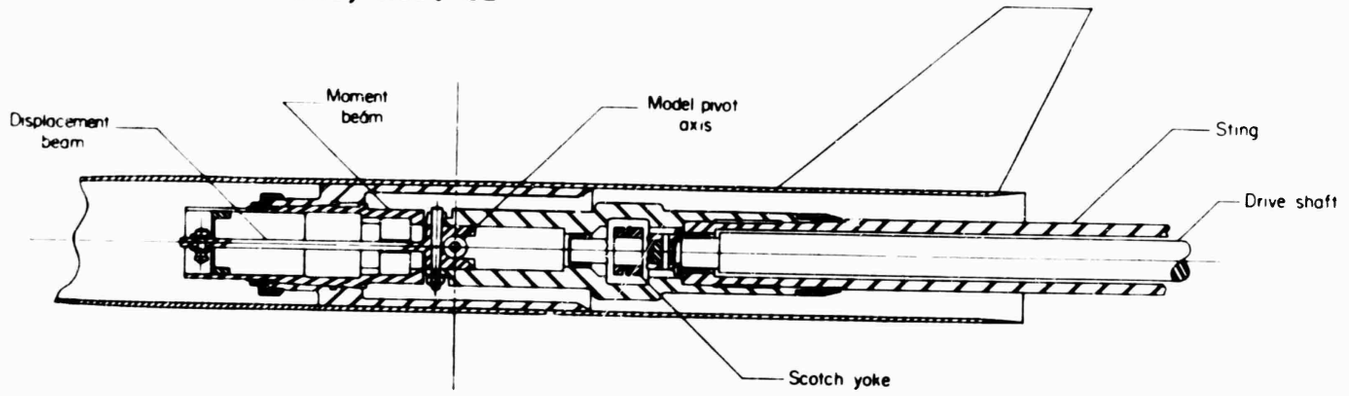

Fig. 67 Details of oscillating mechanism

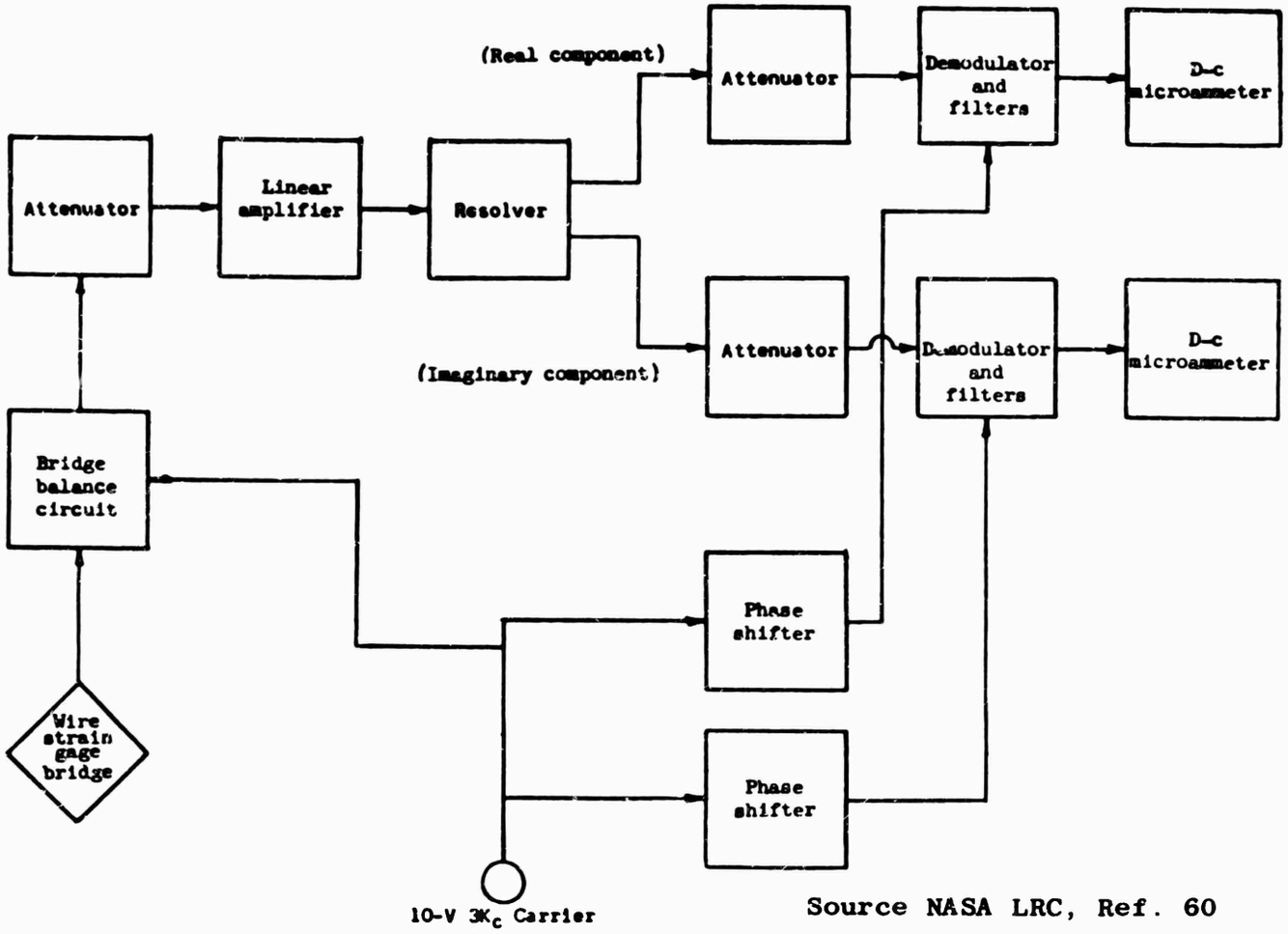

Fig. 68 Block diagram of electronic circuits used to measure model displacement and applied moment

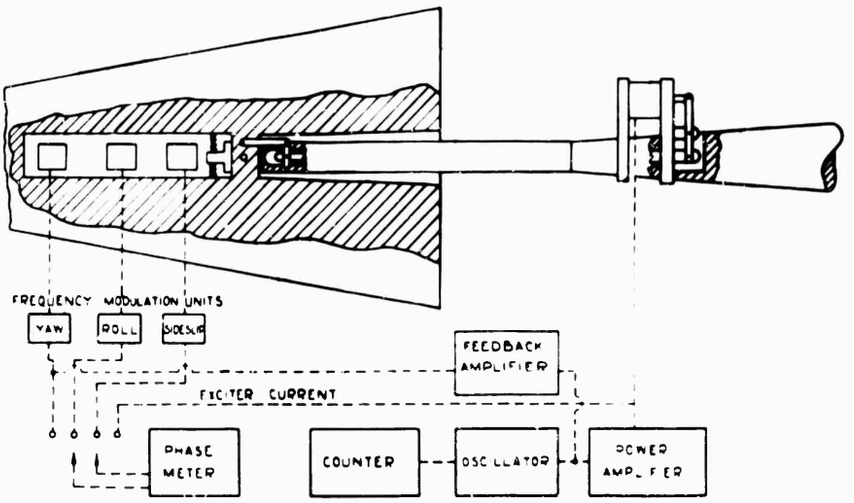

Schematic arrangement for yaw-sideslip oscillations.

Source RAE, Ref. 61

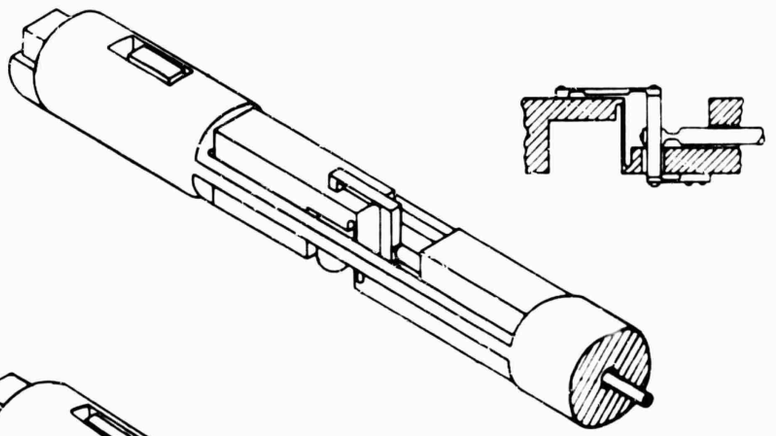

Pitch or yaw spring unit.

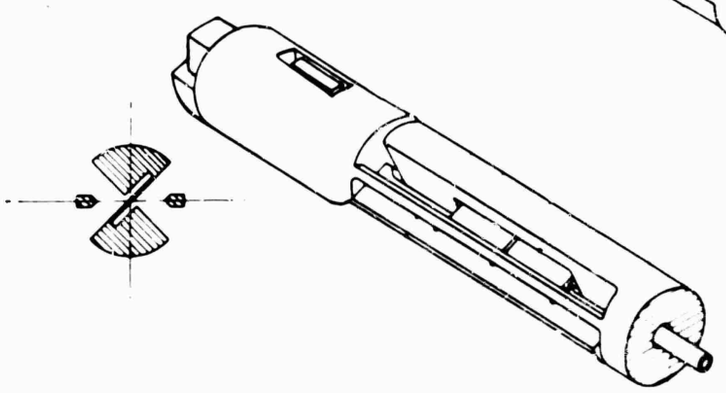

Roll spring unit.

Fig. 69 Forced-oscillation dynamic stability balance

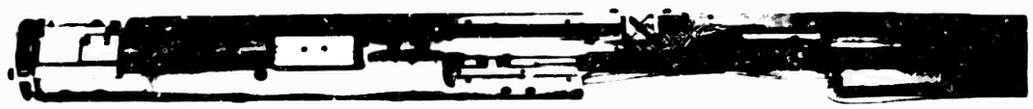

Balance

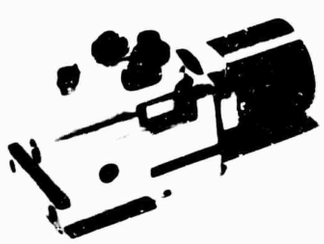

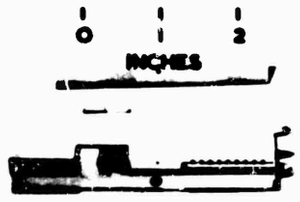

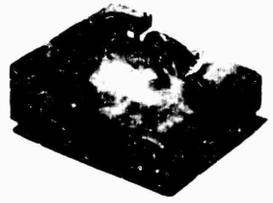

Source RAE, Ref. 61

Accelerometers

Fig. 70 Yaw-roll balance and accelerometers

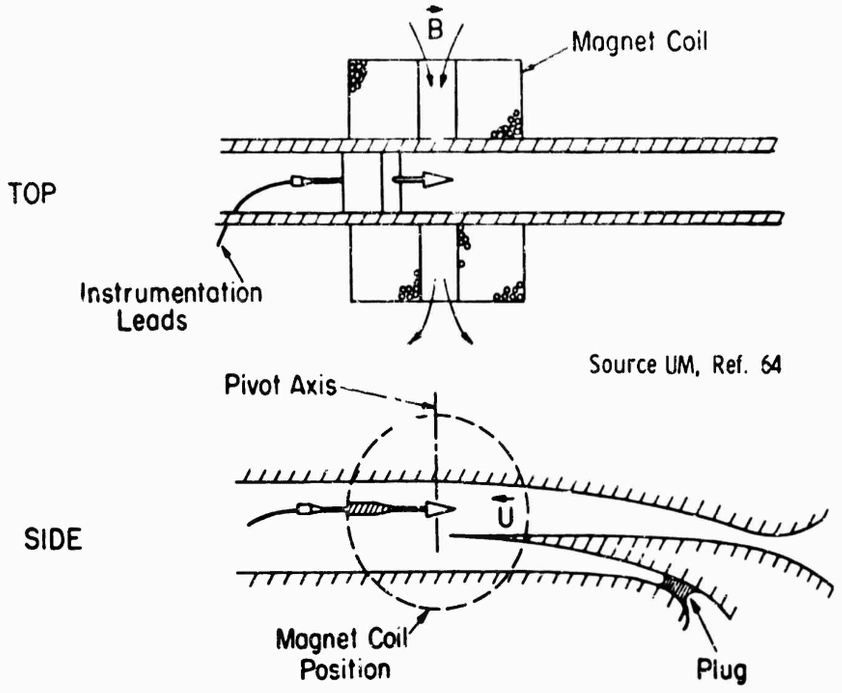

Fig. 71 Forced-oscillation balance with electromagnetic excitation

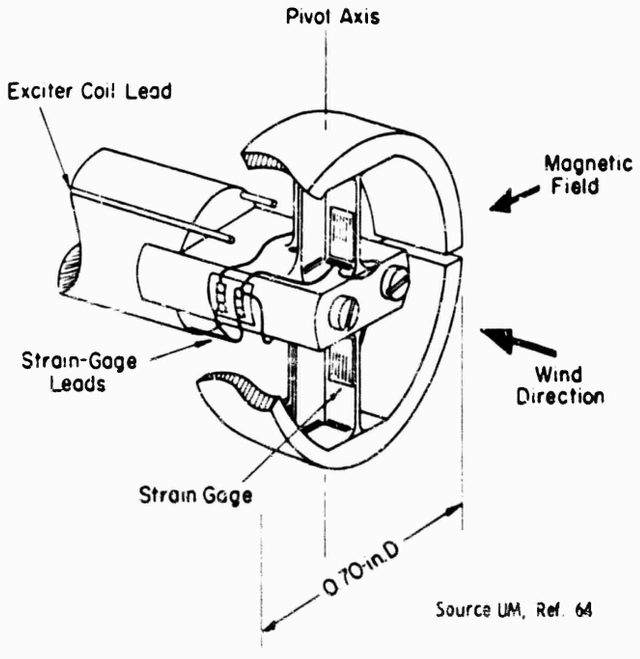

Fig. 72 Cutaway view of torsional flexure pivot with strain gages for forced-oscillation balance with electromagnetic excitation

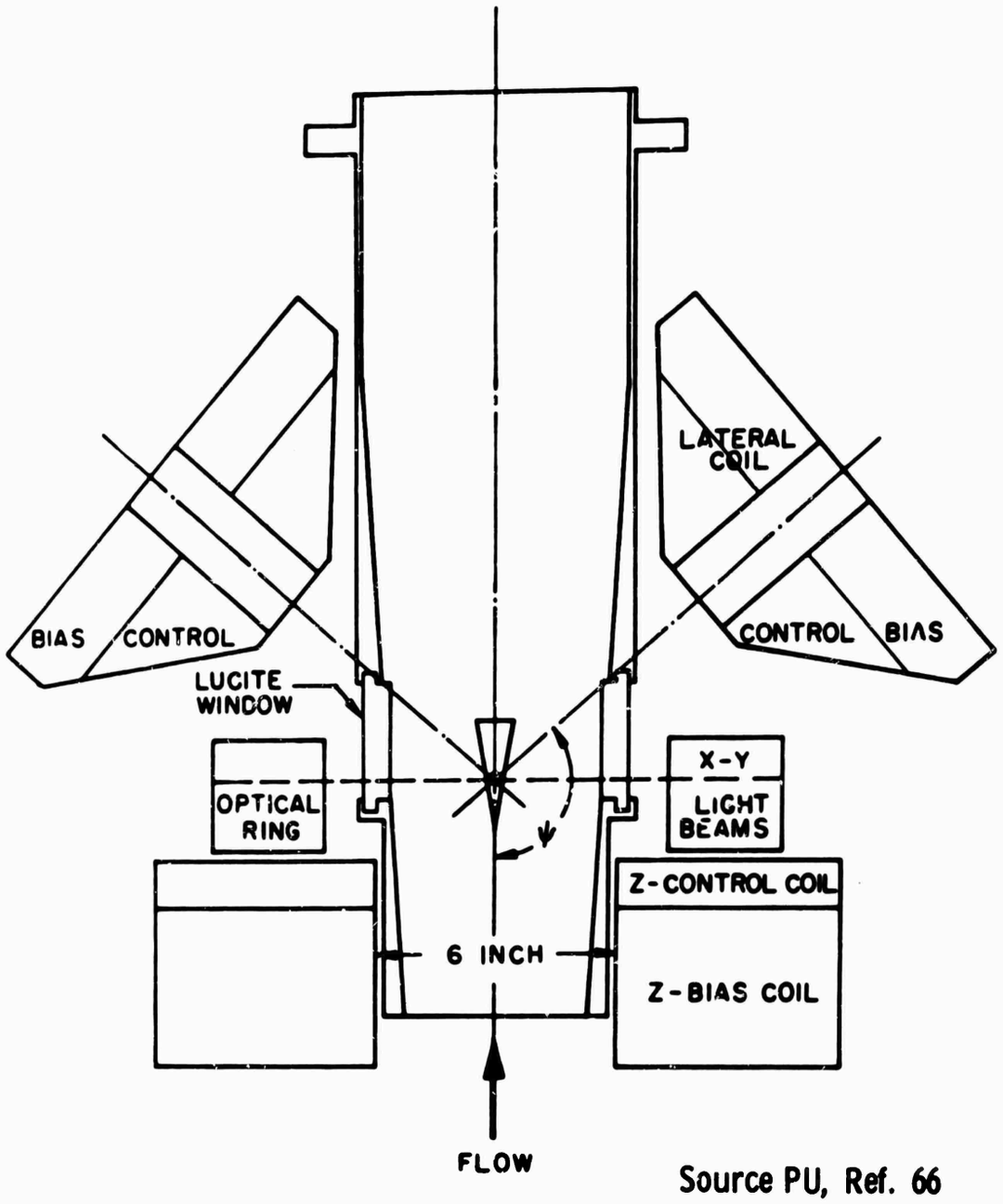

Fig. 73 Magnetic model suspension system

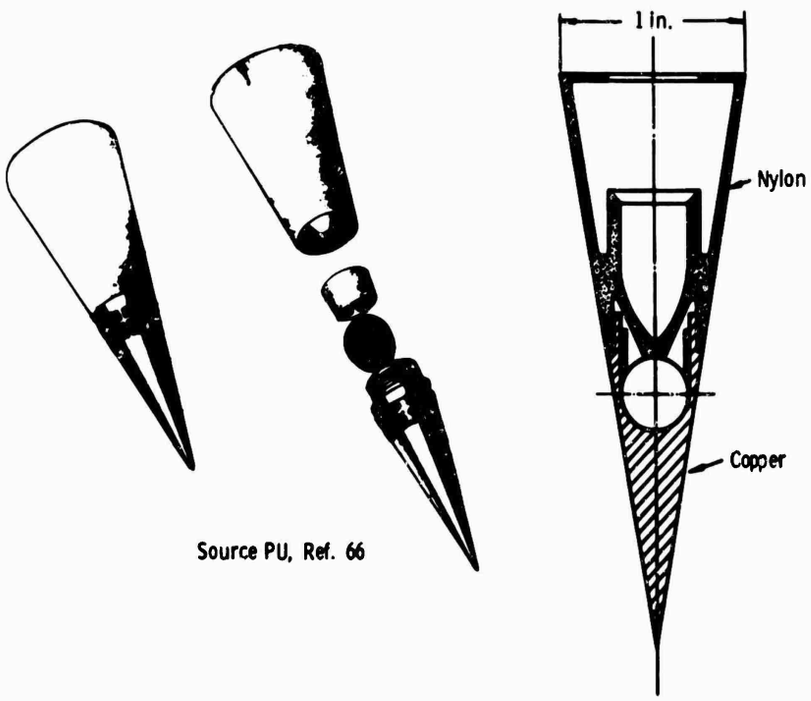

Fig. 74 Cone model for magnetic suspension

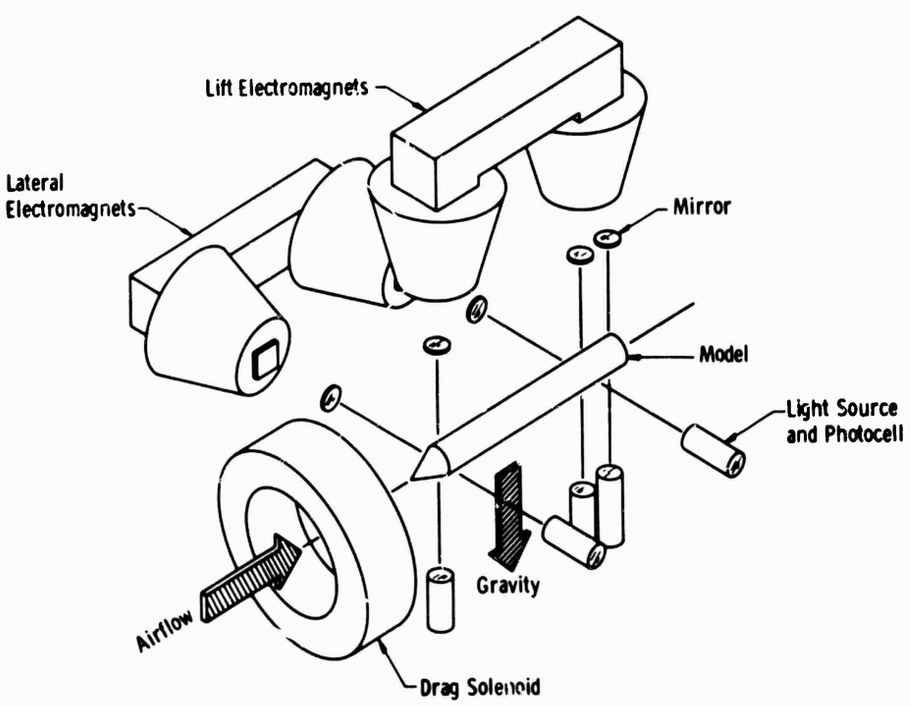

Fig. 75 Basic L configuration magnetic suspension system

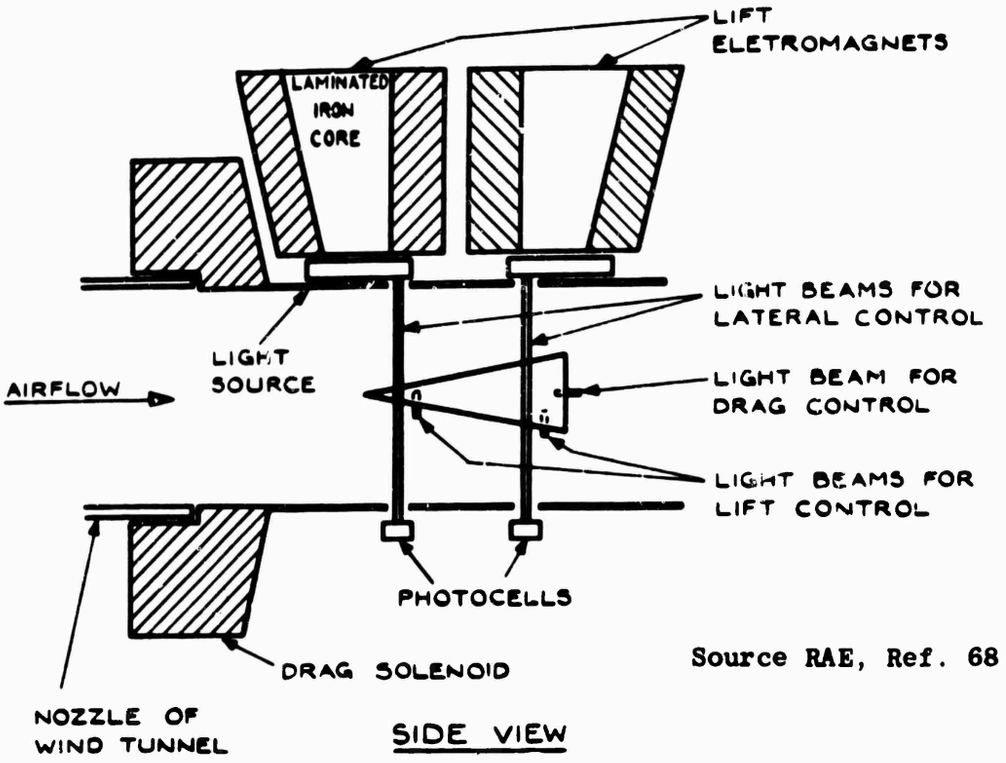

Source RAE, Ref. 68

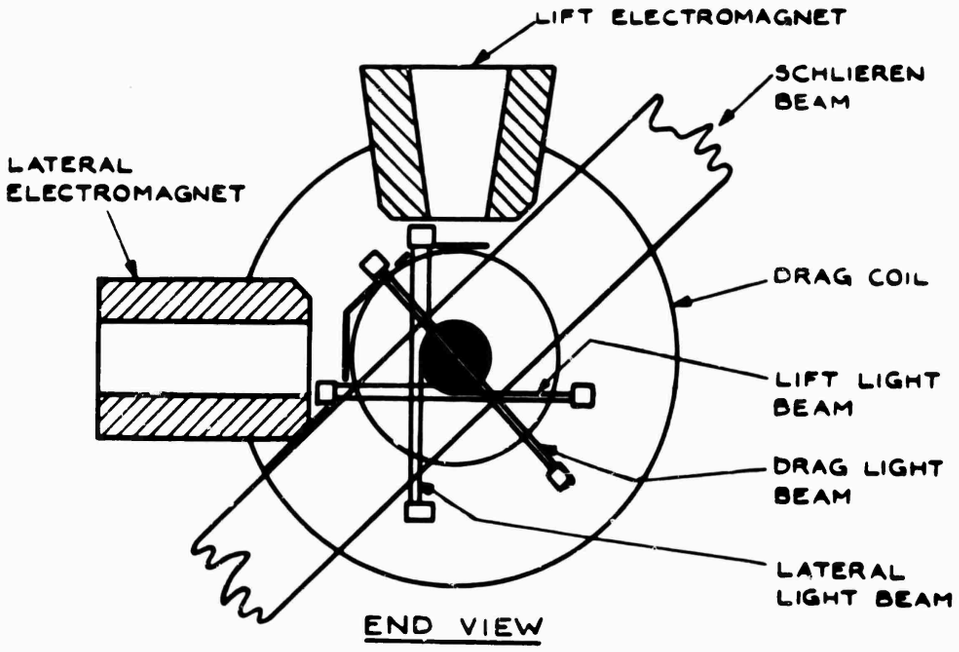

Fig. 76 Magnetic suspension system

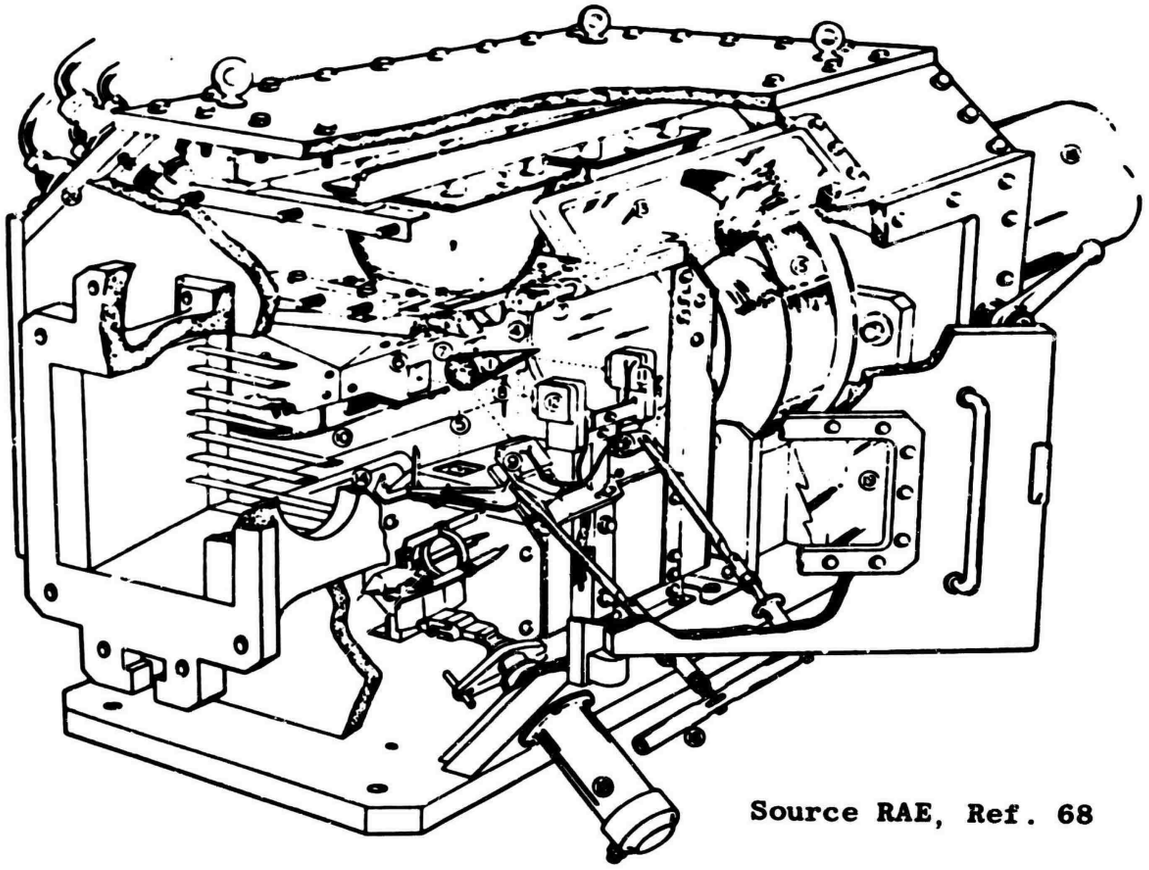

① CONICAL TEST MODEL
② FRONT LIFT ELECTROMAGNET
③ REAR LIFT ELECTROMAGNET
④ FRONT LATERAL LIGHT BEAM
⑤ REAR LATERAL LIGHT BEAM
⑥ QUARTZ WINDOW
⑦ DRAG LIGHT BEAM
⑧ REAR LIFT LIGHT BEAM
⑨ DRAG PHOTOCELL
⑩ REAR LATERAL ELECTROMAGNET
⑪ FRONT LIFT PHOTOCELL
⑫ REAR LIFT PHOTOCELL
⑬ UPPER SCHLIEREN WINDOW
⑭ LOWER SCHLIEREN WINDOW
⑮ DRAG COIL
⑯ INLET NOZZLE (M = 8·63)
⑰ LIGHT SOURCE UNIT
⑱ MODEL LAUNCHING UNITS
⑲ OBSERVATION WINDOW
⑳ SERVICES SUPPLY PANEL

Source RAE, Ref. 68

Fig. 77 Magnetic suspension working section. 7 in. × 7 in. hypersonic wind tunnel

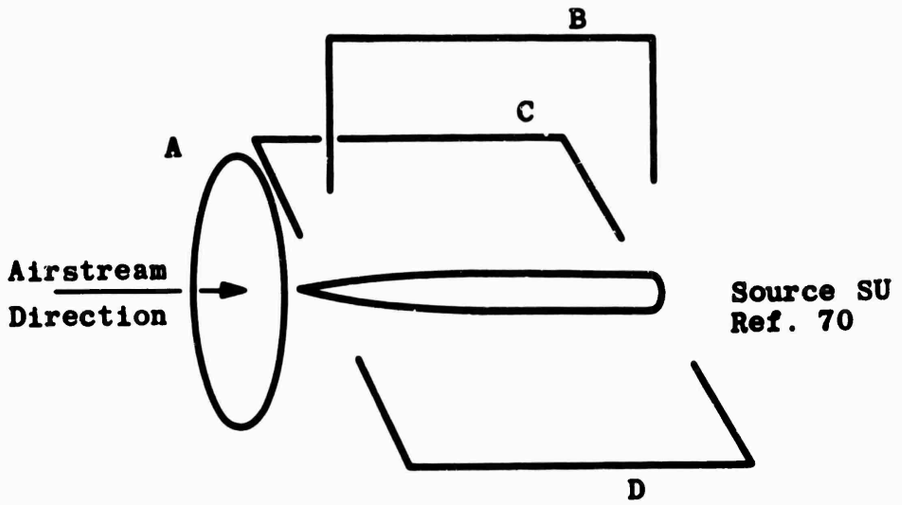

Fig. 78 Schematic diagram of the suspension magnet array of a six-component magnetic wind tunnel balance and suspension system

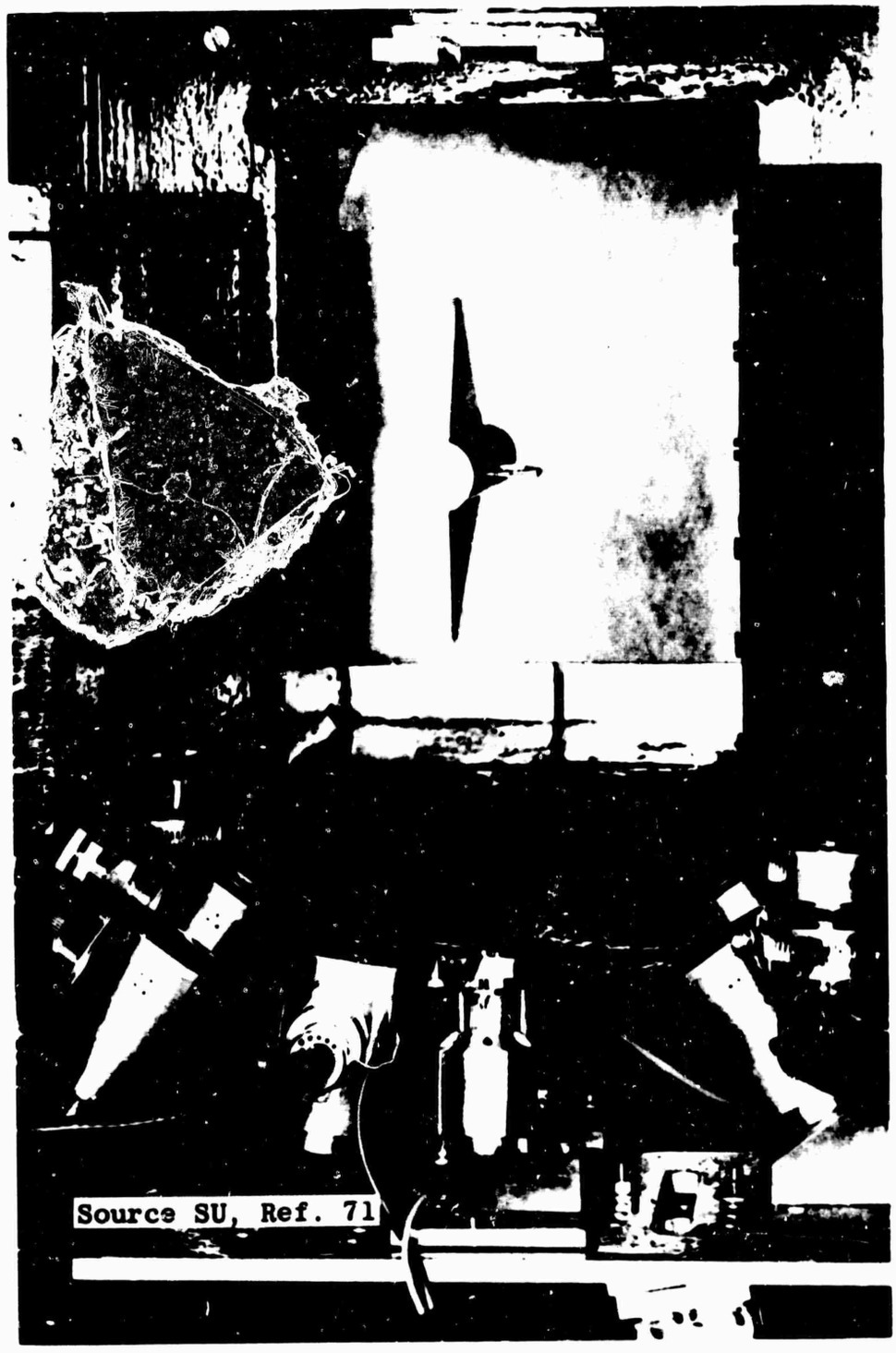

Fig. 79 Model subjected to a forced oscillation in roll while suspended in the six-component balance

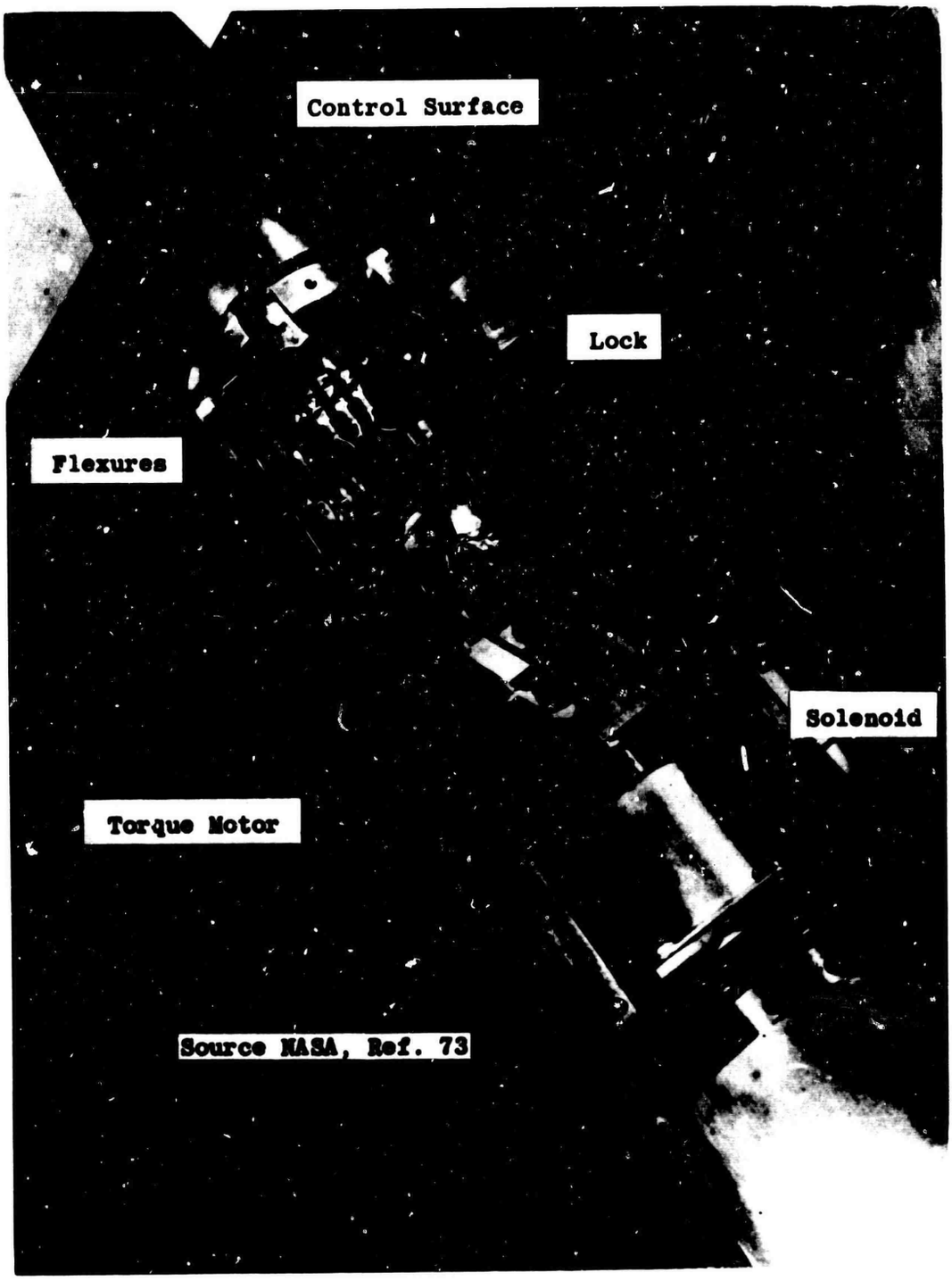

Fig.80 View of control surface drive

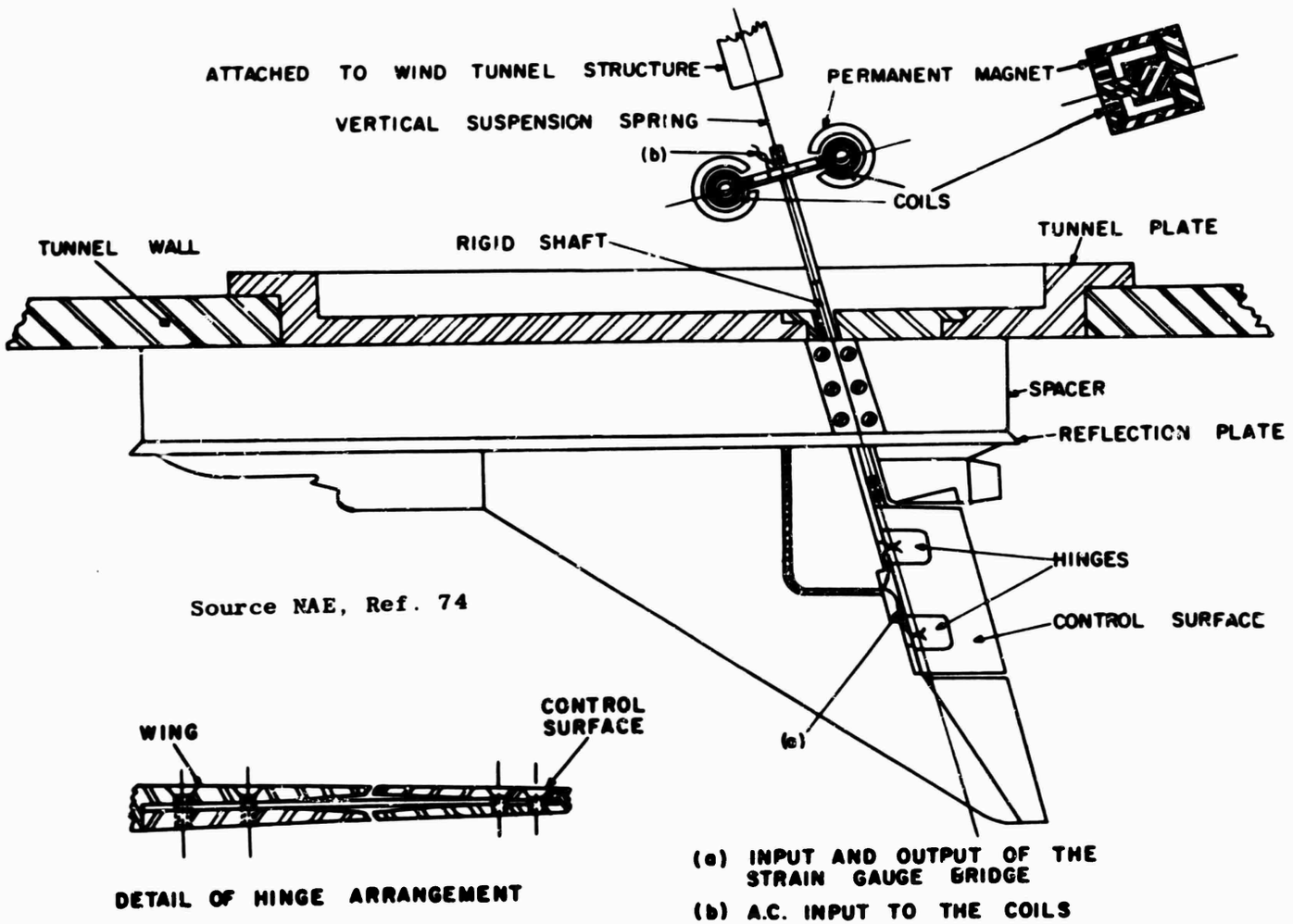

Fig. 81 Apparatus for elevator oscillation

Source NAE, Ref. 74

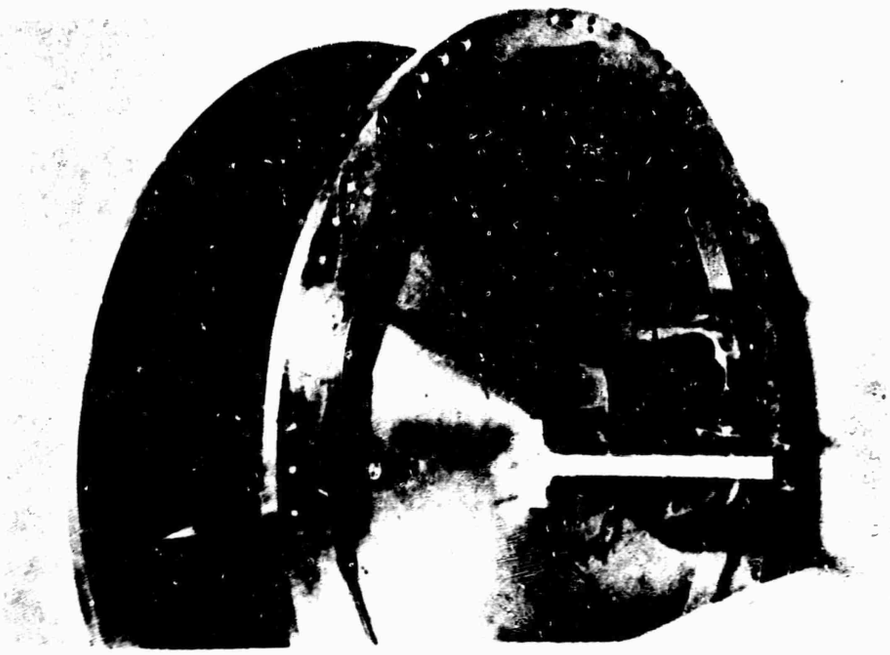

Fig. 82 Apparatus for elevator oscillation

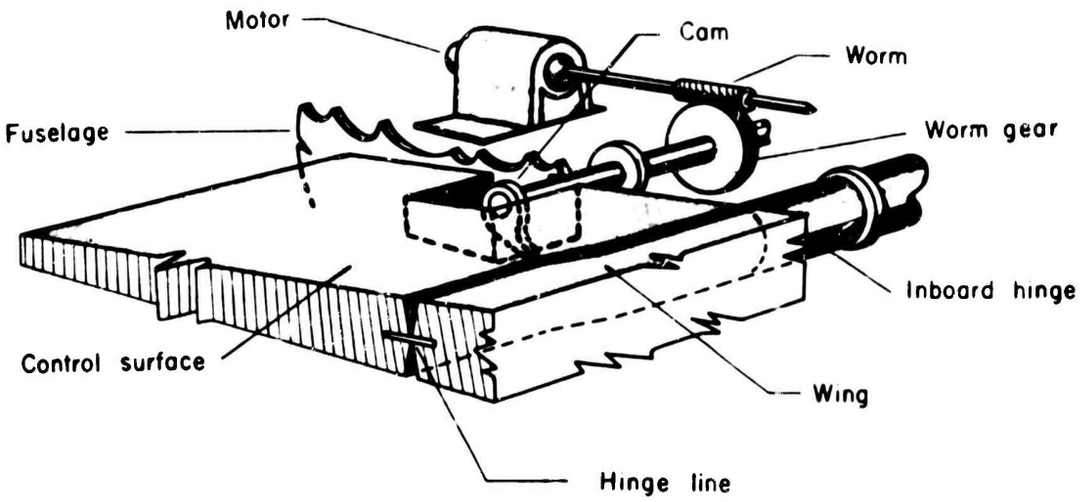

Model B

Source NACA, Ref. 75

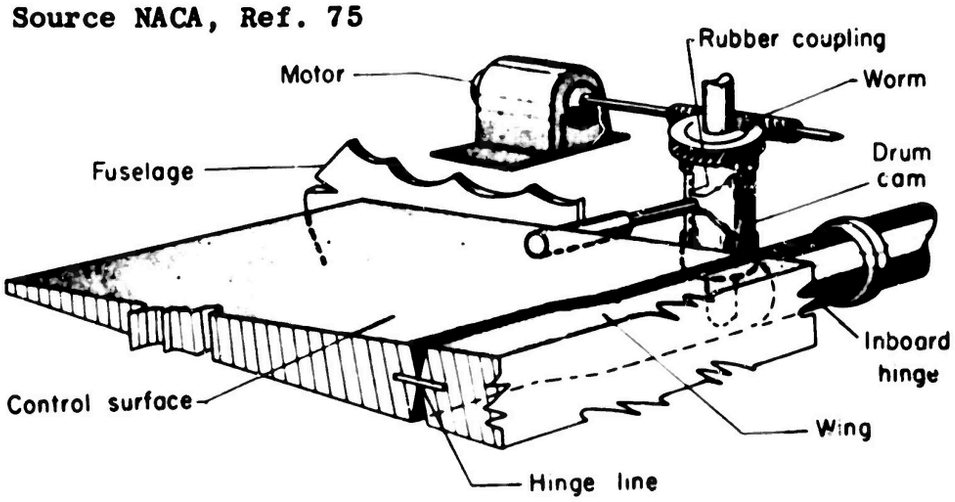

Model A

Fig. 83 Sketch of control surface plucking mechanism

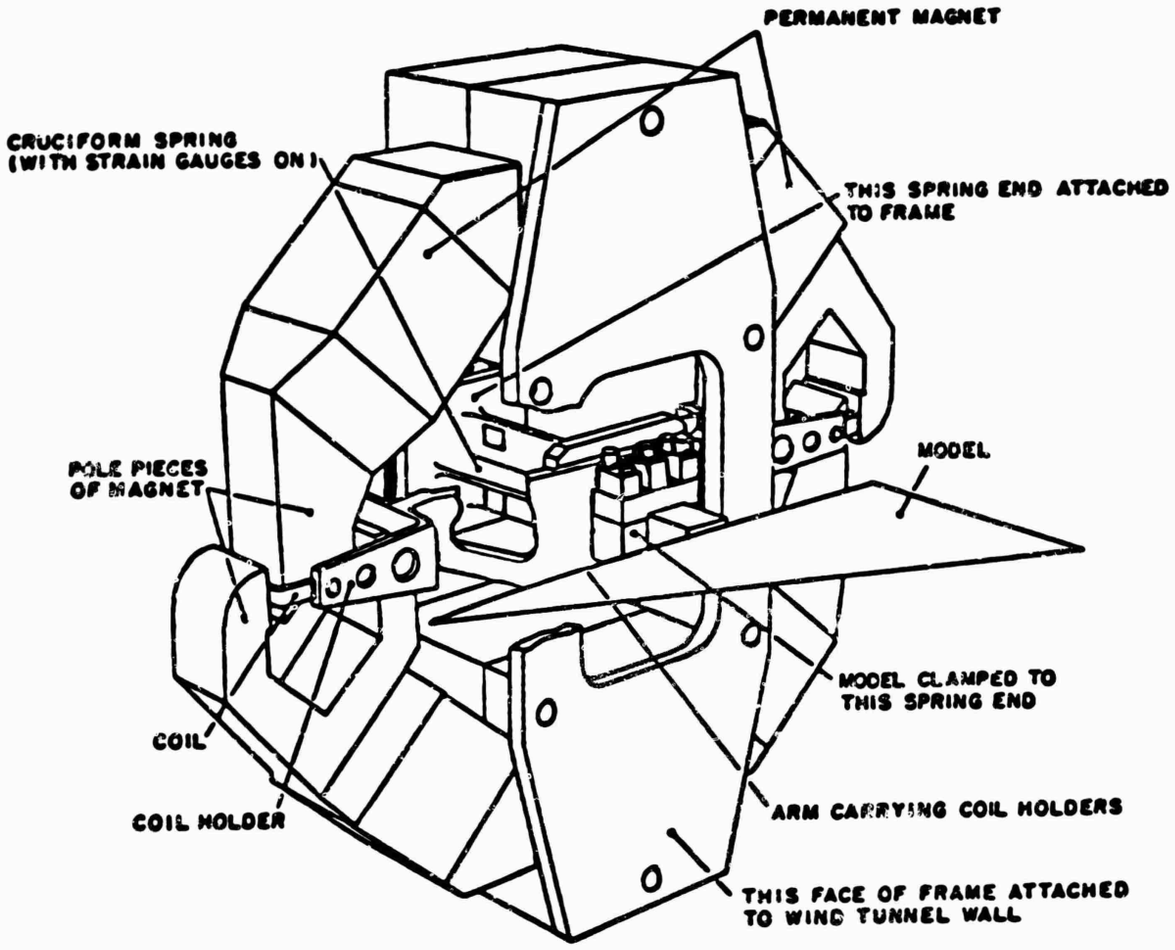

Source NAE, Ref. 76

Fig. 84 Elastic model suspension and electromagnetic oscillator for oscillation-in-pitch

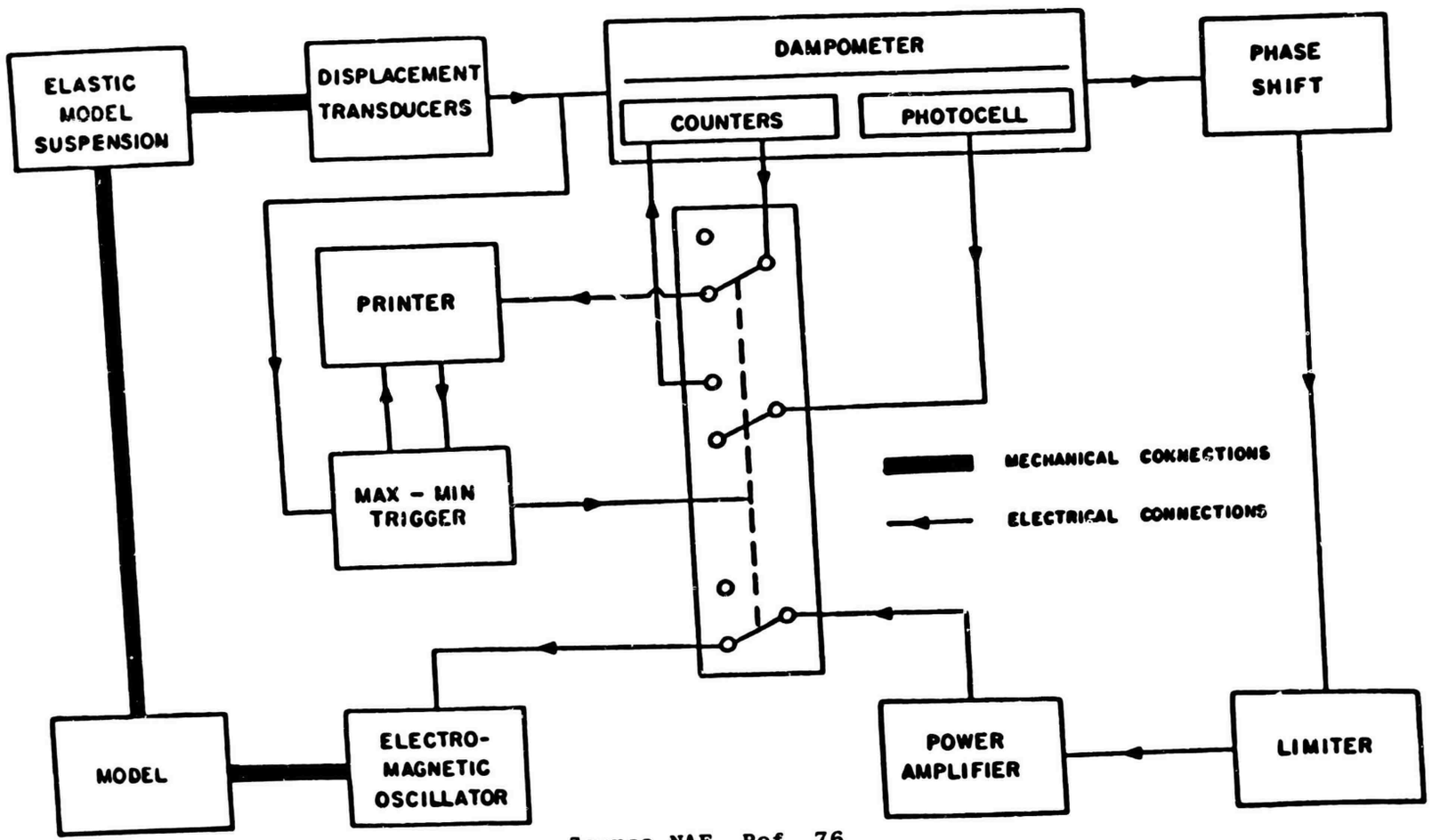

Source NAE, Ref. 76

Fig. 85 Free oscillation with automatically recycled feedback excitation

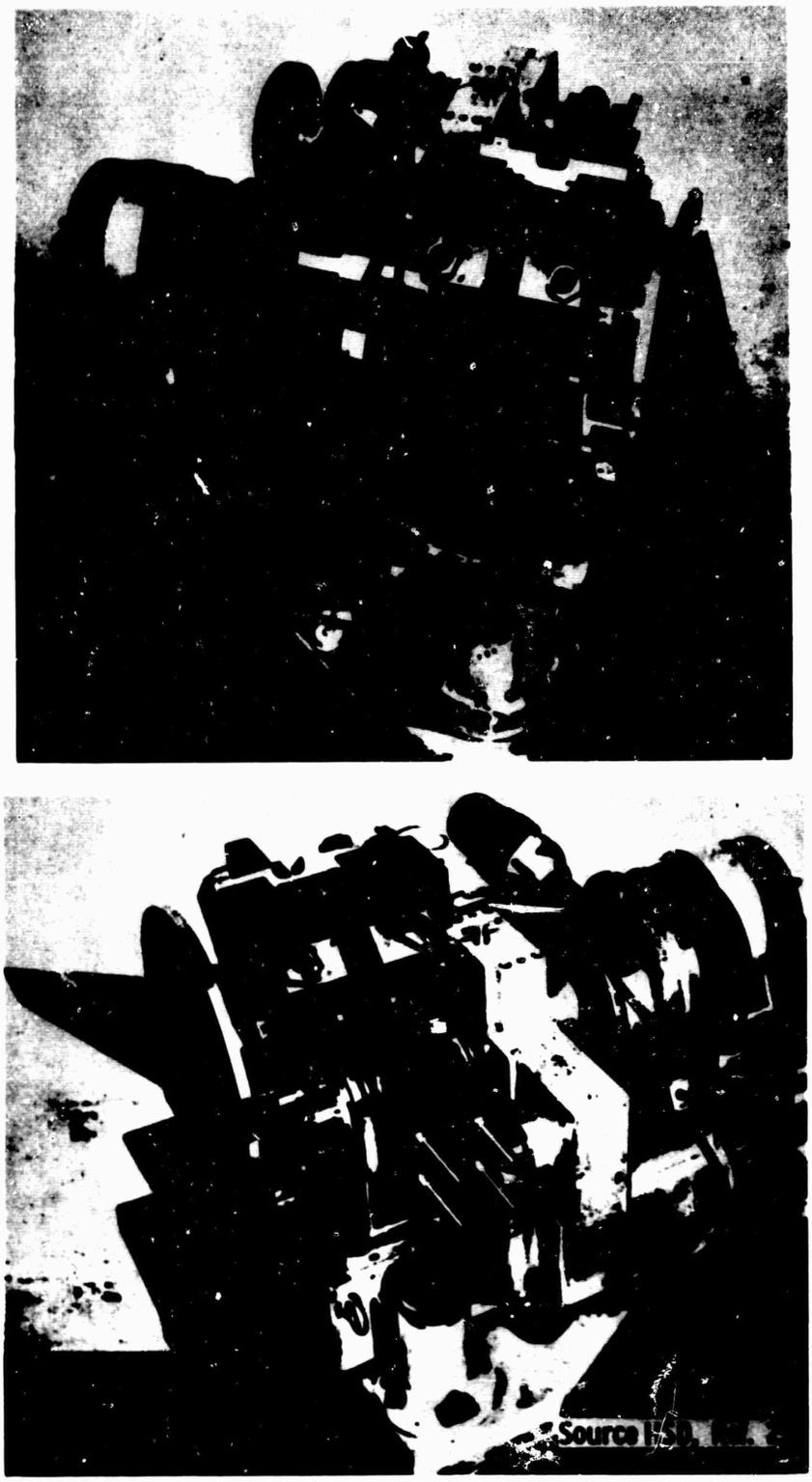

Fig. 86 Half-model oscillating rig

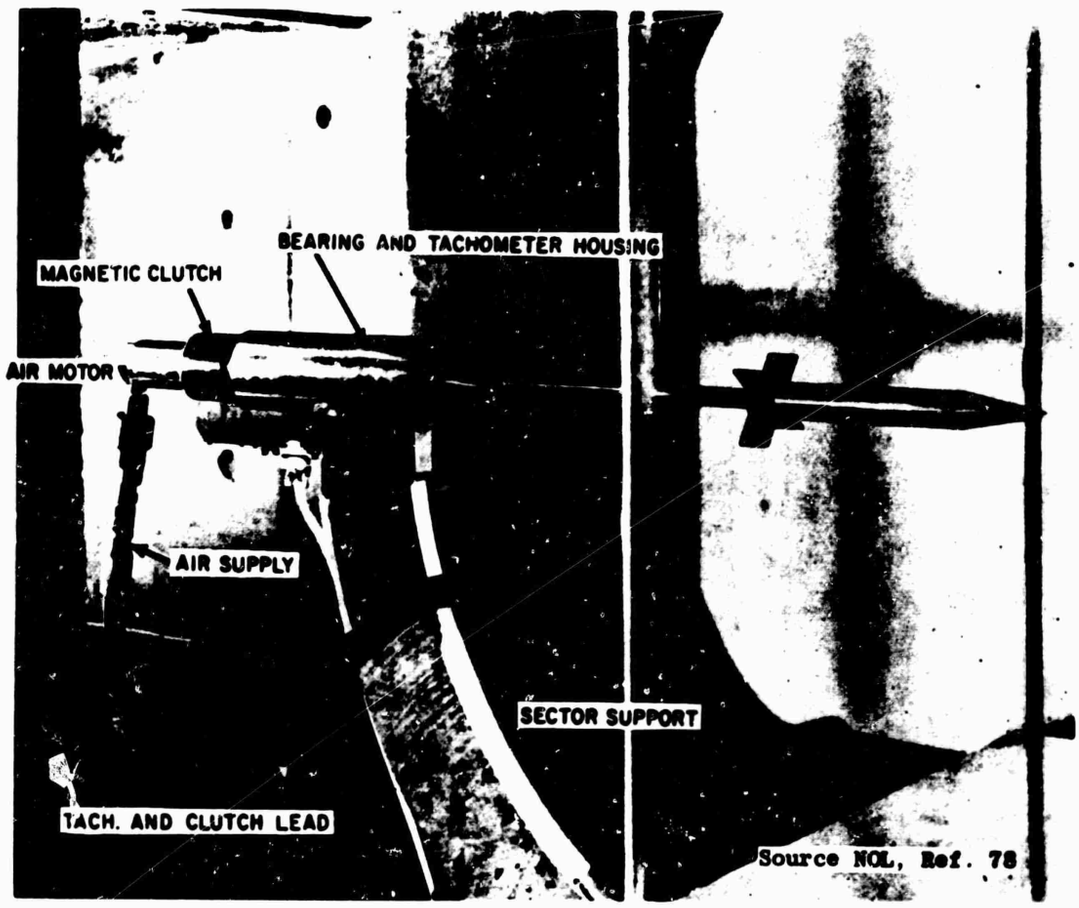

Fig. 87 Roll-damping system

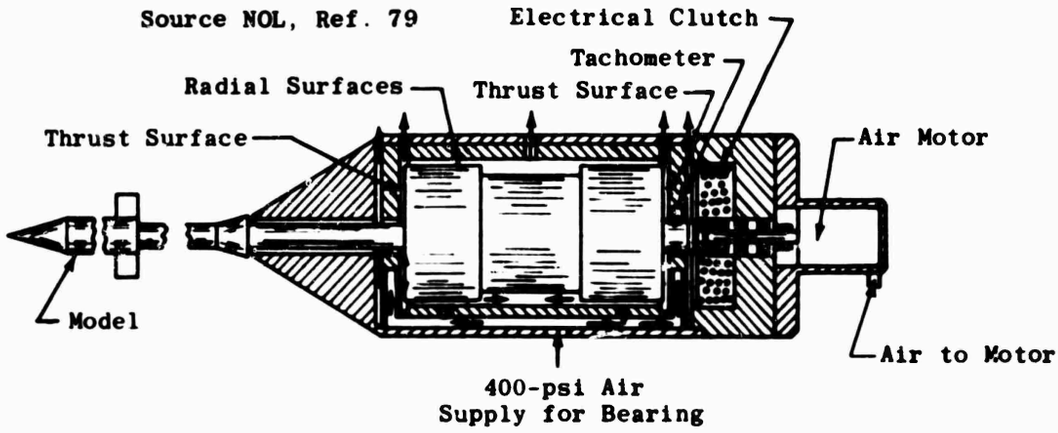

Fig. 88 Air bearing roll-damping mechanism

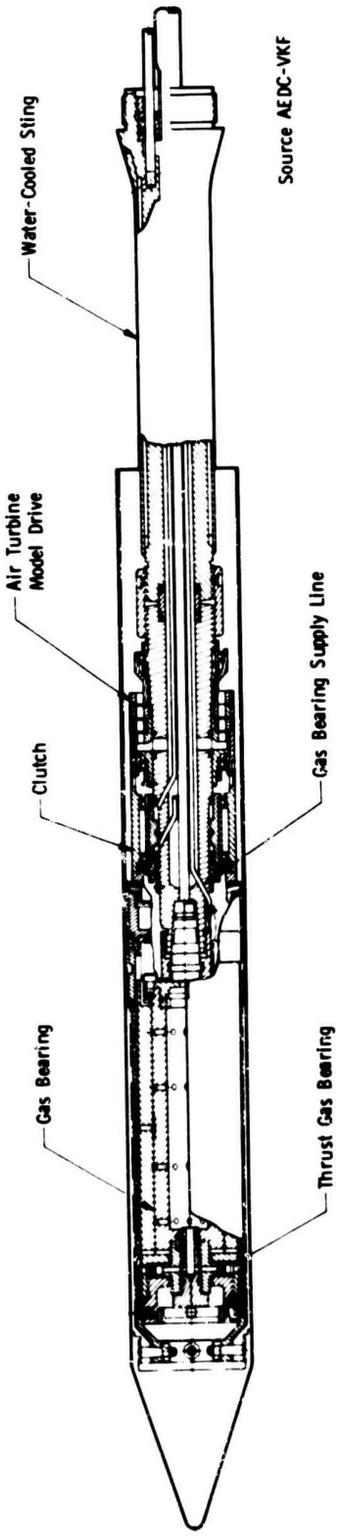

Fig. 89 Air bearing roll-damping balance

Dynamic Steady-Roll Balance, Internal Details

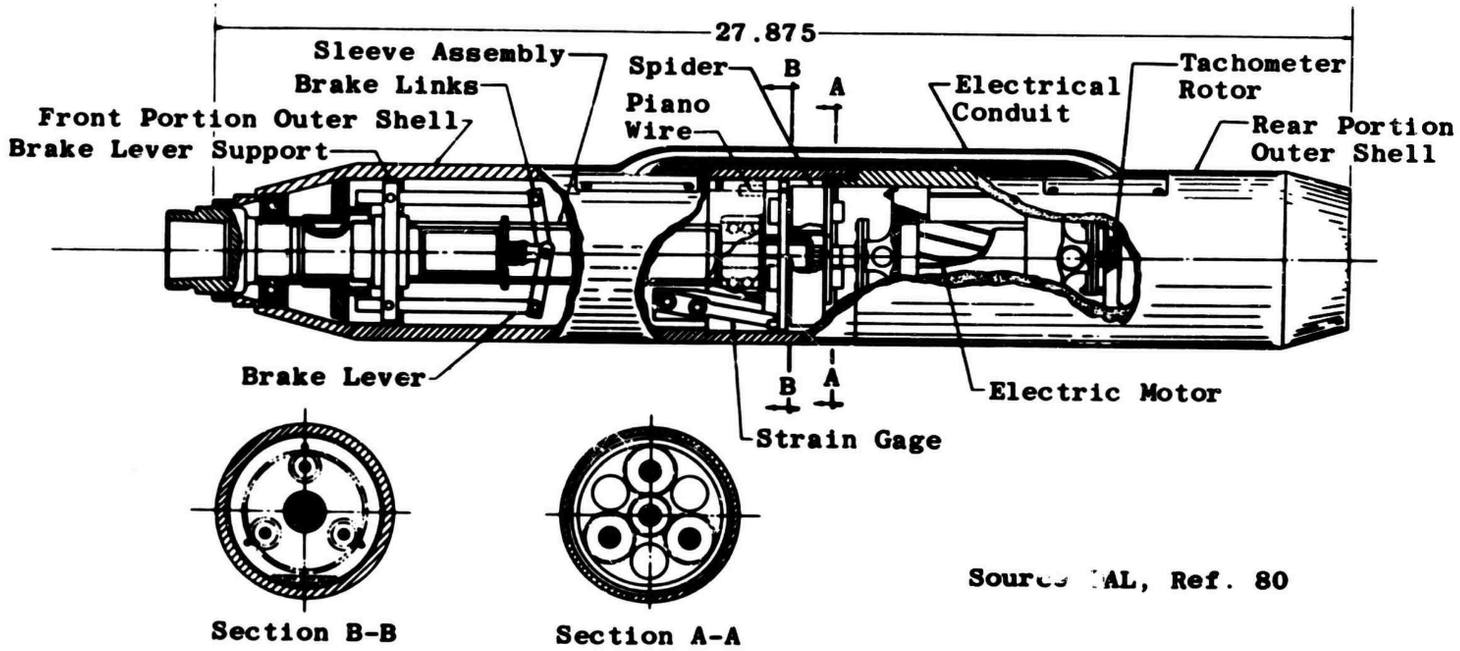

Source: AL, Ref. 80

Fig. 90 Dynamic steady-roll balance

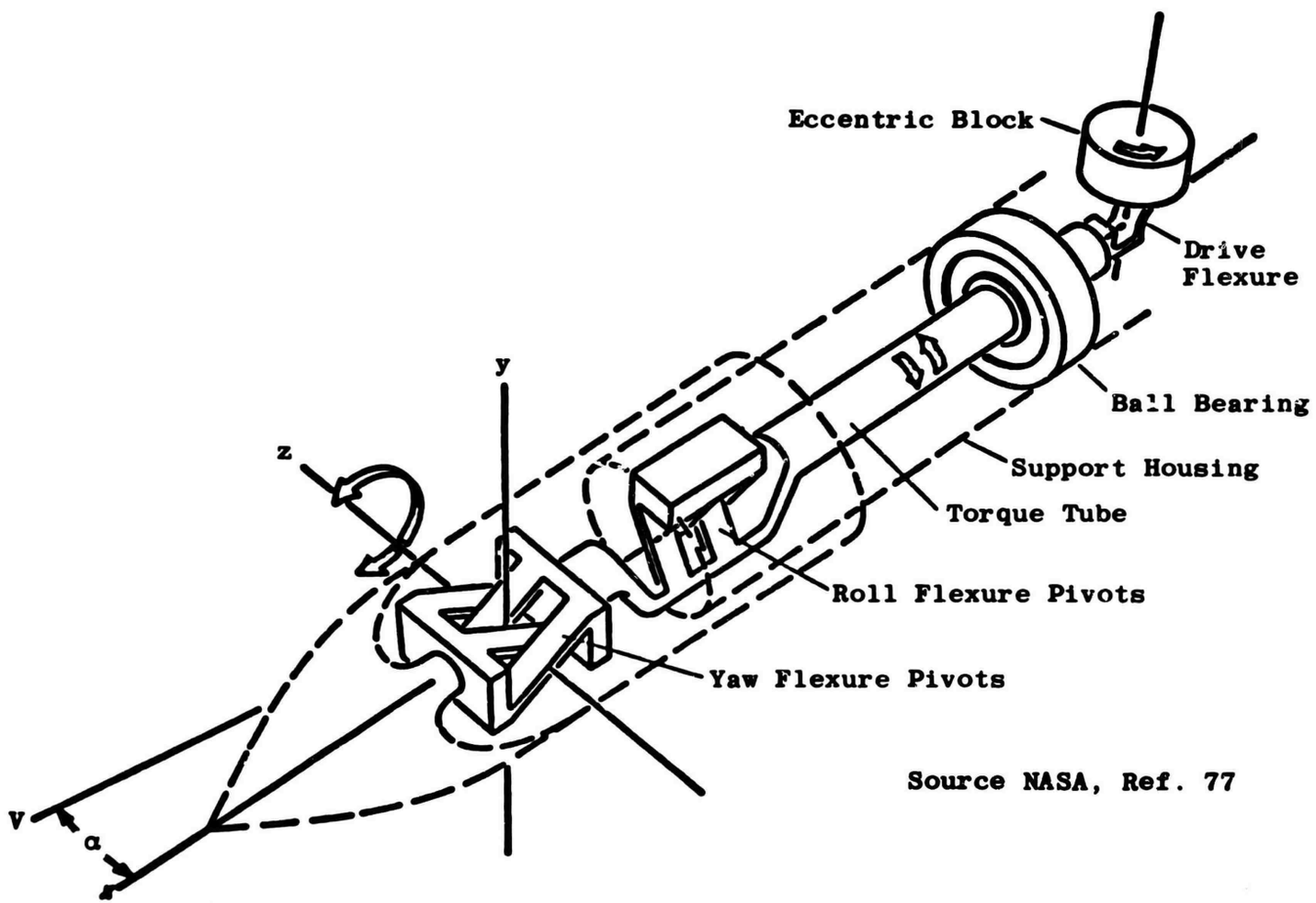

Fig. 91 Forced-oscillation balance

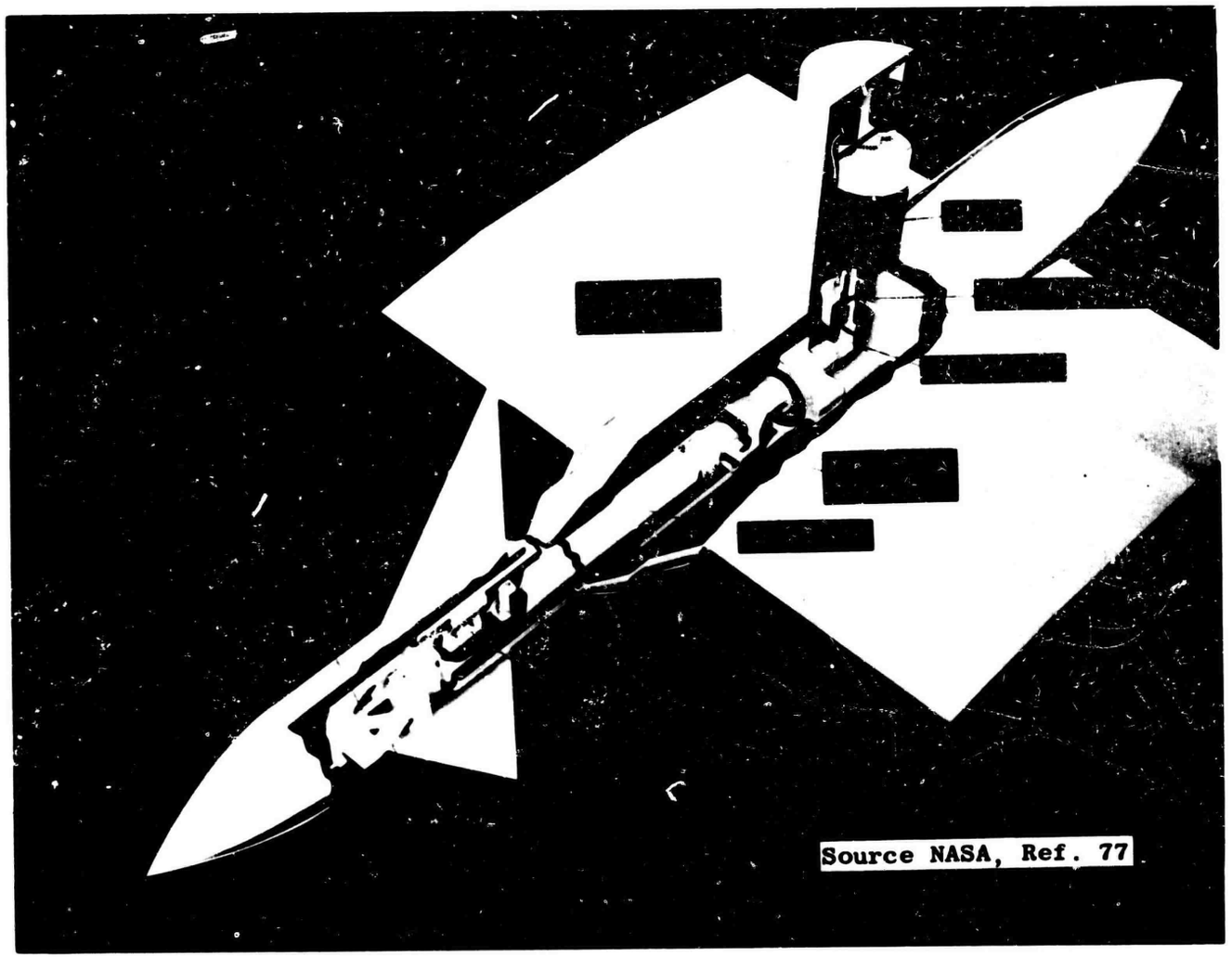

Fig. 92 Pictorial drawing, forced-oscillation balance

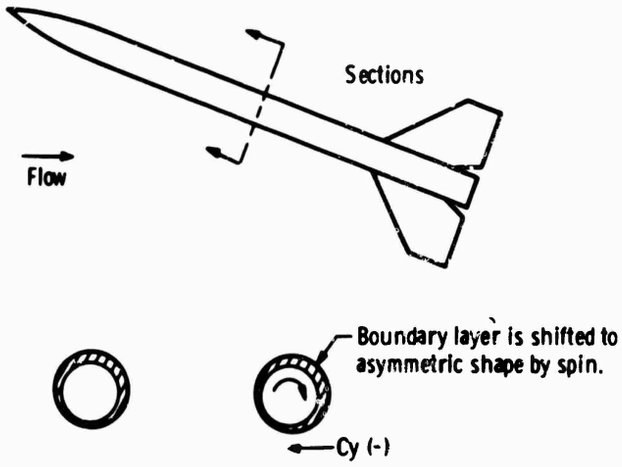

(a) Magnus force at low angles of attack

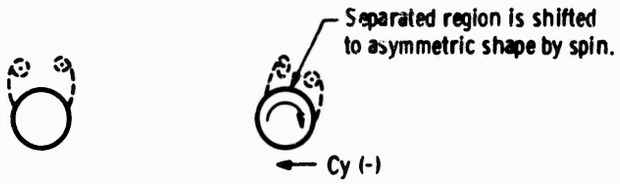

(b) Magnus force at large angles of attack

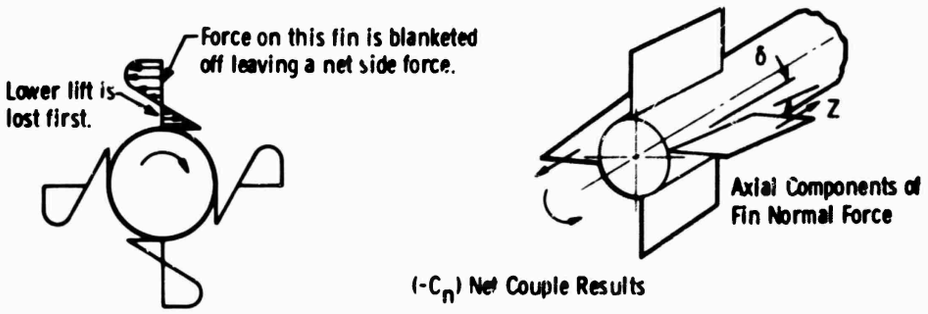

(c) Magnus effects on canted fins

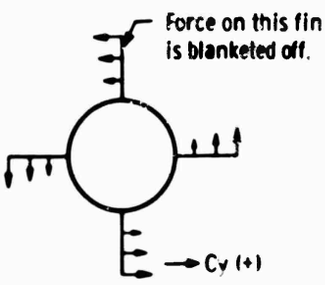

(d) Magnus effects on driven fins

Fig. 93 Illustrations of the various Magnus effects

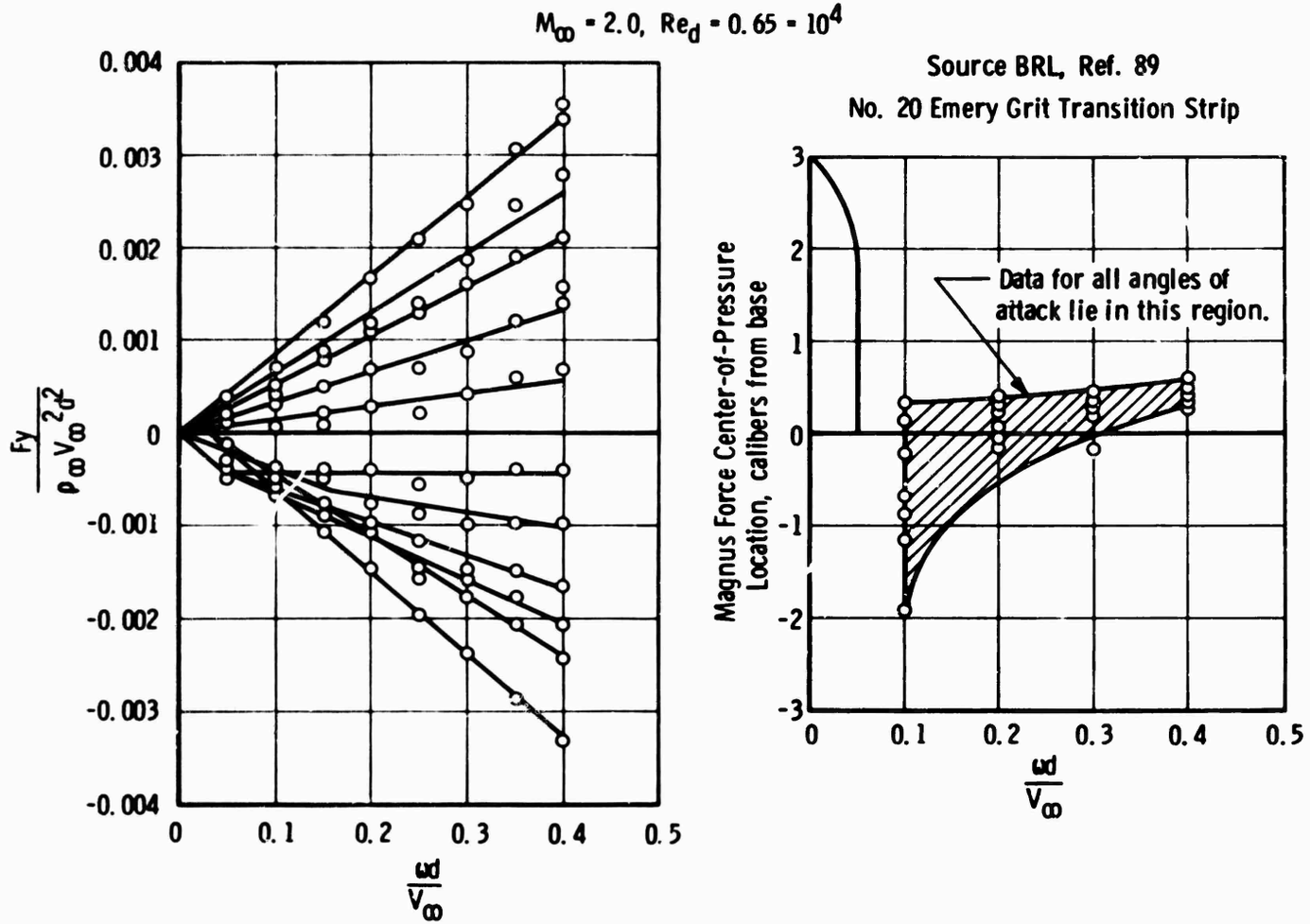

Fig. 94 Effect of spin parameter on the Magnus characteristics

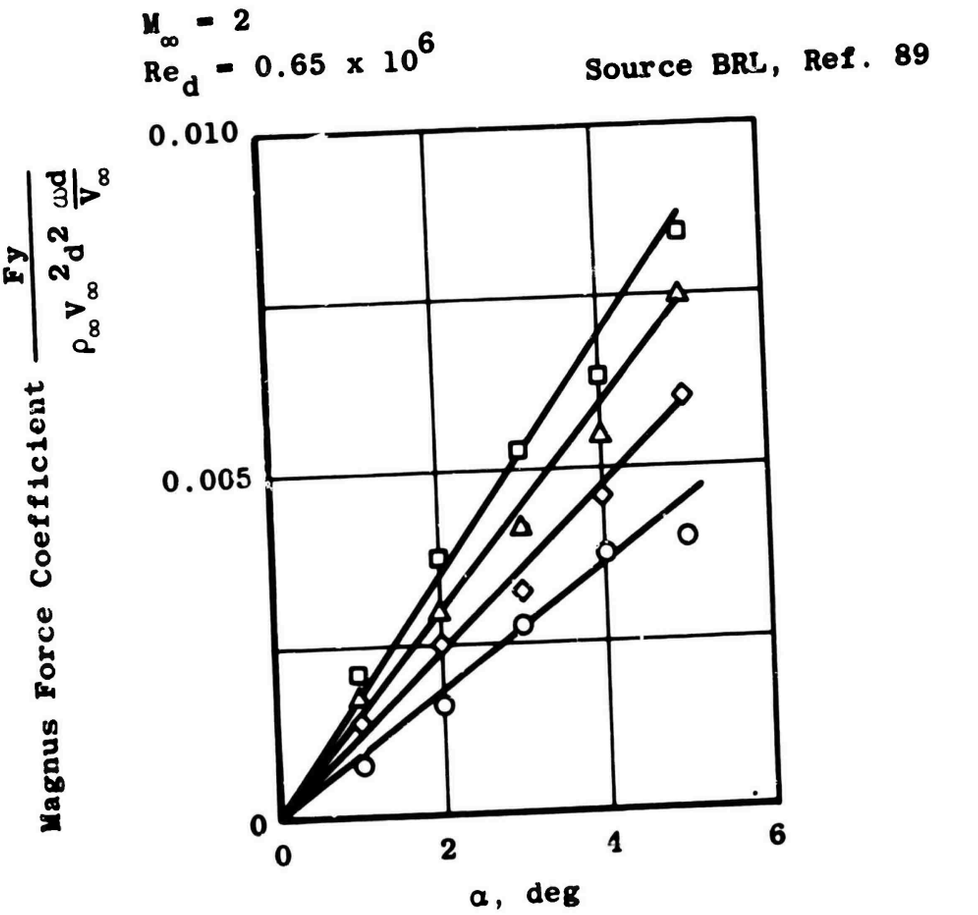

Sym	
○	Laminar Boundary Layer
□	No. 20 Transition Strip (Largest Grit)
△	No. 40 Transition Strip (Medium Grit)
◇	No. 80 Transition Strip (Smallest Grit)

Fig.95 Effect of boundary layer on the Magnus force

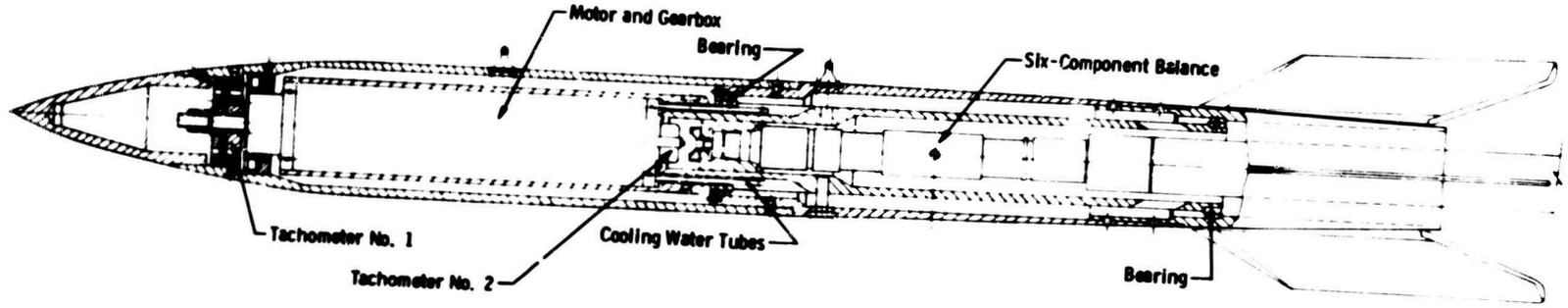

Source Sandia Corp., Ref. 92

Fig. 96 Electric motor drive. Magnus force system

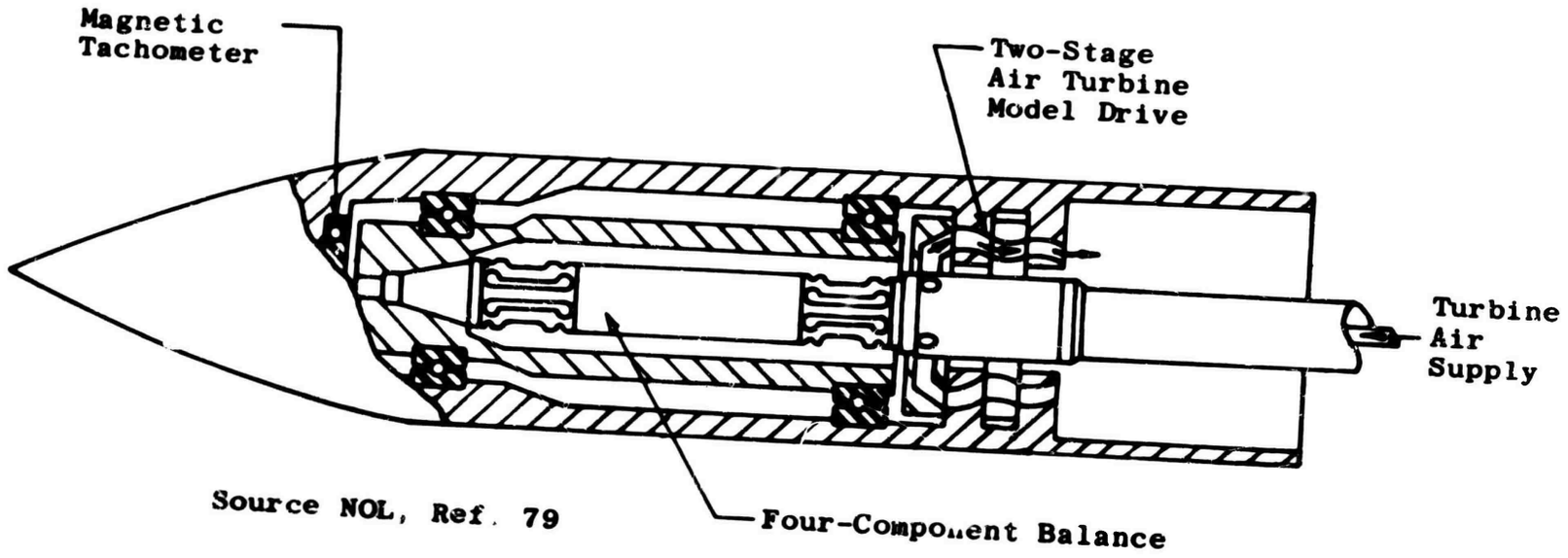

Fig. 97 Magnus force system, turbine drive within the model

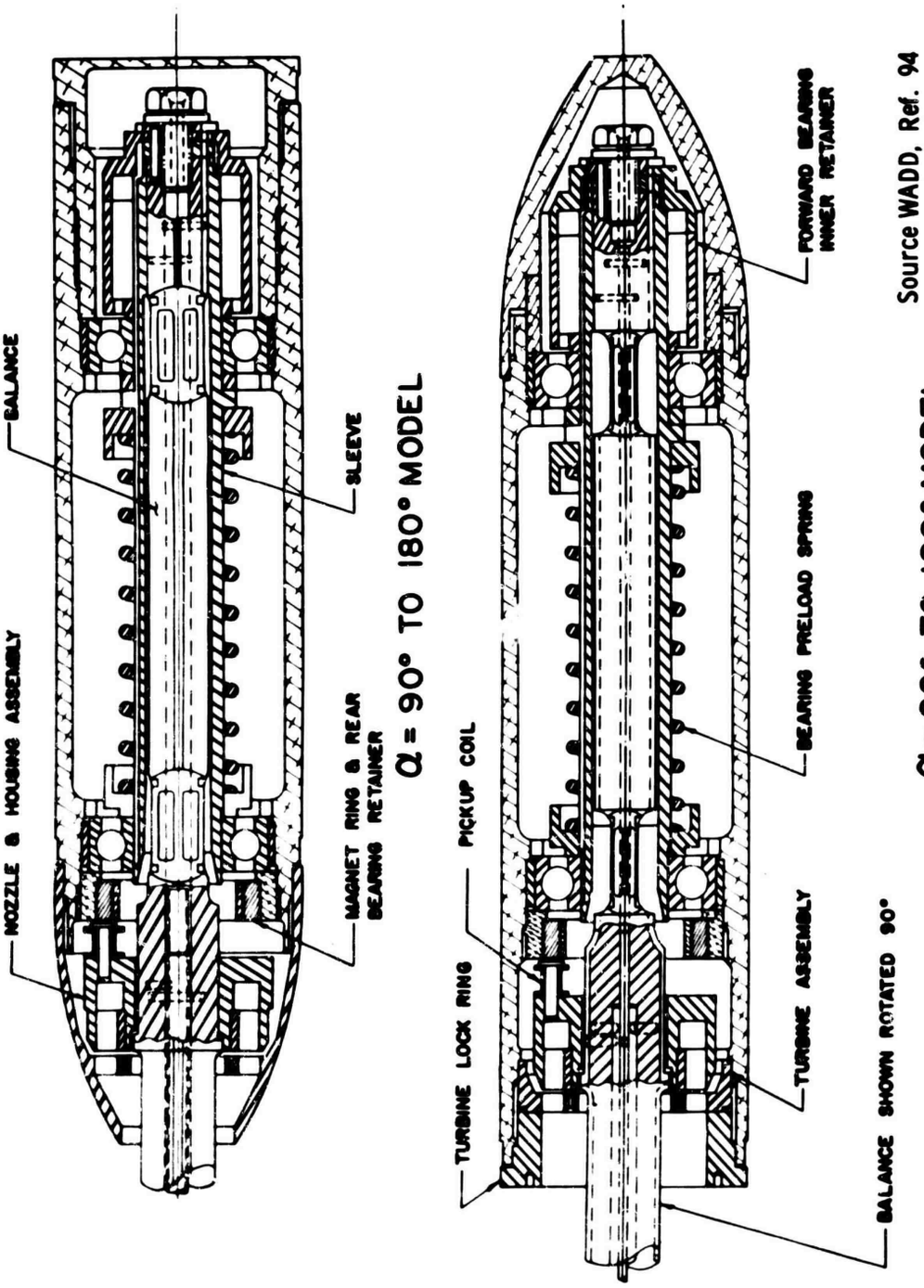

Fig. 98 Magnus force system, turbine drive within the model

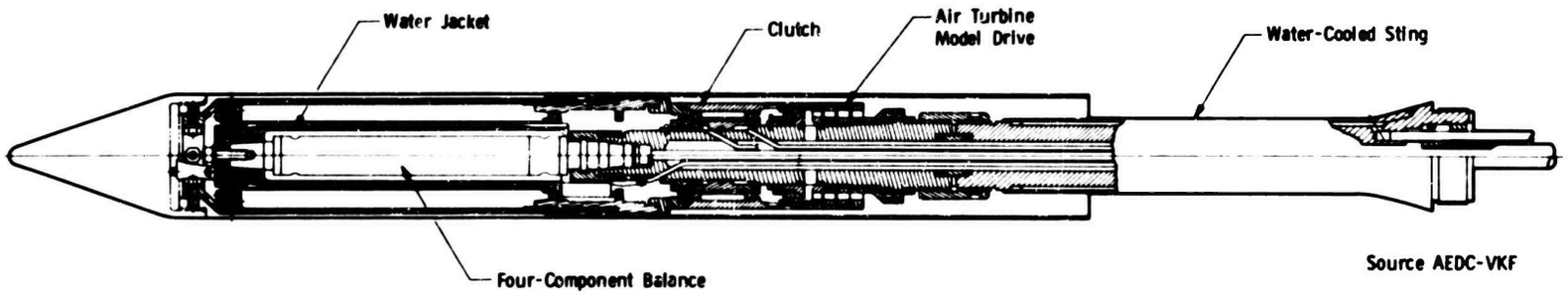

Fig. 99 Magnus force balance

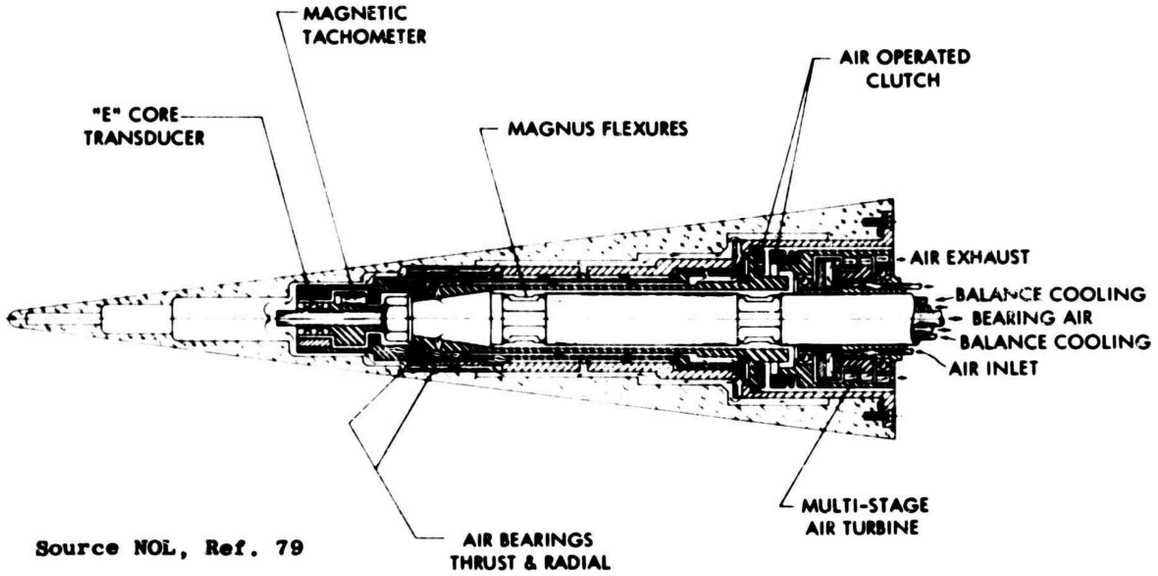

Fig. 100 Magnus-roll damping balance with air bearings

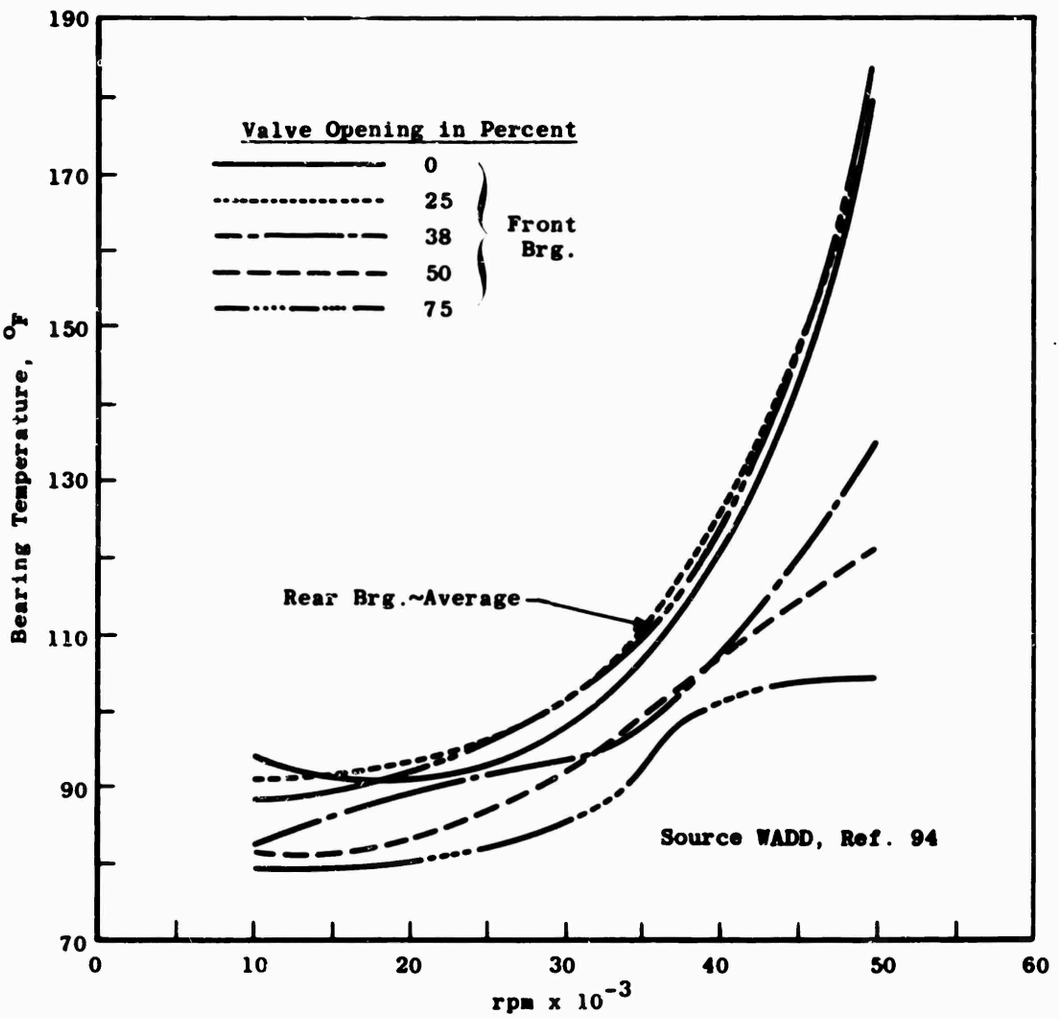

Fig. 101 Variation of bearing temperature with spin rate for bypass air cooling

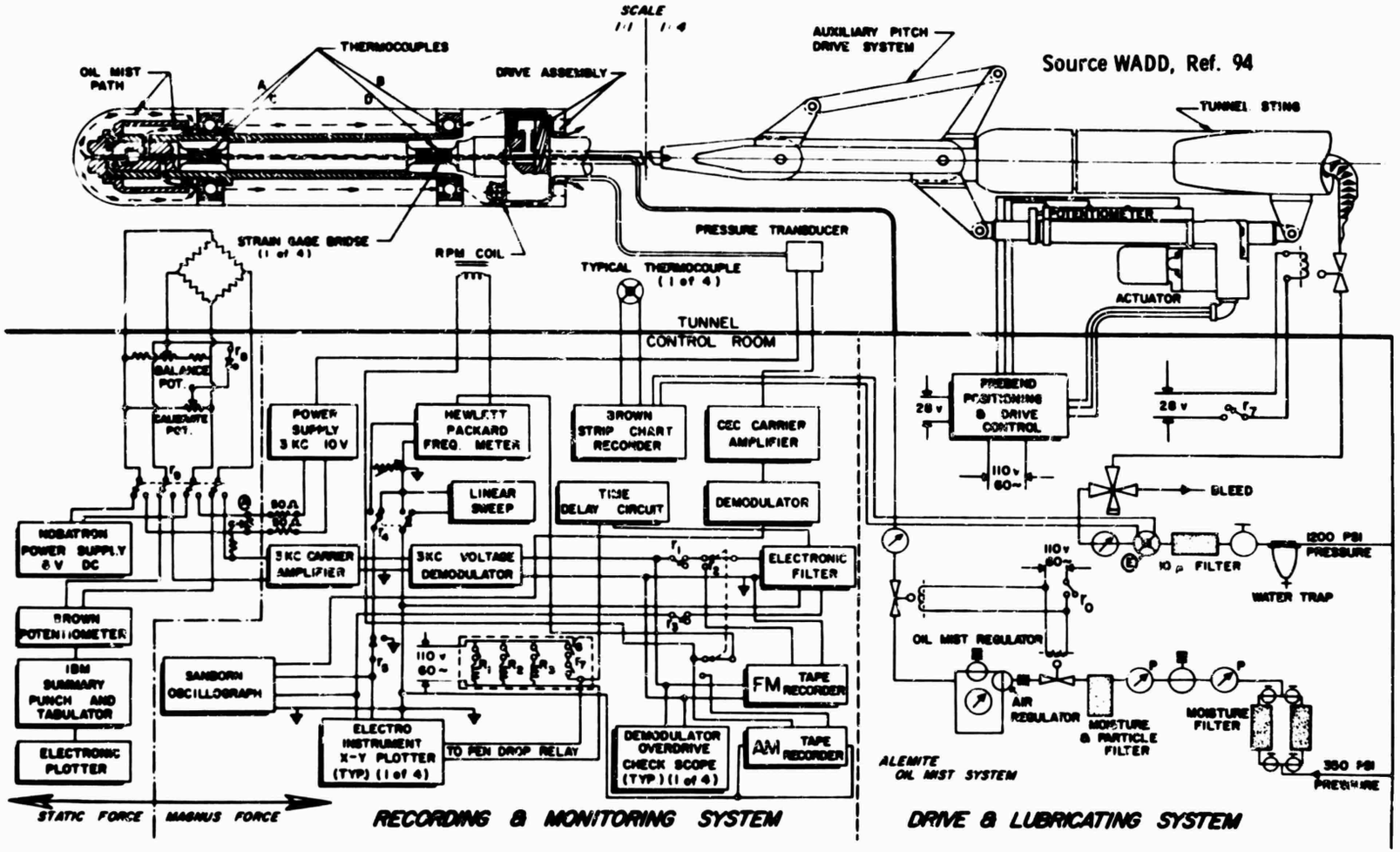

Fig. 102 Oil mist lubricating system and other instrumentation

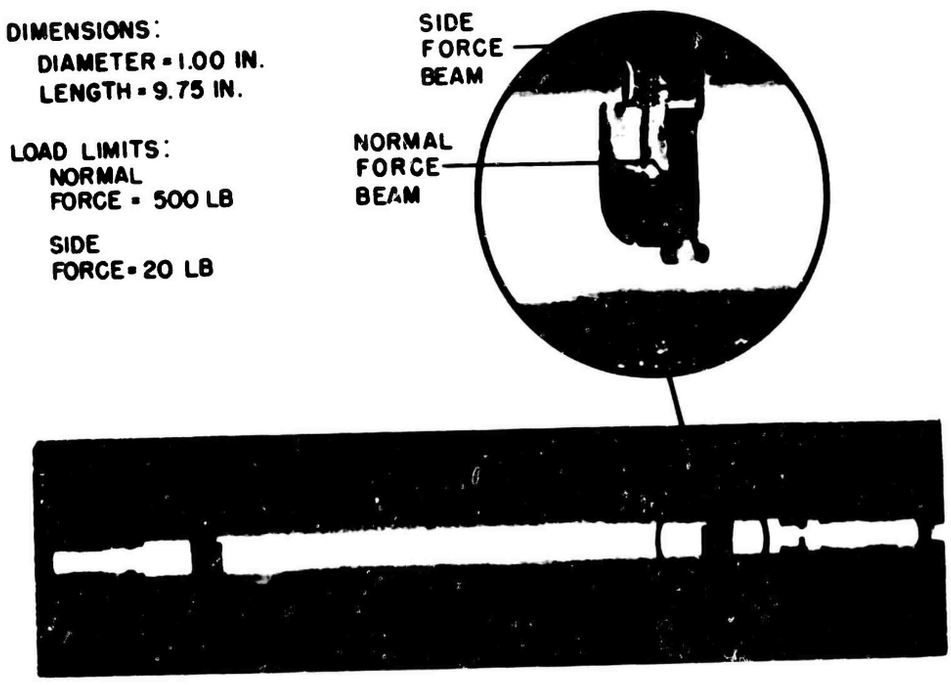

(a) Sandia strain gage balance

SOURCE SANDIA, REF. 95

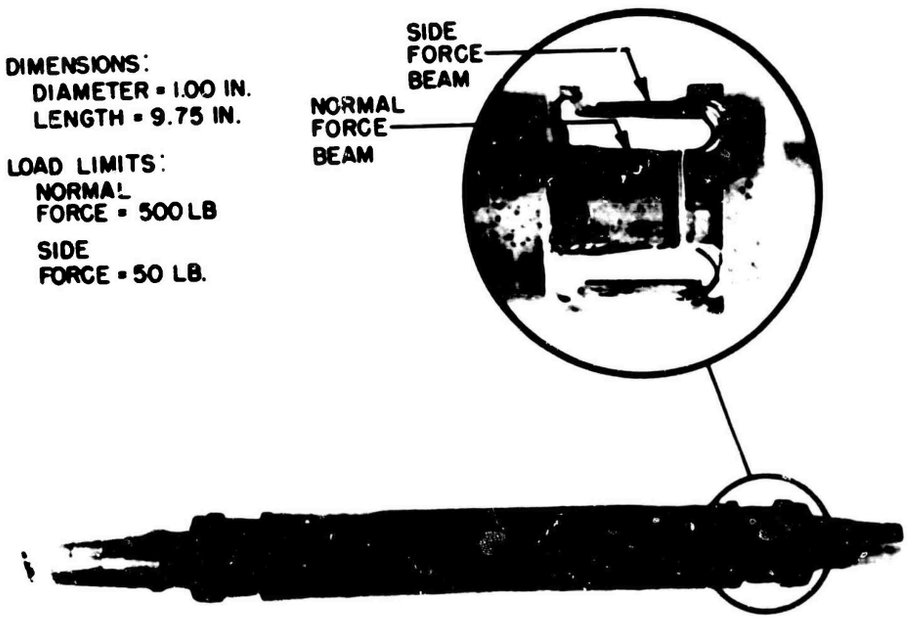

(b) AEDC-VKF strain gage balance

Fig. 103 Two types of Magnus balance gage sections

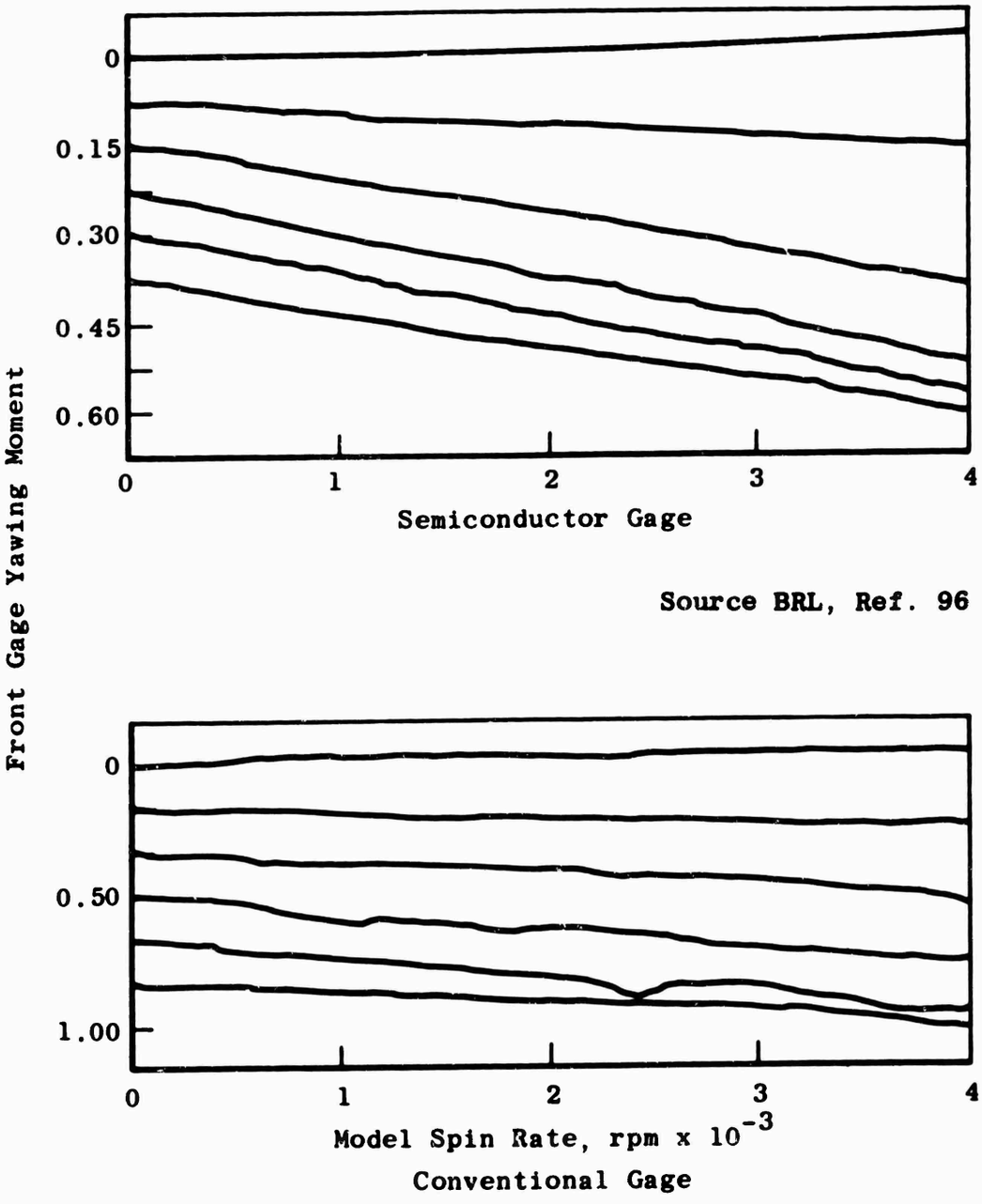

Fig. 104 Comparison of semiconductor and conventional gage outputs

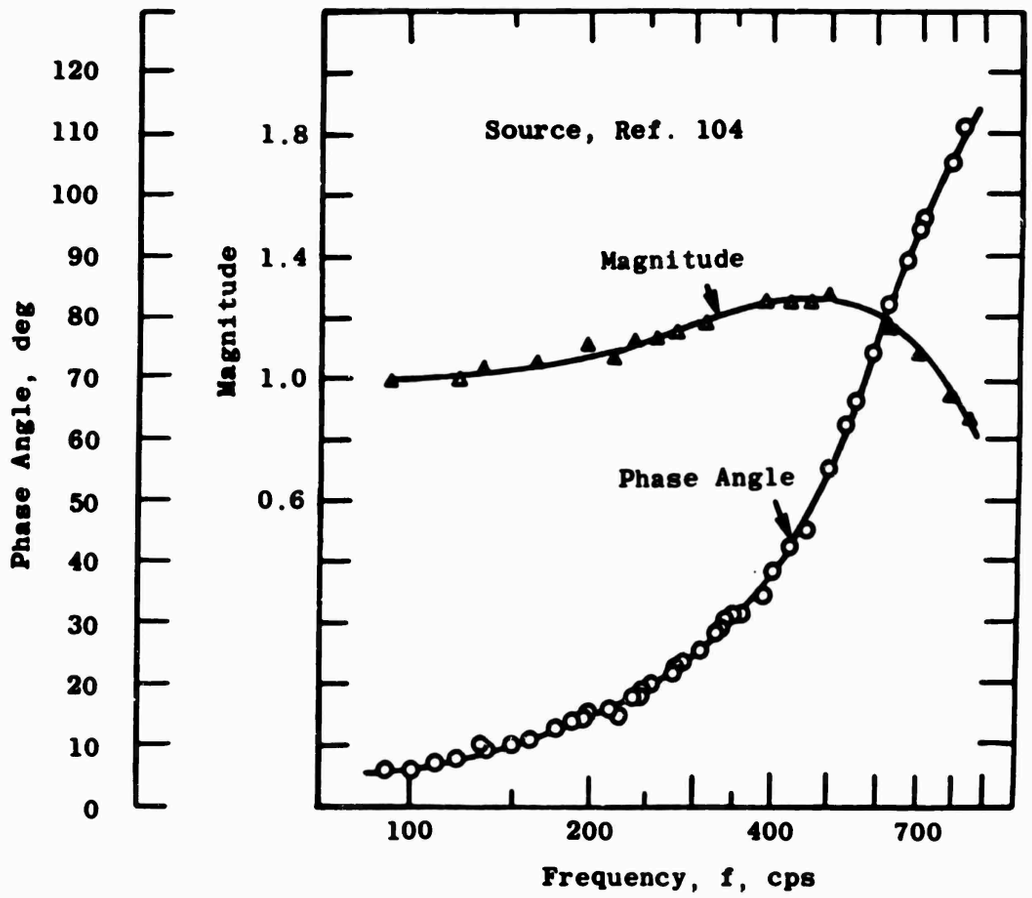

Fig. 105 Experimental response magnitude and phase-angle calibration for 1.38 in. of 0.030 in. nominal-diameter tubing connected to a gage volume of 0.02 cu. in. for air at sea-level conditions

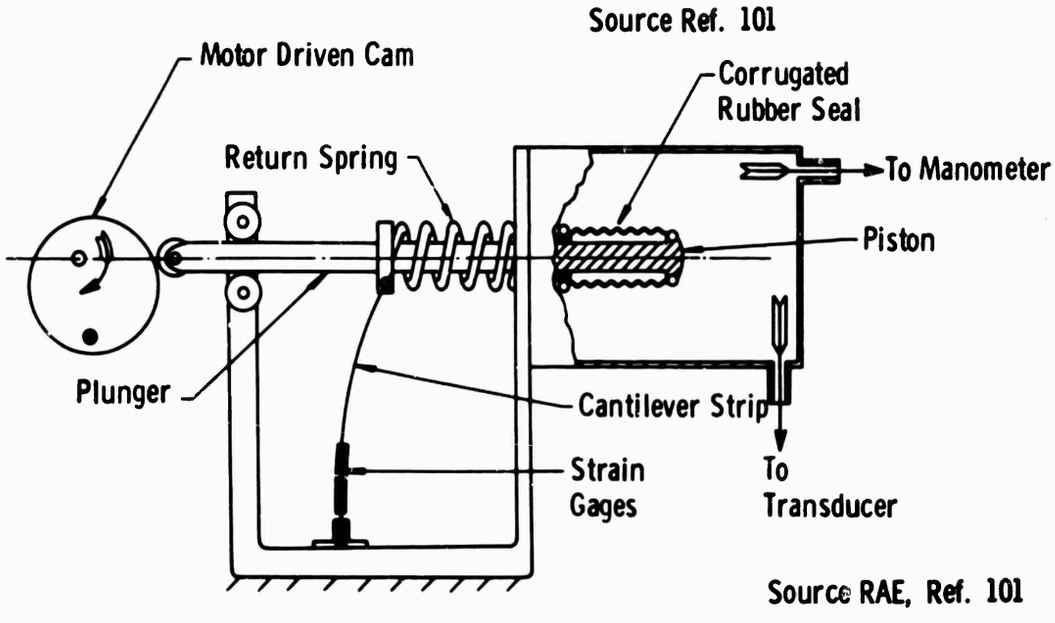

Fig. 106 Pump for sinusoidal oscillating pressure

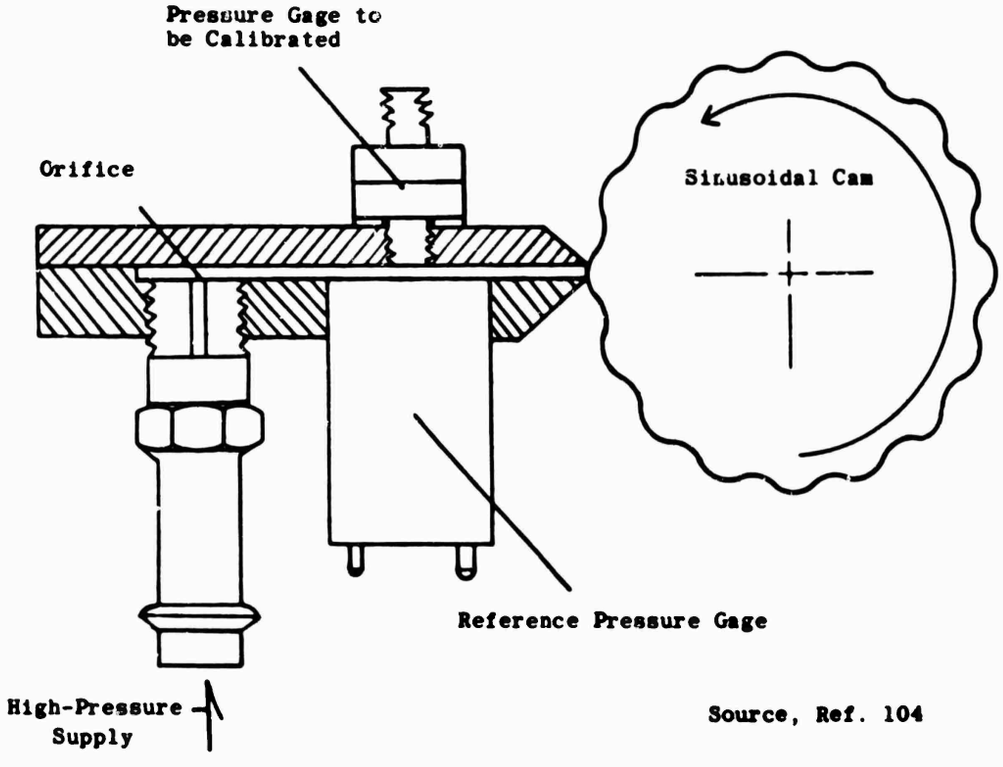

Fig. 107 Cam-type pulsator calibrator